Shock and Vibration

Nonlinear Vibration Isolation

Lead Guest Editor: Zeqi Lu
Guest Editors: Bin Tang, Gianluca Gatti, and Jiaxi Zhou

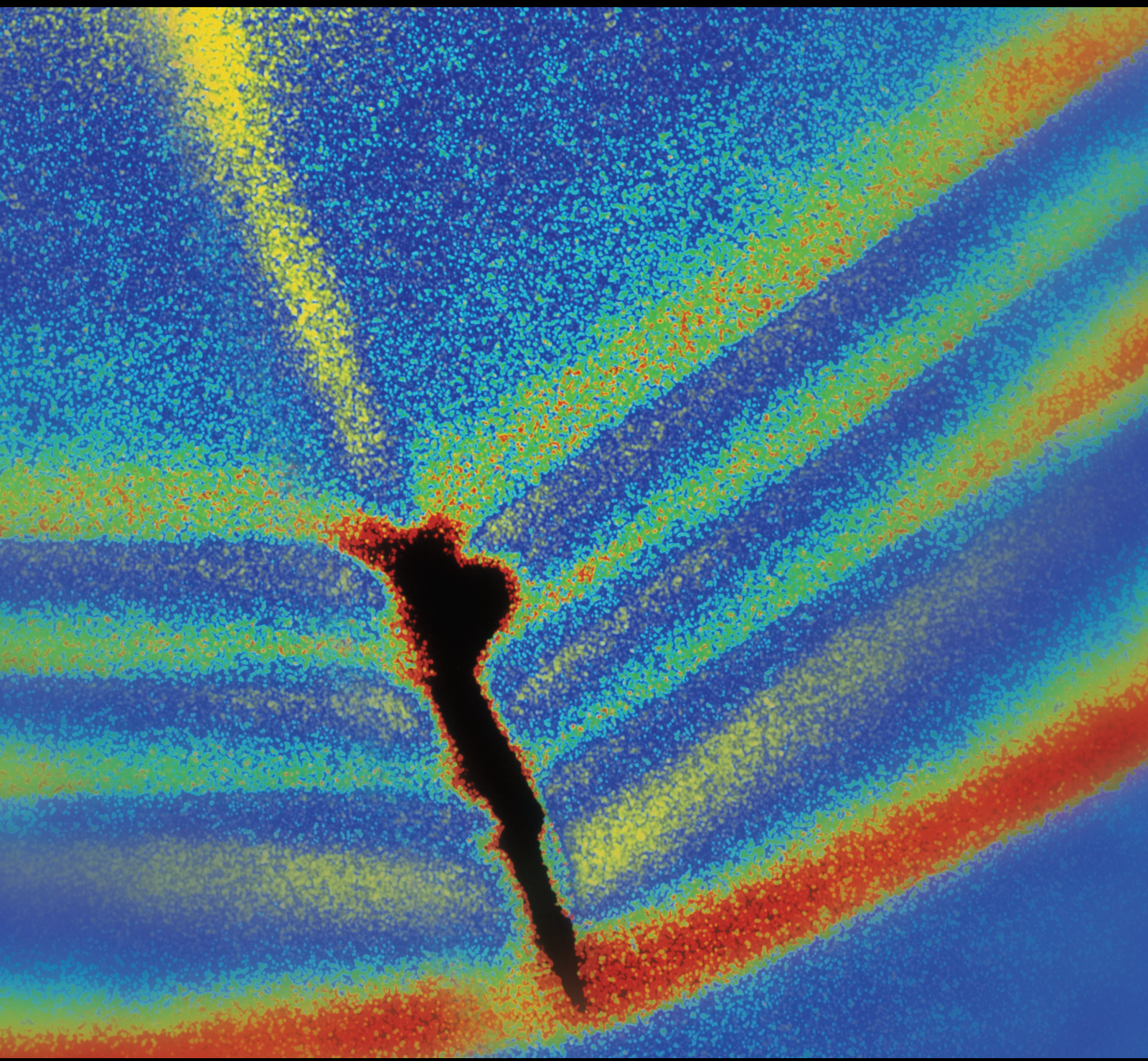

Nonlinear Vibration Isolation

Shock and Vibration

Nonlinear Vibration Isolation

Lead Guest Editor: Zeqi Lu
Guest Editors: Bin Tang, Gianluca Gatti, and Jiaxi Zhou

Chief Editor

Associate Editors

Academic Editors

Contents

Hindawi
Shock and Vibration
Volume 2021, Article ID 5529509, 22 pages
https://doi.org/10.1155/2021/5529509

Research Article

Design and Research of Semiactive Quasi-Zero Stiffness Vibration Isolation System for Vehicles

Shaohua Li[1], **Guizhen Feng**[2,3] **and Quan Zhao**[1,3]

[1]*State Key Laboratory of Mechanical Behavior and System Safety, Train Engineering, Shijiazhuang Tiedao University, Shijiazhuang 050043, China*
[2]*School of Traffic and Transportation, Shijiazhuang Tiedao University, Shijiazhuang 050043, China*
[3]*School of Mechanical Engineering, Shijiazhuang Tiedao University, Shijiazhuang 050043, China*

Correspondence should be addressed to Guizhen Feng; fenggz@stdu.edu.cn

Received 26 January 2021; Revised 16 April 2021; Accepted 25 May 2021; Published 16 June 2021

Academic Editor: Zeqi Lu

The vehicle-mounted equipment is easy to be disturbed by external vibration excitations during transportation, which is harmful to the measurement accuracy and performance of the equipment. Aiming at the vibration isolation of the vehicle-mounted equipment, a semiactively controlled quasi-zero stiffness (QZS) vibration isolator with positive and negative stiffness is proposed. The vertical spring is paralleled with a magnetorheological (MR) damper, and the semiactive on-off control scheme is adopted to control the vibration. The analytical expression of the isolator's displacement transmissibility is derived via the averaging method. Then, the vibration isolation performance under different road excitations and different driving speeds is simulated and compared with the uncontrolled passive QZS vibration isolator. In addition, the mechanical structure of the semiactive QZS isolator is designed and manufactured, and the test system is built by LabVIEW software and PXI embedded system. The isolation effect of the semiactive QZS isolator is verified through test data. It is found that the proposed semiactive QZS isolator shows excellent vibration isolation performance under various road excitations, while the passive QZS isolator is effective only under harmonic excitations. The vertical acceleration of vehicle-mounted device can be decreased over 70% after isolation, and the vibration isolation effect is remarkable. The design idea and research results of the semiactive QZS isolator may provide theoretical guidance and engineering reference for vibration isolation.

1. Introduction

Vibration isolation is a common method to eliminate or weaken vibration [1, 2]. For vehicle vibration, the traditional linear vibration isolator lacks the ability to isolate low-frequency vibration, and the vibration isolation effect is not obvious for 0–20 Hz low-frequency vibration, even having an amplification effect [3]. In transportation, vehicle-mounted equipment is easily disturbed by multiple external vibration sources, which have adverse effects on the accuracy, performance, and the service life of the equipment. Thus, it is quite necessary to design the vibration isolation suitable for excitations with different frequencies to ensure the accuracy and reliability of the vehicle-mounted equipment.

In recent years, QZS vibration isolation has become a research hotspot because of its large bearing capacity and extremely low natural frequency, which can effectively isolate low frequencies. It has various forms, such as cam roller [4–6], oblique spring [7–9], disk spring combined with vertical linear springs [10], circular ring [11], magnet [12], inert elements [13], X-shaped structure [14], strut structure [15, 16], and other structural forms [17–20]. And some researchers studied the resonance response of nonlinear vibration [21] and the damping characteristics [22]. Most of the above literatures focus on the QZS vibration isolation characteristics, but the structure and parameters of the uncontrolled QZS vibration isolation system cannot be changed once determined, which is difficult to meet the complex and changeable working

conditions and restricts the further improvement and universality of the vibration isolation system.

Due to low energy consumption, magnetorheological (MR) damper has been widely used to implement the semiactive control [23, 24]. The modelling of hysteretic characteristics of dampers can be divided into two types: modelling based on physical mechanism and modelling based on external characteristics of macro phenomena. The typical ones are Bouc–Wen model, Preisach model, Duhem model, and neural network model, which can reflect the complex hysteretic characteristics of dampers with multiloops, multibranches, and nonsmoothness. The differential hysteretic model is widely used, such as Duhem model [25]. At present, MR damper is widely used in vehicle suspension control [26–29] and gradually becomes a research hotspot in vehicle vibration isolation. Hu et al. [30] designed a kind of MR damper valve and verified the good damping performance under the sky-hook on-off semiactive control strategy. Dong Chae and Choi [31] proposed a vehicle-mounted vibration isolation system. Using the controllable damping force characteristics of MR damper, the semiactive control effect of the system was analysed and the vibration isolation performance was evaluated. Chae et al. designed a semiactive vibration reduction system for vehicle-mounted stretchers, which used MR dampers as the actuator and realized the vibration isolation control through sliding mode variable structure semiactive control. Gao et al. [32] improved a 4-PUU parallel mechanism as a vehicle stretcher, took MR damper as the output force device, and adopted the LQR method combined with Hrovat algorithm to study the semiactive control and vibration isolation performance of the system. Wang et al. [33] studied the ultralow-frequency vibration isolation in the process of neonatal transport through theory and experiment. However, the research studies considering semiactive control and QZS isolator simultaneously are still seldom found.

In this work, a semiactive QZS vibration isolation system with positive and negative stiffness parallel mechanism is proposed. MR damper is installed in parallel to the vertical spring. Through the analysis of the characteristics of MR damper, an improved Bingham model based on excitation current and response speed is established. The semiactive on-off control scheme is developed, and the control effect is simulated under harmonic, stochastic, and semisinusoidal shock excitations at different vehicle speeds. Finally, the mechanical device of the semiactive QZS isolator is designed and manufactured, and the isolation effect of the system is tested based on LabVIEW software and PXI embedded system to verify the effectiveness of the semiactive control scheme and the good vibration isolation performance of the vibration isolation system.

2. Design of Semiactive QZS Vibration Isolation System

2.1. Modelling of Semiactive QZS Vibration Isolation System. The QZS vibration isolation system controlled by MR semiactive control is shown in Figure 1, which is composed of a positive and negative stiffness spring parallel mechanism and MR damper. Here, m is the mass of the vibration isolated object, k_v and k_h are the vertical spring stiffness and horizontal spring stiffness, respectively, and L is the pre-compressed length of the horizontal spring. When the system reaches the static equilibrium position, the horizontal spring's length is l. y is the vertical displacement of the mass object; $P$is the excitation force of the system. The damping coefficient is set as c_h, and F_c is the damping force provided by MR.

According to D'Alembert's principle, the dynamic equation of the MR semiactive vibration isolation system is obtained.

$$m\ddot{y} + c_h\dot{y}\left(1 - \frac{L}{\sqrt{l^2 + y^2}}\right) + k_h y\left(1 - \frac{L}{\sqrt{l^2 + y^2}}\right) + k_v y + F_c = k_v q - mg. \tag{1}$$

Compared with the semiactive control system shown in Figure 1, the dynamic equation of the passive QZS vibration isolation system is

$$m\ddot{y} + c_h\dot{y}\left(1 - \frac{L}{\sqrt{l^2 + y^2}}\right) + k_h y\left(1 - \frac{L}{\sqrt{l^2 + y^2}}\right) + k_v y + c_v\dot{y} = k_v q - mg, \tag{2}$$

where c_v is the vertical damping coefficient.

To the passive QZS vibration isolation system, it is assumed that the excitation displacement is given by

$$q = A\cos(\omega t), \tag{3}$$

where A is the excitation amplitude, ω is the excitation frequency, and t is the time.

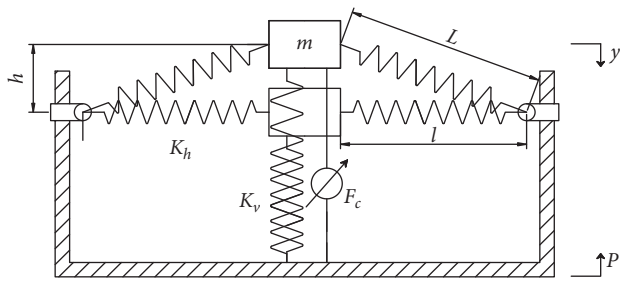

Figure 1: QZS vibration isolation system with MR semiactive control.

Let $x = y/L$, $\alpha = l/L$, $\omega_1 = \sqrt{k_v/m}$, $\omega_2 = \sqrt{k_h/m}$, $\xi_1 = c_v/2\sqrt{k_v m}$, $\xi_2 = c_h/2\sqrt{k_h m}$, $\mu = A/L$, $r = \omega_1^2/\omega_2^2$, $\rho = g/L\omega_1^2$, $\lambda = \omega/\omega_1$, and $\tau = \omega_1 t$; the dimensions of equation (2) can be derived as follows:

$$\mu \sin(\tau) - \rho = \ddot{x} + 2\xi_1\dot{x} + 2\xi_2\dot{x}\left(1 - \frac{1}{\sqrt{\alpha^2 + x^2}}\right) + x + rx\left(1 - \frac{1}{\sqrt{\alpha^2 + x^2}}\right). \tag{4}$$

The approximate analytical solution of equation (5) can be solved by the averaging method as follows:

$$\left.\begin{aligned} \widehat{x} &= \widehat{a}\cos(\omega\tau + \theta) \\ \widehat{x}' &= -\widehat{a}'\omega \sin(\omega\tau + \theta) \end{aligned}\right\}, \tag{5}$$

where $\widehat{a}$ and θ are slowly varying functions of time τ.

According to the averaging method, the amplitude and phase of the first-order approximate solution can be obtained as follows:

$$\left.\begin{aligned} \widehat{a}' &= -\frac{1}{\omega} p(\widehat{a}, \theta)\sin(\omega\tau + \theta) \\ \theta' &= -\frac{1}{\widehat{a}\omega} p(\widehat{a}, \theta)\cos(\omega\tau + \theta) \end{aligned}\right\}, \tag{6}$$

where

$$\begin{aligned} p(\widehat{a}, \theta) = {} & \widehat{a}\omega^2\cos(\omega\tau + \theta) - 2\widehat{a}\omega(\xi_1 + \xi_2)\sin(\omega\tau + \theta) \\ & + \frac{2\widehat{a}\omega\xi_2 \sin(\omega\tau + \theta)}{\sqrt{\alpha^2 + \widehat{a}^2\cos^2(\omega\tau + \theta)}} + \widehat{a}(1 + r)\cos(\omega\tau + \theta) \\ & - \frac{\widehat{a}r\cos(\omega\tau + \theta)}{\sqrt{\alpha^2 + \widehat{a}^2\cos^2(\omega\tau + \theta)}} - \mu\omega^2\cos(\omega\tau + \theta). \end{aligned} \tag{7}$$

In one period of $[0, 2\pi]$, the approximate values of amplitude and phase are obtained as follows:

$$\left.\begin{aligned} \widehat{a}' &= -\frac{1}{2\pi\omega}\int_0^{2\pi} p(\widehat{a}, \theta)\sin\varphi \, d\varphi \\ \theta' &= -\frac{1}{2\pi\widehat{a}\omega}\int_0^{2\pi} p(\widehat{a}, \theta)\cos\varphi \, d\varphi \end{aligned}\right\}. \tag{8}$$

Let $\widehat{a}' = 0$ and $\theta' = 0$; the analytical expression of steady-state amplitude frequency response of the passive QZS vibration isolation system is obtained as follows:

$$\left.\begin{aligned} \omega &= \sqrt{-H(\widehat{a}) \pm \sqrt{[H(\widehat{a})]^2 + \frac{4\widehat{a}^2\omega^2(\xi_1 + \xi_2)^2 + 4\widehat{a}^2\xi_2^2[J(\widehat{a})]^2/\pi^2}{\mu^2 - \widehat{a}^2}}} \\ \theta &= \arctan\frac{2\widehat{a}\omega(\xi_1 + \xi_2) + 2\widehat{a}\omega\xi_2 J(\widehat{a})/\pi}{-\widehat{a}(1 + r) + \widehat{a}\omega^2 + \widehat{a}rI(\widehat{a})/\pi} \end{aligned}\right\}, \tag{9}$$

where

$$I(\widehat{a}) = \int_0^{2\pi} \frac{\cos^2 \varphi}{\sqrt{\alpha^2 + \widehat{a}^2 \cos^2 \varphi}} \mathrm{d}\varphi,$$

$$J(\widehat{a}) = \int_0^{2\pi} \frac{\sin^2 \varphi}{\sqrt{\alpha^2 + \widehat{a}^2 \cos^2 \varphi}} \mathrm{d}\varphi, \tag{10}$$

$$H(\widehat{a}) = \left[4\widehat{a}^2\omega^2(\xi_1 + \xi_2)^2 + \frac{4\widehat{a}^2\xi_2^2[J(\widehat{a})]^2}{\pi^2} - 2\widehat{a}^2(1+r) + \frac{2\widehat{a}^2 r I(\widehat{a})}{\pi}\right] \cdot \left[2\left(\mu^2 - \widehat{a}^2\right)\right]^{-1}.$$

When the passive QZS vibration isolation system is excited by a harmonic force, the steady-state amplitude frequency response is as follows:

$$z = \widehat{a}\cos(\omega\tau + \theta) + \mu\cos(\omega\tau). \tag{11}$$

Then, $z_{\max} = \sqrt{(\widehat{a}\cos\theta + \mu)^2 + (\widehat{a}\sin\theta)^2}$ can be obtained, and the displacement transmissibility of the passive QZS system is obtained as follows:

$$T_f = \left|\frac{z_{\max}}{\mu}\right|. \tag{12}$$

2.2. Characteristics of MR Damper and Semiactive Control Scheme. The damping force of MR damper is expressed by S-shape function as follows [34]:

$$F_c = \frac{2A_c}{1 + \exp(-\alpha y)} - A_c, \tag{13}$$

where A_c is the limit saturation value of the damping force and α is the shape parameter; if the damper structure remains unchanged, αremains unchanged.

According to the parameters of RD-1097-01 MR damper manufactured by Lord company, the resistance of the excitation coil is 20 Ω at 25°C, the maximum damping force is 135 N, the maximum continuous working current is 0.5 A, and the current tends to be saturated when it is greater than 1 A. Then, the damping force of the MR damper can be expressed as follows:

$$\left.\begin{aligned} F_c &= \frac{2A_c}{1 + \exp(-0.0333y)} - A_c \\ A_c &= 222.17I_r^4 - 561.95I_r^3 + 347.26I_r^2 + 112.14I_r + 10.12I \\ I_r &+ 139.4\dot{I}_r + 10164I_r = 10164I_d \\ y &+ 424.4\dot{y} + 90123y = 90123(\dot{x} - \dot{x}_c) \end{aligned}\right\}, \tag{14}$$

where F_c is the output damping force, A_c is the limit saturation value of the damping force, I_d is the given current, $I_r$is the output current, and $\dot{x}$ is the velocity excitation.

The damping force curves under different currents in time domain are shown in Figure 2, and the damping force curves varying with the relative velocity are shown in Figure 3. Figure 4shows the relationship between the excitation current and the damping force of the MR.

Since it is difficult to make the output damping force accurately match the desired control force in experiments and engineering applications, the on-off control scheme is used here due to its good real-time performance.

The control scheme is expressed as follows:

$$F_c = \begin{cases} f_d, & (\dot{y} - \dot{q})\dot{y} \geq 0; \quad I = I_{\text{on}}, \\ f_{\min}, & (\dot{y} - \dot{q})\dot{y} < 0; \quad I = 0, \end{cases} \tag{15}$$

where $\dot{y} - \dot{q}$ is the relative velocity of the mass; $\dot{y}$ is the velocity of the mass; f_d is the semiactive control damping force, which is related to the input current, and $f_d \leq 135$ N; $f_{\min}$ is the minimum value of the output force of the MR damper when the current is the minimum; and $f_{\min} = 0$ when the current is zero.

By judging the direction of relative velocity $\dot{y} - \dot{q}$ and absolute velocity $\dot{y}$ of the controlled mass and controlling the switching of the excitation voltage or current between finite discrete values, the damping force is adjusted. Therefore, when the relative motion of the mass is consistent with the

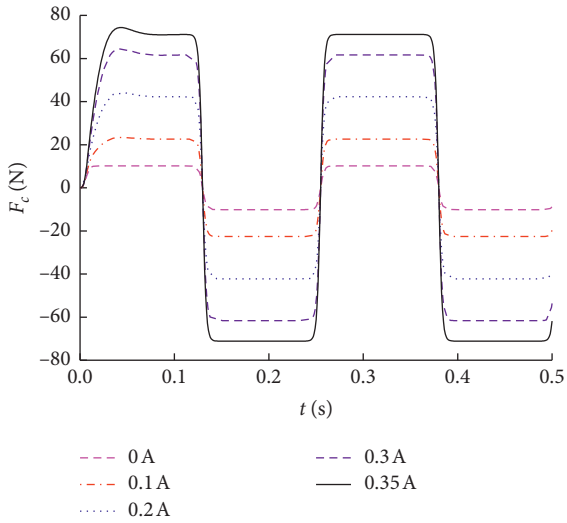

Figure 2: Time domain response of damping force under different currents.

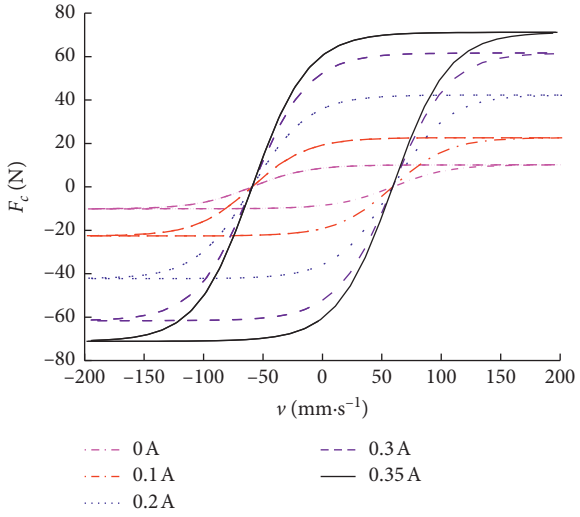

Figure 3: Relationship curve between damping force and velocity under different currents.

direction of the damping force of the MR damper and the excitation current is on, the damper provides the maximum damping force to restrain the mass movement. On the contrary, the damper provides the minimum damping force to reduce the obstruction to the mass movement.

3. Simulation Analysis of Vibration Isolation Effect under Different Excitations

Figure 5 shows the cosimulation scheme of the semiactive MR vibration isolation system based on TruckSim and Matlab/Simulink. The vehicle model is an 8×8 vehicle established in TruckSim. The vertical displacement x_c, vertical velocityv_c, and vertical acceleration a_c of the body centre are taken as the outputs, and x_c is the input.

The parameters of the semiactive QZS vibration isolation system are shown in Table 1.

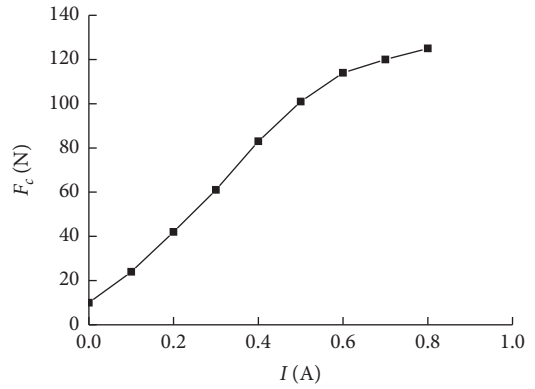

Figure 4: F_c and I curve of MR damper.

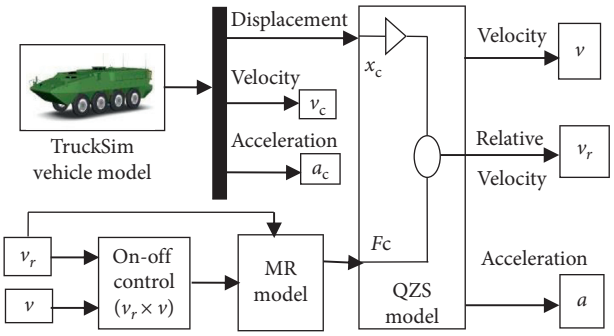

Figure 5: TruckSim/Simulink on-off control cosimulation model.

Table 1: Parameters of the vibration isolation system.

Parameters	Values
M	9.2 kg
k_v	1 017 N/m
k_h	1 010 N/m
c_h	100 N·s/m
L	0.121 m
L	0.081 m
H	0.090 m

3.1. Harmonic Road Excitation. A harmonic road excitation with an amplitude of 5 mm and length of 500 m is used, and the vehicle speed is 30 km/h, 40 km/h, and 50 km/h, respectively. The vibration isolation characteristics of the passive QZS and semiactive QZS isolators are obtained, as shown in Figures 6 and 7. The root mean square and relative differences of the vertical displacement and acceleration of the body centre and the two isolation systems are shown in Table 2 and Figure 8.

It can be seen from Figures 6–8 and Table 2 that

(a) From the vertical displacement response, RMS of the passive QZS vibration isolation system is reduced by 80.6% and the maximum RMS of the semiactive QZS vibration isolation system is reduced by 95.49%, compared with that of the body centre. The maximum vertical displacement reduction of semiactive QZS isolator is 78.1% better than that of the passive QZS isolator.

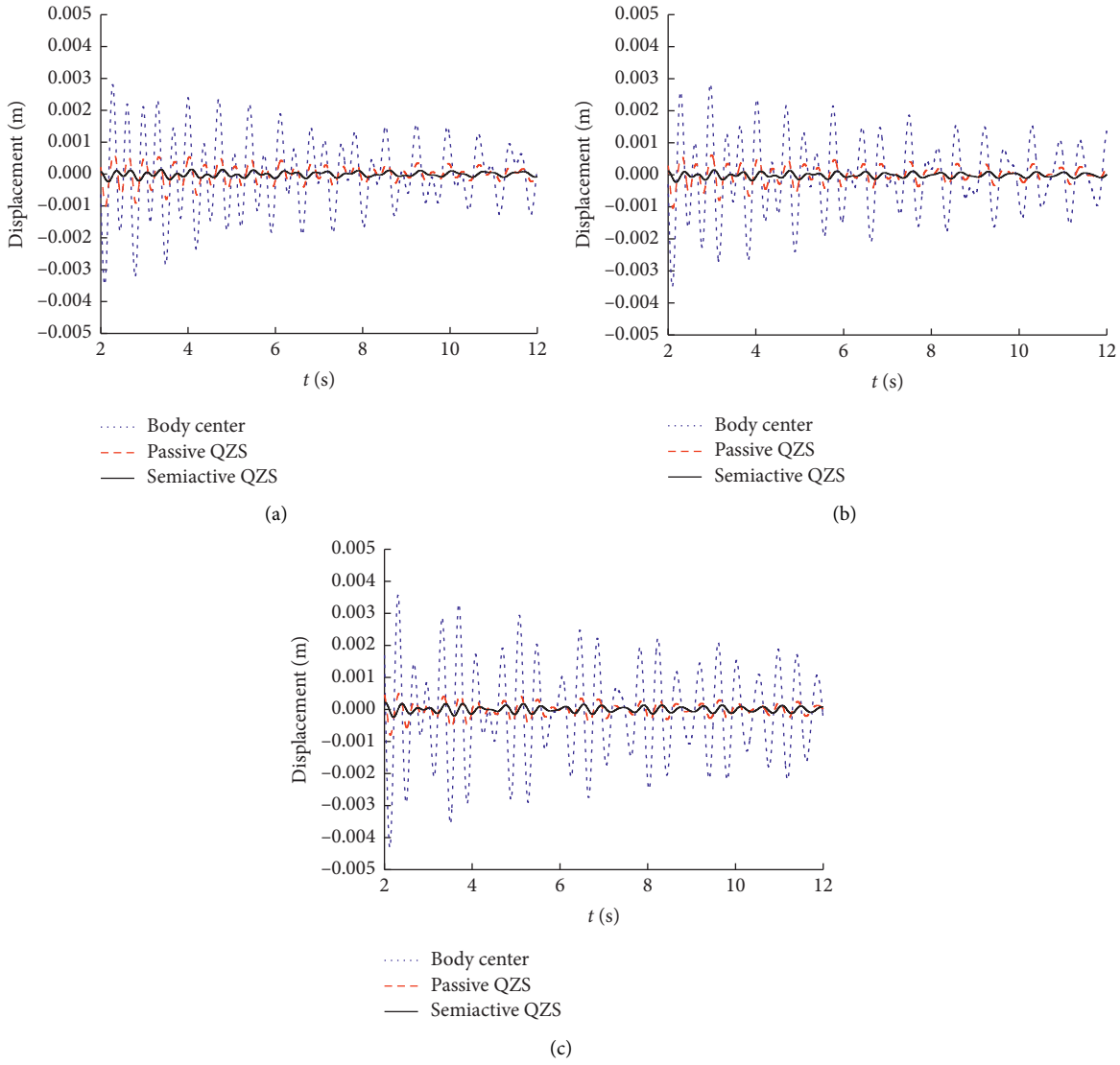

Figure 6: Time domain response of displacement under harmonic excitation: (a) 30 km/h; (b) 40 km/h; (c) 50 km/h.

(b) Compared with the passive vibration isolation system, the maximum vertical acceleration reduction of the semiactive QZS isolator is 74.2%.

(c) Under 5 mm harmonic excitation, the two vibration isolation systems show good vibration isolation performance at different vehicle speeds, but the semiactive QZS vibration isolation system has better vibration isolation performance.

(d) The change trend of body response of the passive and semiactive QZS is the same, but the maximum amplitude and RMS of the semiactive QZS are obviously decreased.

3.2. Stochastic Road Excitation. In practical engineering, the external excitation of a vehicle is mostly random or has strong randomness. The road is built adopting the three-dimensional stochastic road based on fractal theory [35], and the irregularity of the stochastic road surface is given by

$$\dot{q}(t) = -2\pi f_0 v q(t) + 2\pi n_0 \sqrt{G_0 v}\,\omega(t), \tag{16}$$

where q is the stochastic road, v is the speed, G_0 is the road irregularity coefficient, $\omega(t)$ is the Gaussian white noise, f_0 is the cut-off space frequency, generally taken as 0.011 m^{-1}, and n_0 is the reference space frequency, taken as 0.1 m^{-1}.

The three-dimensional road spectrum can better reflect the three-dimensional texture characteristics, which not only reflect the longitudinal irregularity excitation of the road but also meet the requirements of the simulation test for the transverse elevation change, as shown in Figure 9.

Figures 10 and 11 show the vertical time domain response curves of the body centre and two kinds of vibration isolation systems under the condition of C-level stochastic road at different vehicle speeds. See Table 3 and Figure 12 for RMS and relative difference of the two vibration isolation systems and body centre response.

It can be seen from Figures 10–12 and Table 3 that for the road condition of C-level stochastic road excitation, the RMS

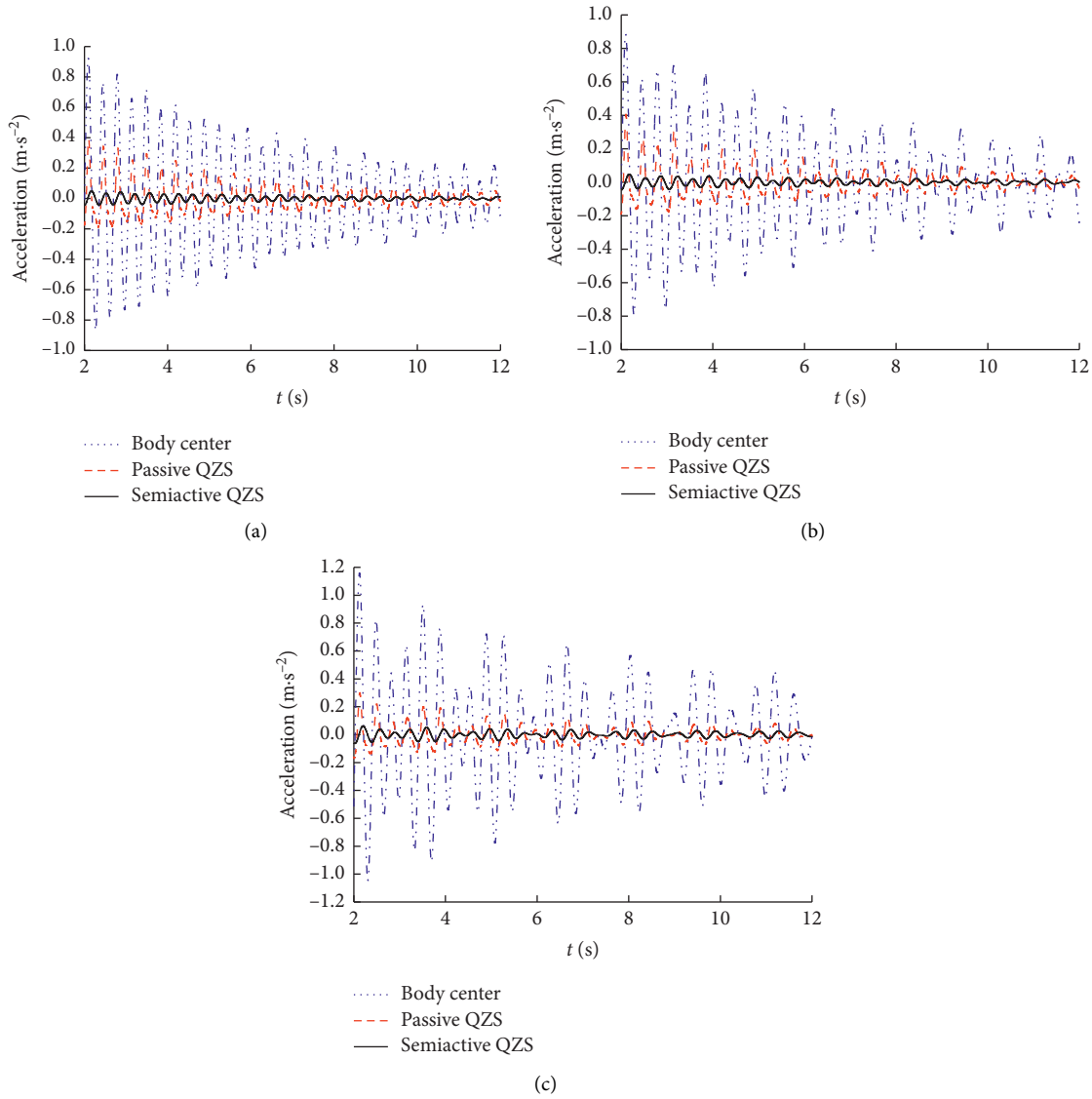

Figure 7: Time domain response of acceleration under harmonic excitation: (a) 30 km/h; (b) 40 km/h; (c) 50 km/h.

of vertical displacement and acceleration of the passive and the semiactive isolators are significantly reduced, with the maximum reduction over 60%. The semiactive vibration isolator shows much better isolation performance than the passive one. At the same time, the passive QZS vibrator is greatly affected by the vehicle speed, the stability is poor, and the vibration isolation efficiency is reduced while the semiactive QZS vibration isolator is less affected by the excitation and vehicle speed, and the vibration isolation efficiency is over 88%.

3.3. Semisinusoidal Shock Road. To verify the shock performance of the isolators, a semisinusoidal shock road with an amplitude of 0.1 m and frequency of 1.4 Hz is established in TruckSim, as shown in Figure 13.

The vertical displacement and acceleration response curves of the body centre and the two vibration isolators are shown in Figures 14 and 15. The RMS and relative differences of the vertical displacement and acceleration response are shown in Table 4 and Figure 16.

As can be seen from Figures 14–16 and Table 4,

(a) The isolation effect of the semiactive QZS isolator is clearly better than that of the passive one under semisinusoidal shock road excitation.

(b) With the increase in vehicle speed, the isolation efficiency of the passive QZS decreases, the response peak value increases, and the stability is poor. While the vibration isolation efficiency of the semiactive control system is about 90%, its stability is better than that of the passive QZS system.

To evaluate the shock resistance performance, the ratio of the peak acceleration response of the isolated object to that of the vehicle body centre is defined as the maximum acceleration ratio, as shown in Table 5.

Table 2: RMS and relative differences of displacement and acceleration under harmonic excitation.

Vehicle speed ($km \cdot h^{-1}$)	Body centre		Passive QZS system				Semiactive QZS system			
	Displacement (m)	Acceleration ($m \cdot s^{-2}$)	Displacement (m)	Displacement difference (%)	Acceleration ($m \cdot s^{-2}$)	Acceleration difference (%)	Displacement (m)	Displacement difference (%)	Acceleration ($m \cdot s^{-2}$)	Acceleration difference (%)
30	1.16×10^{-3}	0.322	2.25×10^{-4}	−80.60	0.066	−79.50	7.68×10^{-5}	−93.38	0.017	−94.72
40	1.64×10^{-3}	0.374	3.42×10^{-4}	−79.15	0.083	−77.81	8.93×10^{-5}	−94.55	0.022	−94.12
50	2.17×10^{-3}	0.396	4.48×10^{-4}	−79.35	0.093	−76.52	9.79×10^{-5}	−95.49	0.027	−93.18

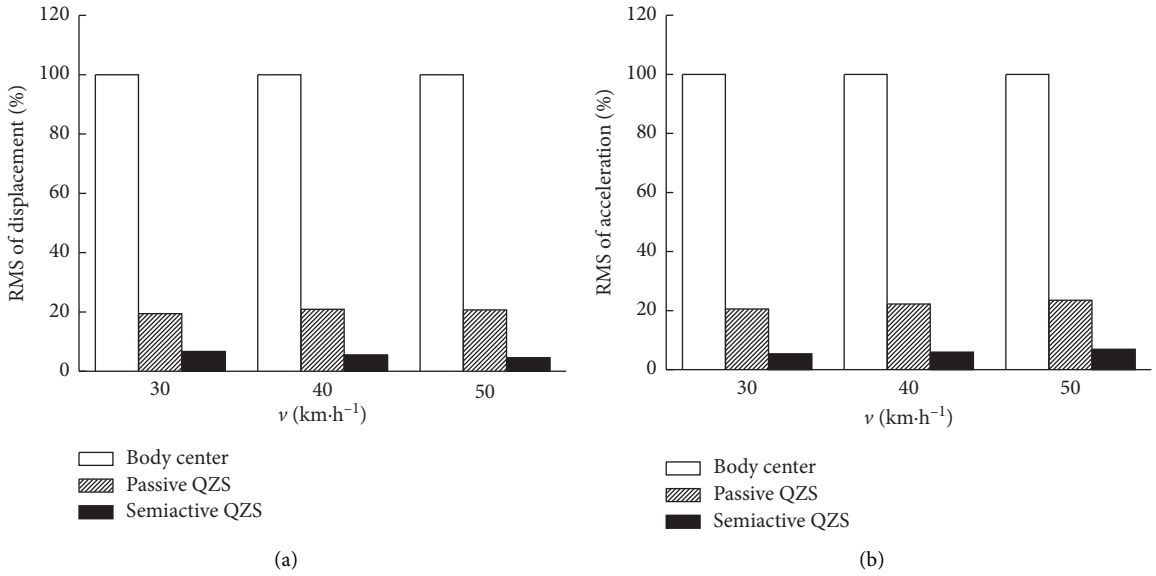

Figure 8: Relative difference between the vibration isolation system and vehicle body under harmonic excitation: (a) displacement; (b) acceleration.

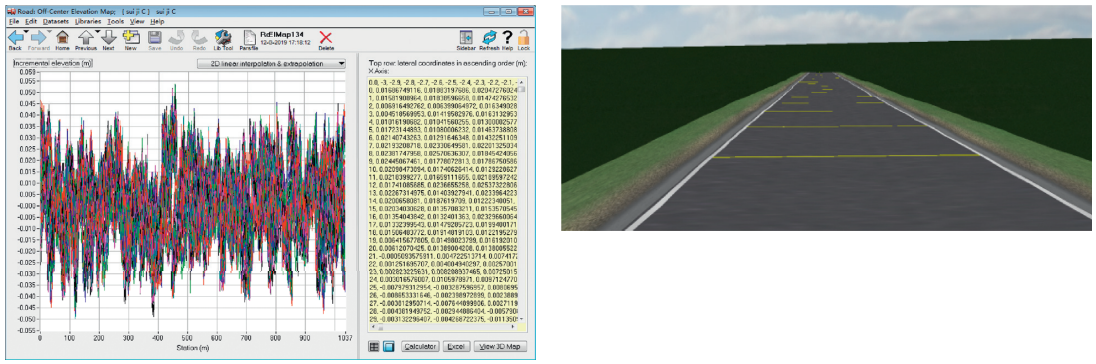

Figure 9: C-level stochastic road excitation: (a) cross section elevation setting; (b) road model.

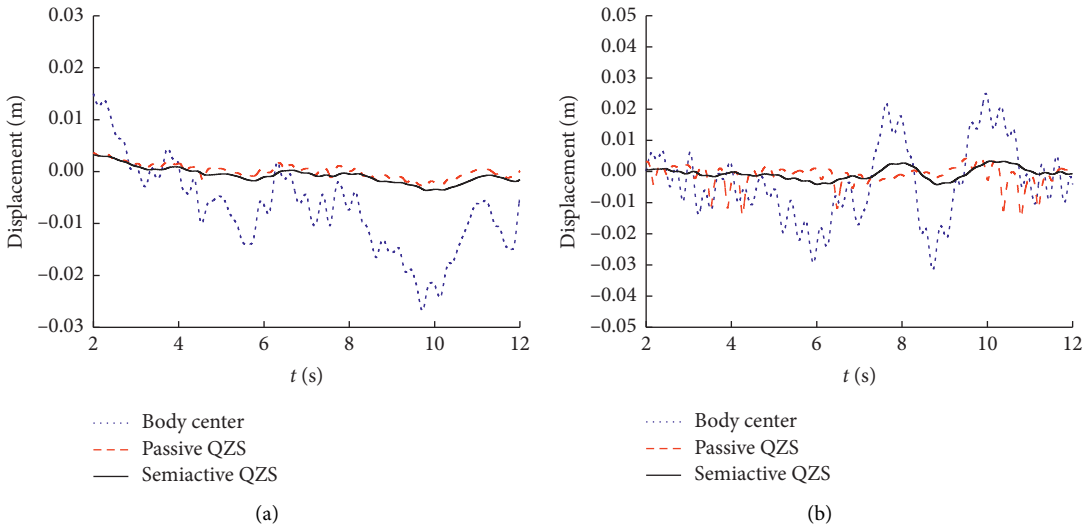

Figure 10: Continued.

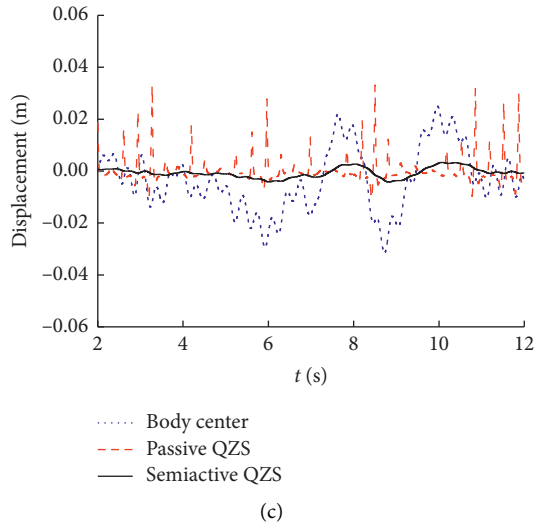

Figure 10: Time domain response of displacement under stochastic road: (a) 30 km/h; (b) 40 km/h; (c) 50 km/h.

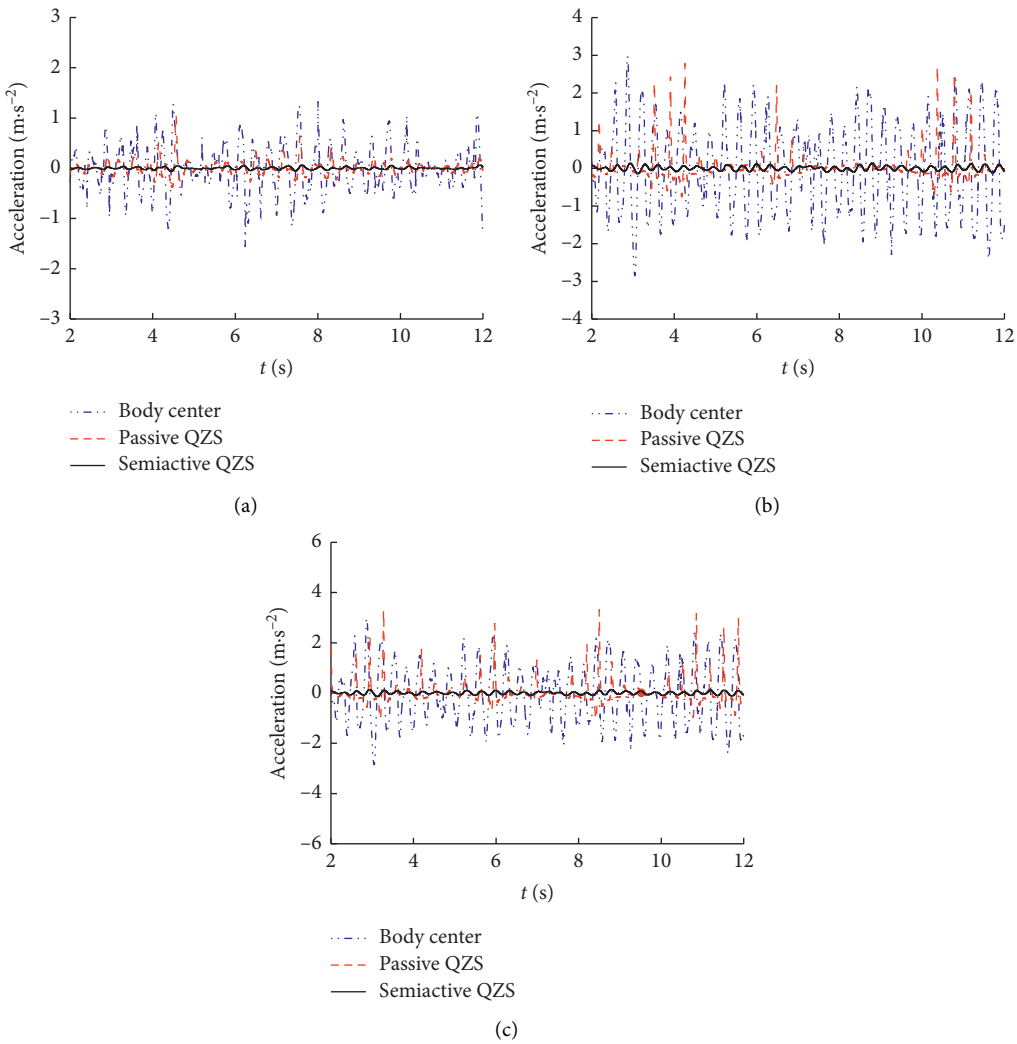

Figure 11: Time domain response of acceleration under stochastic road: (a) 30 km/h; (b) 40 km/h; (c) 50 km/h.

Table 3: RMS and relative differences of displacement and acceleration response under stochastic road.

Vehicle speed ($km \cdot h^{-1}$)	Body centre		Passive QZS system				Semiactive QZS system			
	Displacement (m)	Acceleration ($m \cdot s^{-2}$)	Displacement (m)	Displacement difference (%)	Acceleration ($m \cdot s^{-2}$)	Acceleration difference (%)	Displacement (m)	Displacement difference (%)	Acceleration ($m \cdot s^{-2}$)	Acceleration difference (%)
30	0.011	0.742	2.37×10^{-3}	−78.45	0.242	−67.39	1.67×10^{-3}	−84.82	0.074	−90.03
40	0.013	1.163	3.54×10^{-3}	−72.77	0.441	−62.08	2.04×10^{-3}	−84.31	0.126	−89.17
50	0.021	1.654	5.89×10^{-3}	−71.95	0.647	−60.88	3.35×10^{-3}	−84.05	0.187	−88.69

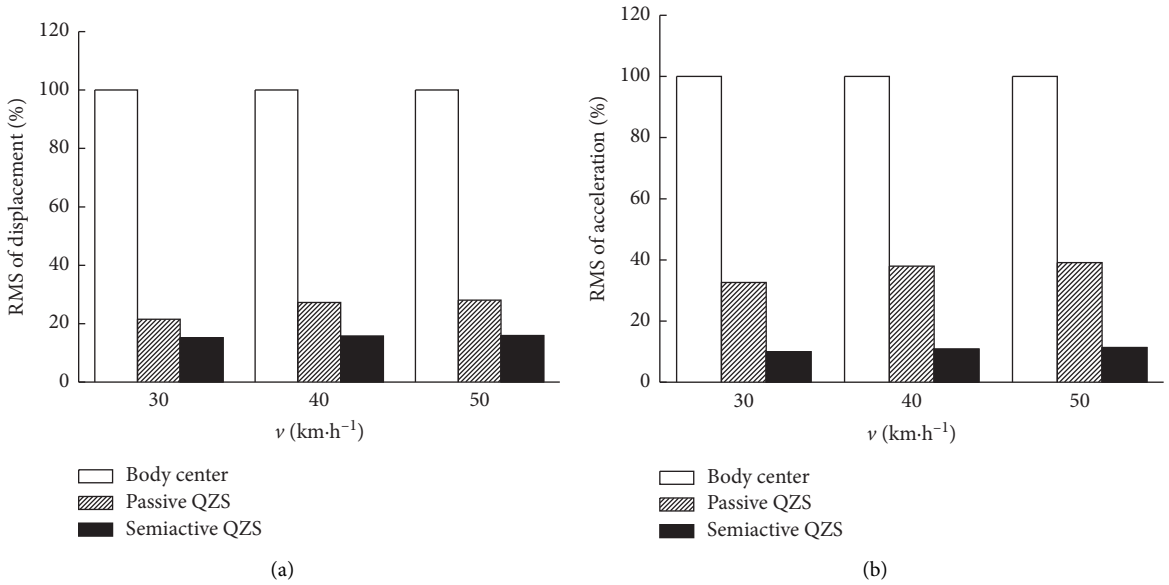

Figure 12: Relative difference of RMS of (a) displacement and (b) acceleration under C-level random pavement

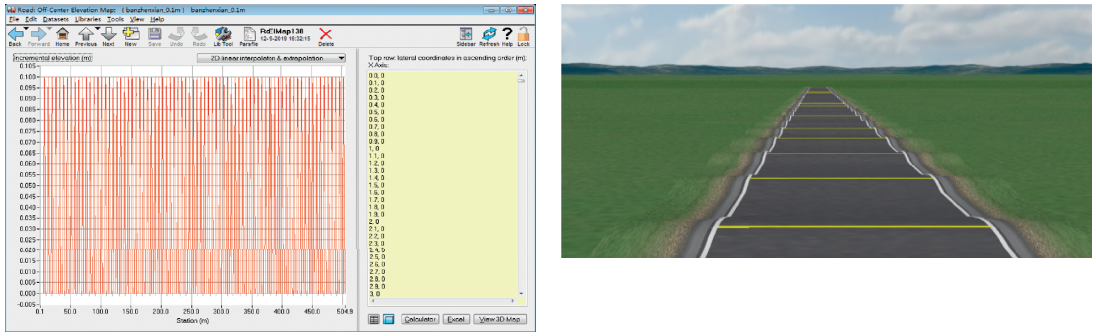

Figure 13: Semisinusoidal shock road: (a) cross section elevation setting; (b) road model.

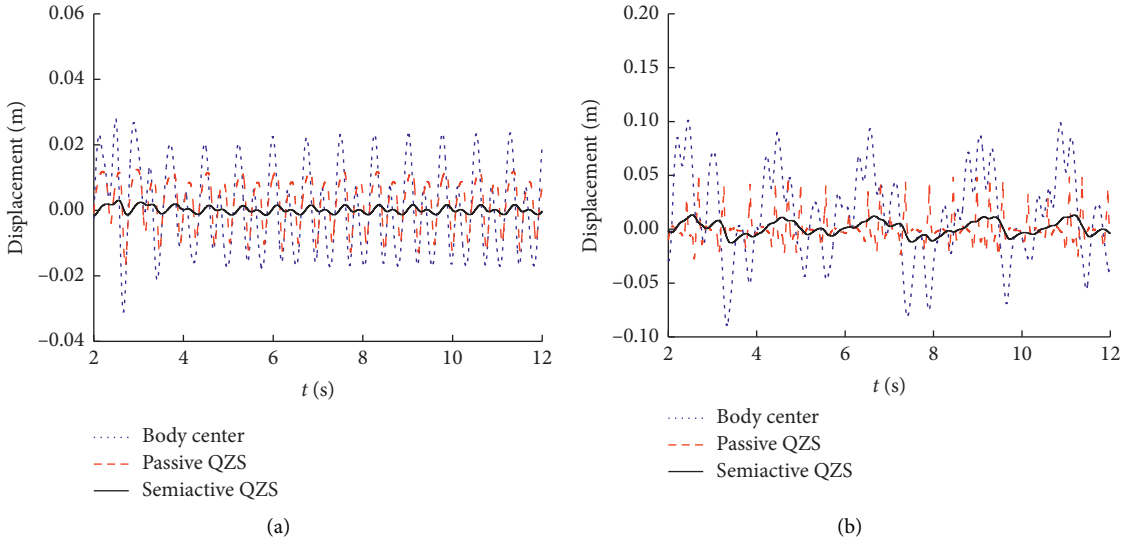

Figure 14: Continued.

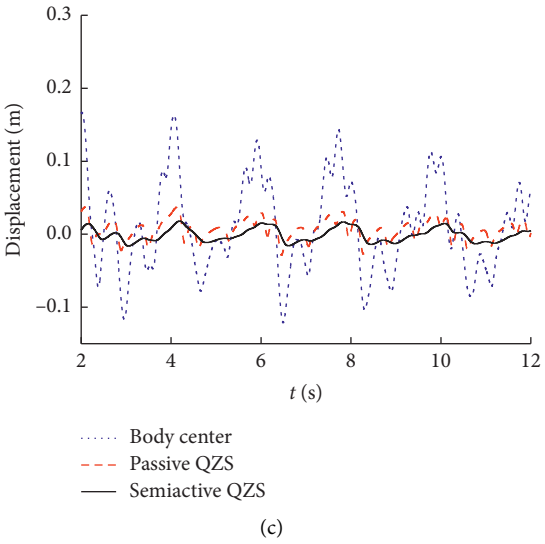

(c)

Figure 14: Time domain response curve of displacement under semisinusoidal shock road: (a) 30 km/h; (b) 40 km/h; (c) 50 km/h.

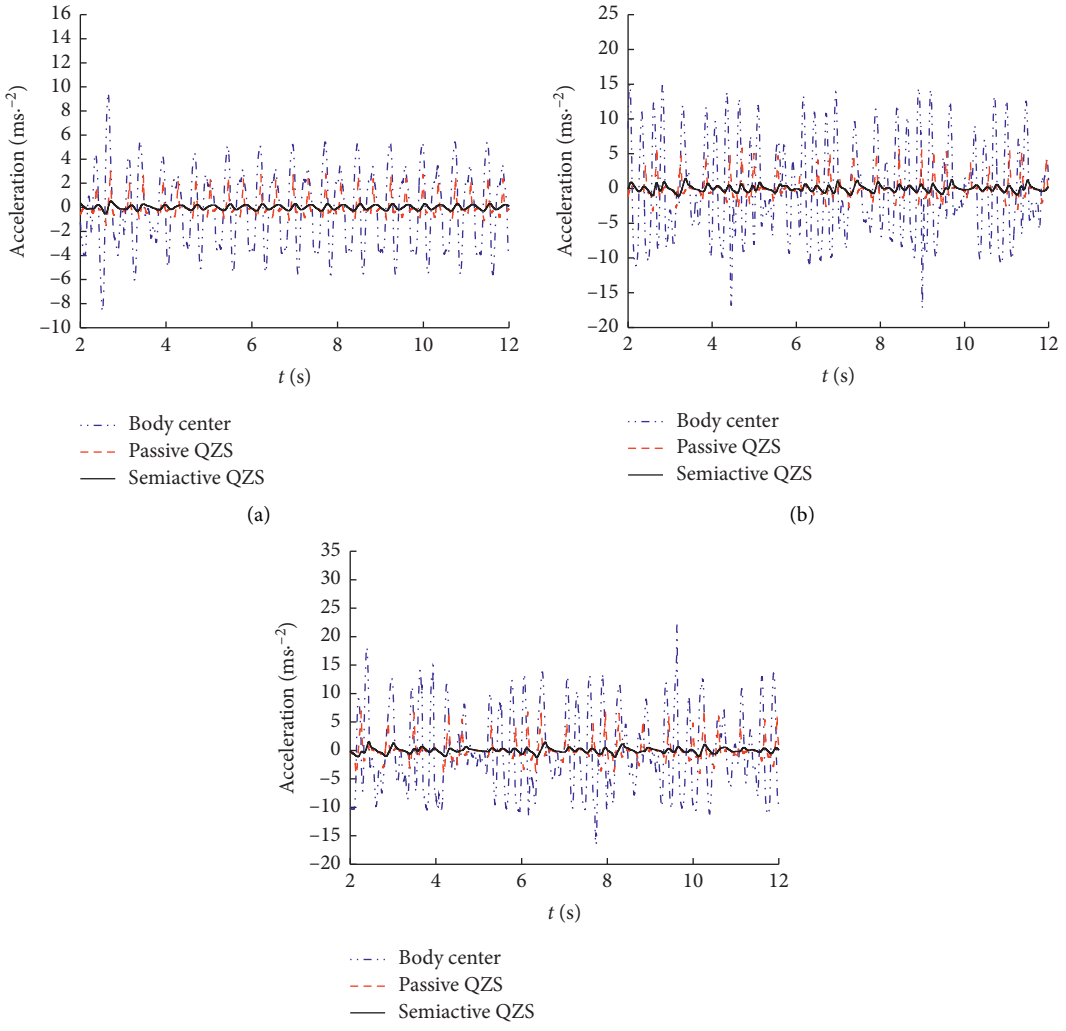

(a)

(b)

(c)

Figure 15: Time domain response curve of acceleration under semisinusoidal shock road: (a) 30 km/h; (b) 40 km/h; (c) 50 km/h.

Table 4: RMS and relative differences of vertical displacement and acceleration under semisinusoidal shock road.

Vehicle speed ($km \cdot h^{-1}$)	Body centre		Passive QZS system				Semiactive QZS system			
	Displacement (m)	Acceleration (m·s-2)	Displacement (m)	Displacement difference (%)	Acceleration ($m \cdot s^{-2}$)	Acceleration difference (%)	Displacement (m)	Displacement difference (%)	Acceleration ($m \cdot s^{-2}$)	Acceleration difference (%)
30	0.032	4.278	0.012	−62.50	1.267	−70.38	2.59×10^{-3}	−91.91	0.38	−91.12
40	0.057	6.096	0.023	−59.65	2.118	−65.26	5.65×10^{-3}	−90.09	0.579	−90.50
50	0.064	7.257	0.029	−54.69	2.626	−63.81	9.37×10^{-3}	−85.36	0.735	−89.87

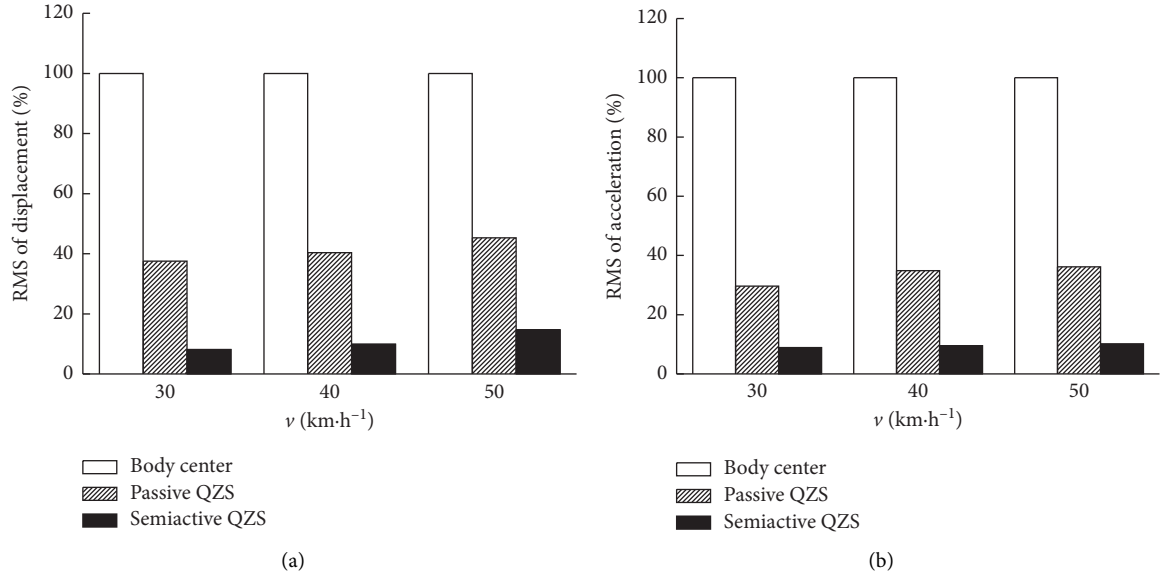

Figure 16: Relative difference of RMS of (a) vertical displacement and (b) acceleration under semisinusoidal shock road.

Table 5: Maximum acceleration ratio at different vehicle speeds under semisinusoidal impact pavement.

Vehicle speed ($km \cdot h^{-1}$)	Body centre	Passive QZS system		Semiactive QZS system	
	Peak acceleration ($m \cdot s^{-2}$)	Peak acceleration ($m \cdot s^{-2}$)	Ratio	Peak acceleration ($m \cdot s^{-2}$)	Ratio
30	9.762	3.356	0.34	0.834	0.086
40	17.187	6.195	0.36	1.787	0.103
50	21.158	8.791	0.42	2.489	0.118

It can be seen from Table 5 that the maximum acceleration ratio of the two isolators at different vehicle speeds increases with the increase in vehicle speed. The maximum acceleration ratio of the passive QZS vibration isolation system is larger than that of the semiactive one, which indicates that the semiactive QZS vibration isolator has better shock resistance performance.

4. Experimental Study on Vibration Isolation System

4.1. Experiment Scheme Design. The semiactive QZS vibration isolation system is composed of a mechanical structure and MR semiactive control system. The mechanical structure is shown in Figure 17. Here, the negative stiffness mechanism mainly includes a spring, an inner and outer sleeve, a screw, and an adjusting nut. The screw is connected to the inner sleeve in a spiral manner. The precompression of the spring is adjusted by the adjusting nut to realize the negative stiffness of the horizontal spring.

The MR semiactive control system is mainly composed of a motion state sensor, controllable constant current power supply, signal conditioning converter, control arithmetic unit, input/output board, and shielded junction box, as shown in Figure 18.

Using LabVIEW RT as the real-time control module can improve the reliability and time certainty of program operation. The program is written and debugged in the upper computer, and the running state of the system is monitored. The lower computer is connected to the upper computer through the network cable to ensure the real-time performance of the system and realizes the functions of data transmission and human-computer interaction.

The hardware of the semiactive control system is listed in Table 6, and the experiment site is shown in Figure 19.

The excitation system is a six-degree-of-freedom vibration test bench jointly developed by the University of Wollongong and Hefei University of Technology, which is mainly composed of NI control system, PC computer controller, DMKE electric cylinder, and so on. The data acquisition system includes keyence LK-G500 laser displacement sensors and data collectors (model: INV306U), and the real-time waveforms are captured through DASP software on PC computed.

4.2. Analysis of Test Results. The design parameter of the spring is shown in Table 7.

When the QZS system is in a static balance, the following relationship should be satisfied:

$$L^2 = l^2 + h^2, \tag{17}$$

where L is the precompressed length of the horizontal spring, which can be adjust by the adjusting nut. When the system reaches the static equilibrium position, the horizontal spring's length is l. h is the compression deformation of the

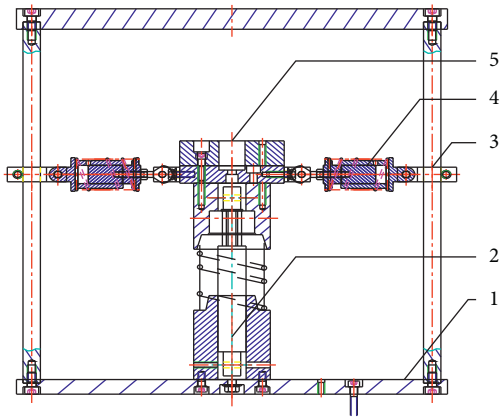

Figure 17: Mechanical structure of the semiactive QZS vibration isolation system: ① device base; ② MR damper; ③ limit adjusting structure; ④ negative stiffness mechanism; ⑤ vibration isolated mass.

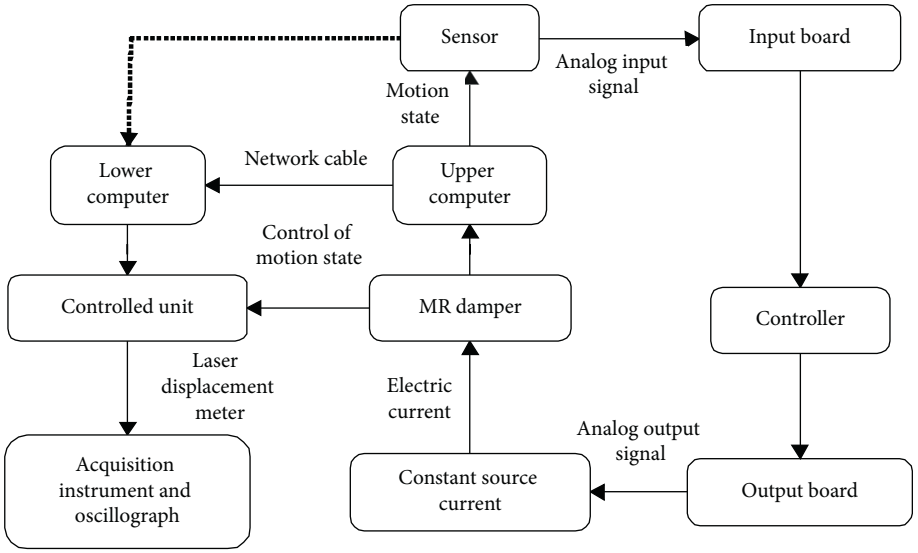

Figure 18: MR semiactive control system block diagram.

Table 6: Hardware of the semiactive control system.

Type	Model	Number
Real-time controller	NI PXIe-8108	1
Data acquisition cabinet	NI PXIe-1082	1
Analog output module	NI 6363	1
Analog input module	NI 4496	1
Power amplifier	TPA10	1
68-pin shielded junction box	NI SCB-68A	1
Acceleration sensor	BK 4528-B	2
Laser displacement meter	LK-G500	1
Data acquisition instrument	INV306U	1

vertical spring under static load, which can be obtained by the relationship $k_v h = mg$. The meaning and value of L, l, and h are shown in Figure 1 and Table 1.

The test conditions include harmonic excitation with different amplitudes and frequencies:

(a) *Test Condition 1*. Harmonic excitation with different amplitudes: The initial vibration isolation frequency of the QZS vibration isolation system is about 1.4 Hz, so the resonance region frequency (1.2 Hz) and the vibration isolation region frequency (1.4 times of the resonance frequency, 2.5 Hz) are selected as the excitation frequency. The vertical amplitudes are chosen as 3 mm, 5 mm, and 7 mm, respectively.

(b) *Test Condition 2*. Harmonic excitation test with different frequencies. The amplitude is 5 mm, and the excitation frequencies are 1.0 Hz, 1.2 Hz, 1.4 Hz, 1.6 Hz, and 1.8 Hz, respectively.

4.2.1. Time Domain Response Analysis. When the excitation frequency is 1.2 Hz and 2.5 Hz, the test and simulation results of the displacement response of the isolated object are shown in Figures 20 and 21. The differences between the test and the theoretical results are shown in Table 8.

From Figures 20 and 21 and Table 8, it can be seen that the test results are in good agreement with the theoretical results. The peak value of the test is slightly larger than the simulation

Figure 19: Experiment site: ① control computer; ② control program interface; ③ PXI embedded system; ④ data acquisition computer; ⑤ acquisition instrument; ⑥ regulated power supply; ⑦ MR damper; ⑧ QZS vibration isolator; ⑨ laser displacement meter.

Table 7: The parameter of the spring.

	Medium diameter (mm)	Material diameter (mm)	Effective laps	Measured stiffness (N/m)
Vertical spring	65	4	8	1017
Oblique spring	42	2.8	7.5	1085

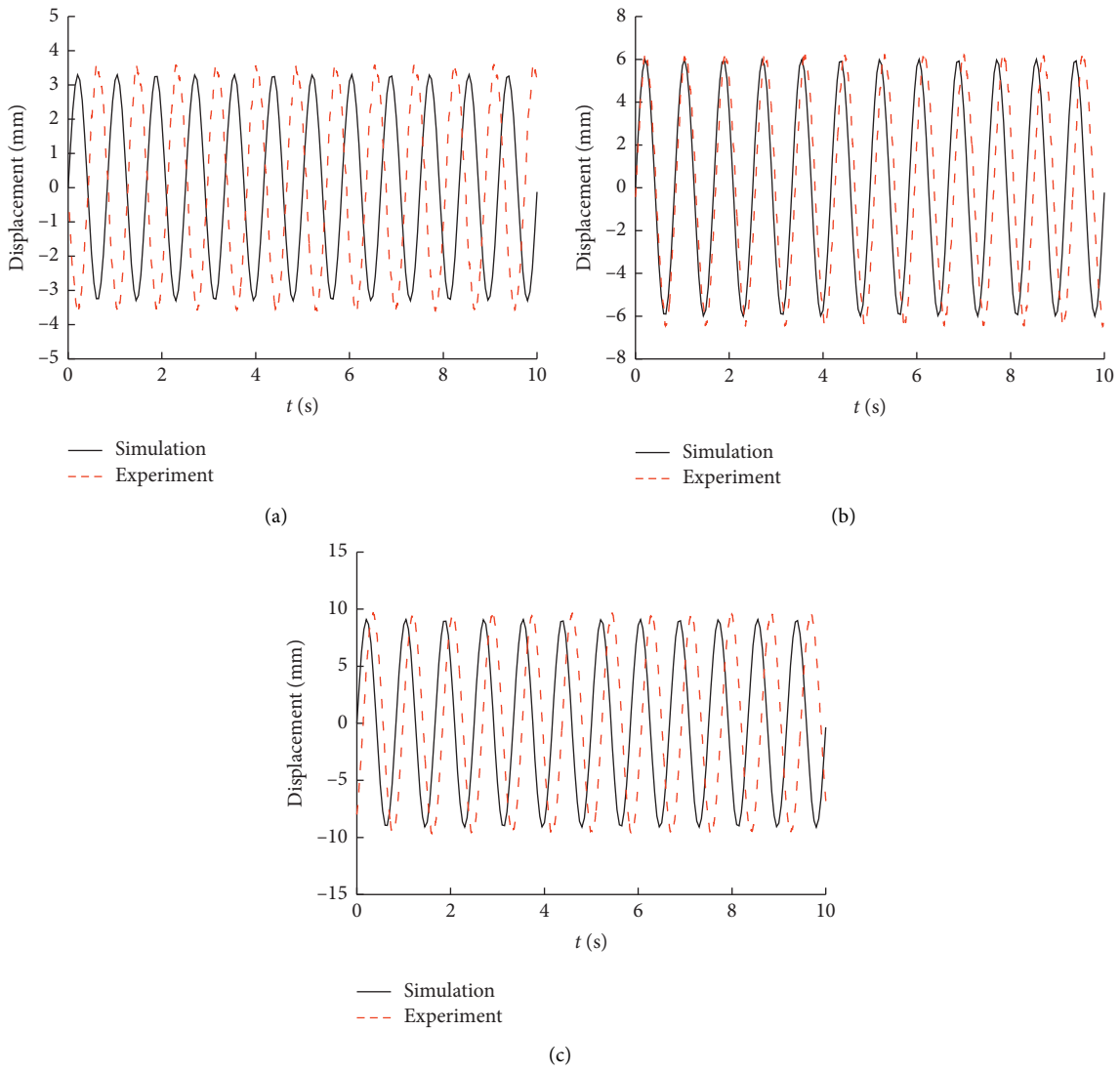

Figure 20: Time domain response of displacement under 1.2 Hz harmonic excitation with different amplitudes: (a) 3 mm; (b) 5 mm; (c) 7 mm.

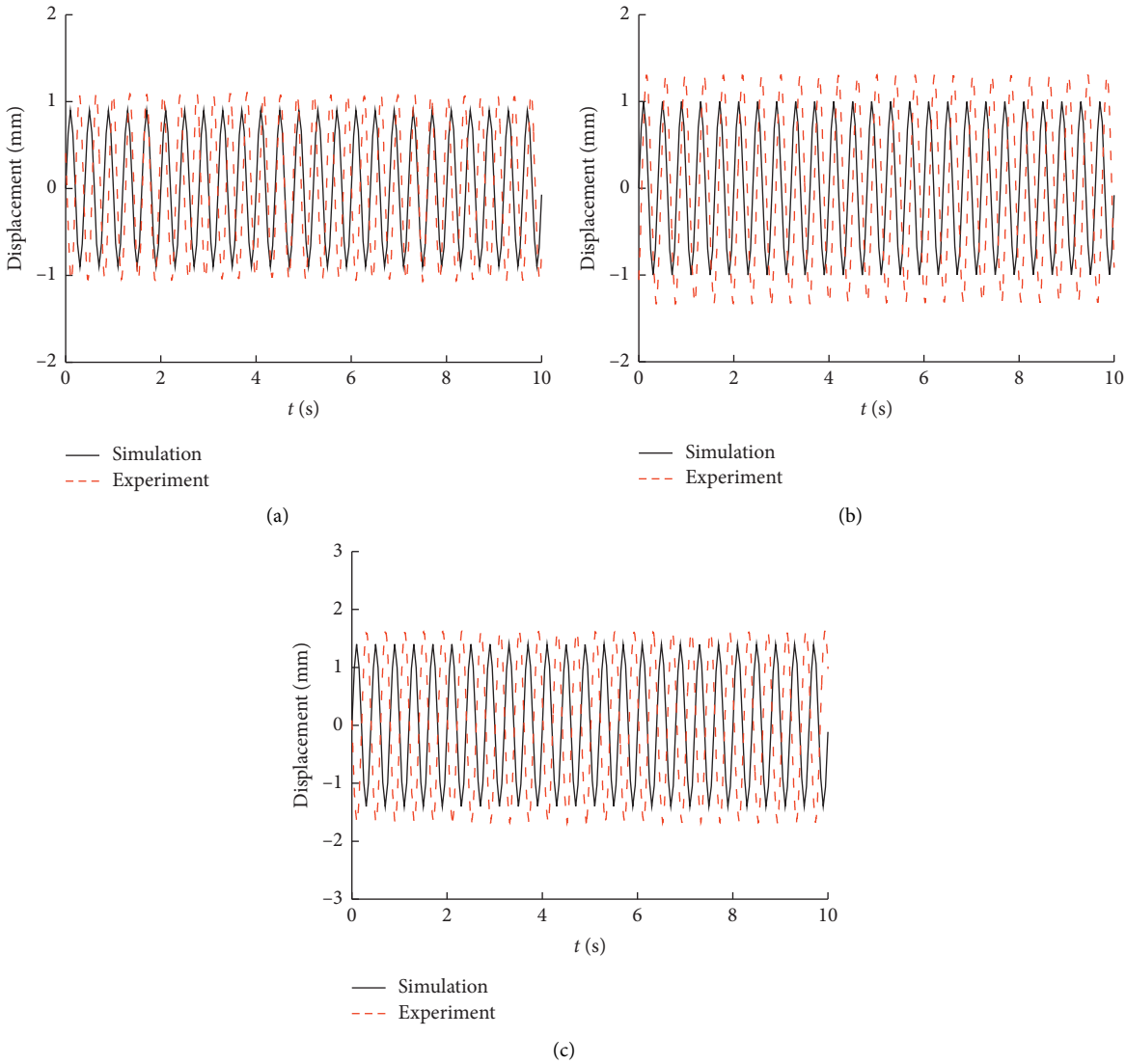

Figure 21: Time domain response of displacement under 2.5 Hz harmonic excitation with different amplitudes: (a) 3 mm; (b) 5 mm; (c) 7 mm.

Table 8: Relative differences of displacement peak between experiment results and simulation results.

Excitation amplitude (mm)	Excitation frequency 1.2 Hz			Excitation frequency 2.5 Hz		
	Simulation (mm)	Experiment (mm)	Difference (%)	Simulation (mm)	Experiment (mm)	Difference (%)
3	3.32	3.451	5.12	0.96	1.047	9.03
5	6.05	6.456	6.71	1.05	1.261	10.54
7	9.17	9.718	5.97	1.47	1.613	9.76

results, and the difference increases with the excitation amplitude. The slight difference is inevitable due to the installation error and the friction between the parts. So, the test results verify the correctness of the established model and simulation results.

The vibration experiment of the semiactive QZS system with different harmonic excitation frequencies is carried out. The amplitude is 5 mm, and the frequencies are 1.0 Hz, 1.2 Hz, 1.4 Hz, 1.6 Hz, and 1.8 Hz, respectively. The tested and simulated displacement responses of the mass block under different excitation frequencies are shown in Figure 22. The relative differences of the peak values are listed in Table 9.

From Figure 22 and Table 9, it can be seen that the change trend of the experiment and the simulation results are the same. With the increase in the excitation frequency, the relative difference between the experiment and the theoretical results increases, and the maximum difference is 11.27%, which further verifies the correctness of the theoretical model and the feasibility of the control scheme.

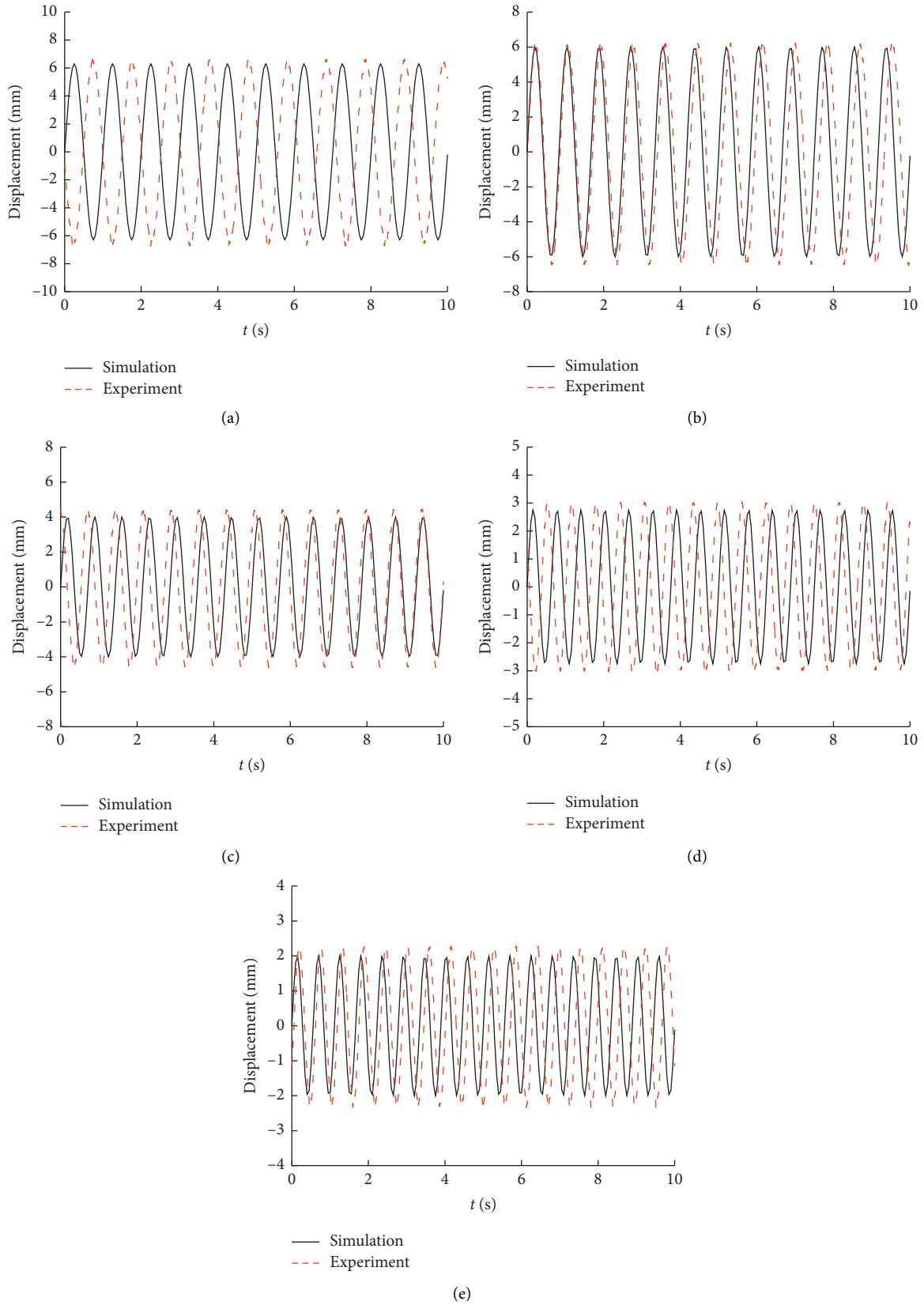

Figure 22: Time domain response of displacement under different excitation frequencies: (a) 1 Hz, (b) 1.2 Hz. (c) 1.4 Hz, (d) 1.6 Hz, and (e) 1.8 Hz.

Table 9: Displacement peaks from experiment results and simulation results under different excitation frequencies.

Excitation frequency (Hz)	Simulation (mm)	Experiment (mm)	Difference (%)
1.0	6.01	6.377	5.93
1.2	6.05	6.456	6.71
1.4	4.04	4.369	8.14
1.6	2.76	3.071	11.27
1.8	2.02	2.234	10.56

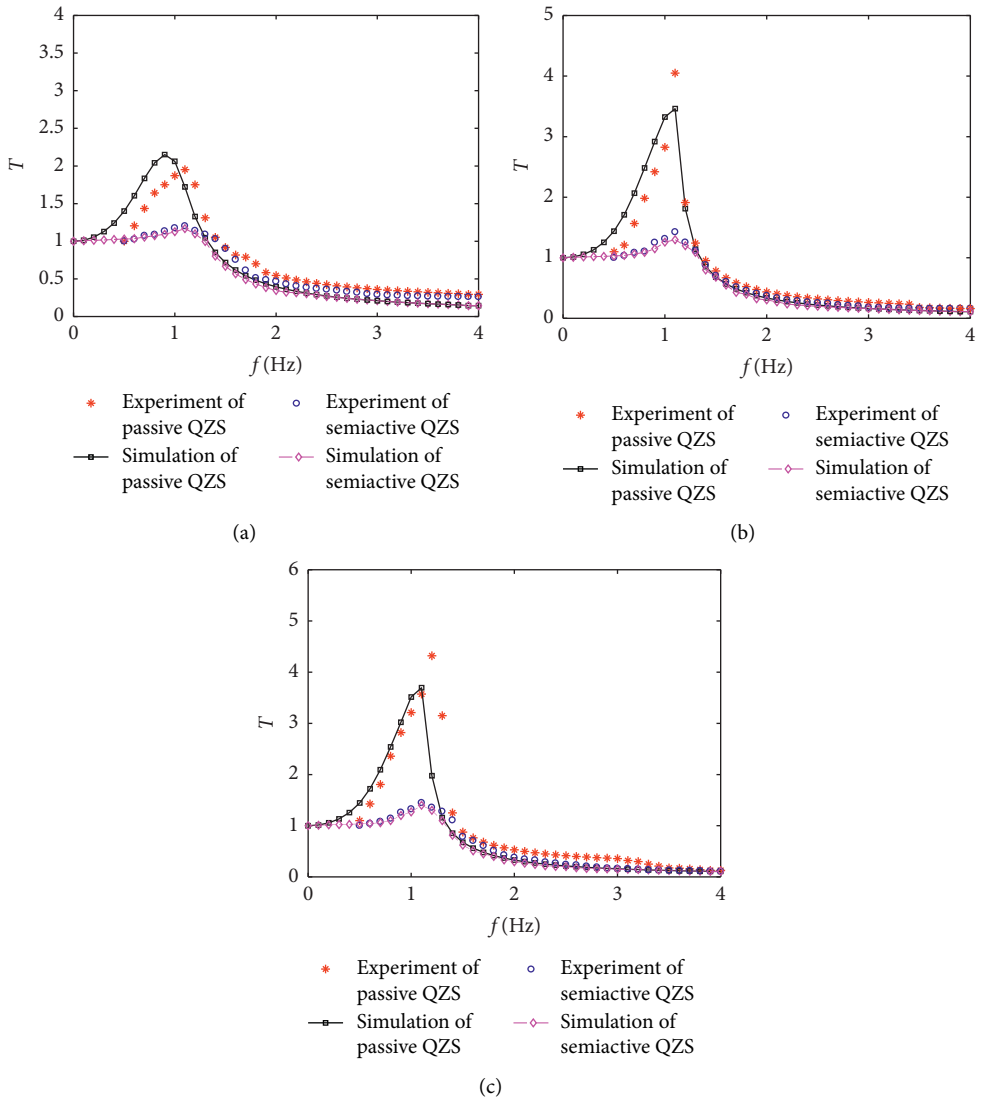

Figure 23: Displacement transmissibility under different harmonic excitation: (a) amplitude is 3 mm; (b) amplitude is 5 mm; (c) amplitude is 7 mm.

4.2.2. Analysis of Vibration Isolation Effect. Let a_{max} and a_{min} be the peaks and troughs of the time domain response waveforms, respectively, and b be the excitation amplitude; the displacement transmissibility of the vibration isolation system is

$$T = \frac{|a_{max} - a_{min}|}{2b}. \quad (18)$$

The tested and simulated displacement transmissibility of the passive and semiactive QZS isolators under different excitation amplitudes is shown in Figure 23.

As can be seen from Figure 23,

(a) The resonance peak of the system increases with the rise of the excitation amplitude. The initial vibration isolation frequencies of the two kinds of isolators are

Table 10: RMS and differences of displacement transmissibility under different harmonic excitations.

Excitation amplitudes (mm)	RMS of passive QZS (mm)	RMS of semiactive QZS (mm)	Differences (%)
3	0.907	0.672	−25.9
5	1.166	0.684	−41.3
7	1.474	0.698	−52.6

the same and lower than those of the corresponding linear system, which indicates that the semiactive QZS vibration isolation system also has the characteristics of low-frequency vibration isolation.

(b) The semiactive QZS vibration isolator can suppress the resonance much better than the passive one. After reaching the initial isolation frequency, the vibration isolation performance of the semiactive QZS isolator is also superior to the passive QZS.

The RMS of the displacement transmissibility of passive and semiactive QZS isolators under different excitation amplitudes is also computed, as shown in Table 10.

It can be seen that the RMS of displacement transmissibility of semiactive QZS isolator is smaller significantly than that of the passive one, and the larger the excitation amplitude is, the more obvious the difference is.

5. Conclusions

A semiactive QZS vibration isolator is proposed and designed based on MR damper. The simulation analysis is carried out under different road conditions and different vehicle speeds. The test device and semiactive on-off control system are developed and manufactured, and the correctness of the theoretical derivation and simulation method is verified by experimental results. It can be concluded that

(a) For the condition of harmonic, stochastic, and shock road excitations, the semiactive QZS isolator is always superior to the passive QZS in different working conditions, with more obvious control effects

(b) The proposed semiactive QZS isolator shows better universality at different frequencies and amplitudes of excitations in the test, and the control algorithms are feasible for the mechanical devices of the isolator and the hardware system

Data Availability

The data used to support the findings of this study are included within the article.

Conflicts of Interest

The authors declare that they have no conflicts of interest regarding the publication of this paper.

Acknowledgments

The work described in this paper was supported by the National Science Foundation of China under grant nos. 11972238 and 11902206.

References

[1] Z. Lu, Z. Wang, Y. Zhou, and X. Lu, "Nonlinear dissipative devices in structural vibration control: a review," *Journal of Sound and Vibration*, vol. 423, pp. 18–49, 2018.

[2] Z. Lu, D. Wu, H. Ding, and L. Chen, "Vibration isolation and energy harvesting integrated in a Stewart platform with high static and low dynamic stiffness," *Applied Mathematical Modelling*, vol. 89, no. 1, pp. 249–267, 2020.

[3] N. Du, M. Hu, Y. Bi, and Q. Zhu, "A low frequency horizontal vibration reduction method for vehicle mounted equipment," *Journal of Vibration and Shock*, vol. 36, no. 7, pp. 184–190, 2017.

[4] Q. Zhang, S. Xia, D. Xu, and Z. Peng, "A torsion-translational vibration isolator with quasi-zero stiffness," *Nonlinear Dynamics*, vol. 99, no. 2, pp. 1467–1488, 2019.

[5] Y. Kan, J. C. Ji, and B. Terry, "Design of a quasi-zero stiffness isolation system for supporting different loads," *Journal of Sound And Vibration*, vol. 471, Article ID 115198, 2020.

[6] J. Han, J. Sun and L. Meng, "Design and characteristics analysis of a nonlinear vibration isolator using a curved surface-spring-roller mechanism as negative stiffness element," *Journal of Vibration and Shock*, vol. 38, no. 3, pp. 170–178, 2019.

[7] K. Wang, J. Zhou, D. Xu, and H. Ouyang, "Lower band gaps of longitudinal wave in a one-dimensional periodic rod by exploiting geometrical nonlinearity," *Mechanical Systems and Signal Processing*, vol. 124, pp. 664–678, 2019.

[8] Q. Meng, X. Yang, W. Li, E. Lu, and L. Sheng, "Research and analysis of quasi-zero-stiffness isolator with geometric nonlinear damping," *Shock and Vibration*, vol. 2017, Article ID 6719054, 9 pages, 2017.

[9] D. Liu, Y. Liu, D. Sheng, and W. Liao, "Seismic response analysis of an isolated structure with QZS under near-fault vertical earthquakes," *Shock and Vibration*, vol. 2018, Article ID 9149721, 12 pages, 2018.

[10] L. Meng, J. Sun, W. Wu, and K. V. Singh, "Theoretical design and characteristics analysis of a quasi-zero stiffness isolator using a disk spring as negative stiffness element," *Shock and Vibration*, vol. 2015, Article ID 813763, 19 pages, 2015.

[11] Z. Q. Lu, D. H. Gu, H. Ding, W. Lacarbonara, and L. Q. Chen, "Nonlinear vibration isolation via a circular ring," *Mechanical Systems and Signal Processing*, vol. 136, Article ID 106490, 2020.

[12] B. Yan, H. Ma, B. Jian, K. Wang, and C. Wu, "Nonlinear dynamics analysis of a bi-state nonlinear vibration isolator with symmetric permanent magnets," *Nonlinear Dynamics*, vol. 97, no. 4, pp. 2499–2519, 2019.

[13] N. Alujević, D. Čakmak, H. Wolf et al., "Passive and active vibration isolation systems using inerter," *Journal of Sound and Vibration*, vol. 418, pp. 163–183, 2018.

[14] Y. Wang and X. Jing, "Nonlinear stiffness and dynamical response characteristics of an asymmetric X-shaped structure," *Mechanical Systems and Signal Processing*, vol. 125, pp. 142–169, 2019.

[15] X. Liu, X. Huang, H. Hua et al., "Influence of excitation amplitude and load on the characteristics of quasi-zero stiffness isolator," *Journal of Mechanical Engineering*, vol. 49, no. 6, pp. 89–94, 2013.

[16] X. Huang, Y. Chen, H. Hua et al., "Shock isolation performance of a nonlinear isolator using Euler buckled beam as negative stiffness corrector: theoretical and experimental study," *Journal of Sound and Vibration*, vol. 345, pp. 178–196, 2015.

[17] Y. Zhou, P. Chen, and G. Mosqueda, "Analytical and numerical investigation of quasi-zero stiffness vertical isolation system," *Journal of Engineering Mechanics*, vol. 145, no. 6, Article ID 04019035, 2019.

[18] H. Yasuda, Y. Miyazawa, C. Efstathios et al., "Origami-based impact mitigation via rarefaction solitary wave creation," *Science Advances*, vol. 5, no. 5, Article ID aau2835, 2019.

[19] X. Sun, J. Xu, F. Wang, and S. Zhang, "A novel isolation structure with flexible joints for impact and ultralow-frequency excitations," *International Journal of Mechanical Sciences*, vol. 146, pp. 366–376, 2018.

[20] X. Liu, S. Chen, J. Wang, and J. Shen, "Analysis of the dynamic behavior and performance of a vibration isolation system with geometric nonlinear friction damping," *Chinese Journal of Theoretical and Applied Mechanics*, vol. 51, no. 2, pp. 371–379, 2019.

[21] Z. Q. Lu, H. Ding, and L. Q. Chen, "Resonance response interaction without internal resonance in vibratory energy harvesting," *Mechanical Systems and Signal Processing*, vol. 121, pp. 767–776, 2019.

[22] C. Liu, K. Yu, and J. Tang, "New insights into the damping characteristics of a typical quasi-zero-stiffness vibration isolator," *International Journal of Non-linear Mechanics*, vol. 124, Article ID 10351, 2020.

[23] Z. Lu and L. Chen, "Some recent progresses in nonlinear passive isolations of vibrations," *Chinese Journal of Theoretical and Applied Mechanics*, vol. 49, no. 3, pp. 550–564, 2017.

[24] X. Li, J. Zhang, and J. Yao, "Effect of the time-varying damping on the vibration isolation of a quasi-zero-stiffness vibration isolator," *Shock and Vibration*, vol. 2020, Article ID 4373828, 10 pages, 2020.

[25] S. Yang and Y. Shen, *Bifurcation and Singularity of Delayed Nonlinear Systems*, Science Press, Beijing, China, 2003.

[26] Q. Pang, L. Zhang, Y. He, Z. Gong, and Z. Feng, "Verification platform for magnetorheological semi-active suspension control algorithm," *Journal of Tsinghua University (Science & Technology)*, vol. 59, no. 7, pp. 567–574, 2019.

[27] Z. Peng, J. Zhang, and X. Fu, "Experimental study on a semi-active magnetorheological suspension," *Automotive Engineering*, vol. 40, no. 5, pp. 561–567, 2018.

[28] K. Hemanth, H. Kumar, and K. V. Gangadharan, "Vertical dynamic analysis of a quarter car suspension system with MR damper," *Journal of the Brazilian Society of Mechanical Sciences and Engineering*, vol. 39, pp. 41–51, 2017.

[29] S. Chen, G. Zu, M. Yao, and X. Zhang, "Taylor series-LQG control for time delay compensation of magneto-rheological semi-active suspension," *Journal of Vibration and Shock*, vol. 36, no. 8, pp. 190–196, 2017.

[30] P. Hu, J. Zhang, Z. Peng, and Y. Zhang, "Verification of magnetorheological damper mechanical model and skyhook on-off control," *Journal of Academy of Armored Force Engineering*, vol. 32, no. 1, pp. pp42–49, 2018.

[31] H. D. Chae and S. B. Choi, "A new vibration isolation bed stage with magnetorheological dampers for ambulance vehicles," *Smart Materials and Structures*, vol. 24, no. 1, Article ID 017001, 2015.

[32] X. Gao, J. Niu, Z. Liu, and J. Tian, "Semi-active control of ambulance stretcher system based on parallel mechanism with MR dampers and perturbation analysis," *International Journal of Mechanics and Materials in Design*, vol. 15, no. 4, pp. 817–831, 2019.

[33] Q. Wang, J. Zhou, D. Xu, and H. Ouyang, "Design and experimental investigation of ultra-low frequency vibration isolation during neonatal transport," *Mechanical Systems and Signal Processing*, vol. 139, Article ID 106633, 2020.

[34] C. Pan, *Research on Vibration Isolation System with Hysteretic Nonlinear Actuator*, Beijing Jiaotong University, Beijing, China, 2009.

[35] S. Li, Y. Lu, and J. Ren, *Study on Dynamics of Three-Dimensional Interaction between Heavy Vehicle and Road*, Science Press, Beijing, China, 2020.

Hindawi
Shock and Vibration
Volume 2021, Article ID 5535192, 12 pages
https://doi.org/10.1155/2021/5535192

Research Article

Experimental and Numerical Studies on Static Aeroelastic Behaviours of a Forward-Swept Wing Model

Yan Ouyang,[1] **Kaichun Zeng**,[2] **Xiping Kou**,[1] **Yingsong Gu**,[1] **and Zhichun Yang**[1]

[1]*Institute of Structural Dynamics and Control, School of Aeronautics, Northwestern Polytechnical University, Xi'an 710072, China*
[2]*High Speed Aerodynamics Institute, China Aerodynamics Research and Development Center, Mianyang 621000, China*

Correspondence should be addressed to Zhichun Yang; yangzc@nwpu.edu.cn

Received 13 January 2021; Accepted 26 May 2021; Published 14 June 2021

Academic Editor: Zeqi Lu

The static aeroelastic behaviours of a flat-plate forward-swept wing model in the vicinity of static divergence are investigated by numerical simulations and wind tunnel tests. A medium fidelity model based on the vortex lattice method (VLM) and nonlinear structural analysis is proposed to calculate the displacements of the wing structure with large deformation. Follower forces effect and geometric nonlinearity are considered to calculate the deformation of the wing by finite element method (FEM). In the wind tunnel tests, the divergence dynamic pressure is predicted by the Southwell method, and the static aeroelastic displacement is measured by a photogrammetric method. The results obtained by the medium fidelity model calculations show reasonable agreement with wind tunnel test results. A high fidelity model based on coupled computational fluid dynamics (CFD) and computational structural dynamics (CSD) predicts better results of the wing tip displacement when the freestream dynamic pressure is approaching the divergence dynamic pressure.

1. Introduction

In static aeroelasticity analysis, the interaction between aerodynamics and structural deflections determines the wing bending and twist at every flight condition. The static aeroelastic deformation in the steady flight condition is of great importance because it governs the aerodynamic performance and flight control characteristics [1]. Under the conditions of small structural deformations and small angle of attack (AOA), linear aeroelastic analysis usually gives accurate results. However, if the wing structure undergoes large deformation, the linear calculation may lead to inaccurate predictions. The nonlinear effect usually plays an important role in the structure dynamics [2, 3] and may also be crucial in statics. For instance, in the linear aeroelastic calculation, the projection of the deformed wing always coincides with that of the undeformed wing. This indicates a nonphysical effect of lengthening the wing structure without axial load [4]. For the highly flexible joined-wing aircraft, the linear aeroelastic analysis may lead to incorrect prediction of the flight envelope [5].

It is well known that the forward-swept wing and straight wing with high aspect ratio are susceptible to large deformation. When the aerodynamic load is heavy, the deformation of the wing structure will become very large. According to the aerodynamic and structural models used in the nonlinear aeroelastic analysis, numerical models can be categorized into three levels, namely, low, medium, and high fidelity models [6]. Two-dimensional aerodynamic models and nonlinear beam theory are usually used in the low fidelity models [7]. For the high-aspect-ratio wing model, the static and dynamic aeroelastic responses calculated by low fidelity model agree well with the experimental results [8, 9]. The nonlinear beam theory is capable of calculating the postcritical deformation of a compliant forward-swept wing, and its capability is validated by wind tunnel tests [10].

Though the low fidelity model provides essential insight and knowledge about the aeroelastic characteristics, it has limitation in evaluating the 3D effect of real flow. The strip theory without tip effects correction may overestimate the outboard wing lift and results in greater vertical wing

displacement and bending rotation [11, 12]. When the spanwise aerodynamic variations are critical for wing structure, the VLM provides a medium fidelity tool for aerodynamic calculation [13]. The VLM can calculate the aerodynamics acting on the wing with large deformation and some pragmatic approaches can be adopted to estimate the effects of drag and camber [14]. The following static structural analysis should be carried out by nonlinear FEM; otherwise, the analysis will yield unrealistic result [15]. Generally speaking, the medium fidelity model is efficient in aeroelastic analysis, so it is widely used in the design optimization process [16, 17].

The high fidelity simulation model is based on CFD/CSD coupled method and has been developed rapidly and applied widely in the study of computational aeroelasticity in last decades. Even at low subsonic speeds, much attention should be paid to the effects of structural nonlinearity on the aeroelastic behaviour. The geometric nonlinearity changes the aerodynamic loads, thus leading to considerable errors in the static aeroelastic predictions [18, 19]. The difference between the maximum deflections of linear and nonlinear wing structure calculations becomes more and more dramatic with increasing aerodynamic loads [20, 21]. Though the low fidelity model gives acceptable results of the static aeroelastic characteristics, the high fidelity model can generate more accurate results and detailed aerodynamic characteristics of the compliant forward-swept wing [22]. The CFD/CSD coupling analysis is essential when the flows are in transonic region because of the shock wave and flow separation [23, 24].

The static divergence of wing structure must be predicted accurately by wind tunnel test, because the divergence speed directly reflects the general stiffness of the wing structure and must be considered in the certification process (CS-25 and FAR-25) [1]. There are four static and two dynamic methods used to predict static divergence of wing model in wind tunnel test [25]. All these methods use subcritical response of the experimental model to predict the static divergence. As a static method, the Southwell method is easy to carry out and shows good agreement with the critical divergence test result [26–28]. So, the Southwell method is adopted in the current study.

Before the occurrence of divergence, we are usually concerned about the maximal wing tip displacements. Photogrammetry is a nonintrusive measurement technique commonly used to determine the geometrical information of object by analyzing images recorded by camera. This technique is useful when the object to be measured is inaccessible and noncontact measurement is required, and it is especially suitable for static aeroelastic wind tunnel test. A detailed description of the related theory can be found in [29]. In a series of research, the photogrammetry is proved to be an accurate and powerful method to measure point displacements and local angular deflections [30, 31]. DLTdv7 is a general-purpose digitizing program and it is suitable for two- or three-dimensional video analysis [32]. This program has been widely used in the measurement of wing kinematics [33] and aeroelastic deformation [34]. In the current study, a feasible method based on single camera and DLTdv7 program is used to measure the wing tip displacement in the wind tunnel test.

The study aims to obtain an improved understanding of the static aeroelastic behaviours of a wing model. According to the performance of the available wind tunnel, a forward-swept layout model is used. This layout has a decreased divergence speed compared to the unswept wing due to increased effective AOA. When the free stream dynamic pressure is in the vicinity of the static divergence boundary, the forward-swept wing model will encounter large deformation. The static aeroelastic deformation is calculated by medium and high fidelity models. Wind tunnel tests are performed to validate the simulation results. Finally, we make a comparison between the results of medium and high fidelity models in the aspects of accuracy and efficiency.

2. Nonlinear Analysis by the Medium Fidelity Model

An aluminum flat-plate wing model is used in the current study, as shown in Figure 1. The planform of the wing structure is a parallelogram. The semispan and the chord length of the model are $s = 750$ mm and $c = 200$ mm, respectively. The plate thickness is 2.5 mm. The material density is $\rho = 2700\,\text{kg/m}^3$. The leading-edge forward-swept angle is 30 deg. Three-fifths of the wing root length are fixed. In order to perform nonlinear static analysis efficiently, quadrilateral plate element is used to model the wing structure. Figure 1(a) shows the structure model consisting of 20×60 elements, whereas Figure 1(b) depicts the corresponding aerodynamic model, which consists of 10×30 aerodynamic panels.

The equation of motion used for general static aeroelastic calculation can be expressed as follows [35]:

$$\left(\mathbf{K}_{aa} - q\mathbf{Q}_{aa}\right)\mathbf{u}_a + \mathbf{M}_{aa}\ddot{\mathbf{u}}_a = q\mathbf{Q}_{ax}\mathbf{u}_x + \mathbf{P}_a, \tag{1}$$

where $\mathbf{K}_{aa}$ and $\mathbf{M}_{aa}$ are the structural stiffness and mass matrices, respectively. q is the flow dynamic pressure. $\mathbf{u}_a$ is the structural displacement vector. $\mathbf{u}_x$ is the vector of aerodynamic extra points used to describe the control surface deflections and overall rigid body motions. $\mathbf{Q}_{aa}$ and $\mathbf{Q}_{ax}$ are the aerodynamic influence coefficient matrices corresponding to the structural deformations and unit deflections of the aerodynamic extra points, respectively. $\mathbf{P}_a$ is the vector of external loads.

The present wing model has neither control surface nor rigid body motions; equation (1) can be simplified to obtain the divergence dynamic pressure by solving an eigenvalue problem:

$$\left(\mathbf{K}_{aa} - q\mathbf{Q}_{aa}\right)\mathbf{u}_a = 0. \tag{2}$$

The eigenvalues $q = q_d$ are the dynamic pressures for divergence. Only positive values of q_d have physical significance and the lowest value is the critical divergence dynamic pressure.

In static aeroelastic analysis, the downwash can be calculated as [36]

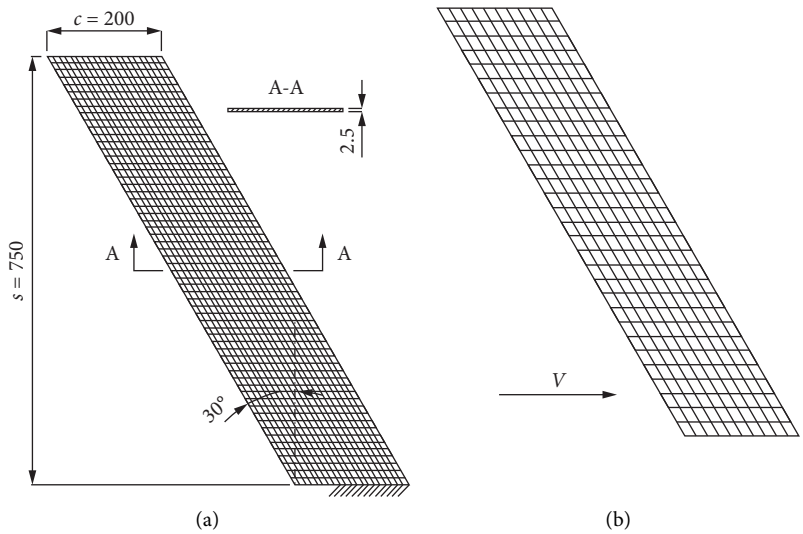

Figure 1: Forward-swept wing structural and aerodynamic models. (a) Finite element model. (b) Aerodynamic model.

$$\mathbf{w}_j = \mathbf{D}_{jk}\mathbf{u}_k + \mathbf{w}_j^g, \tag{3}$$

where $\mathbf{w}_j$ is the downwash vector of the aerodynamic panels and $\mathbf{D}_{jk}$ is the substantial derivative matrix for the aerodynamic displacements. $\mathbf{u}_k$ is the vector of aerodynamic displacement and $\mathbf{w}_j^g$ represents an initial static aerodynamic downwash. The initial AOA, camber, or twist distribution of the wing structure can be taken into account by modifying $\mathbf{w}_j^g$. Then the theoretical aerodynamic pressures are given by

$$\mathbf{f}_j = q\mathbf{A}_{jj}^{-1}\mathbf{w}_j, \tag{4}$$

where $\mathbf{f}_j$ is the pressure vector of the aerodynamic panels. $\mathbf{A}_{jj}$ is the aerodynamic influence coefficient matrix, which is a function of Mach number and reduced frequency. The aerodynamic force and moment at aerodynamic grids are obtained by integrating the pressure vector:

$$\mathbf{P}_k = \mathbf{S}_{kj}\mathbf{f}_j, \tag{5}$$

where $\mathbf{P}_k$ is the vector of force and moment. $\mathbf{S}_{kj}$ is the integration matrix.

To improve the accuracy of aerodynamic calculations, two experimental corrections may be introduced to adjust each theoretical aerodynamic panel lift and moment [37]. These two corrections require that the experimental pressure distribution data at some reference angles of attack be available in advance for numerical calculation. Another correction can be made by adjusting the aerodynamic panels' downwashes [36]. Substitute equations (3) and (4) into (5); the aerodynamic force and moment can be calculated by downwash as

$$\mathbf{P}_k = q\mathbf{S}_{kj}\mathbf{A}_{jj}^{-1}\left(\mathbf{D}_{jk}\mathbf{u}_k + \mathbf{w}_j^g\right). \tag{6}$$

As the downwash of the wing cannot be measured directly in experiments, we use the deformation of the wing model to modify the downwash vector; and an iterative method is used to calculate the static aeroelastic deformation of the wing model.

In static aeroelastic analysis, two types of data transformations are required: the structural equivalent forces from aerodynamic panels to structural grids and the interpolation from the structural deflections to the aerodynamic deflections. The spline methods lead to an interpolation that relates the components of structural grid displacements to the aerodynamic grid displacements. When the deformed structural grids and aerodynamic panels are not coplanar, the local AOA of aerodynamic panel needs to be modified according to structural displacements.

The iteration procedure starts with assigning appropriate initial conditions, as shown in Figure 2. The aerodynamic loads are calculated by VLM. As the aerodynamics is typical follower force, the full geometric nonlinear analysis should be carried out; that is, the aerodynamic loads are treated as following forces and large displacement effect is considered. The surface spline method is applied to transfer the data between structural and aerodynamic grids. The convergence condition of the iteration is that the relative error of the wing tip displacement between two consecutive steps is less than 0.1%. In every iteration cycle, the local AOA, that is the downwash vector of every panel, is updated according to the structural grid displacements. For the purpose of comparison, the results of linear calculation are also included in this paper.

To take the case at AOA $\alpha = 1.5$ deg and dynamic pressure $q = 367$ Pa as an example, the calculation process is shown in Figure 3. The displacements of the leading-edge (LE) point and trailing-edge (TE) point at the wing tip increase and converge gradually after the 22nd iteration step. This indicates that the relative error of the 21st and 22nd iteration steps is less than 0.1%. The final displacements of the LE point and TE point at the wing tip are 239.2 mm and 200.8 mm, respectively. The vertical displacement at the wing tip is more than 30% of semi-span. It means a typical nonlinear case for a flexible wing with large deformation.

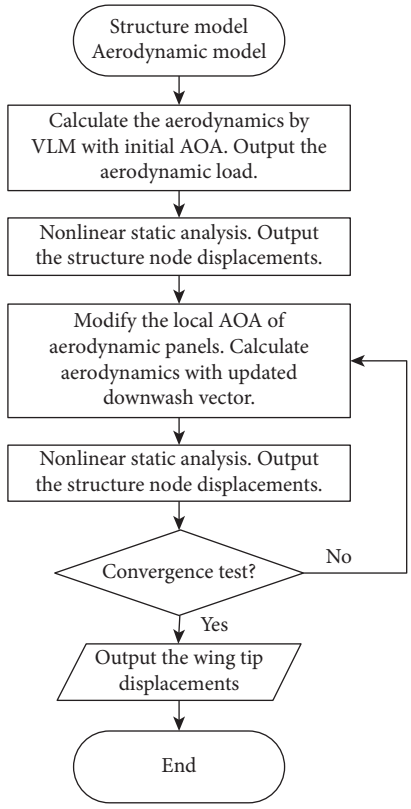

Figure 2: Flowchart of nonlinear static aeroelastic analysis.

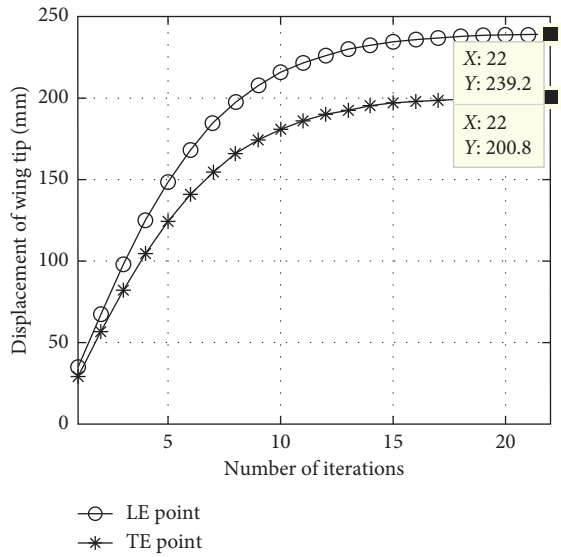

Figure 3: Calculation process by medium fidelity model.

3. Nonlinear Analysis by the High Fidelity Model

In the detailed design phase of a real wing, a more accurate prediction of static aeroelastic behaviour of the wing structure is necessary. In particular, it is important to predict the static aeroelastic behaviour in the vicinity of divergence with sufficient accuracy. Besides the efficient medium fidelity model, a steady-state CFD/CSD coupling simulation of the wing model is also performed to obtain more accurate results. The simulation is carried out using the commercial software package ANSYS for both the structural analysis and aerodynamic analysis.

The flow field consisting of hexahedral cells around the wing is generated using the ICEM CFD as shown in Figure 4. A common block structure is used, and grid density is varied to obtain three levels of grid, namely, coarse (625000 cells), medium (1036800 cells), and fine levels (1423200 cells). The boundary layer was resolved to make sure that the nondimensional wall distance, y^+, is less than 1 for all cases. The governing equations used in the ANSYS CFD tool FLUENT are the Reynolds-averaged Navier-Stokes equations, discretized using a conservative and time-implicit colocated finite volume method. The SST $k-\omega$ two-equation turbulence model is used in the density-based solver. The flow density is constant, and velocity inlet boundary condition is used. Diffusion-based smoothing method is adopted to move the wing model boundary in the updating of the fluid volume mesh. This method allows for large boundary deformation and generates good mesh quality. The lift force on the rigid wing is calculated to conduct a grid convergence test. The results of the case at $\alpha = 1.5$ deg are shown in Figure 5. The total lifts obtained by medium and fine grids agree very well with the increasing flow dynamic pressure. The results showed a maximal 0.2% difference between the medium and fine grid solutions. This indicates that the medium level grid is sufficient for analysis. The structural mesh is built in using 2400 3D 20-node solid elements.

4. Description of Experimental Test Cases

4.1. Measurement of Wing Tip Displacement. A diagram of the photogrammetric measurement with single camera is shown in Figure 6. The camera is fixed right above the wing tip. Two small pieces of reflective tapes are glued onto the wing surface as optical targets, locating on the LE and TE points at the wing tip. The chord of the undeformed wing tip is on the x-axis. Note that the wing tip displacement in the z-axis direction, that is, the horizontal displacement, is focused on in this study. In the wind tunnel test, the camera can be fixed outside the flow field, and the aerodynamics on the wing model will not be affected.

During the deformation of the wing, the whole process is recorded by the camera. Later, frames are grabbed from video and used to track the targets. For this purpose, a Sony digital camera with 1920×1080 pixels is used to acquire images at a rate of 100 frames per second. The measurement error may arise due to nonlinear lens distortion and the inaccurate identification of the target point, so a wind-off experiment is performed to validate this photogrammetric measurement method, as shown in Figure 7. The horizontal displacement of the LE point at the wing tip is set to 105 mm with static loading. The movement of the LE point is tracked by DLTdv7 and the measured displacement is 106.45 mm. By comparing the measured data with the known displacement of the LE point, we find that the measuring error is less than 1.5%. This indicates that the measurement is accurate enough in assessing the numerical results.

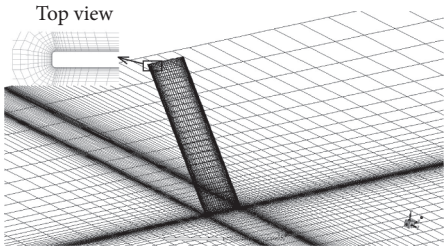

Figure 4: Fluid mesh of the CFD/CSD coupling simulation.

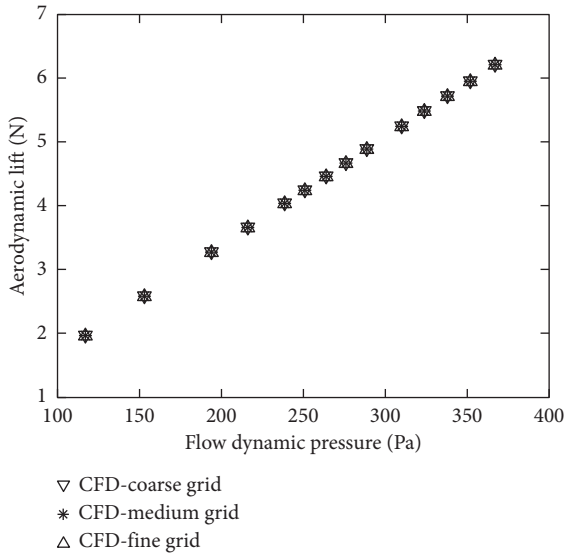

Figure 5: Total lift on the rigid wing at $\alpha = 1.5$ deg.

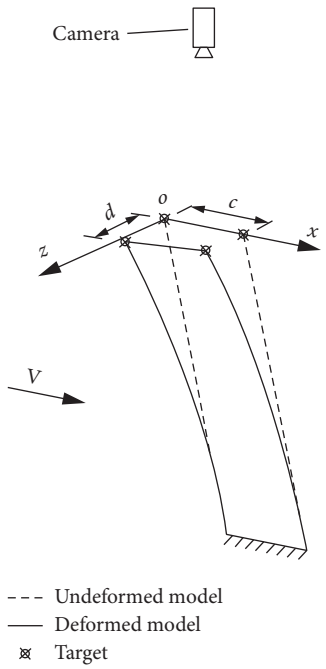

Figure 6: Schema of single-camera measurement system.

Figure 7: Target tracking in image plane for the wind-off experiment.

4.2. Ground Vibration Test. Before conducting the wind tunnel test, it is necessary to perform GVT for model validation and updating. As shown in Figure 8, a SINOCERA shaker (JZK-5) and a power amplifier (YE5874A) are used to excite the model. As the wing structure is very flexible, the drive point is placed near the root of the wing. LMS vibration test system is used to provide random signal to the shaker with a frequency band of 0 to 100 Hz. The force at the joint between the shaker and the model is measured by a PCB force transducer (208C02). The displacement response signal is measured by KEYENCE laser (LK-G150). During the test, the wing structure is kept in microvibration so that the linear case is satisfied. The experimental results of the first five modal shapes and natural frequencies are listed in the first and second column of Table 1, respectively.

After the GVT, a model updating procedure is applied to match the dynamic characteristics of the numerical and the experimental models. The updating procedure performed by solving the optimization problem is defined as follows:

$$\begin{aligned} &\text{Min: } \sum_{i=1}^{5} \left| \frac{f_i^e - f_i^s}{f_i^e} \right| \\ &\text{s.t. } \begin{cases} 0.5E_0 \le E \le 1.5E_0 \\ 0.5\mu_0 \le \mu \le 1.5\mu_0, \end{cases} \end{aligned} \tag{7}$$

where the objective function is the sum of relative errors of the first five natural frequencies obtained by the experiment and simulation. The design variables are Young's modulus E and Poisson's ratio μ of the finite element model. $E_0 = 71$ GPa and $\mu_0 = 0.33$ are the standard material properties of aluminum alloy. Optimization problem

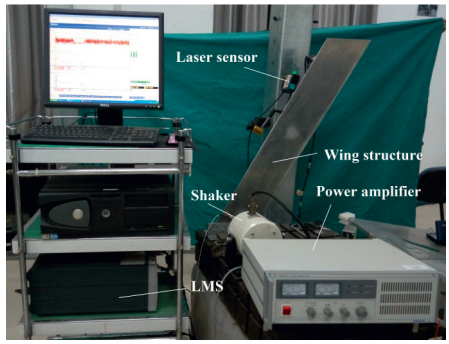

Figure 8: Ground vibration test of the forward-swept wing.

Table 1: The first five natural frequencies and modal shapes of the wing model.

Order (mode)	GVT (Hz)	Calculated by FEM (Hz)	Relative error (%)
1st (1B)	2.39	2.41	0.84
2nd (2B)	15.45	15.16	1.88
3rd (1T)	24.15	24.07	0.33
4th (3B)	43.93	42.87	2.41
5th (2T)	72.46	72.61	0.21

equation (7) is solved by Optimization Toolbox in MATLAB, and the final solutions are $E = 60.37$ GPa and $\mu = 0.31$. The natural frequencies of two models are listed in Table 1. For each of the first five natural frequencies, the relative errors between the computational and experimental values are very small, so the finite element models are validated.

4.3. Wind Tunnel Test. The forward-swept wing model is tested in the NWPU NF-2 acoustic wind tunnel, which is an opening circuit tunnel with a test section of Φ1.5 m and a length of 2 m. The wing model is mounted vertically on a turntable that can rotate to change AOA of the wing, as shown in Figure 9. A wire and pulley mechanism is used to protect the wing model. The wires are loose during the experiment and can be tightened to pull the wing tip from both sides in case of excessive large deformation of the wing model. The experiment process is recorded by the digital camera from the top view of the wind tunnel.

The spanwise bending strain is used in the prediction of the static divergence. For this purpose, two strain gages are used. The lower gage was located at the root of the wing model and the upper one at the fifth semispan station ($(y/s) = 20\%$). The strain response signal is measured by a dynamic strain data acquisition system. At the beginning of the experiment, the turntable is adjusted to ensure that the initial AOA of the wing is 0 deg. Three cases, namely, $\alpha = 0.5$ deg, 1.0 deg, and 1.5 deg, are used to follow the Southwell method.

The divergence dynamic pressure results predicted by experiment and simulation are listed in Table 2. The results obtained by the two strain gages show good agreement, because the Southwell method is independent of the strain gage location. The AOA condition affects the prediction of divergence dynamic pressure and smaller AOA generates higher dynamic pressure prediction. Equation (2) yields a prediction of $q_d^s = 382.5$ Pa, which agrees well with the experiment result $q_d^e = 377.3$ Pa when $\alpha = 0.5$ deg. Finally, at every case of AOA, the average of the two predicted divergence dynamic pressures is treated as the experiment result.

A typical deformation process of wing model in the wind tunnel tests is shown in Figure 10. The movements of LE and TE points are tracked by DLTdv7 continuously. Under this experimental condition, the final measured displacements of the LE point and TE point at the wing tip are 163.0 mm and 140.2 mm, respectively.

5. Results and Discussion

Static aeroelastic deformations of the wing model are computed at two angles of attack ($\alpha = 1.0$ deg and 1.5 deg). The three simulation approaches are VLM coupled with linear structure assumptions, the VLM coupled with the nonlinear structural solver described in the second section, and the CFD/CSD coupling method. The results of three numerical approaches are compared with the experiment data. In order to protect the test model from damage, the performed tests are limited to the subcritical states. The maximum dynamic pressures of the flow are 310 Pa and 289 Pa for the cases of $\alpha = 1.0$ deg and 1.5 deg, respectively; and, in the simulations, the maximum dynamic pressure is set up to a much higher level. The difference among the three simulation results will be shown further.

For $\alpha = 1.0$ deg, the results are shown in Figure 11. When the dynamic pressure is low, the wing tip displacements increase gradually with increasing dynamic pressure. When the dynamic pressure is above the experimental predicted divergence boundary q_d^e, the wing tip displacements increase dramatically. Under the low dynamic pressure condition (lower than 275 Pa), the deformation of the wing model is small, and the geometric nonlinearity is not reflected, so the results of two medium fidelity models and experiment results agree well. When the dynamic pressure is above 287 Pa, the differences between the simulation and experiment results are obvious. The medium fidelity model results are always smaller than those of experiments, while the high fidelity model results are always slightly larger. The effect of the geometric nonlinearity may strengthen the structure, so the wing tip displacement will not tend to infinity when the geometric nonlinearity is taken into account.

Figure 12 shows the results of the case at $\alpha = 1.5$ deg. The same as the aforementioned case, the difference between the results of two medium fidelity models and experiment becomes more and more significant with increasing dynamic pressure. In contrast, the CFD/CSD results agree very well with experiment results, with a slight overestimation of the displacements. When the dynamic pressure is higher than $q_d^e = 357.5$ Pa, the results obtained by linear calculation are totally unrealistic, because the wing tip displacements are even larger than the semispan. Thus, the medium fidelity model based on linear method has limitations when the flow

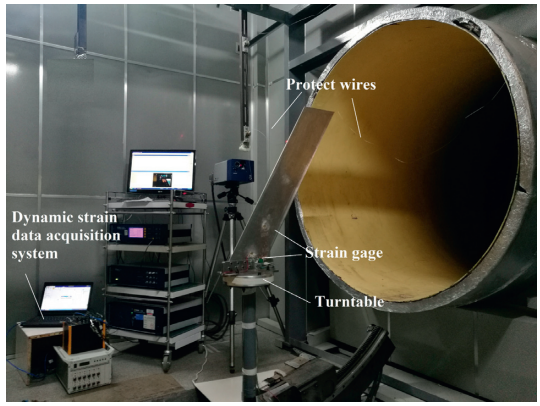

Figure 9: Forward-swept wing model in the test section of wind tunnel (upstream view).

Table 2: Divergence dynamic pressure predicted by wind tunnel test and simulation.

	q_d^e predicted by Southwell method (Pa)			q_d^s calculated by equation (2) (Pa)
	$\alpha = 0.5$ deg	$\alpha = 1.0$ deg	$\alpha = 1.5$ deg	
By upper strain gage	371.6	355.1	338.1	382.5
By lower strain gage	383.0	359.5	337.7	
Average	377.3	357.3	337.9	

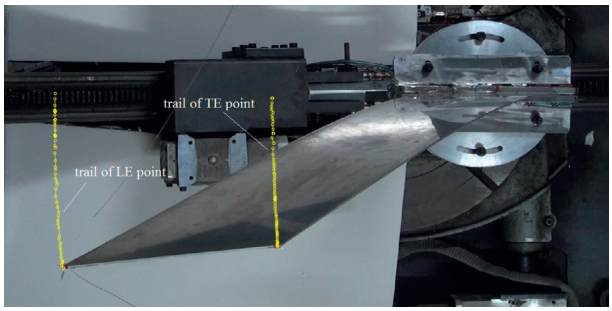

Figure 10: Wing deformation process at $\alpha = 1.5$ deg, from $q = 0$ to 287 Pa.

dynamic pressure approaches the divergence dynamic pressure. The medium fidelity model based on nonlinear method may always underestimate the deformation but keep physical meaning.

The data of the curves in Figures 11 and 12 are listed in Tables 3 and 4, respectively. When the AOA is $\alpha = 1.0$ deg, the accuracies of the medium fidelity and high fidelity models are almost the same. For example, when the dynamic pressure is 310 Pa, the relative errors of the VLM + linear, VLM + nonlinear, and CFD/CSD are 19%, 26%, and 27%, respectively. The data in Table 4 show that the CFD/CSD has better accuracy when $\alpha = 1.5$ deg. For example, when the dynamic pressure is 289 Pa, the relative errors of the VLM + linear, VLM + nonlinear, and CFD/CSD are 31.15%, 36.96%, and 2.33%, respectively. This indicates that when the deformation is large, a high fidelity model is required in the aerodynamic calculation.

In order to find the primary factor for the difference among the three numerical approaches, we compare the status of deformed structure at the beginning of the iterations. Here, we only focus on the case of $\alpha = 1.5$ deg and $q = 367$ Pa for brevity. The deformation of the wing structure is calculated under the aerodynamics of rigid wing, and the results are listed in Table 5. As the wing tip displacements are almost the same, this indicates that the three approaches generate similar results for their following iteration process; and the discrepancy of the final structure deformation mainly comes from the iteration process.

When the iteration process is finished, the wing structure is in a static state under the balance of the aerodynamic load and structure elastic restoring forces. It is well reflected from Figure 13, where the streamlines of the deformed wing at different dynamic pressure are plotted. These CFD calculation results show the flow field near the wing model. When the dynamic pressure is $q = 216$ Pa, as shown in Figure 13(a), the deformation of the wing model is small. The wingtip vortex appears because of the three-dimensional effect. Flows near the wing root and midspan are completely

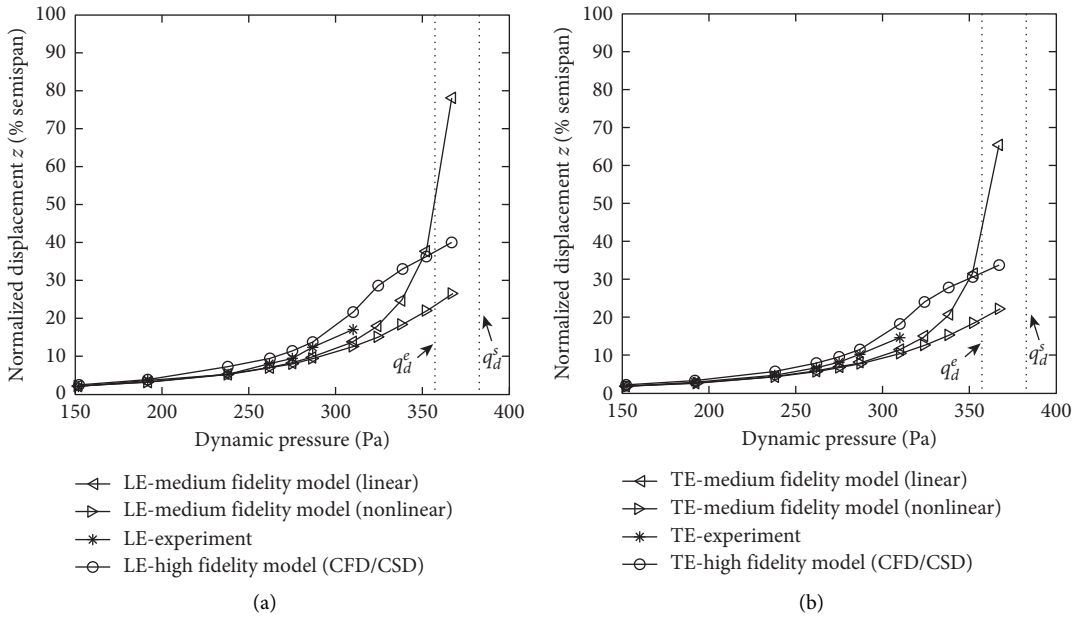

Figure 11: Wing tip displacements versus dynamic pressure for $\alpha = 1.0$ deg. (a) LE point. (b) TE point.

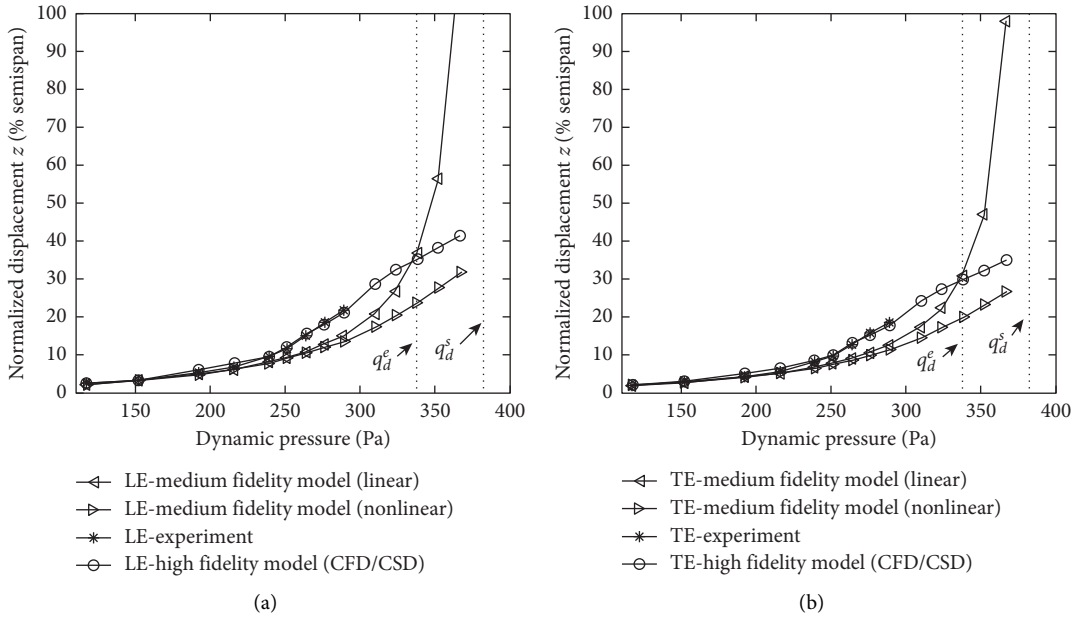

Figure 12: Wing tip displacements versus dynamic pressure for $\alpha = 1.5$ deg. (a) LE point. (b) TE point.

attached. Figure 13(b) is the case of $q = 264$ Pa; flow moves toward the wing root obviously because of the forward-swept effect. Flow separation occurs firstly at the wing root. When the dynamic pressure increases to $q = 310$ Pa, the nondimensional wing tip displacement is larger than 20%, and the local AOA at the wing root and midspan are 8.5 deg and 9.6 deg, respectively. As shown in Figure 13(c), flow separation has extended to the midspan station. Figure 13(d) shows the case of $q = 367$ Pa, and vortices at the wing tip and midspan become stronger than ever. The flow field near the wing model is very complex and fully separated. The VLM is not suitable for this case, and the calculation accuracy cannot be guaranteed. Thus, we can see that the CFD/CSD method has the highest accuracy.

Further insights can be gained by checking the pressure difference distribution when the iteration is finished. A comparison between the pressure difference distributions provided by the medium and high fidelity models is shown in Figure 14 at five spanwise locations $(y/s) = 1.67\%$, 25%, 48.33%, 75%, and 98.33%. Station 1 is

Table 3: Wing tip displacements when $\alpha = 1.0$ deg, %semispan.

q (Pa)	LE				TE			
	VLM + linear	VLM + nonlinear	Experiment	CFD/CSD	VLM + linear	VLM + nonlinear	Experiment	CFD/CSD
152	2.12	2.13	2.11	2.59	1.78	1.78	1.85	2.17
192	3.25	3.25	3.56	4.08	2.72	2.72	3.04	3.42
238	5.31	5.29	5.64	7.00	4.45	4.43	4.85	5.86
262	7.01	6.92	8.08	9.57	5.87	5.80	6.67	8.02
275	8.26	8.07	9.43	11.48	6.91	6.76	8.09	9.63
287	9.71	9.34	12.40	13.78	8.13	7.83	10.42	11.56
310	13.83	12.58	17.09	21.65	11.57	10.53	14.57	18.22
324	17.93	15.16		28.55	15.01	12.71		24.07
338	24.65	18.32		33.09	20.63	15.36		27.92
352	37.62	22.02		36.40	31.49	18.46		30.73
367	78.19	26.47		40.00	65.44	22.21		33.78

Table 4: Wing tip displacements when $\alpha = 1.5$ deg, %semispan.

q (Pa)	LE				TE			
	VLM + linear	VLM + nonlinear	Experiment	CFD/CSD	VLM + linear	VLM + nonlinear	Experiment	CFD/CSD
117	2.13	2.13	2.57	2.51	1.78	1.78	1.90	2.11
153	3.22	3.22	3.42	3.88	2.70	2.70	2.92	3.25
194	4.97	4.96	5.44	6.16	4.16	4.16	4.50	5.17
216	6.27	6.23	6.77	7.90	5.25	5.22	5.69	6.62
239	8.06	7.92	9.62	10.33	6.75	6.64	8.25	8.66
251	9.24	9.01	11.57	12.01	7.73	7.54	9.76	10.07
264	10.78	10.37	15.05	15.72	9.03	8.69	12.71	13.19
276	12.55	11.85	18.69	16.75	10.51	9.92	15.81	14.07
289	14.98	13.71	21.75	21.25	12.54	11.49	18.62	17.89
310	20.74	17.42		28.81	17.37	14.60		24.30
324	26.91	20.42		32.50	22.52	17.12		27.42
338	36.98	23.84		35.47	30.96	19.99		29.93
352	56.44	27.62		38.29	47.24	23.17		32.34
367	117.30	31.89		41.51	98.18	26.77		35.07

Table 5: The wing tip displacements when applying the aerodynamics of rigid wing (mm).

	Medium fidelity model		High fidelity model (CFD/CSD)
	Linear	Nonlinear	
LE point	34.74	34.65	34.59
TE point	29.10	29.03	29.10

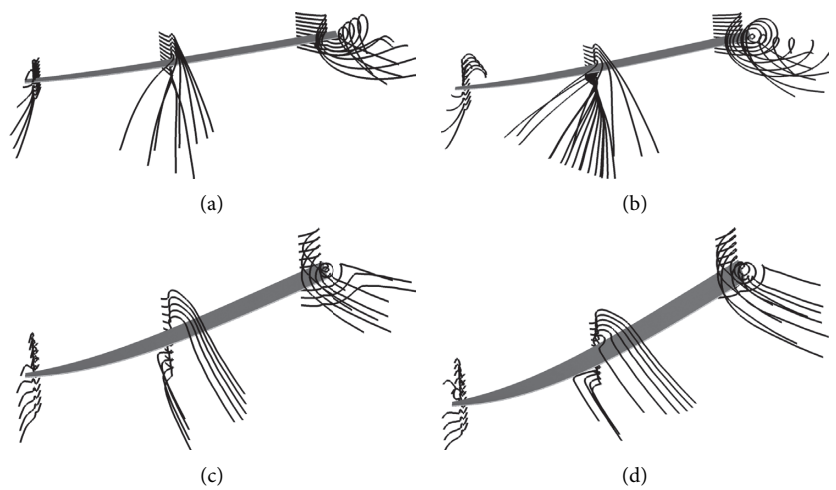

Figure 13: Streamlines of deformed wing at different dynamic pressure, $\alpha = 1.5$ deg. (a) $q = 216$ Pa. (b) $q = 264$ Pa. (c) $q = 310$ Pa. (d) $q = 367$ Pa.

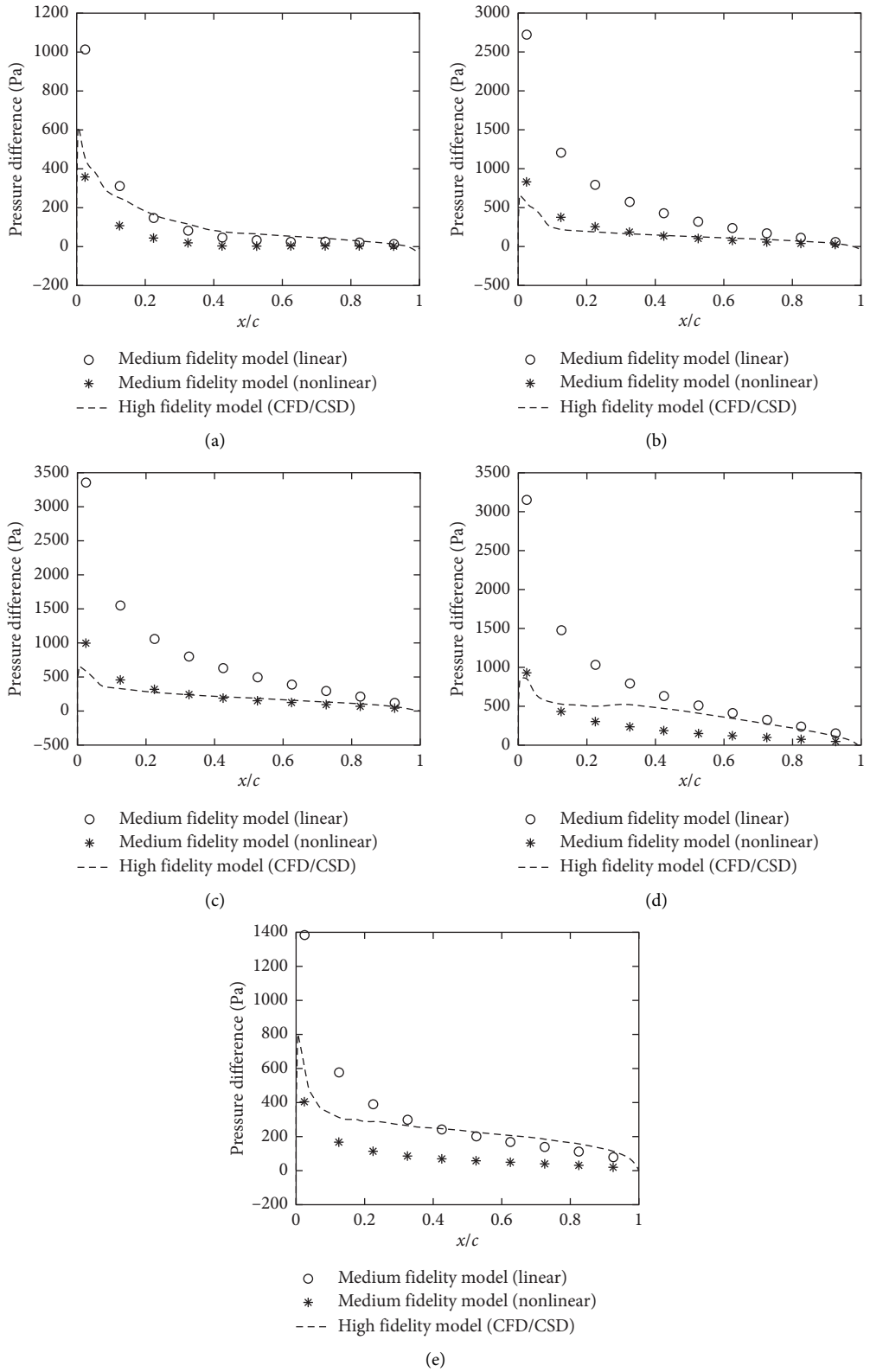

Figure 14: Pressure difference distribution at $\alpha = 1.5$ deg, $q = 367$ Pa. (a) Station 1 ($(y/s) = 1.67\%$). (b) Station 2 ($(y/s) = 25\%$). (c) Station 3 ($(y/s) = 48.33\%$). (d) Station 4 ($(y/s) = 75\%$). (e) Station 5 ($(y/s) = 98.33\%$).

close to the fixed wing root, so the pressure difference distribution obtained by three methods is close except the region near the LE. At stations 2 and 3, the chordwise pressure evolutions calculated by nonlinear method and CFD/CSD coupling are close; and the linear method generates much larger values. In the outboard wing ($(y/s) = 75\%$) and the wing tip ($(y/s) = 98.33\%$), pressure difference distribution calculated by CFD/CSD coupling method becomes closer to the distribution obtained by linear method. When using the nonlinear method, the underestimation of the lift in the outboard wing leads to the underestimation of the structure deformation.

It is worth mentioning here that, with the same computation resource (CPU: Intel Xeon E5-26202.10 GHz, 32 cores), the average computation time of CFD/CSD coupling for a single case is more than 20 hours, while the presented nonlinear analysis on the basis of medium fidelity model takes less than 10 minutes. This difference is mainly caused by the aerodynamics calculation, because the CFD method (solving the NS equations) is much more time-consuming than the VLM. A compromise between the result accuracy and the computation efficiency should be made. When the structure deformation is small, the linear and nonlinear methods based on medium fidelity model have great advantage in efficiency with acceptable accuracy. If the priority is accuracy, the CFD/CSD coupling method can be used especially when the freestream dynamic pressure is high.

6. Conclusions

This study has been one of the first attempts to find out the application condition for the medium and high fidelity models in nonlinear static aeroelastic analysis. The capability of an iterative method in calculating the deformation of forward-swept wing is investigated by comparing experimental data and simulation results. In the given experimental arrangements, the simulation results have an acceptable accuracy compared with the wind tunnel test. The results show that the proposed method is suitable for the static aeroelastic analysis of the flexible wing undergoing large deformation with high computation efficiency.

The conclusions are summarized as follows:

(1) Although it may underestimate the displacements when large deformation occurs, it is advisable to use the proposed method in the framework of preliminary design and optimization when the computation time is concerned.

(2) For large wing deformation, the high fidelity model generates more accurate results compared to the medium fidelity model; however, its capability is limited by being time-consuming. The high fidelity model is recommended to be used in the detailed design phase, in which the accuracy of the result is more important than the computation time.

Data Availability

The numerical and experimental data used to support the findings of this study are available from the corresponding author upon request.

Conflicts of Interest

The authors declare that they have no conflicts of interest.

Acknowledgments

This work was supported by the National Natural Science Foundation of China (Grants nos. 11472216 and 11672240).

References

[1] J. R. Wright and J. E. Cooper, *Introduction to Aircraft Aeroelasticity and Loads*, American Institute of Aeronautics and Astronautics, Reston, VA, USA, 2nd edition, 2007.

[2] Z.-Q. Lu, D.-H. Gu, H. Ding, W. Lacarbonara, and L.-Q. Chen, "Nonlinear vibration isolation via a circular ring," *Mechanical Systems and Signal Processing*, vol. 136, Article ID 106490, 2020.

[3] Z.-Q. Lu, D. Wu, H. Ding, and L.-Q. Chen, "Vibration isolation and energy harvesting integrated in a stewart platform with high static and low dynamic stiffness," *Applied Mathematical Modelling*, vol. 89, pp. 249–267, 2021.

[4] N. Nguyen, E. Ting, and D. Chaparro, "Nonlinear large deflection theory with modified aeroelastic lifting line aerodynamics for a high aspect ratio flexible wing," in *Proceedings of the 35th AIAA Applied Aerodynamics Conference*, Denver, CO, USA, 2017.

[5] C. Zhang, Z. Zhou, X. Zhu, and P. Meng, "Nonlinear static aeroelastic and trim analysis of highly flexible joined-wing aircraft," *AIAA Journal*, vol. 56, no. 12, pp. 4988–4999, 2018.

[6] F. Afonso, J. Vale, É. Oliveira, F. Lau, and A. Suleman, "A review on non-linear aeroelasticity of high aspect-ratio wings," *Progress in Aerospace Sciences*, vol. 89, pp. 40–57, 2017.

[7] X. Liu, R. G. Cook, J. E. Cooper, and Q. Sun, "Static aeroelastic characteristics of a wing including geometric nonlinearities," in *Proceedings of the AIAA Scitech 2019 Forum*, San Diego, CA, USA, 2019.

[8] D. Tang and E. H. Dowell, "Experimental and theoretical study on aeroelastic response of high-aspect-ratio wings," *AIAA Journal*, vol. 39, pp. 1430–1441, 2001.

[9] G. Frulla, E. Cestino, and P. Marzocca, "Critical behaviour of slender wing configurations," *Proceedings of the Institution of Mechanical Engineers, Part G: Journal of Aerospace Engineering*, vol. 224, no. 5, pp. 587–600, 2010.

[10] G. Thwapiah and L. F. Campanile, "Nonlinear aeroelastic behavior of compliant airfoils," *Smart Materials and Structures*, vol. 19, no. 3, Article ID 035020, 2010.

[11] M. Castellani, J. E. Cooper, and Y. Lemmens, "Nonlinear static aeroelasticity of high-aspect-ratio-wing aircraft by finite element and multibody methods," *Journal of Aircraft*, vol. 54, no. 2, pp. 548–560, 2017.

[12] M. J. Patil, D. H. Hodges, and C. E. S. Cesnik, "Nonlinear aeroelasticity and flight dynamics of high-altitude long-endurance aircraft," *Journal of Aircraft*, vol. 38, no. 1, pp. 88–94, 2001.

[13] J. Xiang, Y. Yan, and D. Li, "Recent advance in nonlinear aeroelastic analysis and control of the aircraft," *Chinese Journal of Aeronautics*, vol. 27, no. 1, pp. 12–22, 2014.

[14] M. Ritter, J. Dillinger, and Y. M. Meddaikar, "Static and dynamic aeroelastic validation of a flexible forward swept composite wing," in *Proceedings of the 58th AIAA/ASCE/AHS/ASC Structures, Structural Dynamics, and Materials Conference*, Grapevine, TX, USA, 2017.

[15] C. Xie, L. Wang, C. Yang, and Y. Liu, "Static aeroelastic analysis of very flexible wings based on non-planar vortex lattice method," *Chinese Journal of Aeronautics*, vol. 26, no. 3, pp. 514–521, 2013.

[16] S. Guo, D. Li, and Y. Liu, "Multi-objective optimization of a composite wing subject to strength and aeroelastic constraints," *Proceedings of the Institution of Mechanical Engineers, Part G: Journal of Aerospace Engineering*, vol. 226, no. 9, pp. 1095–1106, 2012.

[17] C. Xie, Y. Meng, F. Wang, and Z. Wan, "Aeroelastic optimization design for high-aspect-ratio wings with large deformation," *Shock and Vibration*, vol. 2017, Article ID 2564314, 16 pages, 2017.

[18] M. Smith, M. Patil, and D. Hodges, "CFD-based analysis of nonlinear aeroelastic behavior of high-aspect ratio wings," in *Proceedings of the 19th AIAA Applied Aerodynamics Conference*, Anaheim, CA, USA, 2001.

[19] H. H. Mian, G. Wang, and Z.-Y. Ye, "Numerical investigation of structural geometric nonlinearity effect in high-aspect-ratio wing using CFD/CSD coupled approach," *Journal of Fluids and Structures*, vol. 49, pp. 186–201, 2014.

[20] H. Dang, Z. Yang, and Y. Li, "Accelerated loosely-coupled CFD/CSD method for nonlinear static aeroelasticity analysis," *Aerospace Science and Technology*, vol. 14, no. 4, pp. 250–258, 2010.

[21] C. Xie, Y. Liu, C. Yang, and J. Cooper, "Geometrically nonlinear aeroelastic stability analysis and wind tunnel test validation of a very flexible wing," *Shock and Vibration*, vol. 2016, Article ID 5090719, 17 pages, 2016.

[22] G. Y. Thwapiah and L. F. Campanile, "Experimental and numerical investigations on nonlinear aeroelasticity of forward-swept, compliant wings," *Journal of Mechanical Design*, vol. 134, Article ID 011009, 2012.

[23] X. Rongrong, Y. Zhengyin, Y. Kun, and W. Gang, "Composite material structure optimization design and aeroelastic analysis on forward swept wing," *Proceedings of the Institution of Mechanical Engineers Part G Journal of Aerospace Engineering*, vol. 233, no. 13, 2019.

[24] C. Zhang, H. Guo, B. Lv, J. Zha, and L. Yu, "Transonic static aeroelastic numerical analysis of flexible complex configuration wing," *Shock and Vibration*, vol. 2021, Article ID 5553304, 9 pages, 2021.

[25] R. H. Ricketts and V. R. Doggett, *Wind-Tunnel Experiments on Divergence of Forward-Swept Wings*, NASA, Washington, DC, USA, 1980.

[26] M. Blair and T. A. Weisshaar, "Swept composite wing aeroelastic divergence experiments," *Journal of Aircraft*, vol. 19, no. 11, pp. 1019–1024, 1982.

[27] S. R. Cole, "Divergence study of a high-aspect-ratio, forward swept wing," *Journal of Aircraft*, vol. 25, no. 5, pp. 478–480, 1988.

[28] Z. Wan, C. Yang, and C. Zou, "Divergence experiment prediction techniques of flat-plate forward-swept wing in wind tunnel," in *Proceedings of the 44th AIAA/ASME/ASCE/AHS/ASC Structures, Structural Dynamics, and Materials Conference*, Norfolk, VA, USA, 2003.

[29] T. Liu, L. N. Cattafesta III, R. H. Radeztsky, and A. W. Burner, "Photogrammetry applied to wind-tunnel testing," *AIAA Journal*, vol. 38, pp. 964–971, 2000.

[30] T. Liu, A. W. Burner, T. W. Jones, and D. A. Barrows, "Photogrammetric techniques for aerospace applications," *Progress in Aerospace Sciences*, vol. 54, pp. 1–58, 2012.

[31] C. Spain, J. Heeg, T. Ivanco et al., "Assessing videogrammetry for static aeroelastic testing of a wind-tunnel model," in *Proceedings of the 45th AIAA/ASME/ASCE/AHS/ASC Structures, Structural Dynamics & Materials Conference*, Palm Springs, CA, USA, 2004.

[32] T. L. Hedrick, "Software techniques for two- and three-dimensional kinematic measurements of biological and biomimetic systems," *Bioinspiration & Biomimetics*, vol. 3, no. 3, Article ID 034001, 2008.

[33] T. Q. Truong, V. H. Phan, H. C. Park, and J. H. Ko, "Effect of wing twisting on aerodynamic performance of flapping wing system," *AIAA Journal*, vol. 51, no. 7, pp. 1612–1620, 2013.

[34] E. C. E. Culler, C. Fagley, J. Seidel, T. E. Mclaughlin, and J. A. N. Farnsworth, "Developing a reduced order model from structural kinematic measurements of a flexible finite span wing in stall flutter," *Journal of Fluids and Structures*, vol. 71, pp. 56–69, 2017.

[35] E. H. Dowell, "A modern course in aeroelasticity," *Meccanica*, vol. 34, no. 2, pp. 140-141, 1999.

[36] W. P. Rodden and E. H. Johnson, *MSC/NASTRAN Aeroelastic Analysis: User's Guide*, MacNeal-Schwendler Corporation, Newport Beach, CA, USA, 1994.

[37] C. D. Wieseman, "Methodology for matching experimental and analytical aerodynamic data," in *Proceedings of the 29th Structures, Structural Dynamics and Materials Conference*, Williamsburg, VA, USA, 1988.

Hindawi
Shock and Vibration
Volume 2021, Article ID 6631180, 19 pages
https://doi.org/10.1155/2021/6631180

Review Article

A Review of Model Order Reduction Methods for Large-Scale Structure Systems

Kuan Lu,[1,2] Kangyu Zhang,[1] Haopeng Zhang,[1] Xiaohui Gu,[3] Yulin Jin ,[2,4] Shibo Zhao,[1] Chao Fu,[1] and Yongfeng Yang[1]

[1]*Institute of Vibration Engineering, Northwestern Polytechnical University, Xi'an 710072, China*
[2]*School of Astronautics, Harbin Institute of Technology, Harbin 150001, China*
[3]*State Key Laboratory Mechanical Behavior and System Safety of Traffic Engineering Structures, Shijiazhuang Tiedao University, Shijiazhuang 050043, China*
[4]*School of Automation Engineering, University of Electronic Science and Technology of China, Chengdu 611731, China*

Correspondence should be addressed to Yulin Jin; jinylly@163.com

Received 5 October 2020; Revised 12 December 2020; Accepted 29 March 2021; Published 8 May 2021

Academic Editor: Zeqi Lu

The large-scale structure systems in engineering are complex, high dimensional, and variety of physical mechanism couplings; it will be difficult to analyze the dynamic behaviors of complex systems quickly and optimize system parameters. Model order reduction (MOR) is an efficient way to address those problems and widely applied in the engineering areas. This paper focuses on the model order reduction of high-dimensional complex systems and reviews basic theories, well-posedness, and limitations of common methods of the model order reduction using the following methods: center manifold, Lyapunov–Schmidt (L-S), Galerkin, modal synthesis, and proper orthogonal decomposition (POD) methods. The POD is a powerful and effective model order reduction method, which aims at obtaining the most important components of a high-dimensional complex system by using a few proper orthogonal modes, and it is widely studied and applied by a large number of researchers in the past few decades. In this paper, the POD method is introduced in detail and the main characteristics and the existing problems of this method are also discussed. POD is classified into two categories in terms of the sampling and the parameter robustness, and the research progresses in the recent years are presented to the domestic researchers for the study and application. Finally, the outlooks of model order reduction of high-dimensional complex systems are provided for future work.

1. Introduction

The large and complex structures exist widely in engineering field of aviation, aerospace, shipping, and so on which are complex, high degrees-of-freedom (DOFs), and coupled with a variety of physical mechanisms. Dynamical systems are the basic framework for modeling and control of these enormous varieties of complex structure systems [1]. Examples include fluid dynamics, design optimization, control, chemically reacting flows, data-driven systems, and vibration suppression in large structure systems and other complex underlying physical process. The mechanism model of any complex structure system can be established by classic mechanics in theory. However, the model is usually a large-scale partial differential system, an approximate simplified high-dimensional ordinary system, a coupling system with partial system, and ordinary system, which cannot be solved by theory directly. The common method for dealing with the abovementioned large complex system in engineering is to use the finite element, finite difference, finite volume, and other methods for numerical simulation analysis [2]. However, the number of DOFs of the complex system obtained by finite element methods may be tens of thousands. If the system has strong fluid-solid coupling effects [3], the number of DOFs may reach millions, even billions. Numerical simulation of large-scale dynamical systems plays a fundamental role in studying a wide range of complex physical phenomena. Although the computer is more

advanced in software and hardware, however, the inherent large-scale nature of the models often leads to unmanageable demands on computational resources and a large amount of calculation time to obtain the accurate solution, such as several hours or even longer [3–6].

The MOR methods were developed in the area of systems and control theory. However, there are several definitions of MOR, and it depends on the context in which one is preferred. A flow chart (Figure 1) for modeling complex physical systems can be elaborated based on time domain, frequency domain, time-frequency domain and optimization techniques, and artificial intelligence as follows [7–12].

In time domain, Chebyshev-based approach for model order reduction of linear systems is presented based on Chebyshev rational functions [7]. Algorithms for the estimation of the moments matching of linear and nonlinear systems are proposed for model order reduction, and the estimates are exploited to construct families of reduced-order models [8]. Wavelet-based approach is proposed for model order reduction of linear circuits in the time-frequency domain [9]. Approaches for model order reduction based on artificial neural network aims at obtaining a reduced-order model out of a relatively complex model, generally obtained in a reasonable time and has accepted error [10]. A low-cost fuzzy rule-based implementation of Sammon's method for structure preserving model order reduction is presented [11]. Particle swarm optimization is usually used to solve optimization problems when the number of parameters is low, and also to find a good solution typically involves multiple evaluations of the objective function [12].

A series of model order reduction methods were proposed to reduce the number of DOFs of the system to improve the efficiency of calculation in the field of science and engineering, for example, center manifold method, Lyapunov–Schmidt (L-S) method, Galerkin method, nonlinear Galerkin method, mode synthesize method, Krylov approximation method, balanced truncation method, and POD method [3–24]. Thus, the area of model reduction contains a broad set of mathematical methods to yield and evaluate the reduced models. These model order reduction methods have been applied in various engineering fields and become more mature, but each method has its adaptability and limitations. Many order reduction methods may fail when the complexity and DOF of the system increase, state parameters vary, and nonlinear factors couple with each other. Then, the order reduction model cannot reflect the real dynamic characteristics of original systems. In this paper, the mature model reduction method in high-dimensional systems will be reviewed, and basic principles, adaptability, and limitations will be expounded.

The POD method is an order reduction method suitable to process large and complex structures quickly and efficiently [2, 23, 24]. The POD method has been widely studied and applied by many scholars in recent years. The method can obtain the main structural components of complex systems with few POD reduced-order modes. The method can reduce the DOFs number of complex systems greatly and improve the computational efficiency significantly while ensuring the accuracy of reduction. The method is important for dynamic analysis and optimized design of parameters in large and complex systems.

The motivation of this paper is to summarize the review of the order reduction methods in large-scale structure systems and provides the classification of POD. In Section 2, the center manifold is introduced. The L-S reduction and Galerkin methods are discussed in Sections 3 and 4, respectively. The mode synthesis method is introduced in Section 5. Several issues of the POD method which are worthy to study in the future will be pointed out based on the characteristics of each order reduction method in Section 6. Finally, the conclusions and outlooks are drawn in Section 7.

2. Center Manifold Order Reduction Method

The center manifold order reduction method is a local order reduction method based on the center manifold theory [13, 23–27]. The method projects the high-dimensional system onto low-dimensional central subspace, according to the differential homeomorphic mapping between central subspace and stable subspace near the equilibrium point, and reserves all the topological properties of the high-dimensional system near the equilibrium point. So, the asymptotic behavior in neighborhood of local bifurcation point and central subspace of the original dynamic system is equal in the high-dimensional nonlinear system [25]. The basic principle of the center manifold order reduction method will be described briefly as follows.

The dynamic equation of the high-dimensional complex nonlinear system in state space is expressed as follows:

$$\dot{x} = \mathbf{f}(\mathbf{x}, \mathbf{a}), \quad \mathbf{x} \in R^n, \mathbf{a} \in R^m, \tag{1}$$

where $\boldsymbol{a}$ is a system parameter, m and n are the number of DOFs in the parameter space and state space, and $\mathbf{f} \in C^r$ $(r \geq 1)$, where $C^r$is r order continuous differentiable function space. Formula (1) is expanded linearly at the equilibrium [23, 24].

$$\dot{x} = \mathbf{A}\mathbf{x} + \mathbf{g}(\mathbf{x}), \tag{2}$$

where $\mathbf{A} = \mathbf{D}_{\mathbf{x}}\mathbf{f}(\mathbf{x}, \mathbf{a})|_{(\mathbf{0},\mathbf{0})}$ is the Jacobian matrix of $\mathbf{f}(\mathbf{x}, \mathbf{a})$ and $\mathbf{g}(\mathbf{x})$ is the nonlinear part. Assuming that the equilibrium point is nonhyperbolic, $\boldsymbol{A}$ has n_0 eigenvalues with the real part of 0. For ease of understanding, assuming that the real part of the remaining eigenvalues is less than 0, formula (2) can be expressed via the coordinate transformation of eigen-space as follows [25]:

$$\dot{u} = \mathbf{B}\mathbf{u} + \boldsymbol{\mu}(\mathbf{u}, \mathbf{v}), \tag{3}$$

$$\dot{v} = \mathbf{C}\mathbf{v} + \boldsymbol{\upsilon}(\mathbf{u}, \mathbf{v}), \tag{4}$$

where $\mathbf{u} \in R^{n_0}, \mathbf{v} \in R^{n-n_0}$, $\boldsymbol{B}$ is a matrix of $n_0 \times n_0$, and $\boldsymbol{C}$ is a matrix of $(n - n_0) \times (n - n_0)$. Nonlinear function is at least second-order differentiable, so according to center manifold theory [13, 23–25], there is a differential homeomorphism mapping in partial neighborhood of $(\mathbf{u}, \mathbf{v}) = (\mathbf{0}, \mathbf{0})$ so that formulas (3) and (4) can be expressed as follows:

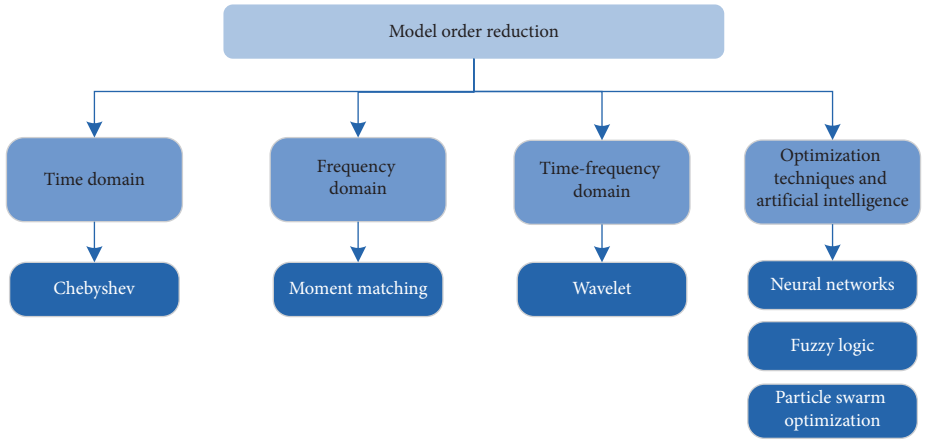

Figure 1: Flow chart of model order reduction.

$$W^C = \{(\mathbf{u}, \mathbf{v}): \mathbf{v} = \mathbf{h}(\mathbf{u})\}. \quad (5)$$

Substituting formula (5) into (3) and (4), we obtain the following:

$$D_u\mathbf{h}(\mathbf{u})[\mathbf{Bu} + \boldsymbol{\mu}(\mathbf{u}, \mathbf{h}(\mathbf{u}))] - \mathbf{Ch}(\mathbf{u}) - \boldsymbol{\upsilon}(\mathbf{u}, \mathbf{h}(\mathbf{u})) = 0. \quad (6)$$

$\mathbf{h}(\mathbf{u})$ can be calculated through formula (6). However, it is difficult to obtain the analytical expression directly through formula (6) in the complex system [23, 24].

$$\dot{u} = \mathbf{Bu} + \boldsymbol{\mu}(\mathbf{u}, \mathbf{h}(\mathbf{u})). \quad (7)$$

Formula (7) in neighborhood of equilibrium point is obtained by differential homeomorphism mapping. Formula (7) and the original system have completely topological equal dynamic behaviors.

The theory of the center manifold order reduction method is rigorous and complete, and the method has simple steps to solve the order reduction model. So, the method is applied widely in high-dimensional complex nonlinear dynamic systems. Cao et al. [25] applied the center manifold theory to study the reduction of Fold bifurcation in three points electrical system voltage collapse. Yoursef and Yoursef [26] and Zhang et al. [27] proposed general program to calculate arbitrary high-dimensional systems by Mathematica, and center manifold dimension is less than 6.

Boyaci et al. [28] established a perfectly balanced symmetric rotor which is supported by two identical floating ring bearings, and the analytical results obtained from the center manifold reduction are compared with numerical results by a continuation method. The random center manifold theory was established to lay the foundation for the theory analysis of the high-dimensional nonlinear random dynamic system in Ref. [29]. Liu et al. [30] used center manifold theory to reduce the nonlinear aeroelastic system with 9 state variables to 2-DOF at the equilibrium. Rendall [31] analyzed some dynamic systems of the spatial isotropic universe model by center manifold theory and obtained progressive behavior of all solution of Einstein equation with Bianchi-III formation.

Sinou et al. [32] applied center manifold theory to analyze the effects of friction of the high-dimensional nonlinear braking model to system stability. Center manifold theory was applied by Hupkees and Lunel [33] to analyze the solution behavior of nonlinear autonomous mixed functional differential equation near the equilibrium. In recent years, Kano et al. [34] investigated the order reduction and bifurcation analysis of a flexible rotor system supported by a full circular journal bearing, and bifurcation phenomena at around the instability point are investigated by applying the center manifold theory and using the normal form theory. Liu et al. [35] investigated the stability and bifurcation behavior of a kind of active magnetic bearing rotor. It is found that a Hopf bifurcation occurs in the system by using center manifold and normal form. Liu et al. [36] established a Jeffcott rotor model for the rotor system of the permanent magnet synchronous motors in electric vehicles, and center manifold theorem and Lyapunov method are used to determine the stabilities of multiple equilibrium points.

The center manifold order reduction method is applied in many fields, but the theory belongs to local redaction method. It is only established near the equilibrium and very difficult to discuss the global behavior of high-dimensional systems. At the same time, nonconvergence problems also occur when using series solutions [23, 24]. In addition, the DOF of the reduced-order system is determined by center manifold. For a nonlinear system with higher DOF, the center manifold dimensions may be still high and it is difficult to handle the method. So, the center manifold order reduction method has significant theoretical values for the complex nonlinear system below a dozen DOF.

3. L-S Method

The Lyapunov–Schmidt (L-S) method [3] is similar to the center method, and it is also a local reduction method.

The difference can be expressed as follows. Center manifold theory reduces the high-dimensional complex nonlinear system to a low-dimensional dynamic system which can remain equivalent to the dynamics topology of the original system. However, the L-S method can process static bifurcation of stationary solution directly in the high-

dimensional complex nonlinear system. From the implicit function theorem, one set of equations has unique solution, the equations are solved and the solution is substituted to the other set of equations, and then the solution of the high-dimensional static bifurcation issue can be reduced to a solution of low-dimensional equations.

The basic principle of the L-S method is to project high-dimensional nonlinear algebra equations to the two mutually orthogonal subspaces of its value space, and two sets of equations can be obtained [13, 24]. The basic principle of the L-S method will be briefly described as follows.

Consider the static bifurcation of the stationary solution of the high-dimensional nonlinear system; from the mapping $\mathbf{f}$: $X \times R^m \longrightarrow Y$ of equation (1), the high-dimensional nonlinear algebraic equation can be expressed as follows:

$$\mathbf{f}(\mathbf{x}, \mathbf{a}) = \mathbf{0}. \tag{8}$$

X and Y are Banach space. The static bifurcation point of the original system can be changed to the coordinate origin by coordinate translation transformation, that is, $\mathbf{f}(\mathbf{0}, \mathbf{0}) = \mathbf{0}$. Assuming that $\mathbf{A} = \mathbf{D}_{\mathbf{x}}\mathbf{f}(\mathbf{x}, \mathbf{a})|_{(\mathbf{0},\mathbf{0})}$ is Fredholm operator, the zero space is $\eta(\mathbf{A})$ and the value space is $R(\mathbf{A})$. And the dimension of the zero space is finite and greater than zero. Then, through the spatial straight sum decomposition near the coordinate origin, the following is obtained [37]:

$$\begin{aligned} X &= \eta(\mathbf{A}) \oplus M, \\ Y &= N \oplus R(\mathbf{A}). \end{aligned} \tag{9}$$

Defining the mapping operator P: $Y \longrightarrow R(\mathbf{A})$ and the complement operator $I - P$: $Y \longrightarrow N$, I is identical operator. The state variable $\mathbf{x} \in X = \eta(\mathbf{A}) \oplus M$ can be expressed as$\mathbf{x} = \upsilon + \omega$, $\upsilon \in \eta(\mathbf{A}), \omega \in M$ based on equation (9). Equation (8) is equivalent to equations (10) and (11) from action of mapping operator and complement operator [23]:

$$P\mathbf{f}(\boldsymbol{\upsilon} + \boldsymbol{\omega}, \mathbf{a}) = \mathbf{0}, \tag{10}$$

$$(I - P)\mathbf{f}(\boldsymbol{\upsilon} + \boldsymbol{\omega}, \mathbf{a}) = \mathbf{0}. \tag{11}$$

Because $P\mathbf{A} = PD_{\mathbf{x}}\mathbf{f}(\mathbf{0}, \mathbf{0})$, if $\boldsymbol{A}$ is limited to M, then A is reversible. It can be known from the implicit function theory that the unique solution $\varphi = \varphi(\upsilon, \mathbf{a})$: $\eta(\mathbf{A}) \times R^m \longrightarrow R(\mathbf{A})$ of equation (10) in the neighborhood of $(\upsilon, \omega, \mathbf{a}) = (\mathbf{0}, \mathbf{0}, \mathbf{0})$ makes $P\mathbf{f}(\upsilon + \varphi(\upsilon, \mathbf{a}), \mathbf{a}) = \mathbf{0}$ and $\varphi(\mathbf{0}, \mathbf{0}) = \mathbf{0}$. Submit the solution of the above equation to equation (11), there is a mapping g: $\eta(\mathbf{A}) \times R^m \longrightarrow N$, so that

$$g(\boldsymbol{\upsilon}, \mathbf{a}) = (I - P)\mathbf{f}(\boldsymbol{\upsilon} + \varphi(\boldsymbol{\upsilon}, \mathbf{a}), \mathbf{a}) = 0. \tag{12}$$

The solution of equation (12) corresponds to the solution of equation (8), thereby the static bifurcation issue near the equilibrium in the high-dimensional complex system can be equivalent to the solution of the low-dimensional nonlinear algebraic equation for the reduction.

The L-S method has strict theoretical basis, and it is used widely to study the bifurcation theory in the high-dimensional complex nonlinear system. Chicone [37] used Melnikov integral and the L-S method to analyze the periodical solution bifurcation issue of the autonomic differential system with small parameters. The L-S numerical iterative method was proposed to solve the reduced-order bifurcation equation and Hopf bifurcation issue in Ref. [38]. Zhang and Stewart [39] applied the L-S method to discuss the existing of the bounded solution of the nonautonomous parabolic equation. Lukas [40] used the Wolfram symbol software package of Mathematica to develop the L-S reduction algorithm, and the algorithm can be applied to calculate the three-dimensional vortex structure of the dispersed nonlinear Schrodinger equation. Sandfry andHall [41] applied the L-S reduction to determine an analytic relationship between parameters to recognize conditions for which a jump phenomenon occurs. In recent year, Buica et al. [42] applied the L-S method to analyze the periodical solution bifurcation issue of the regular nondegenerate cluster in the Lipschitz system. The L-S method was applied by Chen and Zheng [43] to study the solution aggregation behavior of the fractional order nonlinear Schrodinger equation. Pogan et al. [44] studied the O(2) Hopf bifurcation of the viscous shock in tube, and they used L-S method to handle the quasi-linear hyperbolic-parabolic system with hot viscoelastic issue. Cao et al. [45] studied the dynamic property of the damped harmonic oscillator with delayed feedback, and they applied the L-S method to obtain the judging condition for bifurcation of periodical solution and number of branches. Li and Ma [46] promoted the L-S method to the fractional differential system. Guo and Ma [47] analyzed the stability and bifurcation behaviors of the reaction-diffusion equations with the Dirichlet boundary condition and applied the L-S method to prove the existence of the partial nonuniform solution.

The L-S method is complete in theory, and the method can process the bifurcation issue of the high-dimensional nonlinear system effectively, but it is difficult for the method to process the static bifurcation issue of the large and complex nonlinear system. The main reason is as follows. It is difficult to solve the low-dimensional nonlinear algebraic equations in the processing of the high-dimensional space decomposing. The dimension of the obtained low-dimensional nonlinear algebraic equations is still very high after the high-dimensional complex system is decomposed by the L-S method. All the literature about the L-S method known by the authors of this paper can process the DOF of the high-dimensional system which is less than ten, so the L-S method is suitable for studying the bifurcation of the high-dimensional complex system with DOF less than twenty.

4. Galerkin Method

The first two-order reduction methods are mainly used to analyze few high-dimensional nonlinear system models with several DOFs theoretically, but the complex dynamic system in engineering is usually continuous partial differential system, simplified approximate high-dimensional ordinary differential system, or coupling system with both partial and ordinary differential. Galerkin mapping is a bridge from partial differential to ordinary differential, and it is an effective order reduction method to handle this system [2, 15–17]. The final purpose of the Galerkin mapping is to

obtain a low-dimensional dynamic system, which can reflect the dynamic characteristics of the original system. The basic principle of the standard Galerkin method is to map the original system to the mode space and make up the system by intercepting low-order modes and ignoring the effects of the high-order mode to achieve the purpose of reducing the order [15, 17]. The basic principle of the Galerkin method will be described briefly as follows.

The dispersed dynamic equations of the high-dimensional complex system obtained via the finite element or other method are

$$\mathbf{M}\ddot{x} + \mathbf{C}\dot{x} + \mathbf{K}\mathbf{x} = \mathbf{F}(\mathbf{x}, t). \tag{13}$$

M, C, and **K** are total mass matrix, total damping matrix, and total stiffness matrix, respectively, and $\mathbf{F}(\mathbf{x}, t)$ is the nonlinear force. Through the mode coordinate translation, $\mathbf{x} = \psi\mathbf{u} = \psi_m\mathbf{u}_m + \psi_l\mathbf{u}_l$, where $\psi = [\psi_m, \psi_l]$ is the system mode matrix (ψ_m and ψ_l are the matrices constituted by the first m and the remaining l eigenvectors, respectively) and $\mathbf{u} = [\mathbf{u}_m, \mathbf{u}_l]$ represents coordinates. Equations (14) and (15) can be obtained by projecting equation (13) into mode space as follows:

$$\mathbf{M}_m\ddot{u}_m + \mathbf{C}_m\dot{u}_m + \mathbf{K}_m\mathbf{u}_m = \mathbf{F}_m\left(\psi_m\mathbf{u}_m + \psi_l\mathbf{u}_l, t\right), \tag{14}$$

$$\mathbf{M}_l\ddot{u}_l + \mathbf{C}_l\dot{u}_l + \mathbf{K}_l\mathbf{u}_l = \mathbf{F}_l\left(\psi_m\mathbf{u}_m + \psi_l\mathbf{u}_l, t\right). \tag{15}$$

The standard Galerkin method directly ignores the effects of the high-order mode, so the original system can be reduced to the following [15]:

$$\mathbf{M}_m\ddot{u}_m + \mathbf{C}_m\dot{u}_m + \mathbf{K}_m\mathbf{u}_m = \mathbf{F}_m\left(\psi_m\mathbf{u}_m, t\right). \tag{16}$$

When the truncation mode m is taken to a certain extent, the original system can be expressed approximately as follows: $\mathbf{x} = \psi_m\mathbf{u}_m$.

Because of neglecting the effects of the high-order mode, the reduced model of complex nonlinear systems has large errors. So, some scholars proposed the nonlinear Galerkin method, which finds the approximate relationship between the high and the low mode coordinate by constructing inertial manifold [15–17, 24, 49] based on the inertial manifold theory [48]. The nonlinear Galerkin method can improve the approximate accuracy, but the method needs more calculation time [48] because each integral includes the nonlinear factor of the approximate inertial manifold method. Garcia-Archila [50, 51] proposed the posterior Galerkin method to solve the problem, which can save the calculation time [17]. For this method, it is not necessary to calculate the approximate inertia manifold in each step of the integration step and only need to consider the effects of higher order modes in the output of each step.

After decades of the development and application, the Galerkin method has become an important way to obtain the numerical solution of large and complex systems rapidly, and its related application literatures are endless. For example, Wang and Cao [15, 16] proposed the predictive correction Galerkin method, and they used the method to reduce the order of the large rotor-bearing system. Ding and Zhang [52] analyzed an isotropic flexible shaft acted by nonlinear fluid-induced forces and reduced dimensions of the rotor system by both the standard Galerkin method and the nonlinear Galerkin method. An adaptive discontinuous Galerkin method was proposed to obtain a high-resolution numerical solution efficiently in Ref. [53]. Sembera and Benes [54] applied the nonlinear Galerkin method to analyze the reaction-diffusion system in bounded invariant domain and proved the convergence of the method. Chatzisavvas et al. [55] investigated the effect of hydrodynamic thrust bearings on the nonlinear vibrations and the bifurcations occurring in rotor-bearing systems by using a global Galerkin approach. The postprocessing Galerkin method was used to reduce the mode order for nonlinear wind turbines [56]. Boelens et al. [57] used the second-order accurate discontinuous Galerkin finite element method to discretize the governing equations on a hexahedral mesh. Amabili et al. and Sarkar et al. [58, 59] applied Donnell nonlinear cylindrical shell theory to deeply research the great vibration for liquid filled cylindrical shell, and they obtained the 16-DOF accurate response of the system on simple hormonic excitation by using the Galerkin mode truncation method. The Galerkin and the partial POD methods were combined to study two one-dimensional parabolic equations [60]. Xie et al. and Xie et al. [61, 62] applied the Von Karman large deflection plate theory, Galerkin method, and POD method to study the wing aerodynamic flutter problem with supersonic flow condition.

The Galerkin method has been widely applied in engineering, but the method is insufficient, for example, the existence of inertial manifold in high-dimensional complex system, structure issue of inertial manifold, the truncation principle of modal order, and the convergence of the algorithm [23, 24, 63].

5. Modal Synthesis Method

The modal synthesis method is another effective order reduction method; it is essentially a classic Galerkin method, so the method is applied widely to reduce the order of the large and complex system [15–17, 64–78]. The principle of the modal synthesis method is dividing large and complex system into substructures, ignoring the high-mode of substructures, and then synthesizing the system composed of low-order modalities of each substructure, thereby achieving the purpose of reducing system DOF [17, 19, 70, 73]. According to the different connections of substructures, the method can be divided into fixed-interface modal synthesis method, free interface modal synthesis method, and mixed interface modal synthesis method [73, 75]. The basic principle of the method will be introduced briefly as follows.

The discrete dynamic equation of the large and complex system is as follows:

$$\mathbf{M}\ddot{x} + \mathbf{C}\dot{x} + \mathbf{K}\mathbf{x} = \mathbf{F}(\mathbf{x}, t). \tag{17}$$

In equation (17), $\mathbf{M} = \{\mathbf{M}_i\}_1^n$, $\mathbf{C} = \{\mathbf{C}_i\}_1^n$, $\mathbf{K} = \{\mathbf{K}_i\}_1^n$, $\mathbf{x} = \{\mathbf{x}_i\}_1^n$, and $\mathbf{F} = \{\mathbf{F}_i\}_1^n$ are the mass, damping, stiffness matrix, point displacement, and nonlinear force,

respectively, which are composed of n substructure systems. $\mathbf{M}_i$, $\mathbf{C}_i$, and $\mathbf{K}_i$ are the mass, damping, and stiffness matrix of the i-th substructure, respectively. $\mathbf{M}_i$, $\mathbf{C}_i$, $\mathbf{K}_i$, and $\mathbf{F}_i$ of substructure are divided into internal coordinate $\mathbf{x}_{iI}$ and boundary coordinate$\mathbf{x}_{iB}$, and the dynamic equation of the substructure can be written as follows:

$$\mathbf{M}_i\ddot{x}_i + \mathbf{C}_i\dot{x}_i + \mathbf{K}_i\mathbf{x}_i = \mathbf{F}_i(\mathbf{x}_i, t), \tag{18}$$

where $\mathbf{x}_i = \begin{bmatrix} \mathbf{x}_{iI} \\ \mathbf{x}_{iB} \end{bmatrix}$, $\mathbf{F}_i = \begin{bmatrix} \mathbf{F}_{iI} \\ \mathbf{F}_{iB} \end{bmatrix}$, $\mathbf{M}_i = \begin{bmatrix} \mathbf{M}_{iII} & \mathbf{M}_{iIB} \\ \mathbf{M}_{iBI} & \mathbf{M}_{iBB} \end{bmatrix}$, $\mathbf{C}_i = \begin{bmatrix} \mathbf{C}_{iII} & \mathbf{C}_{iIB} \\ \mathbf{C}_{iBI} & \mathbf{C}_{iBB} \end{bmatrix}$, and $\mathbf{K}_i = \begin{bmatrix} \mathbf{K}_{iII} & \mathbf{K}_{iIB} \\ \mathbf{K}_{iBI} & \mathbf{K}_{iBB} \end{bmatrix}$.

To calculate constrained main mode $\psi_{ik} \in R^{n_I \times n_k}$ and constrained mode $\psi_{ic} \in R^{n_I \times n_B}$ with boundary or interface constraint, n_I, n_B, and n_k are the number of coordinates of the substructure internal nodes, the number of boundary coordinates, and the number of retained constraint main modes [1, 72]. ψ_{ik} can be calculated by the constrained boundary$\{\mathbf{x}_{iB} = \mathbf{0}\}$, and then the translation relationship between the physical coordinate $(\mathbf{x}_{iI}, \mathbf{x}_{iB})$and the modal coordinate $(\mathbf{u}_{ik}, \mathbf{u}_{iB})$ can be obtained [1, 75].

$$\begin{bmatrix} \mathbf{x}_{iI} \\ \mathbf{x}_{iB} \end{bmatrix} = \begin{bmatrix} \psi_{ik} & \psi_{ic} \\ 0 & I_{iB} \end{bmatrix} \begin{bmatrix} \mathbf{u}_{ik} \\ \mathbf{u}_{iB} \end{bmatrix} = \mathbf{P} \begin{bmatrix} \mathbf{u}_{ik} \\ \mathbf{u}_{iB} \end{bmatrix}. \tag{19}$$

The structural dynamic reduction modal can be obtained via substituting equation (19) to equation (18):

$$\overline{M}_i\ddot{u}_i + \overline{C}_i\dot{u}_i + \overline{K}_i\mathbf{u}_i = \overline{F}_i, \tag{20}$$

where $\overline{M}_i = \mathbf{P}^T\mathbf{M}_i\mathbf{P}$, $\overline{C}_i = \mathbf{P}^T\mathbf{C}_i\mathbf{P}$, $\overline{K}_i = \mathbf{P}^T\mathbf{K}_i\mathbf{P}$, and $\overline{F}_i = \mathbf{P}^T\mathbf{F}_i$. The total reduction modal of the high-dimensional complex structural system can be obtained by integrating the reduced modal of each substructure.

$$\overline{M}\ddot{u} + \overline{C}\dot{u} + \overline{K}\mathbf{u} = \overline{F}, \tag{21}$$

where $\mathbf{u} = \{\mathbf{u}_i\}_1^n$, $\overline{M} = \{\overline{M}_i\}_1^n$, $\overline{C} = \{\overline{C}_i\}_1^n$, $\overline{K} = \{\overline{K}_i\}_1^n$, and $\overline{F} = \{\overline{F}_i\}_1^n$.

The modal synthesis method has simple principles and good robustness, and the method is easy to operate. So, the method is widely used to reduce the order of the engineering complex structure system. Yang [1] used finite element software to establish discrete dynamic modal of five points reverse rotation dual-rotor system, and they divided dual-rotor into two substructures of inner and outer rotors. They reduced the order of the system by the fixed-interface mode synthesis method and researched the moment response in processing of accelerating of five points reverse rotation dual-rotor system, and then the calculation scale is reduced. Glasgow [64] calculated the critical speed and the modal shape of the dual-rotor-bearing system by using the substructural modal synthesis method, and the calculation scale is reduced greatly, and then they discussed the calculation accuracy and the error of the method in detail. The mode synthesis method was used to reduce the linear part of the rotor-bearing system modally, and as the boundary coordinate, the nonlinear part together with the reduced modal constitutes a reduced-order system [66]. Wang and Kirkhope [67] improved the free interface mode synthesis method and applied it to reduce the order of multirotor-bearing system. Sundararajan and Noah [68] used the modal synthesis method to reduce the order of the nonlinear rotor system and analyzed the stability and the bifurcation of the reduced modal. Iwatsubo et al. [69] proposed an effective procedure using the component mode synthesis and the method of multiple scales or the harmonic balance method for the nonlinear vibration analysis of rotor systems. The mixed interface modal synthesis method was used to reduce the order for the rotary symmetry impeller structure [71]. Shanmugam and Padmanabhan [72] proposed the mixed interface modal synthesis method, which is more suitable to the dynamic analysis of the two rotors system. In recent years, Beck et al. [73] applied the modal synthesis method to reduce the order of integrally bladed rotors and analyzed the dynamic characteristics of the reduced modal. Zheng et al. [74] proposed a generalized and efficient method for parametric response analysis of large-scale asymmetric rotor in order to avoid costly approach, and the fixed-interface component mode synthesis is employed to form a reduced-order model. Zhang [75] combined the Ansys software and the mixed constraint modal synthesis method to study the large civil structure with nonlinear part. Luo et al. [76] used finite element software and the free interface modal synthesis method to establish the dynamic modal of the high-dimensional two rotors system with collision friction failure. The nonlinear factors of intermediate bearing and the squeeze film damper are taken into account in the modal. They used unit impulse response and the Duhamel integral method to obtain the numerical solution of the equation, and they studied the collision friction response characteristics of the reverse rotary two rotors system. The assessment method was studied by Kim et al. [77] to select the modal in the synthesis method. Joannin et al. [78] combined the complex mode and the modal synthesis method to solve the steady state response in the unconservative system.

The modal synthesis method is suitable for dealing with the large and complex structure, but the method mainly performs modal reduction for linear substructure and ignores the effect of high-order mode and system partial mode, so the reduction modal may have great error. The method is not accurate [23, 24], and the effect of reducing the order is not obvious for the large deformation and strong coupling nonlinear structural system.

6. Proper Orthogonal Decomposition (POD)

In this section, the basic principles will be introduced in Section 6.1. The classification of POD is provided in Sections 6.2 and 6.3 based on sampling and parameter adaption. In Section 6.4, some improved POD methods and related issues are discussed. The POD method is the specific recommendation method which will be widely applied in actual engineering. The POD method contains sample, parameter adaptation problems, and other improved methods, and the classifications are listed in Table 1. The POD methods based on sampling and parameter adaptation problems are introduced briefly as follows.

Table 1: The classification of the POD method.

POD method		
Sampling	Parameter adaptation	Other improved POD methods

The construction of reduced-order models (ROMs) plays a key issue in POD methods. Different sampling signals can yield different ROMs via POD, so many researchers have focused on determining the sampling methods that will yield the optimal ROMs. ROMs can be obtained from the following types of response signals: chaotic response signals, random response signals, transient response signals, and signals obtained through combined sampling methods.

The responses of a complex dynamic system are closely related to the system parameters and initial conditions. The ROMs obtained via POD usually lack robustness against variations in the system parameters. In principle, new ROMs should be constructed for new parameters; however, the number of calculations required to calculate each possible parameter response of a complex system to construct the corresponding ROMs would be very large. To resolve the problem of model order reduction for a complex system over a broad parametric domain and ensure the robustness of the ROMs, many modified methods have been proposed by researchers, including global POD methods, local POD methods, and adaptive POD methods.

6.1. Basic Principles, Advantages, and Disadvantages. The proper orthogonal decomposition (POD) method is also a powerful order reduction method to deal with the large and complex system. Other names of the method are Karhunen–Loève decomposition, principle component analysis (PCA), singular value decomposition (SVD), and Hotelling translation [79, 80]. In the middle of the twentieth century, these methods were proposed, respectively, by Kosambi [81], Karhunen [82], Lorenz [83], Pougachev [84], and Hotelling [85].

The POD method is a projection-based order reduction method, which is similar as the projection/Galerkin method which maps the high-dimensional system to a low-dimensional subspace. The difference between the two methods is as follows. POD is a statistics method, and the POD reduction modal or the reduction basic function is obtained by solving eigenvector of the autocorrelation matrix. The autocorrelation matrix is statistically significant 2nd center moment [79]. The basic principle of the POD method is that the autocorrelation matrix is constructed from numerical simulation snapshot signal or experimental data snapshot signal in the original system. The POD reduced modal or reduced basic function is obtained by solving the eigenvector of autocorrelation matrix and then the high-dimensional system is projected onto the subspace of the reduced-order modal corresponding to first maximum eigenvalues, thereby achieving the purpose of reducing the order. The basic principle will be briefly described as follows.

For the state variables of the high-dimensional complex system (nth dimension) $\mathbf{y}(\mathbf{x}, t)$, the discrete time series$\mathbf{y}(\mathbf{x}, t_i), i = 1, \ldots, N$ can be obtained from numerical simulation signal or experimental signal, and the time series is projected onto the space opened by complete orthogonal specification base $\phi = \{\phi_k(\mathbf{x})\}_{k=1}^{n}$, that is:

$$\mathbf{y}(\mathbf{x}, t_i) = \sum_{k=1}^{n} u_k(t_i)\phi_k(\mathbf{x}), \quad i = 1, \ldots, N. \tag{22}$$

We hope to find a group of orthogonal specification base that satisfies the minimum value constraint under the square norm [23, 24]:

$$\min\langle \left\| \mathbf{y}(\mathbf{x}, t_i) - P\mathbf{y} \right\|^2 \rangle, \quad \|\phi\|^2 = 1. \tag{23}$$

In equation (23), $\langle \cdot \rangle$ indicates the average operator during the sampling period, $P\mathbf{y} = ((\mathbf{y}, \phi)/(\phi, \phi))\phi$ denotes mapping operator, $(\cdot, \cdot)$ represents the inner product on Hilbert space, and $\| \cdot \|^2$ is the L^2 norm.

The orthogonal specification base satisfying the above conditions can be obtained by the Lagrange multiplier method. The objective function is defined as follows [3, 23, 24]:

$$J[\phi] = \langle \|(\mathbf{y}, \phi)\|^2 \rangle - \lambda\left(\|\phi\|^2 - 1 \right). \tag{24}$$

In equation (24), λ is the Lagrange operator. The extreme value of formula (24) is found, and let $\delta J = 0$, we can get the following [79, 80, 86]:

$$\int_{\Omega_x} \langle \mathbf{y}(\mathbf{x})\mathbf{y}(x') \rangle \phi(x') \mathrm{d}x' = \lambda\phi(\mathbf{x}). \tag{25}$$

Formula (25) is second class Fredholm equation, and its kernel function is autocorrelation: $R(\mathbf{x}, x') = \langle \mathbf{y}(\mathbf{x})\mathbf{y}(x') \rangle$. We can prove that the orthonormal basis $\phi = \{\phi_k(\mathbf{x})\}_{k=1}^{n}$ which is also called POD order reduction modes which are the eigenvectors of the autocorrelation matrix $R = (1/N)[\mathbf{y}^T\mathbf{y}]_{n\times n}$ based on equations (22) and (25) and normal orthogonal condition.

The high-dimensional state variables are projected onto the subspace of first few POD modes (eigenvectors are arranged in descending order of corresponding eigenvalues), thereby the best square approximation of original system state variables during the sampling period can be obtained with the least reduced-order mode number m, that is:

$$\mathbf{y}(\mathbf{x}, t_i) \approx \sum_{k=1}^{m} u_k(t_i)\phi_k(\mathbf{x}), \quad i = 1, \ldots, N, m = n. \tag{26}$$

On the other hand, the signal matrix composed of discrete time series $\mathbf{y}(\mathbf{x}, t_i), i = 1, \ldots, N$ can be obtained by the numerical simulation snapshot signal and the experiment signal. The signal matrix can be decomposed by singular value decomposition (SVD) theory [87].

$$[\mathbf{y}]_{N\times n} = [U]_{N\times n}[S]_{n\times n}\left[V^T\right]_{n\times n}. \tag{27}$$

In equation (27), U and $V$are orthogonal matrices, which satisfy $U^TU = V^TV = I_{n\times n}$, diagonal matrix $S = \mathrm{diag}[\sigma_1, \sigma_2, \ldots, \sigma_n]$ is a singular matrix of the sampling signal matrix, and $\sigma_1 \geq \sigma_2 \geq \cdots \geq \sigma_n > 0$. Comparing equations (22), (26), and (27), the matrix translation relationship can be obtained

between the eigenvalue of autocorrelation matrix and singular value decomposition of signal matrix.

$$\mathbf{P} = [\phi_1, \phi_2, \ldots, \phi_m]_{n\times m} = \left[V^T\right]_{n\times n}[S]_{n\times m}. \tag{28}$$

The coordinate translation relationship $\mathbf{y} = \mathbf{Pu}$ can be defined by formula (28). The high-dimensional complex system is projected onto subspaces of a few POD reduced-order modes; $\mathbf{P}$ and $\mathbf{u}(t) = [u_1(t), u_2(t), \ldots, u_m(t)]^T$, respectively, are reduced-order modal translation matrix and the POD modal coordinate. Substitute equation (28) into dynamic equation of the large and complex structure system (17), and then simplifying the formula, we can obtain the following [87]:

$$\widetilde{M}\ddot{u} + \widetilde{C}\dot{u} + \widetilde{K}\mathbf{u} = \widetilde{F}. \tag{29}$$

In equation (29), $\widetilde{M} = \mathbf{P}^T\mathbf{MP}$, $\widetilde{C} = \mathbf{P}^T\mathbf{CP}$, $\widetilde{K} = \mathbf{P}^T\mathbf{KP}$, and $\widetilde{F} = \mathbf{P}^T\mathbf{F}$. A low-dimensional dynamic modal can be obtained. This is the traditional POD reduction method.

In many literatures [79, 87–89], the dimensional number of the reduced-order m is determined by defining the singular values or energy percentage of autocorrelation matrix eigenvalues.

$$\varepsilon = \frac{\sum_{i=1}^{m}\sigma_i}{\sum_{i=1}^{n}\sigma_i} \quad \text{or } \varepsilon = \frac{\sum_{i=1}^{m}\lambda_i}{\sum_{i=1}^{n}\lambda_i}, \tag{30}$$

where $\lambda_i = \sigma_i^2$ is the eigenvalue of the autocorrelation matrix, and the eigenvalue is determined $\varepsilon \geq 95\%$, sometimes $\varepsilon \geq 99\%$ [87, 89], for ensuring the reduced-order signal and the original sampled signal matrixL^2norm approximation.

$$\|\mathbf{y}\|^2 = \left(\sqrt{\mathbf{y}^T\mathbf{y}}\right)^2 = VS^TU^TUSV^T = \sum_{i=1}^{n}\sigma_i^2 \approx \sum_{i=1}^{m}\sigma_i^2. \tag{31}$$

The DOF of the reduction modal obtained by the POD method is very low, and DOF is the best square approximation of the original system, so the method has obvious advantages in reducing DOF of the high-dimensional system and improving computation efficiency. However, from the basic theory of the method, the disadvantages of the method can be obtained. The advantages and disadvantages of the method will be described as follows.

According to the basic theory of the POD method, the method is easy to operate. The most significant advantage is as follows. The most important components of the infinite dimensional or high-dimensional complex system can be obtained with very few POD reduced-order modes, and the method has the optimal approximation under square norm. The DOF of the original system is greatly reduced [79, 80, 87] by using the POD method. So, the POD method is widely used in area of engineering, for example, fluid dynamics [86, 90–95], signal and image processing [96–99], optimal design [100–103], ocean engineering [104], and structural dynamic mechanics [58, 59, 61–63, 105–109].

However, according to the basic theory of the POD method, we can easily find that the POD modes come from the eigenvectors of the autocorrelation matrix, which is constructed by numerical simulation signal or experiment signal. As a result, for different sampling data, the POD modes are different with different sampling parameters, method, or length, which significantly influence the reduced modal. And the actual constructed modes just are the optimal approximation [110] for the original system under recent sampling length, which is not the optimal approximation for the original system of all states, so the constructing of the POD reduced modes is key for the POD method. In response to these problems, scholars have proposed a number of improved POD methods. Through the author's literature research, it is found that these methods can be divided into two categories: one to solve the sampling problem of the POD method and the other to solve the parameter autocorrelation problems of the POD method. The two types of POD methods will be, respectively, reviewed as follows.

6.2. Sampling Study of POD Method. According to previous description of the POD method, the most important part is the construction of reduced-order mode. In view of the sampling point, the different sampling signal can obtain different POD reduced modes; therefore, what kind of sampling signal and how to sample can obtain the optimal reduced-order mode have become a research issue for scholars. By reviewing the relative literature about POD sampling, it is found that some scholars obtained POD reduced modes from chaos response signal [58, 59, 79, 87, 88, 111, 112], random response signal [87, 113–115], moment response signal [116–125], different sampling method [126–133], and constructing different autocorrelation matrix [134].

Kerschen et al. [88] used the finite element method to discretize fixed beam; they used two permanent magnets to act a nonlinear constraint force on free ends of the beam, and then they used the POD method to analyze the reduced order of the discrete high-dimensional nonlinear system. When the outer excitation frequency of this nonlinear system is fixed, they change the excitation amplitude, and then the periodic, almost periodic, and chaos movements have appeared. They found that the POD reduced-order mode obtained from the chaotic response signal is more effective than other nonchaotic response signals in reduction.

Amabili et al. [58, 59] used Donnell nonlinear cylindrical shell theory to go further into the large vibration issue of the simple supporting fluid filled cylindrical shell, and they used the Galerkin modal truncation method to obtain the accurate response of the original system with 16-DOF under the periodic excitation condition. However, they combined the POD method and Galerkin method and then found that only 3-DOF can be used to approximate the periodic, almost periodic response of a 16-DOF system, but extracting the POD modal response must be noticed. They also found that extracting POD reduced-order modal from chaos movement is more effective than from periodic and almost periodic response. Meanwhile, they used the method to analyze the

bifurcation, set the external excitation frequency near the inherent fundamental frequency of the system, and selected the excitation amplitude as the bifurcation parameter. Then, it is found that when the external excitation amplitude varies within a large range, even if the reduced-order mode is extracted from the chaotic response, it cannot be guaranteed that the reduced-order system is similar to the bifurcation structure of the original system. The results indicate that the POD method is not robust in the wide-range parameter domain.

Bizon et al. [111] applied the POD method to research the reduced-order reaction dynamic modal of the one-dimensional tubular reactor with additional thermal cycling; according to calculation maximum orbital entropy index, they proved that the reduced modal fundamental function constructed from chaos sampling is optimal. Xie et al. [61, 62] applied Von Karman large deflection plate theory and combined the POD method and Galerkin method to study the wing aerodynamic vibration under the supersonic flow. They found that POD reduced-order modes obtained from chaotic response signal is more accurate than from period response to approximate the original system. Moreover, the reduced-order mode obtained from the chaotic motion under a certain parameter can also be applied to reduce other parameters in a certain parameter range. The research by the above scholars shows that the chaotic response signal in the complex system includes abundant physical process and state information of the original system, so we extract POD reduced-order modes from chaotic response signal in recent [62, 88].

The complex nonlinear system of actual engineering may appear the chaos motion in some parameter domain, but the complex movements are often avoided in design, processing, and maintenance in these complex structural systems. So, the chaos motion of the system is difficultly obtained in actual engineering. When constructing the signal, the POD reduced-order mode is sampled from the periodic signal of the normal operation of the complex system. The reduced-order modes obtained by this way may include less structural information of the original system, so it is difficult that a few reduced-order modes can obtain the optimal approximation of the original system. Under the random excitation, the system power spectrum is continuous, and the random response is as same as chaos response which has abundant physical processing and state information of the original system, and it is easy to obtain the random excitation, so some scholars [87, 113–115] researched that the POD reduced-order mode is constructed from the random response signal.

Kumar [87, 113] analyzed two high-dimensional nonlinear systems: one is nonlinear fixed beam system [88] and another is multiple spring-mass-damping chain system with Duffing nonlinear factors. They found that under a random excitation of certain bandwidth, the reduced-order modes extracted from random response can obtain better order reduction effect, but the frequency bandwidth of random excitation must cover the main frequency domain, and the extracted response contains many high-frequency components and requires more POD modes to obtain accurate reductions. The random signals were used by Yu and Chakravorty [114] to obtain a global optimal POD reduction mode. Segala [115] used the POD method to process the parameter modal reduction of the nonlinearly supported beams; they also found that the reduced-order mode constructed by random excitation signal can contain the main structural components of the original system with few modal numbers, thus obtaining a lower-dimensional reduced-order model. Therefore, when we do not know that chaotic motion occurs under what parameters in the high-dimensional system, the POD reduction mode can be obtained from the random response.

Some scholars used the POD method to reduce the order of high-dimensional complex systems and found that the better order reduction effect also can be obtained when sampling signal contains the transient response of the original system. In 1998, when Park and Lee [116] studied the flow optimization control issue for two-dimensional viscous flow, they found that the POD reduced-order mode sampled from the flow field displacement signal can only simulate effectively the flow of the original system if it contains the transient flow field signal of the original system. Terragni and Valero [117–121] applied the POD method to reduce the order of a class of continuous dissipative systems; they compared and analyzed the complex bifurcation characteristics of the original system in the parameter domain by the low-dimensional reduced-order system. They found that the reduced-order mode extracted from the snapshot containing the transient motion of the system has a larger parameter applicable range than the reduced-order mode extracted from the attractor.

Yang [121] applied the POD method to research the model reduction and parameter identification of high-dimensional chaotic/linear systems; it is found that the POD reduced-order mode constructed by unstable transient period response signal can approximate to the chaotic motion of the original system. Yu et al. and Lu et al. [122, 123] applied the POD method to reduce the order of high-dimensional nonlinear rotor systems with loose, crack, rubbing, and other faults. The system transient response, which has more motion information, contains free and forced vibrations under given initial conditions. Therefore, they also found that the POD reduced-order mode extracted from the transient motion signal can obtain better order reduction effect. Lu et al. [124, 125] also obtained the POD reduced-order sampled from the system transient response and reduced the order of the multidisk rotor-bearing system.

The above is the study about types of sampling signals of the POD method. However, the snapshot signals of the physical quantities of the original system obtained by numerical simulation or experiment involve how to sample, so some scholars have studied the sampling methods of POD methods [126–135]. Standard sampling methods include uniform sampling, random sampling, and hierarchical sampling [133]. Uniform sampling, which samples the motion state of each parameter in the system parameter space, requires a large computational cost. Especially, when the dimension of the parameter space is very high, uniform sampling will lose the application value. Random sampling

may not be able to obtain information on some important areas of the parameter space [126]. It is difficult for the standard sampling method to obtain the construction of optimal reduced-order mode in high-dimensional parameter space, so scholars proposed some autocorrelation sampling methods: model constraint (MC-POD) method [126], greedy sampling (GS-POD) method [127–130], confidence domain (TR-POD) method [131], optimal component (OS-POD) method [132, 130], and some other sampling methods [132–135]. These methods mainly optimize snapshot signals by various sampling methods, which allow more state information of the original system to be included in different parameter domains or some important parameter domains, thereby obtaining an optimal POD reduced-order mode basis function.

For multifield, multiphysics coupled high-dimensional complex systems, we can extract multiple sets of state vector signals from the original system, such as velocity and displacement of the flow field, temperature field, pressure field, velocity, and displacement of the structure. It should be considered that which state vector should be chosen to construct the autocorrelation matrix and how to construct it. Kirby et al. [136] proposed putting together groups of state variables of the coupled system to construct a total state vector. By constructing the autocorrelation matrix by this state vector, the POD reduced mode of the coupled system is obtained and then this reduced-order mode was used to reduce the governing equations of the coupled system. This method has been successfully applied to model reduction of complex multifield coupled systems [92, 137–139]. However, the constructed total autocorrelation matrix contains the coupling of the state vectors of each parts of the system. This kind of coupling is generated by the total state vector in the process of numerically calculating the autocorrelation matrix, which is inconsistent with the coupling of the actual system, and the problem of nonconvergence of the reduced-order model often occurs. Brenner et al. [134] proposed that the state vectors of the components of the coupled system separately construct the autocorrelation matrix, and the mutual coupling term between the components is set to zero. The reduced-order model obtained by the total autocorrelation matrix constructed by this method is more accurate and convergent than the method proposed by Kirby et al.

In summary, the sampling issue of the POD method is very important for constructing reduced-order modes. The signal that constructs the reduced-order mode should contain more abundant and detailed physical processes and state information of the original system, such as chaotic signals, random signals, transient signals, and signals obtained by various sampling methods. The POD reduced-order modes sampled from these signals can obtain high-precision approximation to the original system with few DOFs. Now, scholars generally extract POD reduced modes from chaotic signals. When the system chaotic motion signal cannot be obtained in advance, a random response signal of a certain bandwidth or a transient motion signal can be used to extract the reduced mode. The above is a review of the POD method in the sampling issue, and then we will elaborate on another type of issue of the POD method.

6.3. Parameter Adaptation of POD Method. The response of the complex dynamic system is related closely to system parameters, initial conditions, and so on. Therefore, the reduced-order mode obtained by the POD method usually lacks robustness [140, 141] when the system parameters change. In principle, the reduced-order mode under the new parameters should be reconstructed. However, constructing the POD reduced mode of the corresponding parameter by constructing the response of each parameter in the complex system is not allowed from the point of calculation cost. In order to reduce the order of the complex system in parameter range and ensure the parameter robustness of POD reduced-order mode, scholars have proposed many improved POD methods: global POD method [142–145], local POD method [60, 117, 146–149], adaptive POD method-POD modal interpolation method [141, 152–156], subspace angle interpolation method [157–162], Grassmann manifold tangent space interpolation method [163–171], and other adaptive POD methods.

The global POD method aims to construct a global POD reduced-order mode that covers the entire parameter domain by using a snapshot set composed of different parameter values in a certain parameter domain and then uses the reduced-order mode to obtain the reduced-order modal of system parameter domain. This method is very simple and easy to implement. However, this method extracts snapshot sets with different parameters and needs proper positioning in the parameter domain while how to reasonably determine the parameters of the snapshot signal is irregular. There may be multiple solutions in the parameter domain of complex strong nonlinear systems. This method requires a lot of POD reduced-order modes to obtain a more accurate reduced-order model of the original system. However, in practice, it has been proved that in many cases, this method is not reliable. Because there are numerous parameters affecting the dynamics of high-dimensional complex systems, the globally optimal POD reduction modes may not exist, which causes the method to lose the best approximation [161, 163–166].

The local POD method is a local reduction method. The whole parameter domain is divided into multiple subparameter domains. The POD method is used to reduce the system of each subparameter domain. The POD reduced-order mode is constructed by using the snapshot signals of some local parameter domains obtained in advance, and then the original system is projected onto the subspaces of these local reduced-order modes to obtain the price reduction model. Rapún and Vega [60] combined the local POD method with the Galerkin method to study the two one-dimensional parabolic equations (nonautonomous Fisher-like equations and complex Ginzburg–Landau equations). They proved the effectiveness of the method and its robustness in the numerical way in the range of local parameters.

Terragni and Valero [117] also combined the local POD method and the Galerkin method to study the two-dimensional roof-driven cavity flow issue. Compared with commercial software solution, this method can significantly reduce the calculation cost and be applied to reduce the

order of different parameters within the range of system adjustable parameters, which is convenient for checking complex systems. Sahyoun and Djouadi [150] used the local POD method based on clustering vector space to reduce the order of high-dimensional nonlinear systems. Compared with the global POD method, the local POD method further reduces the system dimension and ensures the calculation accuracy. However, the method is divided into multiple subparameter domains, so the approximate solution is not smooth, and the robustness of the method in the parameter domain and the scope of its application are not yet rigorously proved [117, 148].

The adaptive POD method [150, 151] essentially achieves the best approximation for each parameter of the original system by updating the POD reduced-order mode within the parameter range. This method has better parameter robustness than the above two methods. In the literature about the POD method, there are many methods called adaptive POD methods, such as POD modal interpolation method [141, 152–156], subspace angular interpolation method [157–162], Grassmann manifold spatial interpolation method [163–171], and other adaptive POD methods [59, 118–120, 172].

The POD modal interpolation method is to use some interpolation methods (such as empirical discrete interpolation and Lagrange interpolation) to construct reduced-order modes of other parameters [141, 152–156] in the parameter domain by obtaining the reduced order of other parameters in the parameter domain. Xu and Lin [153] combined the POD method and empirical discrete interpolation method through greedy sampling to obtain interpolation points and reduced order of nonlinear parameter systems. Opmeer [154] combined the balanced-POD method and rational interpolation method to reduce the order of control systems.

Yao and Marques [155] used the POD method and the empirical discrete interpolation method to obtain the optimal POD reduction mode under the new parameters by training the radial basis function artificial neural network in the parameter space. They used the radial basis function artificial neural network of each interpolation point to reconstruct the flow field under the new parameters. The POD modal interpolation method is simple. However, the reduced-order mode is the orthogonal norm base vector, and the reduced-order modes, which are obtained by some direct interpolation methods under the new parameters, are no longer orthogonal normative. Therefore, in many cases, the accurate reduction model cannot be obtained by using the reduced-order mode obtained by direct interpolation. For example, when Lieu and Lesoinne [156] applied this method to analyze the aerodynamic problems of the F16 machine, accurate results were obtained at subsonic flight, but the method did not obtain correct results at transonic and supersonic speeds.

Generally, in the linear interpolation process of any two base vectors, their angles are not guaranteed to be linear interpolation. The subspace angle interpolation method is proposed based on the concepts of the main vector and the protagonist of the two subspaces [157]. The method can guarantee that the angles of the two interpolation basis vectors are also linear interpolation. By obtaining the POD reduced-order modal vector of some two parameters in the parameter domain in advance and then using the subspace angle interpolation method to obtain the POD reduced-order mode of other parameter values, the method has been successfully applied to the F16 machine in different freedoms by Lieu [158–161] for pneumatic analysis under the Mach number and angle of attack parameters. However, the subspace angle interpolation method is a low-order interpolation method, an accurate reduced-order model that cannot be obtained when two parameter values are far apart in the parameter space. The computational efficiency will be too low and lose the significance for order reduction when the distance is too close [160, 161, 165, 166].

In recent years, Amsallem proposed a more robust adaptive POD method, Grassmann manifold tangent spatial interpolation method [163–171]. The method is based on some concepts and mathematical conclusions in differential geometry, such as the Grassmann manifold, the calculation of the tangent space on the manifold, and the geodesic path. Amsallem [160, 161] used this method to study the aerodynamic problems of F16 and F18. Compared with POD modal interpolation and subspace angle interpolation, this method is not only suitable for subsonic and transonic aerodynamic analysis but also for supersonic aerodynamic analysis, which has good robustness. At the same time, Amsallem and Farhat [165, 166] also proved that the two-point interpolation of this method is equivalent to the subspace angle interpolation method. Amsallem and Cortial [167] also used this method to reduce the order of 24-DOF spring-mass-damping system and continuous wing structure system. Comparing the reduced-order model with the response of the original system, they proved its effectiveness and also showed that the method is universal and suitable for the reduction of other complex structural systems. Paquay [171] used this method to reduce the model of the nonlinear magnetic dynamic system and compared it with the direct POD model reduction and POD modal interpolation method, showing the superiority of the method.

The above are several major adaptive POD methods, and of course there are some other adaptive POD methods, such as Terragni and Valero [118–120] proposed an adaptive POD method in 2014 to analyze the distribution characteristics of complex systems in certain parameters. Because it is very difficult to analyze the bifurcation characteristics of complex systems in the parameter domain by direct numerical calculation, some scholars have considered the bifurcation characteristics of the low-dimensional reduced-order model to reflect the bifurcation characteristics of complex high-dimensional systems. Amabili et al. [59] used the POD method to analyze the bifurcation characteristics of complex structural dynamic systems in the parameter domain in 2006. However, this method has robustness problems in the parameter domain. They found that if the POD reduced-order mode is extracted from the chaotic motion signal, the method can be applied within a certain parameter range. However, for a larger parameter range, even if the method is sampled from chaotic signals, it is difficult to obtain an

accurate reduced-order model, so they warned scholars not to use this method blindly.

In literature [172], Amabili et al. also compared the POD method with another reduced-order method of nonlinear structural dynamic systems, i.e., the nonlinear modal methods (NNMs). The results show that the POD method can obtain a more accurate reduced-order model than the nonlinear mode method (NNMs). However, Amabili and others used traditional POD methods, not adaptive POD methods. Terragni and Valero [118–120] determined the transient motion response of complex systems in advance with different parameter values through the Galerkin method, as a snapshot signal for updating the POD reduced-order mode in the parameter domain; they used the truncation error function to detect when the reduced-order modes should be updated and how many reduced-order modes need to be selected. The strategy for updating the POD reduced-order mode is to mix the modal vectors of the old and new parameters with appropriate weights. Then, they combined the POD method and the Galerkin method to obtain a bifurcation diagram of the complex Ginzburg–Landau equation with periodic parameters, almost periodic periods and chaotic motions on larger parameter range. Compared with the original system bifurcation diagram obtained by direct numerical calculation, it is proved that the proposed method has better robustness in a larger parameter range and can swiftly analyze the bifurcation characteristics of complex systems in the parameter range.

6.4. Other Improved POD Methods and Related Issues. The above is the classification of various improved POD methods. Of course, there are some other improved POD methods, such as the POD-Galerkin method [58–62, 117–120, 173], which regards the POD reduced-order modal basis function as the orthogonal modal function of the Galerkin method. The POD method based on frequency domain obtains the POD reduced-order modal basis function in the frequency domain, balanced-POD method (BPOD) [3, 154, 176–178]. These improved POD methods are all proposed by combining traditional POD methods with other methods. In this paper, various improved POD methods are mainly divided into two categories related to sampling and parameters. On the one hand, the POD method is essentially a statistical analysis method, which involves how to sample, which method should be used to sample it, when to sample the signal, which part of the signal should be extracted, and how long the signal should be extracted. These are directly related to sampling. On the other hand, from the basic theory of the POD method, the original system is projected onto the subspace of the first few reduced modes by the POD reduced mode of the snapshot signal constructed by a certain parameter value of the original system. The resulting reduced-order model is only the best approximation of the original system for this particular parameter. Since the infinitesimal neighborhood of the parameter point can be linearized, the method can also obtain a better approximation for the system near the specific parameter value [79, 179]. We hope that the POD reduced-order mode obtained from a certain parameter can also be applied to the model reduction of other parameters in the system so that the reduced-order model under other parameters also has the optimal approximation characteristics. However, such a conclusion is not given in the basic theory of the POD method, so the POD method lacks robustness in the parameter domain.

Some POD methods for solving parameter robustness have been proposed, but each has its own advantages and disadvantages. At present, the adaptive POD method is more mature in dealing with parameter robustness, but it still needs to be continuously developed. For example, the adaptive POD method, Grassmann manifold tangent space interpolation method, proposed in recent years has achieved good results in dealing with parameter robustness problems. However, we know that manifold tangent spaces have local properties, and the method still has limitations in large parameter domain.

The POD method projects a high-dimensional system onto the space spanned by a few reduced-order modes, which is essentially a projection reduction method. The adaptive POD method can solve the problem of parameter robustness of the reduced-order system to certain extent. However, the reduced-order model on the parameter domain is obtained by continuously updating the POD reduced-order mode or adjusting the number of modes, resulting in the reduced-order model being some discrete numerical equations, and there is no invariant reduced-order mathematical model in the parameter domain. Even the reduced-order model dimensions of different subparameter domains are inconsistent. Therefore, a low-dimensional model that can approximately reflect the dynamic characteristics of complex high-dimensional systems cannot be obtained through the adaptive POD method in the parameter domain so that it is difficult to carry out in-depth theoretical analysis of high-dimensional systems. How to use the POD method to obtain the invariant reduced-order model of the high-dimensional system in the parameter domain? The POD method is a projection order reduction method, so it is impossible to update the POD reduced-order mode in the parameter domain, and only the reduced-order mode of the parameter domain can be obtained by constructing a reduced-order mode which is optimal in the entire parameter domain. What conditions can the POD reduced-order modes reduce the parameter domain or is there an optimal POD reduced-order mode for the entire parameter domain? How many DOF can the invariant reduced-order model reflect the dynamics of the original system over the entire parameter domain? In what manner does the method interact with uncertainty [180–184] for the high-dimensional mechanical systems?

Computers nowadays can handle real-time calculations using the finite element method. The finite element model and POD order reduction techniques will be applied to study real-time computer modeling [185], e.g., surgical simulations [186, 187] (for doctor training, sometimes in VR) and hybrid simulation [188, 189] (HIL of mechanical systems where mode superposition or other methods are applied to

reduce the model order). In real-time simulations, high computational effort to reduce the model is worth it even if the real-time computations can be slightly minimized.

Machine learning can also be used for model order reduction [190, 191]; manifold learning and manifold processes for model order reduction should be discussed in detail in our future work. Chaos features can improve the efficiency of reduction models [192–194] and the combination method of uncertainty quantification [195, 196], and model order reduction will be efficient to study the complex dynamic systems. Another point is the systems with substructures. The way it works and method for choosing the approximation order are elaborated by researchers [197, 198]. As a commonly used method in model updating, the quadratic inverse eigenvalue problem (QIEP) aims to construct the mass, stiffness, and damping matrices and can be employed to assist model order reduction for large-scale engineering systems [199, 200].

The above questions are all about the POD order reduction methods that deserve further study in the future.

7. Conclusions and Outlooks

The model order reduction for the high-dimensional complex nonlinear system is one of the important issues in the field of engineering research, and it is one of the advanced issues in the area of nonlinear science research. Many scholars from various countries have obtained some mature order reduction methods for a long research process. However, modern engineering structural systems are more and more complex, operating conditions are complex and variable, and various nonlinear factors are coupled to each other. As a result, many model reduction methods are no longer applicable. This is a challenge to the study of dynamic characteristics of high-dimensional complex systems and system parameter optimization design. According to the characteristics of each order reduction method, the worthy problems of further study on the order reduction of high-dimensional complex system models in the future are as follows:

(1) Multiple order reduction methods are combined for second-level order reduction on high-dimensional complex systems. For example, the complex system is divided into several substructures, and the modal synthesis method is used to reduce the order, and then the center manifold method or the L-S method is used for further analysis. For another example, the complex system is reduced by the Galerkin method or the POD method, and then the center manifold or the L-S method is used for the order reduction study. The center manifold and the L-S method can reserve the topology properties of the original system. Therefore, the reduced-order model of the complex structural system can be obtained by the Galerkin method, the modal synthesis method, or the POD method, and then the theoretical research is carried out by using the center manifold and the L-S method.

(2) The adaptive model order reduction method with system parameter variation and various nonlinear model reduction methods should be further studied. For example, the adaptive order reduction method based on Grassmann manifold tangent space interpolation has local properties in manifold tangent space, and it is worthy of further study to solve robustness problem in large parameter domain. Some new nonlinear model order reduction methods have been proposed based on neural networks, local reduced-order bases, and manifold learning, but each has its own advantages and disadvantages, which still need further study.

(3) A low-dimensional model in the parameter domain can approximately reflect the dynamic characteristics of complex high-dimensional systems which cannot be obtained by the adaptive POD method, and it is difficult to carry out in-depth theoretical analysis of high-dimensional systems. How to use the POD method to obtain the invariant order reduction model of the high-dimensional system in the parameter domain? The POD method is a projection reduction method, and the POD reduced-order modes cannot be updated in the parameter domain. Therefore, order reduction of the parameter domain can be obtained only by constructing a reduced-order mode which is optimal in the entire parameter domain. Under what conditions can the POD reduced-order modes reduce the dimension of parameter domain or is there an optimal POD reduction mode for the entire parameter domain? How many DOF can the invariant order reduction model reflect the dynamics of the original system over the entire parameter domain? The POD order reduction method can be applied for further study for these problems.

(4) Special attention should be taken to the model reduction of interconnected systems in order to preserve the integrity and interconnection structure among different subsystems. For example, the dual-rotor system contains high pressure and low pressure rotors, the system is complex and high dimensional, and the nonlinearity is strong between the joints of high and low pressure rotors. It will be a challenge to apply the POD method in this kind of system.

Conflicts of Interest

The authors declare that they have no conflicts of interest.

Acknowledgments

This study was funded by the National Natural Science Foundation of China (grant nos. 12072263, 11802235, and 11972295), the Natural Science Foundation of Shaanxi Province (grant no. 2020JQ-129), and the Aviation Engine Innovation Center of National Defense Science, Technology and Industry (grant no. CXZX-2019-001).

References

[1] P. Benner, S. Gugercin, and K. Willcox, "A survey of projection-based model reduction methods for parametric dynamical systems," *Siam Review*, vol. 57, no. 4, pp. 483–531, 2015.

[2] D. Amsallem, M. Zahr, Y. Choi, and C. Farhat, "Design optimization using hyper-reduced-order models," *Structural and Multidisciplinary Optimization*, vol. 51, no. 4, pp. 919–940, 2015.

[3] G. Chen, J. Sun, and Y. M. Li, "A Active flutter suppression control law design method based on balanced proper orthogonal decomposition reduced order model," *Nonlinear Dynamics*, vol. 70, pp. 1–12, 2012.

[4] G. Chen, Y. M. Li, and H. Patrick, "Design of active control law for aeroelastic system based on proper orthogonal decomposition reduced order model," in *Proceedings of the 51st AIAA/ASME/ASCE/AHS/ASC Structures, Structural Dynamics, and Materials Conference*, pp. 1–9, Orlando, FL, USA, 2010.

[5] G. Chen, J. Sun, and Y.-m. Li, "Adaptive reduced-order-model-based control-law design for active flutter suppression," *Journal of Aircraft*, vol. 49, no. 4, pp. 973–980, 2012.

[6] G. Chen, Y.-M. Li, and G.-R. Yan, "Limit cycle oscillation prediction and control design method for aeroelastic system based on new nonlinear reduced order model," *International Journal of Computational Methods*, vol. 8, no. 1, pp. 77–90, 2011.

[7] H. N. Soloklo and M. M. Farsangi, "Chebyshev rational functions approximation for model order reduction using harmony search," *Scientia Iranica D*, vol. 20, no. 3, pp. 771–777, 2013.

[8] G. Scarciotti and A. Astolfi, "Data-driven model reduction by moment matching for linear and nonlinear systems," *Automatica*, vol. 79, pp. 340–351, 2017.

[9] K. Zong, F. Yang, and X. Zeng, "A wavelet-collocation-based trajectory piecewise-linear algorithm for time-domain model-order reduction of nonlinear circuits," *IEEE Transactions on Circuits and Systems I: Regular Papers*, vol. 57, no. 11, pp. 2981–2990, 2010.

[10] H. M. R. Ugalde, J. C. Carmona, V. M. Alvarado, and J. Reyes-Reyes, "Neural network design and model reduction approach for black box nonlinear system identification with reduced number of parameters," *Neurocomputing*, vol. 101, pp. 170–180, 2013.

[11] N. R. Pal, V. K. Eluri, and G. K. Mandal, "Fuzzy logic approaches to structure preserving dimensionality reduction," *IEEE Transactions on Fuzzy Systems*, vol. 10, no. 3, pp. 277–286, 2002.

[12] J. L. Fernandez, T. Mukerji, E. Garcia-Gonzalo, and Z. Fernandez-Muniz, "Uncertainty assessment for inverse problems in high dimensional spaces using particle swarm optimization and model reduction techniques," *Mathematical and Computer Modelling*, vol. 54, pp. 2889–2899, 2011.

[13] Y. S. Chen and Y. T. Leung, *Bifurcation and Chaos in Engineering*, vol. 93-102, pp. 154–158, Springer-Verlag, London, UK, 1998.

[14] Y. Chen, *Bifurcation and Chaos Theory of Nonlinear Vibration Systems*, vol. 135-144, pp. 229–239, Higher Education Press, Beijing, China, 1993.

[15] A. Kelley, "The stable, center-stable, center, center-unstable, unstable manifolds," *Journal of Differential Equations*, vol. 3, no. 4, pp. 546–570, 1967.

[16] V. A. Pliss, "Principal reduction in the theory of the stability of motion," *Izv. Akad. Nauk SSSR, Mat Ser.*vol. 28, pp. 1297–1324, 1964.

[17] J. C. Ser, "Applied mathematical sciences series," in *Applications of Centre Manifold Theory*p. 35, Springer-Verlag, New York, NY, USA, 1985.

[18] W. H. Huang, X. H. Wu, Y. H. Jiao et al., "Review of nonlinear rotor dynamics," *Journal of Vibration Engineering*, vol. 13, no. 4, pp. 497–509, 2000.

[19] J. Guckenheimer and P. Holmes, *Nonlinear Oscillations, Dynamical Systems, and Bifurcations of Vector Fields*, p. 42, Springer Science & Business Media, New York, NY, USA, 2013.

[20] S. Chandraker, H. Roy, and Asme, *A Balanced IIRS Model for Investigating the Dynamics of Damped Rotor Bearing Syste*, Amer Soc Mechanical Engineers, New York, NY, USA, 2014.

[21] T. Takagi, G. Chen, and I. Takami, *Model Reduction via Subsystem Decomposition for Flexible Rotor-Magnetic Bearing with Gyroscopic Effect*, pp. 104–109, IEEE, New York, NY, USA, 2018.

[22] A. S. Das and J. K. Dutt, "Reduced model of a rotor-shaft system using modified SEREP," *Mechanics Research Communications*, vol. 35, no. 6, pp. 398–407, 2008.

[23] H. Yu and Y. S. Chen, "Recent developments in order reduction methods for high-dimension dynamical systems," *Advances in Mechanics*, vol. 39, no. 2, pp. 154–164, 2009.

[24] Z. Zhang, X. Yang, and G. Lin, "POD-based constrained sensor placement and field reconstruction from noisy wind measurements: a perturbation study," *Mathematics*, vol. 4, no. 2, p. 26, 2016.

[25] G. Y. Cao, C. Wang, and C. Chen, "Center manifold method to simplify the analysis of fold bifurcation associated with voltage collapse," *Proceedings of the CSEE*, vol. 22, no. 7, pp. 40–43, 2002.

[26] A. Yousef and F. B. Yousef, "Bifurcation and stability analysis of a system of fractional-order differential equations for a plant-herbivore model with allee effect," *Mathematics*, vol. 7, no. 5, p. 454, 2019.

[27] J. Zhang, L. Zhang, and Y. Bai, "Stability and bifurcation analysis on a predator-prey system with the weak allee effect," *Mathematics*, vol. 7, no. 5, p. 432, 2019.

[28] A. Boyaci, H. Hetzler, W. Seemann, C. Proppe, and J. Wauer, "Analytical bifurcation analysis of a rotor supported by floating ring bearings," *Nonlinear Dynamics*, vol. 57, no. 4, pp. 497–507, 2009.

[29] B. Petra, "A stochastic version of center manifold theory," *Probability Theory and Related Fields*, vol. 83, pp. 509–545, 1989.

[30] L. Liu, Y. S. Wong, and B. H. K. Lee, "Application of the centre manifold theory in non-linear aeroelasticity," *Journal of Sound and Vibration*, vol. 234, no. 4, pp. 641–659, 2000.

[31] A. D. Rendall, "Cosmological models and centre manifold theory," *General Relativity and Gravitation*, vol. 34, no. 8, pp. 1277–1294, 2002.

[32] J.-J. Sinou, F. Thouverez, and L. Jezequel, "Analysis of friction and instability by the centre manifold theory for a non-linear sprag-slip model," *Journal of Sound and Vibration*, vol. 265, no. 3, pp. 527–559, 2003.

[33] H. J. Hupkes and S. M. V. Lunel, "Center manifold theory for functional differential equations of mixed type," *Journal of Dynamics and Differential Equations*, vol. 19, no. 2, pp. 497–560, 2007.

[34] H. Kano, M. Ito, and T. Inoue, "Order reduction and bifurcation analysis of a flexible rotor system supported by a

full circular journal bearing," *Nonlinear Dynamics*, vol. 95, no. 4, pp. 3275–3294, 2019.

[35] X. Liu, Y. Liu, S. Wang, H. Yan, and P. Liao, "Bifurcation analysis of a magnetically supported rigid rotor in auxiliary bearings," *Chaos, Solitons & Fractals*, vol. 118, pp. 328–336, 2019.

[36] F. Liu, C. Xiang, H. Liu et al., "Asymmetric effect of static radial eccentricity on the vibration characteristics of the rotor system of permanent magnet synchronous motors in electric vehicles," *Nonlinear Dynamics*, vol. 96, no. 4, pp. 2581–2600, 2019.

[37] C. Chicone, "Lyapunov-Schmidt reduction and Melnikov integrals for bifurcation of periodic solutions in coupled oscillators," *Journal of Differential Equations*, vol. 112, no. 2, pp. 407–447, 1994.

[38] P. Ashwin, K. B{öhmer, and Z. Mei, "A numerical Liapunov-Schmidt method with applications to Hopf bifurcation on a square," *Mathematics of Computation*, vol. 64, no. 210, pp. 649–670, 1995.

[39] W. Zhang and I. Stewart, "Bounded solutions for non-autonomous parabolic equations," *Dynamics and Stability of Systems*, vol. 11, no. 2, pp. 109–120, 1996.

[40] M. Lukas, D. Pelinovsky, and P. G. Kevrekidis, "Lyapunov-Schmidt reduction algorithm for three-dimensional discrete vortices," *Physica D: Nonlinear Phenomena*, vol. 237, no. 3, pp. 339–350, 2008.

[41] R. A. Sandfry and C. D. Hall, "Bifurcations of relative equilibria of an oblate gyrostat with a discrete damper," *Nonlinear Dynamics*, vol. 48, no. 3, pp. 319–329, 2007.

[42] A. Buica, J. Llibre, and O. Makarenkov, "Bifurcations from nondegenerate families of periodic solutions in Lipschitz systems," *Journal of Differential Equations*, vol. 252, pp. 3899–3919, 2012.

[43] G. Chen and Y. Zheng, "Concentration phenomenon for fractional nonlinear Schrödinger equations," *Communications on Pure and Applied Analysis*, vol. 13, no. 6, pp. 2359–2376, 2014.

[44] A. Pogan, J. Yao, and K. Zumbrun, "Hopf bifurcation of viscous shock waves in a channel," *Physica D Nonlinear Phenomena*, vol. 308, pp. 59–79, 2014.

[45] J. Cao, R. Yuan, H. Jiang, and J. Song, "Hopf bifurcation and multiple periodic solutions in a damped harmonic oscillator with delayed feedback," *Journal of Computational and Applied Mathematics*, vol. 263, pp. 14–24, 2014.

[46] C. Li and L. Ma, "Lyapunov-schmidt reduction for fractional differential systems," *ASME Journal of Computational and Nonlinear Dynamics*, vol. 11, no. 5, Article ID 051022, 2016.

[47] S. Guo and L. Ma, "Stability and bifurcation in a delayed reaction-diffusion equation with dirichlet boundary condition," *Journal of Nonlinear Science*, vol. 26, no. 2, pp. 545–580, 2016.

[48] C. Foias, G. R. Sell, and R. Temam, "Inertial manifolds for nonlinear evolutionary equations," *Journal of Differential Equations*, vol. 73, no. 3, pp. 309–353, 1988.

[49] M. Marion and R. Temam, "Nonlinear Galerkin methods," *SIAM Journal on Numerical Analysis*, vol. 26, no. 5, pp. 1139–1157, 1989.

[50] B. García-Archilla, J. Novo, and E. S. Titi, "Postprocessing the Galerkin method: a novel approach to approximate inertial manifolds," *SIAM Journal on Numerical Analysis*, vol. 35, no. 3, pp. 941–972, 1998.

[51] B. Garcia-Archilla, J. Novo, and E. S. Titi, "An approximate inertial manifolds approach to postprocessing the Galerkin method for the Navier-Stokes equations," *Mathematics of Computation*, vol. 68, no. 68, pp. 893–911, 1999.

[52] Q. Ding and K. Zhang, "Order reduction and nonlinear behaviors of a continuous rotor system," *Nonlinear Dynamics*, vol. 67, no. 1, pp. 251–262, 2012.

[53] S. L. Ho, Y. P. Zhao, and W. N. Fu, "Adaptive discontinuous Galerkin method for transient analysis of eddy current fields in high-speed rotating solid rotors," *IEEE Transactions on Magnetics*, vol. 50, no. 2, p. 4, 2014.

[54] J. Sembera and M. Benes, "Nonlinear Galerkin method for reaction-diffusion systems admitting invariant regions," *Journal of Computational and Applied Mathematics*, vol. 136, pp. 163–176, 2001.

[55] I. Chatzisavvas, A. Boyaci, P. Koutsovasilis, and B. Schweizer, "Influence of hydrodynamic thrust bearings on the nonlinear oscillations of high-speed rotors," *Journal of Sound And Vibration*, vol. 380, pp. 224–241, 2016.

[56] H. G. Matthies and M. Meyer, "Nonlinear Galerkin methods for the model reduction of nonlinear dynamical systems," *Computers & Structures*, vol. 81, no. 12, pp. 1277–1286, 2003.

[57] O. J. Boelens, H. Van Der Ven, B. Oskam, and A. A. Hassan, "Boundary conforming discontinuous Galerkin finite element approach for rotorcraft simulations," *Journal of Aircraft*, vol. 39, no. 5, pp. 776–785, 2002.

[58] M. Amabili, A. Sarkar, and M. P. Païdoussis, "Reduced-order models for nonlinear vibrations of cylindrical shells via the proper orthogonal decomposition method," *Journal of Fluids and Structures*, vol. 18, no. 2, pp. 227–250, 2003.

[59] M. Amabili, A. Sarkar, and M. P. Païdoussis, "Chaotic vibrations of circular cylindrical shells: Galerkin versus reduced-order models via the proper orthogonal decomposition method," *Journal of Sound and Vibration*, vol. 290, no. 3-5, pp. 736–762, 2006.

[60] M.-L. Rapún and J. M. Vega, "Reduced order models based on local POD plus Galerkin projection," *Journal of Computational Physics*, vol. 229, no. 8, pp. 3046–3063, 2010.

[61] D. Xie, M. Xu, and E. H. Dowell, "Proper orthogonal decomposition reduced-order model for nonlinear aeroelastic oscillations," *AIAA Journal*, vol. 52, no. 2, pp. 229–241, 2014.

[62] D. Xie and M. Xu, "A comparison of numerical and semi-analytical proper orthogonal decomposition methods for a fluttering plate," *Nonlinear Dynamics*, vol. 79, no. 3, pp. 1971–1989, 2015.

[63] G. Rega and H. Troger, "Order reduction of dynamical systems: methods, models, applications," *Nonlinear Dynamics*, vol. 41, no. 1-3, pp. 1–15, 2005.

[64] D. A. Glasgow and H. D. Nelson, "Stability analysis of rotor-bearing systems using component mode synthesis," *Journal of Mechanical Design*, vol. 102, no. 2, pp. 352–359, 1980.

[65] C.-P. Zou, H.-X. Hua, and D.-S. Chen, "Modal synthesis method of lateral vibration analysis for rotor-bearing system," *Computers & Structures*, vol. 80, no. 32, pp. 2537–2549, 2002.

[66] H. D. Nelson, W. L. Meacham, D. P. Fleming et al., "Nonlinear analysis of rotor-bearing systems using component mode synthesis," *Journal of Mechanical Design*, vol. 102, no. 2, pp. 352–359, 1982.

[67] W. Wang and J. Kirkhope, "Component mode synthesis for multi-shaft rotors with flexible inter-shaft bearings," *Journal of Sound and Vibration*, vol. 173, no. 4, pp. 537–555, 1994.

[68] P. Sundararajan and S. T. Noah, "An algorithm for response and stability of large order non-linear systems - application to rotor systems," *Journal of Sound and Vibration*, vol. 214, no. 4, pp. 695–723, 1998.

[69] T. Iwatsubo, K. Shimbo, and S. Kawamura, "Nonlinear vibration analysis of a rotor system using component mode synthesis method," *Archive of Applied Mechanics*, vol. 72, no. 11-12, pp. 843–855, 2003.

[70] A. Karkkainen, J. Sopanen, and A. Mikkola, "Dynamic simulation of a flexible rotor during drop on retainer bearings," *Journal of Sound and Vibration*, vol. 306, no. 3-5, pp. 601–617, 2007.

[71] D.-M. Tran, "Component mode synthesis methods using interface modes. Application to structures with cyclic symmetry," *Computers & Structures*, vol. 79, no. 2, pp. 209–222, 2001.

[72] A. Shanmugam and C. Padmanabhan, "A fixed-free interface component mode synthesis method for rotordynamic analysis," *Journal of Sound and Vibration*, vol. 297, no. 3-5, pp. 664–679, 2006.

[73] J. A. Beck, J. M. Brown, C. J. Cross, and J. C. Slater, "Component-mode reduced-order models for geometric mistuning of integrally bladed rotors," *AIAA Journal*, vol. 52, no. 7, pp. 1345–1356, 2014.

[74] Z. Zheng, F. Zhu, D. Zhang, and Y. Xie, "A developed component mode synthesis for parametric response analysis of large-scale asymmetric rotor," *Journal Of Mechanical Science And Technology*, vol. 33, no. 3, pp. 995–1005, 2019.

[75] H. Zhang, *Study on mixed constraint modal synthesis method for local nonlinear of soil-structure interaction*, [PhD Thesis], Tianjin University, Tianjin, China, 2015.

[76] C. F. Li, J. S. Dai, X. P. Li et al., *Dynamic Characteristic and Experiment Research of a Rotor-Bearing System Supported by Oil-Film, Applied Mechanics and Mechanical Engineering, Pts 1-3*, pp. 1732–1737, Trans Tech Publications Ltd, Stafa-Zurich, Switzerland, 2010.

[77] S. M. Kim, J.-G. Kim, S.-W. Chae, and K. C. Park, "Evaluating mode selection methods for component mode synthesis," *AIAA Journal*, vol. 54, no. 9, pp. 2852–2863, 2016.

[78] C. Joannin, B. Chouvion, F. Thouverez et al., "A nonlinear component mode synthesis method for the computation of steady-state vibrations in non-conservative systems," *Mechanical Systems and Signal Processing*, vol. 83, pp. 75–92, 2016.

[79] G. Kerschen, J.-c. Golinval, A. F. Vakakis, and L. A. Bergman, "The method of proper orthogonal decomposition for dynamical characterization and order reduction of mechanical systems: an overview," *Nonlinear Dynamics*, vol. 41, no. 1-3, pp. 147–169, 2005.

[80] T. R. Smith, "Low-Dimensional models of plane coquette flow using the proper orthogonal decomposition," Princeton University, Princeton, NJ, USA, 2003pp. 15–18, [PhD Thesis].

[81] D. D. Kosambi, "Statistics in function space," *Journal of the Indian Mathematical Society*, vol. 7, no. 1, pp. 166–178, 1943.

[82] K. Karhunen, "Zur spektraltheorie stochastischer prozesse. (German)," *Annales Academiæ Scientiarum Fennicæ*.vol. 34, 1946.

[83] E. N. Lorenz, "Empirical orthogonal functions and statistical weather prediction," *Science Reports*, vol. 409, no. 2, pp. 997–999, 1956.

[84] V. S. Pougachev, "General theory of the correlations of random functions," *Izv. Akad. Nauk. SSSR. Math. Ser.*vol. 17, pp. 401–420, 1953.

[85] H. Hotelling, "Analysis of a complex of statistical variables into principal components," *Journal of Educational Psychology*, vol. 24, no. 6, pp. 417–441, 1933.

[86] P. Holmes, J. L. Lumley, and G. Berkooz, *Turbulence, Coherent Structures, Dynamical Systems and Symmetry*, Cambridge University Press, Cambridge, UK, 2012.

[87] N. Kumar, "Model reduction of large structural dynamic models using proper orthogonal decomposition," New Mexico State University, Las Cruces, NM, USA, 2008pp. 1–24, [PhD Thesis].

[88] G. Kerschen, B. F. Feeny, and J. C. Golinval, "On the exploitation of chaos to build reduced-order models," *Computer Methods in Applied Mechanics and Engineering*, vol. 192, no. 13-14, pp. 1785–1795, 2003.

[89] L. G. Bleris and M. V. Kothare, "Low-order empirical modeling of distributed parameter systems using temporal and spatial eigenfunctions," *Computers & Chemical Engineering*, vol. 29, no. 4, pp. 817–827, 2005.

[90] J. H. Citriniti and W. K. George, "Reconstruction of the global velocity field in the axisymmetric mixing layer utilizing the proper orthogonal decomposition," *Journal of Fluid Mechanics*, vol. 418, no. 418, pp. 137–166, 2000.

[91] K. Kunisch and S. Volkwein, "Galerkin proper orthogonal decomposition methods for a general equation in fluid dynamics," *SIAM Journal on Numerical Analysis*, vol. 40, no. 2, pp. 492–515, 2002.

[92] C. W. Rowley, T. Colonius, and R. M. Murray, "Model reduction for compressible flows using POD and Galerkin projection," *Physica D Nonlinear Phenomena*, vol. 189, no. 1-2, pp. 115–129, 2003.

[93] B. R. Noack and H. Eckelmann, "A low-dimensional Galerkin method for the three-dimensional flow around a circular cylinder," *Physics of Fluids*, vol. 6, no. 1, pp. 124–143, 1994.

[94] J. L. Lumley, "Early work on fluid mechanics in the IC engine," *Annual Review of Fluid Mechanics*, vol. 33, no. 33, pp. 319–338, 2001.

[95] K. E. Meyer, J. M. Pedersen, and O. Özcan, "A turbulent jet in crossflow analysed with proper orthogonal decomposition," *Journal of Fluid Mechanics*, vol. 583, no. 583, pp. 199–227, 2007.

[96] R. J. Vaccaro, "SVD and signal processing, II. Algorithms, analysis and applications," *Journal of Geophysical Research Atmospheres*, vol. 45, no. 1, p. 106, 1991.

[97] A. Rosenfeld and A. C. Kak, *Digital Picture Processing*, Academic Press, New York, NY, USA, 1982.

[98] D. Malioutov, M. Cetin, and A. S. Willsky, "A sparse signal reconstruction perspective for source localization with sensor arrays," *IEEE Transactions on Signal Processing*, vol. 53, no. 8, pp. 3010–3022, 2005.

[99] M. Aharon, M. Elad, and A. Bruckstein, "$rm K$-SVD: an algorithm for designing overcomplete dictionaries for sparse representation," *IEEE Transactions on Signal Processing*, vol. 54, no. 11, pp. 4311–4322, 2006.

[100] I. B. Oliveira and A. T. Patera, "Reduced-basis techniques for rapid reliable optimization of systems described by affinely parametrized coercive elliptic partial differential equations," *Optimization and Engineering*, vol. 8, no. 1, pp. 43–65, 2007.

[101] R. F. Coelho, P. Breitkopf, and C. Knopf-Lenoir, "Model reduction for multidisciplinary optimization-application to a 2D wing," *Structural and Multidisciplinary Optimization*, vol. 37, no. 1, pp. 29–48, 2008.

[102] A. Agarwal, L. T. Biegler, and S. E. Zitney, "Simulation and optimization of pressure swing adsorption systems using reduced-order modeling," *Industrial & Engineering Chemistry Research*, vol. 48, no. 5, pp. 2327–2343, 2009.

[103] A. Hay, J. Borggaard, I. Akhtar, and D. Pelletier, "Reduced-order models for parameter dependent geometries based on shape sensitivity analysis," *Journal of Computational Physics*, vol. 229, no. 4, pp. 1327–1352, 2010.

[104] R. W. Preisendorfer, *Principal Component Analysis in Meteorology and Oceanography*, Elsevier, Amsterdam, Netherlands, 1988.

[105] J. P. Cusumano, M. T. Sharkady, and B. W. Kimble, "Experimental measurements of dimensionality and spatial coherence in the dynamics of a flexible-beam impact oscillator," *Philosophical Transactions of the Royal Society B Biological Sciences*, vol. 347, no. 1683, pp. 421–438, 1994.

[106] E. Kreuzer and O. Kust, "Proper orthogonal decomposition-An efficient means of controlling self-excited vibrations of long torsional strings," *ASME Nonlinear Dynamics and Control*, vol. 91, pp. 105–110, 1996.

[107] A. Benguedouar, *Proper Orthogonal Decomposition in Dynamical Modeling: A Qualitative Dynamic Approach*, Boston University, Boston, MA, USA, 1995.

[108] I. T. Georgiou and I. B. Schwartz, "Dynamics of large scale coupled structural/mechanical systems: a singular perturbation/proper orthogonal decomposition approach," *SIAM Journal on Applied Mathematics*, vol. 59, no. 4, pp. 1178–1207, 1999.

[109] G. Kerschen and J. C. Golinval, "Physical interpretation of the proper orthogonal modes using the singular value decomposition," *Journal of Sound and Vibration*, vol. 249, no. 5, pp. 849–865, 2002.

[110] C. Xu and E. Schuster, *Model Order Reduction for High Dimensional Linear Systems Based on Rank-1 Incremental Proper Orthogonal Decomposition*, pp. 2975–2981, American Control, San Francisco, CA, USA, 2011.

[111] K. Bizon, G. Continillo, M. Berezowski, and J. Smuła-Ostaszewska, "Optimal model reduction by empirical spectral methods via sampling of chaotic orbits," *Physica D: Nonlinear Phenomena*, vol. 241, no. 17, pp. 1441–1449, 2012.

[112] A. Vecchio, V. Carbone, F. Lepreti et al., "Proper orthogonal decomposition of solar photospheric motions," *Physical Review Letters*, vol. 95, no. 6, Article ID 061102, 2005.

[113] N. Kumar and T. D. Burton, "Use of random excitation to develop POD based reduced order models for nonlinear structural dynamics," in *Proceedings of the ASME International Design Engineering Technical Conference*, Las Vegas, NV, USA, 2007.

[114] D. Yu and S. Chakravorty, *A Randomized Proper Orthogonal Decomposition Technique*, pp. 1137–1142, American Control, Chicago, IL, USA, 2015.

[115] D. B. Segala and P. Naseradinmousavi, "On the inclusion of time derivatives of state variables for parametric model order reduction for a beam on a nonlinear foundation," *Journal of Dynamic Systems, Measurement, and Control*, vol. 139, no. 8, 2017.

[116] H. M. Park and M. W. Lee, "An efficient method of solving the Navier-Stokes equations for flow control," *International Journal for Numerical Methods in Engineering*, vol. 41, no. 6, pp. 1133–1151, 1998.

[117] F. Terragni, E. Valero, and J. M. Vega, "Local POD plus Galerkin projection in the unsteady lid-driven cavity problem," *SIAM Journal on Scientific Computing*, vol. 33, no. 6, pp. 3538–3561, 2011.

[118] F. Terragni and J. M. Vega, "On the use of POD-based ROMs to analyze bifurcations in some dissipative systems," *Physica D: Nonlinear Phenomena*, vol. 241, no. 17, pp. 1393–1405, 2012.

[119] F. Terragni and J. M. Vega, "Construction of bifurcation diagrams using POD on the fly," *SIAM Journal on Applied Dynamical Systems*, vol. 13, no. 1, pp. 339–365, 2014.

[120] F. Terragni and J. M. Vega, "Efficient computation of bifurcation diagrams via adaptive ROMs," *Fluid Dynamics Research*, vol. 46, no. 4, Article ID 041412, 2014.

[121] L. Yang, "Parametric identification of chaotic/nonlinear systems and reduced order models based on proper orthogonal decomposition," [PhD Thesis], Michigan State University, East Lansing, MI, USA, 2005.

[122] H. Yu, Y.-S. Chen, and Q.-J. Cao, "Bifurcation analysis for nonlinear multi-degree-of-freedom rotor system with liquid-film lubricated bearings," *Applied Mathematics and Mechanics*, vol. 34, no. 6, pp. 777–790, 2013.

[123] K. Lu, Y. Jin, P. Huang et al., "The applications of POD method in dual rotor-bearing systems with coupling misalignment," *Mechanical Systems and Signal Processing*, vol. 150, Article ID 107236, 2021.

[124] K. Lu, Y. Jin, Y. Chen, Q. Cao, and Z. Zhang, "Stability analysis of reduced rotor pedestal looseness fault model," *Nonlinear Dynamics*, vol. 82, no. 4, pp. 1611–1622, 2015.

[125] K. Lu, Y. Chen, Y. Jin, and L. Hou, "Application of the transient proper orthogonal decomposition method for order reduction of rotor systems with faults," *Nonlinear Dynamics*, vol. 86, no. 3, pp. 1913–1926, 2016.

[126] T. Bui-Thanh, K. Willcox, and O. Ghattas, "Model reduction for large-scale systems with high-dimensional parametric input space," *SIAM Journal on Scientific Computing*, vol. 30, no. 6, pp. 3270–3288, 2007.

[127] M. Grepl, "Reduced-basis approximation and A posteriori error estimation for parabolic partial differential equations," [PhD Thesis], Cambridge University, Cambridge, UK, 2005.

[128] M. A. Grepl and A. T. Patera, "A posteriorierror bounds for reduced-basis approximations of parametrized parabolic partial differential equations," *ESAIM: Mathematical Modelling and Numerical Analysis*, vol. 39, no. 1, pp. 157–181, 2005.

[129] K. Veroy and A. T. Patera, "Certified real-time solution of the parametrized steady incompressible Navier-Stokes equations: rigorous reduced-basis a posteriori error bounds," *International Journal for Numerical Methods in Fluids*, vol. 47, no. 8-9, pp. 773–788, 2005.

[130] G. Rozza, D. B. P. Huynh, and A. T. Patera, "Reduced basis approximation and a posteriori error estimation for affinely parametrized elliptic coercive partial differential equations," *Archives of Computational Methods in Engineering*, vol. 15, no. 3, pp. 229–275, 2008.

[131] M. Bergmann, L. Cordier, and J. P. Brancher, "Drag minimization of the cylinder wake by trust-region proper orthogonal decomposition," *Active Flow Control*, Springer, Berlin, Germany, 2007.

[132] K. Karl and V. Stefan, "Proper orthogonal decomposition for optimality systems," *ESAIM Mathematical Modelling and Numerical Analysis*, vol. 42, no. 1, pp. 1–23, 2008.

[133] K. Carlberg and C. Farhat, "A compact proper orthogonal decomposition basis for optimization-oriented reduced-order models," in *Proceedings of the 12th AIAA/ISSMO Multidisciplinary Analysis and Optimization Conference*, Columbia, Canada, 2008.

[134] T. A. Brenner, P. Cizmas, T. O'Brien et al., "Practical aspects of the implementation of proper orthogonal decomposition," in *Proceedings of the AIAA Aerospace Sciences Meeting*, Orlando, FL, USA, 2009.

[135] S. S. Ravindran, "A reduced-order approach for optimal control of fluids using proper orthogonal decomposition," *International Journal for Numerical Methods in Fluids*, vol. 34, no. 5, pp. 425–448, 2000.

[136] M. Kirby, J. P. Boris, and L. Sirovich, "A proper orthogonal decomposition of a simulated supersonic shear layer," *International Journal for Numerical Methods in Fluids*, vol. 10, no. 4, pp. 411–428, 1990.

[137] L. S. Ukeiley, C. Kannepalli, and S. Arunajatesan, "Low-dimensional description of variable density flows," in *Proceedings of the AIAA Aerospace Sciences Meeting and Exhibition*, Reno, NV, USA, 2001.

[138] C. W. Rowley, T. Colonius, and R. M. Murray, "Dynamical models for control of cavity oscillations," in *Proceedings of the 7th AIAA/CEAS Aeroacoustics Conference*, Maastricht, Netherlands, 2001.

[139] T. Colonius, C. W. Rowley, J. B. Freund et al., "On the choice of norm for modeling compressible flow dynamics at reduced-order using the POD," in *Proceedings of the 41st IEEE Conference on Decision and Control*, Las Vegas, NV, USA, 2002.

[140] B. I. Epureanu, "A parametric analysis of reduced order models of viscous flows in turbomachinery," *Journal of Fluids and Structures*, vol. 17, no. 7, pp. 971–982, 2003.

[141] T. Lieu, "Adaptation of reduced order models for applications in aeroelasticity," [PhD Thesis], University of Colorado, Boulder, CO, USA, 2004.

[142] J. Taylor, "Dynamics of large scale structures in turbulent shear layers," [PhD Thesis], Clarkson University, New York, NY, USA, 2001.

[143] J. A. Taylor and M. N. Glauser, "Towards practical flow sensing and control via POD and LSE based low-dimensional tools," *Journal of Fluids Engineering*, vol. 126, no. 3, pp. 337–345, 2004.

[144] R. Schmit and M. Glauser, "Improvements in low dimensional tools for flow-structure interaction problems: using global POD," in *Proceedings of the 42nd AIAA Aerospace Sciences Meeting and Exhibit*, Reno, NV, USA, 2004.

[145] M. Fossati and W. G. Habashi, "Multiparameter analysis of aero-icing problems using proper orthogonal decomposition and multidimensional interpolation," *AIAA Journal*, vol. 51, no. 4, pp. 946–960, 2013.

[146] D. Amsallem, M. J. Zahr, and C. Farhat, "Nonlinear model order reduction based on local reduced-order bases," *International Journal for Numerical Methods in Engineering*, vol. 92, no. 10, pp. 891–916, 2012.

[147] L. Peng and K. Mohseni, *Nonlinear Model Reduction for Parameterized Partial Differential Equation*, Fluid Dynamics and Co-located Conferences, San Diego, CA, USA, 2013.

[148] D. Amsallem, M. J. Zahr, and K. Washabaugh, "Fast local reduced basis updates for the efficient reduction of nonlinear systems with hyper-reduction," *Advances in Computational Mathematics*, vol. 41, no. 5, pp. 1187–1230, 2015.

[149] S. Samir and D. Seddik, "Local proper orthogonal decomposition based on space vectors clustering," in *Proceedings of the 3rd International Conference on Systems and Control*, Algiers, Algeria, 2013.

[150] J. P. Thomas, E. H. Dowell, and K. C. Hall, "Three-dimensional transonic aeroelasticity using proper orthogonal decomposition-based reduced-order models," *Journal of Aircraft*, vol. 40, no. 3, pp. 544–551, 2003.

[151] B. I. Epureanu, E. H. Dowell, and K. C. Hall, "Mach number influence on reduced-order models of inviscid potential flows in turbomachinery," *Journal of Fluids Engineering*, vol. 124, no. 4, pp. 977–987, 2002.

[152] J. Christopher, "Sensitivity based proper orthogonal decomposition for nonlinear parameter dependent systems," in *Proceedings of the American Control Conference*, pp. 135–140, Hilton, Portland, 2014.

[153] Z. Xu, X. Lin, H. Zhuang et al., "A new nonlinear parameterized model order reduction technique combining the interpolation method and Proper Orthogonal Decomposition," *International Conference on ASIC*, pp. 886–889, 2011.

[154] M. R. Opmeer, "Model order reduction by balanced proper orthogonal decomposition and by rational interpolation," *IEEE Transactions on Automatic Control*, vol. 57, no. 2, pp. 472–477, 2012.

[155] W. Yao and S. Marques, "Nonlinear aerodynamic and aeroelastic model reduction using a discrete empirical interpolation method," *AIAA Journal*, vol. 55, no. 2, pp. 624–637, 2017.

[156] T. Lieu and M. Lesoinne, "Parameter adaptation of reduced order models for three-dimensional flutter analysis," *//AIAA Aerospace Sciences Meeting and Exhibit*, vol. 16, no. 4, pp. 929–955, 2004.

[157] A. Björck and G. H. Golub, "Numerical methods for computing angles between linear subspaces," *Mathematics of Computation*, vol. 27, no. 123, pp. 579–594, 1973.

[158] T. Lieu, C. Farhat, and M. Lesoinne, "POD-based aeroelastic analysis of a complete f-16 configuration: rom adaptation and demonstration," in *Proceedings of the 46th AIAA/ASME/ASCE/AHS/ASC Structures, Structural Dynamics and Materials Conference*, Austin, TX, USA, 2005.

[159] T. Lieu and C. Farhat, "Adaptation of POD-based aeroelastic ROMs for varying Mach number and angle of attack: application to a complete F-16 configuration," in *Proceedings of the Air Force T&E Days*, Nashville, TN, USA, 2005.

[160] T. Lieu, C. Farhat, and M. Lesoinne, "Reduced-order fluid/structure modeling of a complete aircraft configuration," *Computer Methods in Applied Mechanics and Engineering*, vol. 195, no. 41-43, pp. 5730–5742, 2006.

[161] T. Lieu and C. Farhat, "Adaptation of aeroelastic reduced-order models and application to an F-16 configuration," *AIAA Journal*, vol. 45, no. 6, pp. 1244–1257, 2007.

[162] T. Braconnier, M. Ferrier, J.-C. Jouhaud, M. Montagnac, and P. Sagaut, "Towards an adaptive POD/SVD surrogate model for aeronautic design," *Computers & Fluids*, vol. 40, no. 1, pp. 195–209, 2011.

[163] D. Amsallem, C. Farhat, and T. Lieu, "Aeroelastic Analysis of F-16 and F-18/A Configurations Using Adapted CFD-Based Reduced-Order Models," in *Structural Dynamics, and Materials*Honolulu, HI, USA, 2007.

[164] D. Amsallem, C. Farhat, and T. Lieu, *High-Order Interpolation of Reduced-Order Models for Near Real-Time Aeroelastic Prediction*, International Forum on Aeroelasticity and Structural Dynamics, Stockholm, Sweden, 2007.

[165] D. Amsallem and C. Farhat, "Interpolation method for adapting reduced-order models and application to aeroelasticity," *AIAA Journal*, vol. 46, no. 7, pp. 1803–1813, 2008.

[166] C. Farhat and D. Amsallem, *Recent Advances in Reduced-Order Modeling and Application to Nonlinear Computational Aeroelasticity*, AIAA Aerospace Sciences Meeting and Exhibit, Reno, NV, USA, 2008.

[167] D. Amsallem, J. Cortial, K. Carlberg, and C. Farhat, "A method for interpolating on manifolds structural dynamics reduced-order models," *International Journal for Numerical Methods in Engineering*, vol. 80, no. 9, pp. 1241–1258, 2009.

[168] D. Amsallem, *Interpolation on Manifolds of CFD-Based Fluid and Structural Reduced-Order Models for On-Line Aeroelastic Predictions*, Stanford University, Stanford, CA, USA, 2010.

[169] D. Amsallem and C. Farhat, "Stabilization of projection-based reduced-order models," *International Journal for Numerical Methods in Engineering*, vol. 91, no. 4, pp. 358–377, 2012.

[170] B. A. Freno, T. A. Brenner, and P. G. A. Cizmas, "Using proper orthogonal decomposition to model off-reference flow conditions," *International Journal of Non-linear Mechanics*, vol. 54, no. 3, pp. 76–84, 2013.

[171] Y. Paquay, O. Brüls, and C. Geuzaine, "Nonlinear interpolation on manifold of reduced-order models in magnetodynamic problems," *IEEE Transactions on Magnetics*, vol. 52, no. 3, Article ID 7204804, 2016.

[172] M. Amabili and C. Touzé, "Reduced-order models for nonlinear vibrations of fluid-filled circular cylindrical shells: comparison of POD and asymptotic nonlinear normal modes methods," *Journal of Fluids and Structures*, vol. 23, no. 6, pp. 885–903, 2007.

[173] K. Kunisch and S. Volkwein, "Galerkin proper orthogonal decomposition methods for a general equation in fluid dynamics," *SIAM Journal on Numerical Analysis*, vol. 40, no. 2, pp. 492–515, 2002.

[174] T. Kim, "Frequency-domain karhunen-loeve method and its application to linear dynamic systems," *AIAA Journal*, vol. 36, no. 11, pp. 2117–2123, 1998.

[175] K. C. Hall, J. P. Thomas, and E. H. Dowell, "Proper orthogonal decomposition technique for transonic unsteady aerodynamic flows," *AIAA Journal*, vol. 38, no. 10, pp. 1853–1862, 2000.

[176] K. Willcox and J. Peraire, "Balanced model reduction via the proper orthogonal decomposition," *AIAA Journal*, vol. 40, no. 11, pp. 2323–2330, 2002.

[177] C. W. Rowley, "Model reduction for fluids, using balanced proper orthogonal decomposition," *International Journal of Bifurcation and Chaos*, vol. 15, no. 03, pp. 997–1013, 2005.

[178] M. Ilak and C. W. Rowley, "Modeling of transitional channel flow using balanced proper orthogonal decomposition," *Physics of Fluids*, vol. 20, no. 3, Article ID 034103, 2008.

[179] M. J. Balajewicz, E. H. Dowell, and B. R. Noack, "Low-dimensional modelling of high-Reynolds-number shear flows incorporating constraints from the Navier-Stokes equation," *Journal of Fluid Mechanics*, vol. 729, pp. 285–308, 2013.

[180] C. Fu, Y. Xu, Y. Yang, K. Lu, F. Gu, and A. Ball, "Response analysis of an accelerating unbalanced rotating system with both random and interval variables," *Journal of Sound and Vibration*, vol. 466, Article ID 115047, 2020.

[181] K. Lu, Y. Jin, Y. Chen et al., "Review for order reduction based on proper orthogonal decomposition and outlooks of applications in mechanical systems," *Mechanical Systems and Signal Processing*, vol. 123, pp. 264–297, 2019.

[182] Y. F. Yang, Q. Y. Wu, Y. L. Wang, W. Y. Qin, and K. Lu, "Dynamic characteristics of cracked uncertain hollow-shaft," *Mechanical Systems and Signal Processing*, vol. 124, pp. 36–48, 2019.

[183] C. Fu, X. Ren, Y. Yang, Y. Xia, and W. Deng, "An interval precise integration method for transient unbalance response analysis of rotor system with uncertainty," *Mechanical Systems and Signal Processing*, vol. 107, pp. 137–148, 2018.

[184] C. Sun, S. Li, and Y. Deng, "Determining weights in multi-criteria decision making based on negation of probability distribution under uncertain environment," *Mathematics*, vol. 8, no. 2, p. 191, 2020.

[185] S. Niroomandi, A. Perrier, M. Bucki, and Y. Payan, "Real-time computer modeling in prevention of foot pressure ulcer using patient-specific finite element model and model order reduction techniques," *Innovations and Emerging Technologies in Wound Care*, pp. 87–102, 2020.

[186] C. Teeranoot, P. D. Jaydev, and C. W. L. Alan, "Modeling soft-tissue deformation prior to cutting for surgical simulation: finite element analysis and study of cutting parameters," *IEEE Transactions on Biomedical Engineering*, vol. 54, no. 3, pp. 349–359, 2007.

[187] F. Chinesta, P. Ladeveze, and E. Cueto, "A short review on model order reduction based on proper generalized decomposition," *Archives of Computational Methods in Engineering*, vol. 18, no. 4, pp. 395–404, 2011.

[188] M. J. Hochrainer and P. Schattovich, "Real-time hybrid simulation of an unmanned aerial vehicle," *Dynamics of Coupled Structures, Volume 4*, vol. 4, pp. 41–48, 2017.

[189] T. Letrouve, W. Lhomme, A. Bouscayrol, and N. Dollinger, "Control validation of peugeot 3∞8 HYbrid4 vehicle using a reduced-scale power HIL simulation," *Journal of Electrical Engineering and Technology*, vol. 8, no. 5, pp. 1227–1233, 2013.

[190] M. H. C. Law and A. K. Jain, "Incremental nonlinear dimensionality reduction by manifold learning," *IEEE Transactions on Pattern Analysis and Machine Intelligence*, vol. 28, no. 3, pp. 377–391, 2006.

[191] R. Calandra, J. Peters, C. E. Rasmussen, and M. P. Deisenroth, "Manifold Gaussian processes for regression," *International Joint Conference on Networks*, 2016.

[192] E.. Emary and C. Grosan, "Feature selection via chaotic antlion optimization," *PLoS One*, vol. 11, no. 3, Article ID e0150652, 2016.

[193] A. Doostan, R. G. Ghanem, and J. Red-Horse, "Stochastic model reduction for chaos representations," *Computer Methods in Applied Mechanics and Engineering*, vol. 196, no. 37-40, pp. 3951–3966, 2007.

[194] M. Raisee, D. Kumar, and C. Lacor, "A non-intrusive model reduction approach for polynomial chaos expansion using proper orthogonal decomposition," *International Journal for Numerical Methods in Engineering*, vol. 103, no. 4, pp. 293–312, 2015.

[195] C. Fu, X. Ren, and Y. Yang, "Vibration analysis of rotors under uncertainty based on Legendre series," *Journal of Vibration Engineering & Technologies*, vol. 7, no. 1, pp. 43–51, 2019.

[196] X. Guo, H. Ma, X. Zhang et al., "Uncertain frequency responses of clamp-pipeline systems using an interval-based method," *IEEE Access*, vol. 8, pp. 29370–29384, 2020.

[197] H. Sandberg and R. M. Murray, "Model reduction of interconnected linear systems," *Optimal Control Applications and Methods*, vol. 30, no. 3, pp. 225–245, 2009.

[198] A. Vandendorpe and P. Van Dooren, "Model reduction of interconnected systems," *Model Order Reduction: Theory, Research Aspects and Applications*, pp. 305–321, Springer, Berlin, Germany, 2008.

[199] W. H. A. Schilders, H. A. Van der Vorst, and J. Rommes, *Model Order Reduction: Theory, Research Aspects and Applications*, Springer, Berlin, Germany, 2008.

[200] B. N. Datta and V. Sokolov, "Quadratic inverse eigenvalue problems, active vibration control and model updating," *Applied and Computational Mathematics*, vol. 8, no. 2, pp. 170–191, 2009.

Hindawi
Shock and Vibration
Volume 2021, Article ID 5553304, 9 pages
https://doi.org/10.1155/2021/5553304

Research Article

Transonic Static Aeroelastic Numerical Analysis of Flexible Complex Configuration Wing

Changrong Zhang, Hongtao Guo, Binbin Lv, Jun Zha, and Li Yu

Institute of High Speed Aerodynamics, China Aerodynamics Research & Development Center, Beichuan 622763, Sichuan, China

Correspondence should be addressed to Hongtao Guo; ght@cardc.cc

Received 10 January 2021; Revised 5 April 2021; Accepted 10 April 2021; Published 20 April 2021

Academic Editor: Zeqi Lu

Diamond back wing is subjected to large deformation while gliding, which significantly changes characteristics of the lift as well as the static stability. For this reason, conventional rigid aircraft assumption cannot meet the requirements of the aerodynamic analysis of such aircrafts for accuracy. In this paper, based on CFD/CSD methods, the static aeroelasticity of a small diameter bomb with diamond back wing was studied. The results showed that static aeroelastic effects cause the slope of lift line to drop by 21% and the aerodynamic centre to move backwards by a 1.5% bomb body length, which will deviate the actual flight performance from the design point, thereby decreasing the cruise efficiency and the cruise range.

1. Introduction

As illustrated in Figure 1, diamond back missile wing is a gliding range extended component which has been successfully applied to the American small diameter bomb (SDB) GBU-39 USA and the Chinese Feiteng series guided bomb. The SDB diamond back wing has a compact structure and can be installed in a small embedded bomb cabin. After unfolding the back-extended component, it can be launched outside the defense area with a larger gliding range. Considering its advantages of high lift-to-drag ratio and strong ability of gliding, its stiffness and strength of high-aspect-ratio wing can be increased to avoid flutter [1]. In order to reduce the resistance and installation space, the thickness of the front and rear wings of diamond backed projectile wing is small while its aspect ratio is large for the purpose of high lift-to-drag ratio. This however would lead to a large aeroelastic deformation when it glides. The aerodynamic load of the projectile wings differs significantly from that of the original shape, which greatly affects the aerodynamic characteristics of the whole projectile.

The classical static aeroelastic analysis method adopts the hypothesis of potential flow theory and thus is unable to predict the nonlinear phenomena such as shock wave flow separation in transonic region. The computational fluid dynamic (CFD) and computational structural mechanics (CSD) make it possible to accurately calculate aeroelastic problems by coupling CFD and CSD [2–11]. The coupling methods of CFD and CSD are generally divided into tight coupling and loose coupling.

The tight coupling method can simultaneously solve the fluid control equation and structural dynamic equation in each internal time step and can simulate the real situation. However, it costs a lot of computing resources, and it is still difficult to use this method to solve the complex three-dimensional problems in engineering applications. The loose coupling method solves the fluid dynamic and structural dynamics equations separately and can apply the existing aerodynamic and structural solution modules. It needs to exchange the data of the aerodynamic/structural interface at an appropriate time point and iterate repeatedly until the solution converges. The method can be applied to the static aeroelastic calculation without time variables [12–16].

There are extensive foreign and domestic studies on folding and connecting wing [17–19] and aerodynamic characteristics and layout optimization design of diamond back projectile wing [20,21]. Nevertheless, few of them are regarding the static aeroelastic effect of diamond back

Figure 1: Sketch of small diameter bomb with diamond back wing.

projectile wing, and they are still in the infancy [22–25]. In this paper, the static aeroelastic numerical simulation of a diamond back SDB is realized by the coupling of RANS equation and the static equilibrium equation and combining the structured dynamic grid with multifield data interpolation technology. The affection of static aeroelasticity on the geometric deformation characteristics, surface pressure distribution, and aerodynamic performance of the diamond back projectile wing are analyzed based on the numerical simulation results.

2. Computing Method

2.1. CFD Governing Equations. The governing equation is a time-dependent, three-dimensional conservation compressible RANS equation. In the curvilinear coordinate system (ξ, η, and ζ), its dimensionless form is expressed as follows:

$$\frac{\partial Q}{\partial t} + \frac{\partial (F\text{-}F_v)}{\partial \xi} + \frac{\partial (G - G_v)}{\partial \eta} + \frac{\partial (H - H_v)}{\partial \zeta} = 0, \quad (1)$$

where t is time, Q is conservation variable, F, G, and H are inviscid vector flux, and F_y, G_y, and H_y are viscous vector flux.

The S-A model of equation (1) is applied to turbulence simulation. The body surface is adiabatic sliding free boundary condition, the boundary condition of far field is pressure free, and the multigrid technology is applied to accelerate the computational convergence of CFD.

2.2. CSD Governing Equation. The structural elastic equilibrium equation is applied to solve the elastic deformation of the structure. The calculation equation is

$$u_s = CF_s, \quad (2)$$

where C is the flexibility matrix, u_s is the deformation displacement of the structural finite element node, and F_s is the column vector of external load which acts on the structural points.

2.3. Interpolation Method for Fluid Structure Coupling Data. When CFD and CSD are coupled to solve nonlinear aeroelastic problems, data exchange is required on the coupling surface of aerodynamic structure. The aerodynamic force obtained by the aerodynamic calculation is applied to the structural nodes, and the structure is subjected to deformation. The displacement of the structural nodes should be fed back to the aerodynamic grid nodes. Considering the calculation efficiency and interpolation accuracy, the three-dimensional thin plate spline interpolation method (TPSI) is adopted in this paper. The calculation method of TPSI can be found in [26–28].

2.4. Generation Method for Dynamic Mesh. This paper combines RBF and TFI method to generate dynamic grid. The RBF can be regarded as a three-dimensional extension of the surface spline interpolation method [29]. Its interpolation formula is expressed as

$$f(r) = \sum_{i=1}^{n} a_i \varphi\left(\|r - r_i\|\right) + \psi(r), \quad (3)$$

where $r_i = (x_i, y_i, z_i)$ is the coordinates of the point whose displacement is known and number is n and φ is the basic function of the displacement $\|r - r_i\|$. In this paper, $\varphi\|r - r_i\| = \|r - r_i\|^3$ and $\psi = b_0 + b_1 x + b_2 y + b_3 z$, and the coefficients of the interpolation formula can be obtained by the displacement and equilibrium conditions of the known points.

Based on the mesh block surface, the displacements of the points in the mesh block can be obtained by TFI interpolation. Similarly, the displacements of the points on the edge of each grid block are obtained by the RBF method [30].

3. Calculation and Verification

3.1. Calculation Process. Static aeroelastic calculation is an iterative process of CFD/CSD. The flowchart of loose coupling method is presented in Figure 2. The topological structure and the number of grids will not change during the calculation. Thus, the CFD calculation results of the previous deformation step can be applied to the next step as the initial value, and the iteration step of CFD calculation can be decreased. In general, the computational results tend to convergence with 6-7 iteration steps which is 1.5 to 2 times to its rigid CFD counterpart [31–33].

3.2. Calculation Model. In this paper, the numerical calculation of the static aeroelastic for a diamond back SDB is carried out, and the results are compared with the wind tunnel test results. The projectile wing combines the high-aspect ratio with the layout scheme of "×" tail rudder. Figure 3 shows the calculation grid near the rigid bomb wing surface. There are about 16.5 million space grid elements of the whole bomb in total.

The structure diagram of the diamond back projectile wing is shown in Figure 4. The chord length of the front wing is 23 mm, and the sweptback angle is 30 degrees; the chord length of the rear wing is 21 mm, and the forward-swept angle is 10 degrees. The distance between the front and rear wings is 145 mm, and the half span length is 200 mm. In

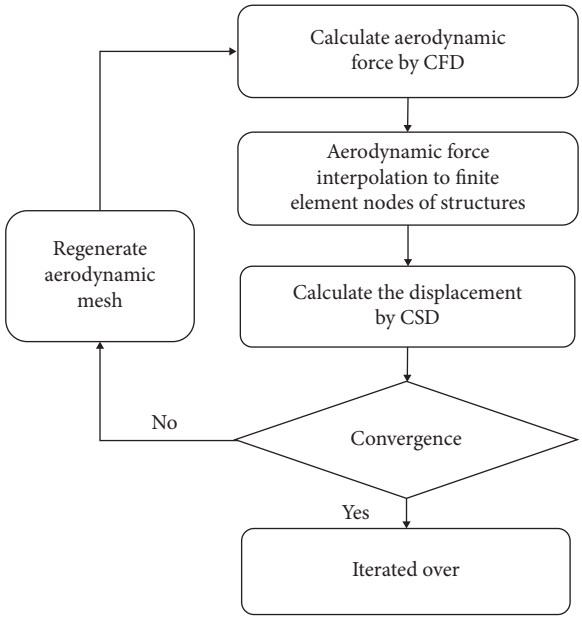

Figure 2: Loose coupling flowchart.

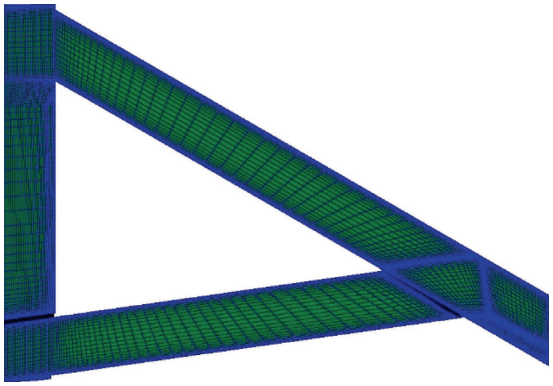

Figure 3: Surface mesh on diamond back wing.

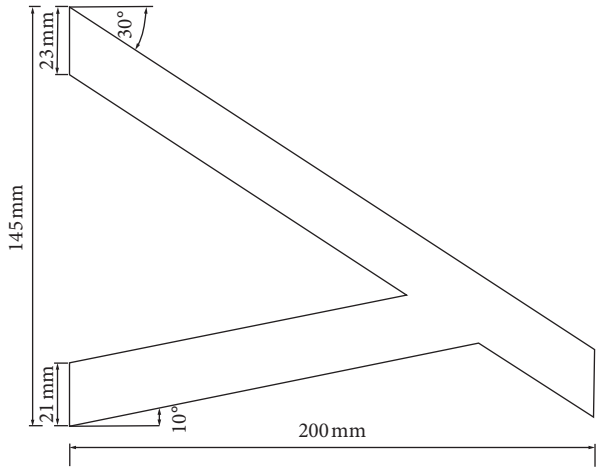

Figure 4: Sketch of diamond back wing.

order to improve the aerodynamic performance, a supercritical airfoil with a relative thickness of 10% is adopted to the diamond back projectile wing, and the installation angles of front and rear wings are 2.5 degrees. The flexibility matrix is obtained by the commercial software, and the material of the whole bomb adopts 45-type steel.

3.3. Verification of Calculation Method. The parameters of the verification sample are set as follows: Ma = 0.8, $H = 0$ km, and the attack angle ranges from 0° to 4°. The displacement convergence process of the front wing is shown in Figure 5. It can be seen that the deformation of the wing tends to converge with a few iteration steps.

The calculation results are compared with the wind tunnel test results. The comparison results of coefficient for lift force C_L, pitching moment C_m, and bending deformation are shown in Figure 6, which are consistent with the experimental results. As shown in Figure 6, both the calculation results of C_m and the bending trend of the front and rear wing are consistent with the experimental results, and the error is less than 2 mm in all spanwise section. The calculated bending displacement curve is smoother than the experimental one. And, this difference may be attributed to the measurement error of measuring equipment. The difference of C_L appears when airflow separation occurs at the larger angle of attack on the airfoil. The reason lies in two aspects. One is the insufficient simulation of turbulence and the inaccurate simulation of flow separation characteristics caused by the RANS equation that the current CFD calculation follows. The second is that the CSD calculation uses the structural statics balance equation based on the linearization theory; but, in actual situations, the airfoil will have structural geometric nonlinearity under heavy loads.

4. Analysis of Calculation Results

To obtain a large lift-to-drag ratio, the SDB diamond back projective wing has a large aspect ratio and adopts supercritical airfoil with a relatively small thickness. At transonic speed, the viscous effect should not be ignored due to the strong interaction between shock wave and boundary layer, though the angle of attack is very small. It is therefore necessary to calculate the aerodynamic force by N-S equation. In general, this paper focuses on the static aeroelastic characteristics of the sample model with the parameters of Ma = 0.8 and $H = 0$ km.

4.1. Effect of Geometric Deformation. The variation curves of Δz and $\Delta\varepsilon$ (elastic torsion angle) of the front and rear wings along the spanwise are shown in Figure 7, where Ma = 0.8, $H = 0$ km, and $\alpha = [-8^\circ \sim 8^\circ]$. From Figure 7, it can be seen that the calculation boundary is $\alpha = -4^\circ$. When the value of α is larger than -4°, the static aeroelastic effect makes the front and rear wings produce bending deformation along the spanwise direction and produce a negative elastic torsion angle along the flow direction of wing, whereas when the value of α is less than -4°, the result is opposite. The wing has a certain initial installation angle and a geometric torsion

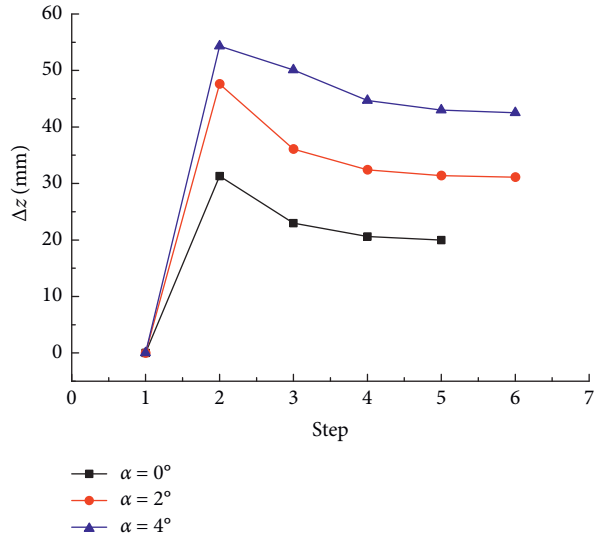

Figure 5: Iteration convergence of static aeroelastic deformation.

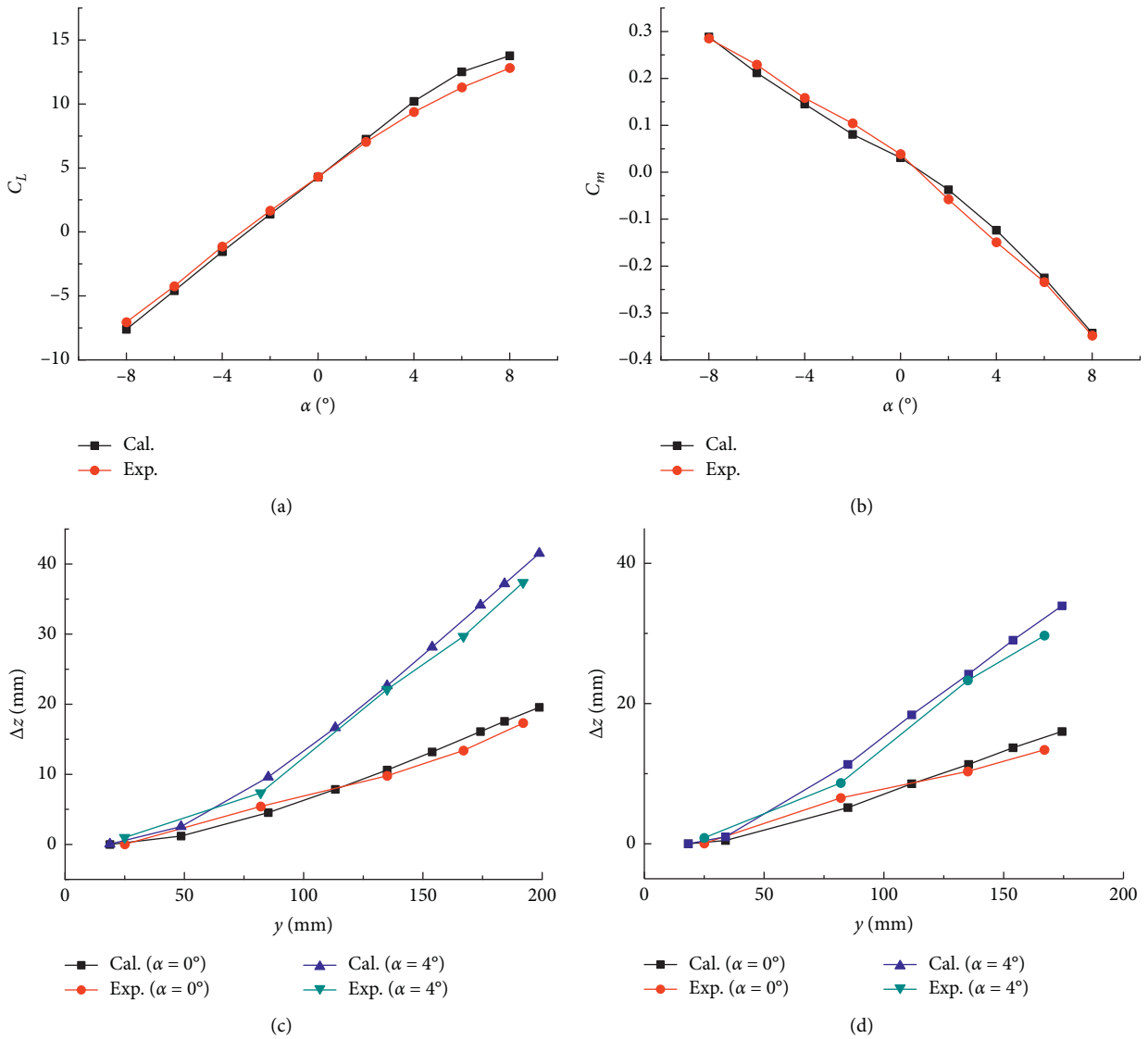

Figure 6: Comparison between numerical computation and wind tunnel test. (a) C_L~α. (b) C_m~α. (c) Δ (z)~α (front wing). (d) Δ (z)~α (rear wing).

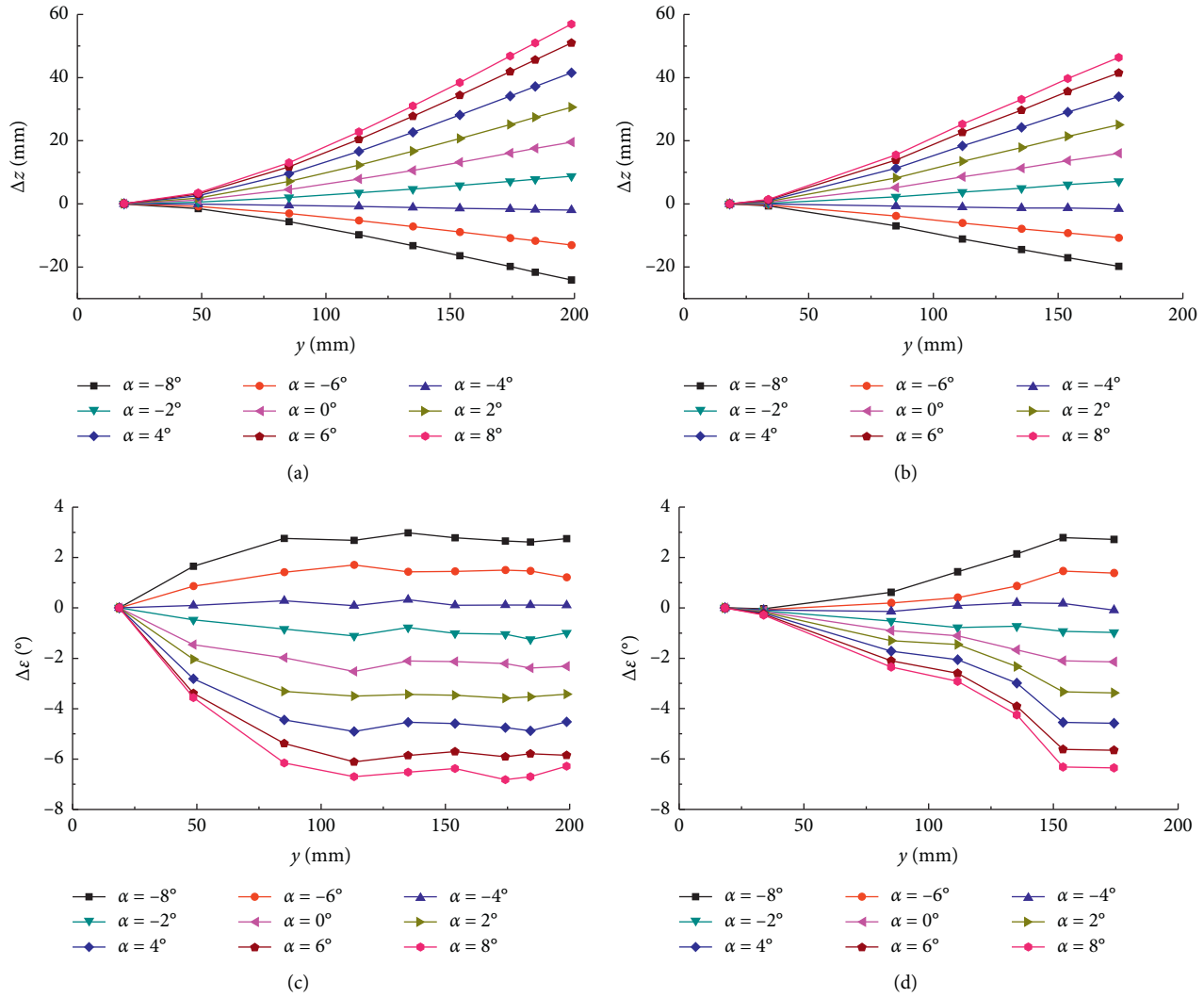

Figure 7: Geometry deformation characteristics of wing. (a) $\Delta z \sim \alpha$ (front wing). (b) $\Delta z \sim \alpha$ (rear wing). (c) $\Delta \varepsilon \sim \alpha$ (front wing). (d) $\Delta \varepsilon \sim \alpha$ (rear wing).

angle. The changing law corresponds to the aerodynamic load and the gradual decrease of the wing stiffness along the spanwise direction along the span. Its zero-lift angle of attack appears when the value of α is about -4°. It can also be seen from Figure 7 that, according to the calculation results in this paper, when $\alpha = 4$, the bending deformation of the front wing tip can reach 23% of the half span of the front wing, and the downstream elastic torsional deformation of the front wing tip profile can reach -4.5°.

4.2. Effect of Surface Flow Pattern. The surface pressure coefficient of cloud chart and flow spectrum of the body near the projective wing for rigid and elastic wings are shown in Figure 8 when Ma = 0.8, $H = 0$ km, and $\alpha = -4^{\circ}$, 0°, and 4°. Corresponding to the geometric deformation characteristics of the whole projectile body, the static aeroelasticity has little influence on the surface pressure and flow characteristics of the projectile body under different angles of attack. And, there is almost no difference between rigidity and elasticity. The main reason is that the projective wing is greatly affected, especially at a high angle of attack. The specific analysis is as follows: when $\alpha = -4^{\circ}$, the lift force generated by the wing is close to zero, and the geometric deformation is small. The surface flow of rigid and elastic wings is very uniform, and the change characteristics are similar. The pressure recovery is realized in the form of a series of compression waves, and the flow presents a typical attached flow pattern. The pressure distribution on the upper surface of the wing is similar, and the aerodynamic characteristics of the rigid and elastic projective body are similar. When $\alpha = 0^{\circ}$, there is no obvious shock wave and separation stall phenomenon on the rigid wing while the effective angle of attack of the elastic wing is reduced due to the static aeroelastic effect. Accordingly, the peak negative pressure and the negative pressure range on the upper surface of the elastic wing are also significantly reduced, so is the corresponding aerodynamic load. When $\alpha = 4^{\circ}$, the peak negative pressure on the upper surface of the rigid wing is greatly enhanced, and separation and reattachment are formed along the flow

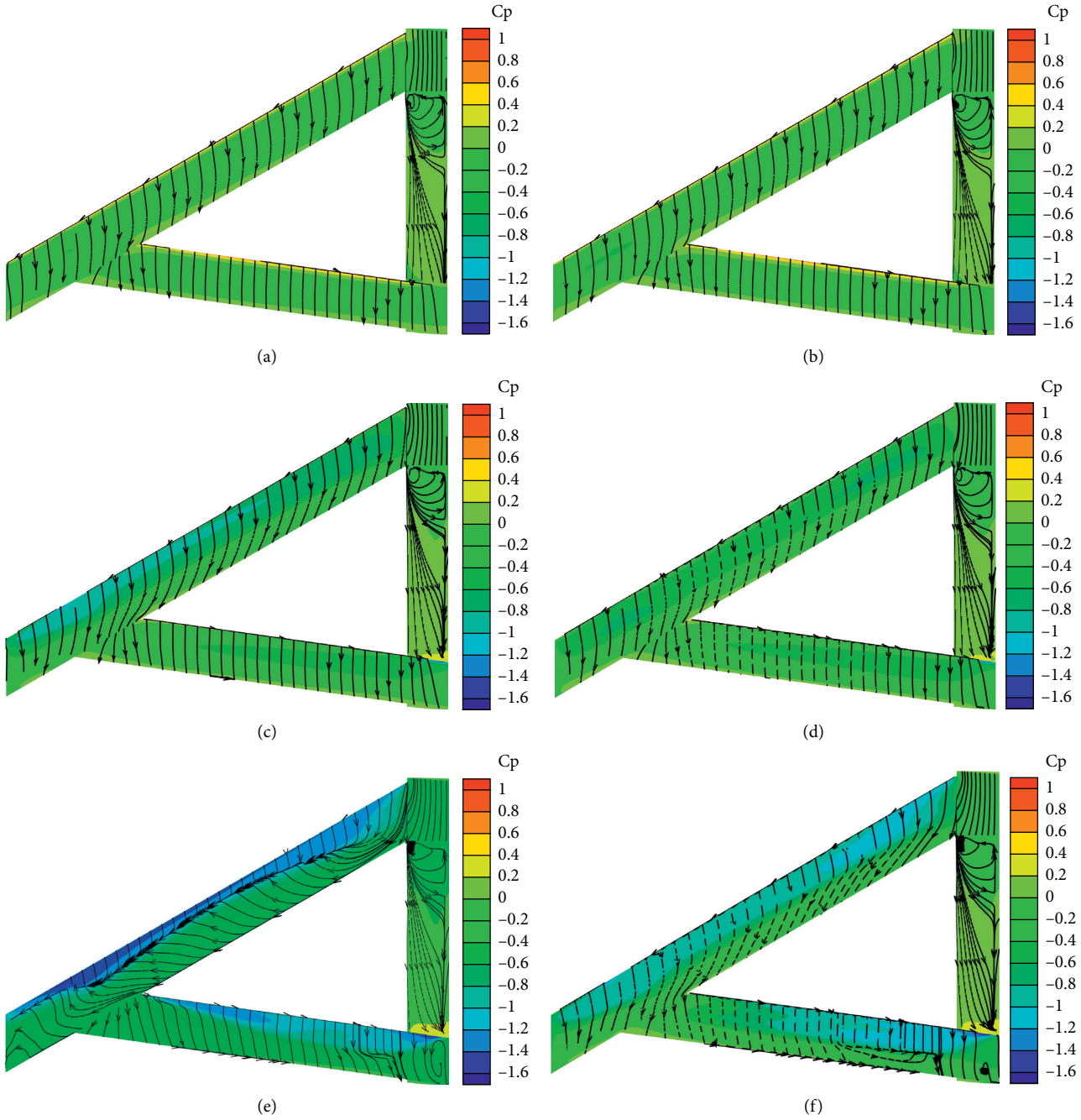

Figure 8: Effects of static aeroelasticity on wing surface pressure. (a) Rigid wing ($\alpha = -4^{\circ}$). (b) Flexible wing ($\alpha = -4^{\circ}$). (c) Rigid wing ($\alpha = 0^{\circ}$). (d) Flexible wing ($\alpha = 0^{\circ}$). (e) Rigid wing ($\alpha = 4^{\circ}$). (f) Flexible wing ($\alpha = 4^{\circ}$).

direction. By contrast, the elastic wing does not have the similar phenomenon and still maintains the attached flow pattern. A weak shock wave appears on the upper surface of the wing near the projective body, and it leads to a slight deflection of the surface streamline. With the increasing attack angle, the shock intensity on the upper surface of the rigid wing will increase, which will induce a large range of flow separation. As for elastic wing, due to the static aeroelastic effect, the effective angle of attack will decline, and the shock intensity as well as the stall separation range will be reduced. Therefore, in the range of high attack angle, the static aeroelasticity will delay the stall separation characteristics of projective wings.

4.3. Effect of Aerodynamic Performance. The elastic curves and rigid curves for C_L~α, C_L~C_D, and L/D~α of the whole bomb are shown in Figure 9 when Ma = 0.8, $H = 0$ km, and $\alpha \in [-8^{\circ}\sim 8^{\circ}]$. It can be observed that the difference of aerodynamic characteristics between rigid and elastic bomb is quite obvious owing to the static aeroelastic effect. As the aerodynamic load increases, the static aeroelasticity exerts a great influence on the aerodynamic force.

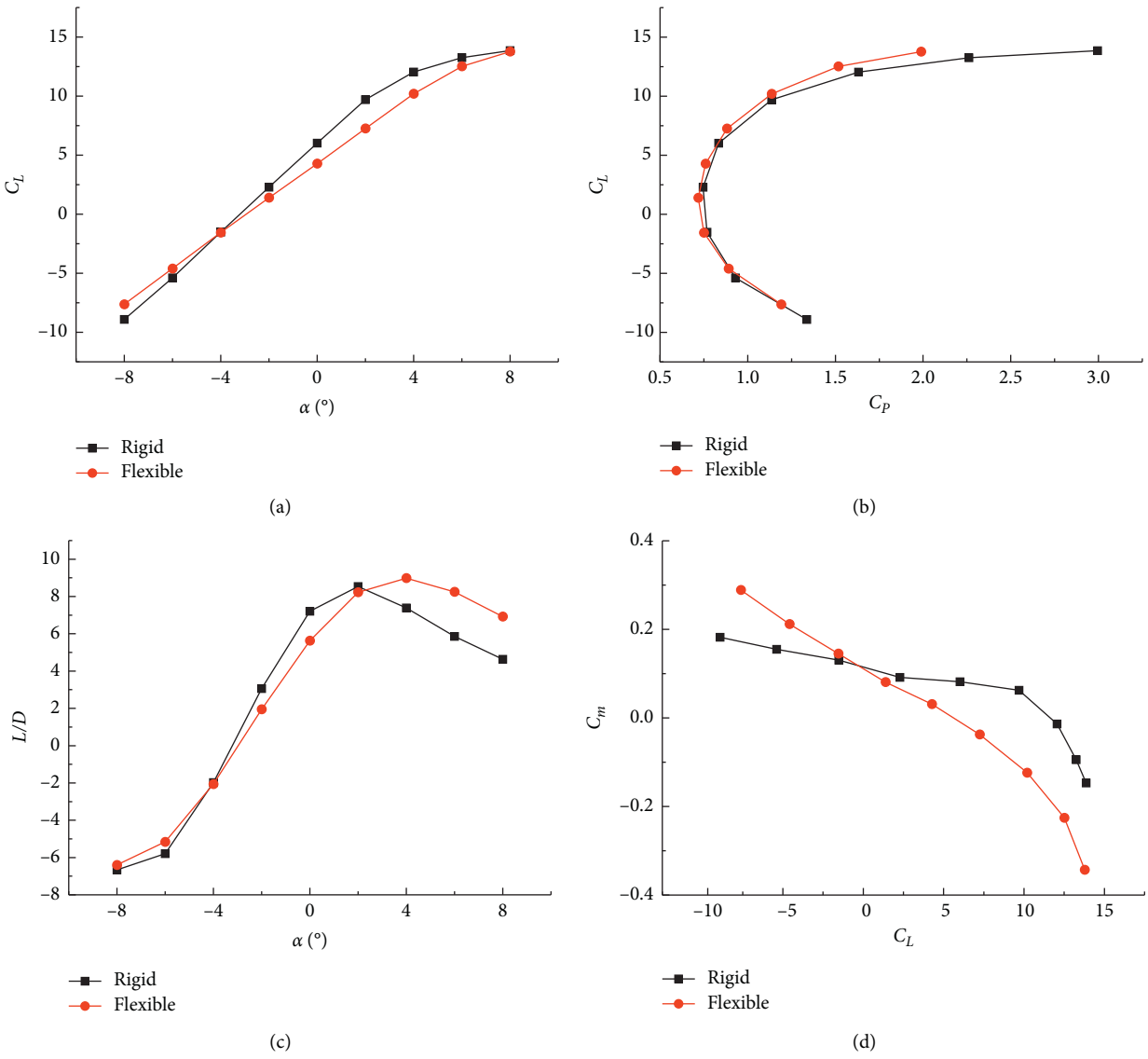

Figure 9: Effects of static aeroelasticity on bomb's aerodynamic characteristics. (a) C_L~α. (b) C_L~C_D. (c) L/D~α. (d) C_m~C_L.

Specifically, the static aeroelastic effect reduces the line slope of lift force $C_{L\alpha}$ and the drag force, while the angle of attack related to the maximum lift drag ratio (L/D) increases.

Additionally, under the static aeroelastic effect, the whole projectile focus moves backward, resulting in the enhancement of longitudinal static stability. The result is consistent with the geometric deformation and surface flow pattern of the projective wing. From the geometric deformation characteristics, it can be found that the static aeroelastic effect not only causes significant bending deformation of the wing but also produces torsion deformation which makes the wing to unload. Therefore, the line slope of lift force and drag force of the whole bomb will be reduced. Moreover, the static aeroelasticity delays the stall separation of the wing, which further delays the inflection point of the lift moment curve and the angle of attack corresponding to the maximum lift-drag ratio.

According to our calculation example, compared with the rigid projectile, the slope of lift line ($C_{L\alpha}$) decreases by 21% on the same angle of attack, the maximum lift drag ratio (L/D) increases from 2° to 4°, and the focus X_F moves backward by 1.5% of the body length. The adverse effect of static aeroelasticity on its aerodynamic characteristics is mainly reflected in the deviation of cruise flight state from the design point. For a given bomb mass, if the bomb is rigid, the angle of attack will be 0° so as to satisfy the requirements of lift force. In terms of an elastic bomb, the angle will be about 1°. The cruise aerodynamic efficiency will be signifi-

cantly reduced and the total glide range will be shortened.

5. Conclusions

The paper studies the static aeroelastic characteristics of a SDB diamond back projective wing based on RANS equation and the coupling of CFD and CSD methods. The effectiveness of the method is verified by wind tunnel test results. The static aeroelastic effect causes the bending deformation of the front and rear wings to increase gradually along the spanwise direction and also causes the torsion deformation to the wing which is favorable to the unloading of the wing. When the angle of attack α is 4°, the bending deformation at the tip of the wing can reach 23% of the half-span length of the wing, and the torsion deformation along the flow direction reaches −4.5°. At a high angle of attack, the static aeroelasticity will delay the stall separation characteristics of the wing. Compared with the rigid projectile, the lift line slope $C_{L\alpha}$ decreases by 21% and the focus X_F is moved backward by 1.5% of the body length. These will cause the cruise flight to deviate from the design point, thereby reducing the cruise aerodynamic efficiency and the total glide range.

Data Availability

No data were used to support this study.

Conflicts of Interest

The authors declare no potential conflicts of interest with respect to the research, authorship, and/or publication of this article.

Acknowledgments

This work was funded by the Science, Technology and Innovation Commission of Shenzhen Municipality (Grant no. JCYJ20190806153615091) and project of Shaanxi Key Laboratory of Mine Electromechanical Equipment Intelligent Monitoring in Xi'an University of Science and Technology (no. SKL-MEEIM201902).

References

[1] J. Chen, Z. Wang, L. Zhang et al., "Numerical simulation for influence of vertical height difference to aerodynamic characteristics of diamond back wing," *Journal of Projectiles, Rockets, Missiles and Guidance*, vol. 35, no. 2, pp. 109–113, 2015, (in Chinese).

[2] M. Sayed, T. Lutz, E. Kramer et al., "High fidelity CFD-CSD aeroelastic analysis of slender bladed horizontal-axis wind turbine," *Journal of Physics: Conference Series*, vol. 753, no. 4, p. 13, Article ID 042009, 2016.

[3] P. A. Inthra, "Full vehicle simulations for a coaxial rotorcraft using high-fidelity CFD/CSD coupling," in *Proceedings of the AIAA Aerospace Sciences Meeting*, Kissimmee, FL, USA, January 2018.

[4] H. Cho, S. J. Shin, and H. S. Joo, "Computational approach for vertical launcher by coupled cfd/csd with hybrid particle level-set method," in *Proceedings f the Structural Dynamics, and Materials Conference*, Grapevine, TX, USA, January 2017.

[5] Z.-Q. Lu, K.-K. Zhang, H. Ding, and L.-Q. Chen, "Nonlinear vibration effects on the fatigue life of fluid-conveying pipes composed of axially functionally graded materials," *Nonlinear Dynamics*, vol. 100, no. 2, pp. 1091–1104, 2020.

[6] Z. Q. Lu, D. H. Gu, H. Ding, W. Lacarbonara, and L. Q. Chen, "Nonlinear vibration isolation via a circular ring," *Mechanical Systems and Signal Processing*, vol. 136, Article ID 106490, 2020.

[7] R. Prasad, S. Choi, D. Im, and D. Lee, "Spectral formulation-based fsi and coupled sensitivity analysis for dynamic aeroelastic problems," in *Proceedings of the 33rd AIAA Applied Aerodynamics Conference*, Dallas, TX, USA, June 2015.

[8] J. Allan, A. Lyrio, J. L. Azevedo, D. A. Rade, and G. D. Silva, "Computational static aeroelastic analyses in transonic flows," in *Proceedings of the AIAA AVIATION 2020 FORUM*, June 2020.

[9] Z.-Q. Lu, D. Wu, H. Ding, and L.-Q. Chen, "Vibration isolation and energy harvesting integrated in a stewart platform with high static and low dynamic stiffness," *Applied Mathematical Modelling*, vol. 89, pp. 249–267, 2021.

[10] Z. Q. Lu, K. K. Zhang, H. Ding, and L. Q. Chen, "Internal resonance and stress distribution of pipes conveying fluid in supercritical regime," *International Journal of Mechanical Sciences*, vol. 186, Article ID 105900, 2020.

[11] C. Yang, L. Yang, and C. Xie, "Development of aerodynamic methods in aeroelastic analysis for high aspect ratio flexible wings," *Acta Aerodynamic Sinica*, vol. 36, no. 6, pp. 1009–1018, 2018, (in Chinese).

[12] P. Bekemeyer and S. Timme, "Reduced order transonic aeroelastic gust response simulation of large aircraft," in *Proceedings of the 35th AIAA Applied Aerodynamics Conference*, Denver, CO, USA, June 2017.

[13] J. Huang, Z. Zhou, H. Liu, Z. Gao, and G. Li, "Numeric simulation of aircraft gust response considering aeroelastic deformation," in *Proceedings of the 21st AIAA International Space Planes and Hypersonics Technologies Conference*, Xiamen, China, March 2017.

[14] R. Cavallaro and L. Demasi, "Challenges, ideas, and innovations of joined-wing configurations: a concept from the past, an opportunity for the future," *Progress in Aerospace Sciences*, vol. 87, pp. 1–93, 2016.

[15] C. Zhang, Z. Zhou, X. Zhu, and P. Meng, "Nonlinear static aeroelastic and trim analysis of highly flexible joined-wing aircraft," *AIAA Journal*, vol. 56, no. 12, pp. 4988–4999, 2018.

[16] Z. Sotoudeh, "For challenges in the design of joined wings special session: comparison of aeroelastic stability of conventional and joined-wing highly flexible aircraft," in *Proceedings of the 56th AIAA/ASCE/AHS/ASC Structures, Structural Dynamics, and Materials Conference*, Kissimmee, Florida, January 2015.

[17] D. Luciano, G. Monegato, and R. Cavallaro, "Minimum induced drag theorems for multi-wing systems," in *Proceedings of the 57th AIAA/ASCE/AHS/ASC Structures, Structural Dynamics, and Materials Conference*, San Diego, CA, USA, January 2016.

[18] X. Wu, J. Lei, and J. Wu, "Numerical simulation for aerodynamic characteristics of diamond back wing," *Acta Armamentarii*, vol. 31, no. 8, pp. 1048–1052, 2010, (in Chinese).

[19] T. Han and X. Lian, "Design of improved diamond wing in glide bomb," *Journal of Projectiles, Rockets, Missiles and Guidance*, vol. 30, no. 2, pp. 190–194, 2010, (in Chinese).

[20] L. Demasi, E. Santarpia, A. Dipace, R. Cavallaro, and R. E. Gordnier, "Aerodynamic and structural studies of a flapping wing in forward flight," *AIAA Journal*, vol. 54, no. No. 9, pp. 2768–2781, 2016.

[21] N. Teunisse, P. Tiso, L. Demasi, and R. Cavallaro, "Reduced order methods for structurally nonlinear joined wings," in *AIAA SciTech >56th AIAA/ASCE/AHS/ASC Structures, Structural Dynamics, and Materials Conference*, Kissimmee, FL, USA, January 2015.

[22] L. Demasi, R. Cavallaro, and F. Bertuccelli, "Post-critical analysis of highly deformable joined wings: the concept of snap-divergence as a characterization of the instability," *Journal of Fluids and Structures*, vol. 54, pp. 701–718, 2015.

[23] Z. Xu, J. Wu, and X. Xue, "Structural optimization of the diamond back wing of cruise missile," *Machine Design & Research*, vol. 27, no. 1, pp. 87–90, 2010, (in Chinese).

[24] J. Zhang, "Study on the interpolation method to calculate the aircraft wing aerodynamic press distribution on FEM nodes," *Aeronautical Science & Technology*, vol. 28, no. 12, pp. 14–18, 2017, (in Chinese).

[25] F. R. Menter, R. B. Langtry, S. R. Likki, Y. B. Suzen, P. G. Huang, and S. Volker, "A correlation-based transition model using local variables part ii-test cases and industrial applications," in *Proceedings of the ASME Turbo Expo 2004: Power for Land, Sea, and Air*, Vienna, Austria, June 2004.

[26] M. E. Biancolini, U. Cella, C. Groth et al., "Static aeroelastic analysis of an aircraft wind-tunnel model by means of modal RBF mesh updating," *Journal of Aerospace Engineering*, vol. 29, no. 6, p. 14, Article ID 04016061, 2016.

[27] W. Liu, C. Huang, and G. Yang, "Time efficient aeroelastic simulations based on radial basis functions," *Journal of Computational Physics*, vol. 330, pp. 810–827, 2017.

[28] H. Guo, D. Chen, and C. Zhang, "Numerical applications on transonic static areoelasticity based on CFD/CSD method," *Acta Aerodynamica Sinica*, vol. 36, no. 1, pp. 12–16, 2018, (in Chinese).

[29] H. Guo, G. Li, D. Chen, and B. Lu, "Numerical simulation research on the transonic aeroelasticity of a high-aspect-ratio wing," *International Journal of Heat and Technology*, vol. 33, no. 4, pp. 173–180, 2015.

[30] P. Guo and J. Xie, "Two-dimensional CFD modeling of hysteresis behavior of MR dampers," *Shock and Vibration*, vol. 2019, Article ID 9383047, 14 pages, 2019.

[31] J. Zornl and R. L. Davis, "3D aeroelastic simulation of flow over a solid airfoil," in *Proceedings of the 2018 Applied Aerodynamics Conference*, Atlanta, GA, USA, June 2018.

[32] V. Joshi, R. Jaiman, G. Li, K. Breuer, and S. Swartz, "Full-scale aeroelastic simulations of hovering bat flight," in *Proceedings of the AIAA Scitech 2020 Forum*, Orlando, FL, USA, January 2020.

[33] X. Wang, Z. Wan, and C. Yang, "A method of static aeroelastic analysis based on three dimension aerodynamic force and aeroelastic correction for hypersonic vehicles," in *Proceedings of the 55th AIAA Aerospace Sciences Meeting*, Grapevine, TX, USA, January 2017.

Hindawi
Shock and Vibration
Volume 2021, Article ID 5588056, 11 pages
https://doi.org/10.1155/2021/5588056

Research Article

Study on Flow Mechanism of a Morphing Supercritical Airfoil

Yuanjing Wang, Binbin Lv, Pengxuan Lei, Wenkui Shi, and Yu Yan

High Speed Aerodynamics Institute, China Aerodynamics Research and Development Center, Mianyang 621000, China

Correspondence should be addressed to Binbin Lv; lbin@cardc.cc

Received 7 January 2021; Revised 18 March 2021; Accepted 8 April 2021; Published 20 April 2021

Academic Editor: Zeqi Lu

In order to maintain the best performance in flight, a new concept, morphing aircraft, has been proposed, which can change the real-time aerodynamic characteristics under different flight conditions. The key problem is to figure out the response of strong flow instability caused by structure changes during the morphing. To solve this problem, computational fluid dynamics (CFD) and wind tunnel tests (WTT) were employed. The results show that the deformation of thickness and camber angle of the airfoil will significantly change the distribution of pressure and result in obvious hysteresis loops of lift and drag. With the increase of deformation frequency and amplitude, the instability increases correspondingly. Moreover, the unsteady effect caused by camber deformation is much stronger than that caused by thickness deformation. In addition, the flow structures on the airfoil, such as the shock strength and boundary separation location, have a delay in response to structure changes. Therefore, there will be a hysteresis between airfoil deformation and aerodynamic characteristics, which means strong flow instability.

1. Introduction

With the development of technology and science, more and more attentions have been paid to the quality and performance of aircrafts [1–3]. Nowadays, it is expected that changes in flow conditions have been adopted for aircraft configuration in order to maintain the optimal performance throughout the flight. Therefore, morphing airfoil is developed gradually. However, the impact of configuration changes on the flow structure and aircraft performance is not yet understood, which may hinder the progress of the morphing airfoil. Therefore, it is necessary to study the relationship and response law between the flow and configuration deformation.

Research institutes, such as NASA and DAPPA, have conducted long-term research on the related technologies of morphing vehicles [4–6], as well as a lot of research on aerodynamics. In the research of Ajaj et al. [7], the deformation technology was classified to put forward the concept of continuous deformation. Nekoubin and Nobari [8] calculated the deformation of the trailing edge of NACA0012 airfoil under the transonic condition and explained the influence of control parameters. Walker and Patil [9] derived the functions of unsteady lift, drag, and pitch moment and expressed them using the form of Chebyshev polynomials. Gandhi and Anusonti-Inthra [10] investigated the skin structure of variable camber wings. In the study of Adesen et al. [11], a dynamic stall model of variable trailing edge airfoil was derived based on the theory. As for domestic research, the development of morphing technology is later than foreign research. Xu et al. [12] proposed different types of morphing schemes for airfoils. Lv et al. [13, 14] conducted wind tunnel tests to study the aerodynamic characteristics under transonic conditions. Hao and Yang [15] analyzed the influence of camber change on steady-state and unsteady-state aerodynamic characteristics under low Reynolds number. Chen et al. [16] discussed the influence of wing sweep changes on aerodynamic features, as well as its mechanism. At the same time, using analytical and discrete vortex methods proposed by Gao et al. [17, 18], the unsteady aerodynamic characteristics of the morphing airfoil under subsonic/supersonic speed conditions were specifically studied.

The research on morphing technology mainly focuses on the design of intelligence structure [19, 20], but there are few studies on aerodynamic characteristics and flow mechanism

of morphing airfoil. Therefore, through CFD and wind tunnel tests, the influence of supercritical airfoil deformation on aerodynamic characteristics and flow structure has been discussed, and the results will be helpful for smart structure parameter choice and analysis on aerodynamic characteristics morphing airfoils.

2. Research Methods

2.1. Research Topic Introduction

2.1.1. The Issue and the Object. Typical supercritical airfoil designated by RAE2822 was chosen as the research target. Configuration of RAE2822 and its aerodynamic characteristics were plenty and open to researchers.

In this paper, effect of airfoil thickness and camber on its unsteady aerodynamic characteristics was studied by CFD simulation. When CFD was applied, the chord of RAE2822 was designated to 1 unit, based on which the parameters of the flow were obtained, such as the Reynolds number, and unsteady aerodynamic characteristics coefficients.

Only effect of airfoil camber changing through trailing edge deflection driven by a SMA smart structure on surface pressure distribution was measured in wind tunnel. Strictly speaking, this kind of deflection of wind tunnel model was not a real camber due to the difficulty in smart structure designing and wind tunnel experiments simulation. Experiment results could not be compared with those obtained by CFD, which was still helpful to recognize the flow phenomenon during model deformation in the wind tunnel environment. The model was extracted to a 2D wing based on RAE2822 airfoil, wing span and chord length of which were 365 mm and 150 mm, respectively (Figure 1).

2.1.2. Parameters for CFD Simulations. Aerodynamic characteristics of wing were decided by its airfoil parameters, of which airfoil camber and thickness were the most important parameters. Unsteady effect of morphing on aerodynamic characteristics over supercritical airfoil was mainly studied by CFD.

Flow structure and aerodynamic forces under different airfoil camber and thickness were simulated with Mach number ranging from 0.7 to 0.78, Reynolds number ranging from 5×10^6 to 30×10^6, and angles of attack ranging from 0° to 8°.

The variation of real-time airfoil thickness ranged from -15 percent to 20 percent of the basis airfoil thickness, and the angle which was used to measure airfoil camber between the chord trailing edge tangent and the horizontal axis ranged from -5° to 5°. Definition of airfoil thickness and camber would be introduced in Section 2.1.3. Camber and thickness morphing frequency ranged from 0 Hz to 2 Hz when the effect was simulated with CFD.

2.1.3. Contents in Wind Tunnel Experiments. When experiments were conducted in the wind tunnel, Mach number ranged from 0.4 to 0.8, test Reynolds number was kept at 2×10^6 approximately, and angles of attack ranged from 0° to 6°.

SMA material phase transition would result in the problem of slow response of smart structure, which made flow over supercritical airfoil kept in steady state during the trailing edge deflection. Wind tunnel experiments would be used only to recognize the steady flow structure evolution when trailing edge was deflected. Because of the effect of aerodynamic loads brought about by the dynamic pressure of the wind tunnel flow, the trailing edge deflection magnitude could not exceed 10.9°. It is not reasonable to compare wind tunnel experiment results with those obtained by CFD due to the different morphing mode and flow mode.

2.2. Computational Fluid Dynamic Method

2.2.1. CFD Methods. N-S equation based on finite volume was applied:

$$\iiint_{\Omega} \frac{\partial W}{\partial t} \, dV + \oiint_{\partial\Omega} H \cdot \vec{n} \, dS = 0. \quad (1)$$

The convective item was discretized with central scheme and the viscous item was discretized with ROE scheme. The time discretization of the unsteady-state calculation is carried out on the basis of the dual time step. When the maximum error of the basis variable quantity was less than 0.00001, the iteration was considered to be converged. At the same time, endless loop was avoided by designating inner time step. In addition, ideal-gas far field conditions were used as boundary conditions. The wall was adiabatic and nonslip. S-A turbulence model was applied.

2.2.2. Grid and Validation. C grid containing 941×144 grid nodes is used (Figure 2). In order to avoid the negative volume caused by chaotic deformation of large aspect ratio, the mesh field is divided into two parts, and only grid deformation is allowed. Since Reynolds number effect is not our main purpose, only characteristics are considered under full turbulence. $y+$ and the height of the first layer grid are 2 and 0.00002664, respectively.

The effectiveness of the steady method is verified according to Case 9 in the research of Zhang and Zhang [21], and the parameters are shown in Table 1. The comparison between the results of Case 9 and present study is shown in Table 2. The results are consistent with Case 9, showing that the steady method applied for the study was effective.

The effectiveness of the unsteady method is verified according to AGARD CT1 case [21], and the parameters are shown in Table 3.

The comparison of unsteady method with CT1 case is shown in Figure 3. It can be seen that dual time step discretization was qualified for unsteady computation; and the consistency of both results was well.

2.2.3. Timestep Determination. Lift coefficient under different timestep is shown in Figure 4. As can be seen, results of C_L coefficient were converged when real-time step size

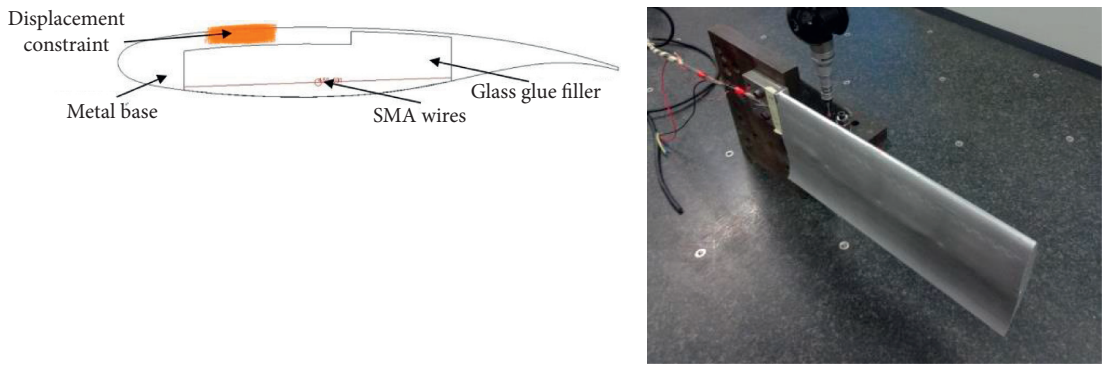

Figure 1: Sketch of the model.

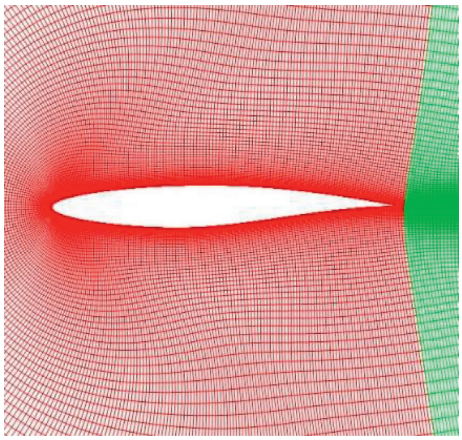

Figure 2: Grid of calculation field.

Table 1: Steady computational condition.

Flow condition	Mach number	Angles of attack (°)	Reynolds number
Case 9	0.734	2.79	1.0656×10^7

Table 2: Steady results of Case 9 and the present study.

	CL	Cd
EXP_Case 9	0.803	0.0168
Present study	0.804	0.0197

was larger than 1000. Therefore, inner iteration step size and the real time step size were assigned as 50 and 1000, respectively.

2.2.4. Definition of Airfoil Thickness and Camber Changes in CFD Simulation. The change of airfoil thickness is obtained by increasing the coordinates of all the original airfoil control points on average. Then, the coordinate equation of the control points is recommended:

$$Y = Y_{\text{init}} \times [1 + A \cdot \sin(2\pi f t)], \quad (2)$$

where Y_{init} is the initial coordinate of the airfoil control point, f is the deformation frequency of the airfoil thickness, and A is the relative amplitude of the thickness change, as shown in Figure 5.

It is difficult to express airfoil centerline equation algebraically. So, the airfoil chord was defined as a parabola to describe the camber. In order to keep the thickness constant during the camber change, the equation of camber changes is given as follows:

$$\begin{aligned} P &= A \cdot \sin(2\pi f t), \\ \Delta y &= -4Px^2 + 4Px, \end{aligned} \quad (3)$$

where P is the vertex instantaneous coordinate and Δy is the increase of the longitudinal coordinates of the surface control points. For convenience, the angle (θ) between the tangent of deformed chord at the trailing vertex and abscissa was used to measure chord camber changing. The camber change is shown in Figure 6.

2.3. Wind Tunnel Test

2.3.1. Facility. The test was conducted in a transonic wind with a Mach number ranging from 0.4 to 3.5. It is a semireturn wind transient wind tunnel with a cross-sectional dimension of 0.6×0.6 m. The upper and lower walls of this section are slotted, and the side walls are solid with rectangular optical windows and suitable for camera shooting.

2.3.2. Smart Actuator Structures. To understand the flow mechanism on morphing airfoils, a typical 2D supercritical airfoil test model was designed. The cantilever flexible flexure structure was applied to drive the trailing edge flexure. The structure is driven by a shape memory alloy (SMA) actuator, which can deflect the trailing edge by 10.9°. The cavity on the lower surface of the model was filled with glass glue to maintain the smoothness of the lower surface. In Figure 7, the SMA actuator model is recommended.

2.3.3. Test Technology. Since the lower surface was filled with glass glue, it is difficult to fix the pressure orifice. Therefore,

Table 3: Unsteady computational condition.

Flow condition	Mach number	Angles of attack (°)	Frequency reduction
CT1	0.6	2.89 + 2.41sin(w∗t)	0.0808

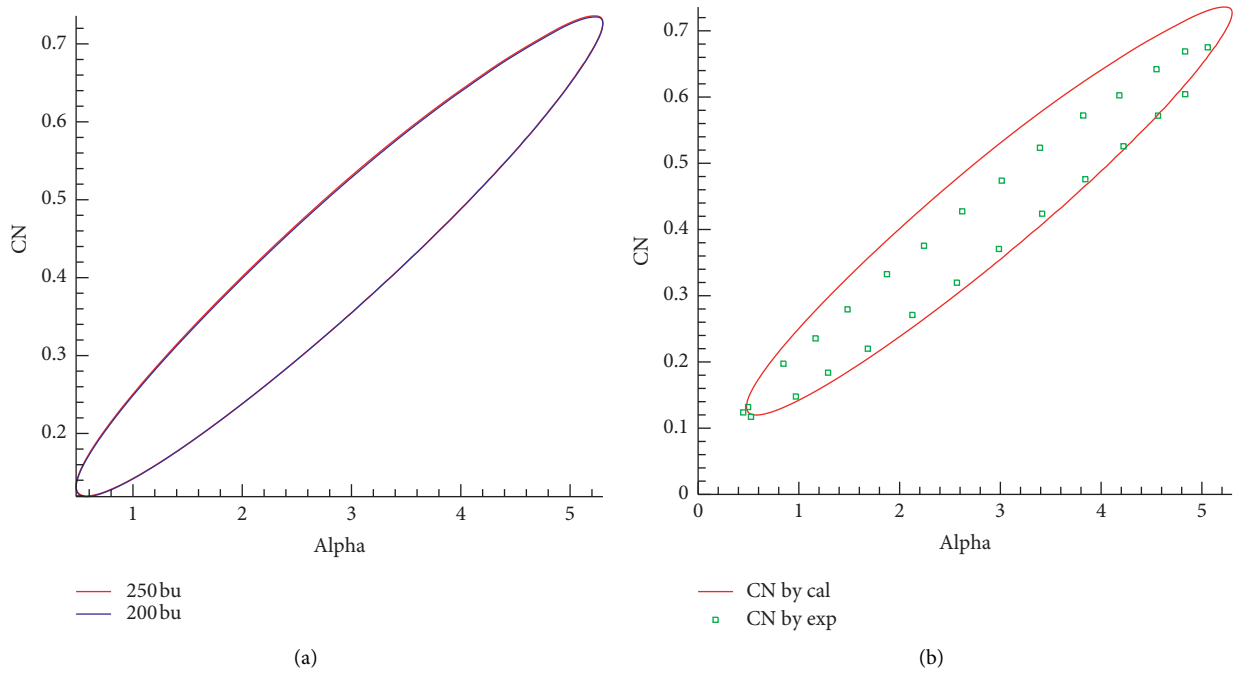

Figure 3: Numerical method and result compared with CT1 case.

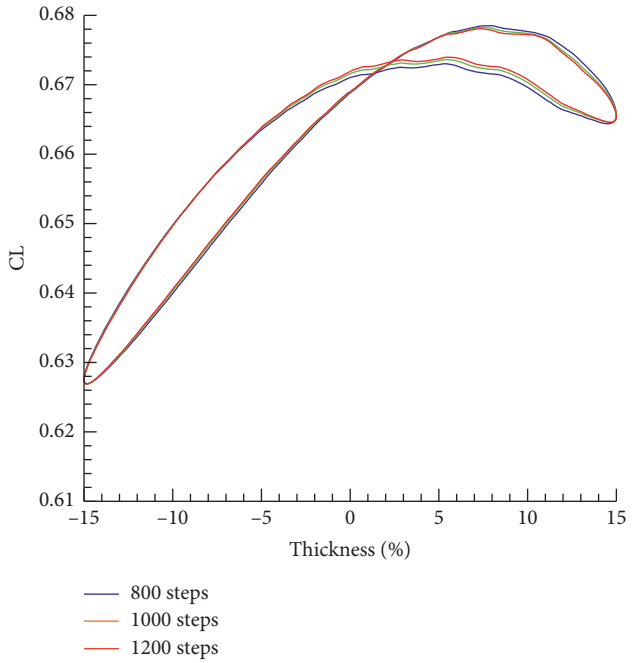

Figure 4: Comparison of C_L in different time step sizes ($M = 0.74$, $\alpha = 2^\circ$, and $F = 1$ Hz).

PSP technology was used to obtain the model surface pressure distribution under the condition of boundary layer natural transition. Image acquisition was composed of light source, camera, and control software. The excitation light source was a kind of LED cold light source with 12 W output power. The camera type was PCO.1600. In order to fix the deflection angle of the trailing edge, deformation measurement technology (VMD) was applied. In Figure 8, the position of the model in the test section is presented.

3. Results and Analysis

3.1. Influence of Thickness Deformation on Aerodynamic Characteristics. Figure 9 shows the influence of three thickness amplitudes (10%, 15%, and 20%) on the aerodynamic characteristics. It suggests that, with the increase of the deformation amplitude, the hysteresis phenomenon becomes more obvious, which is caused by the pressure and vorticity difference at the same position during the thickness deformation process (Figure 10). The area of the hysteresis loop formed by the lift coefficient can be understood as the work required by the external force during the deformation of airfoil. The greater the area, the greater the power required [22].

The influence of thickness deformation frequency is shown in Figure 11. The higher the deformation frequency, the greater the lift/drag force generated by the rate of change of the velocity potential over time. Within a certain range of frequency and amplitude, the difference between lift and drag is close to 0.015 and 0.0019, respectively, when the trailing edge passes through the same position of reciprocating motion.

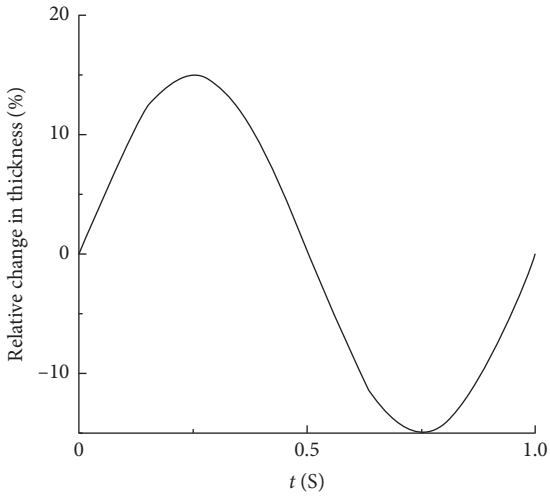

Figure 5: Relative change in thickness over time.

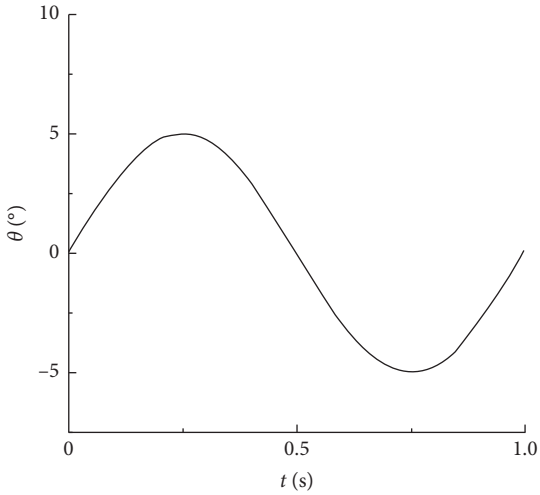

Figure 6: Camber changes over time.

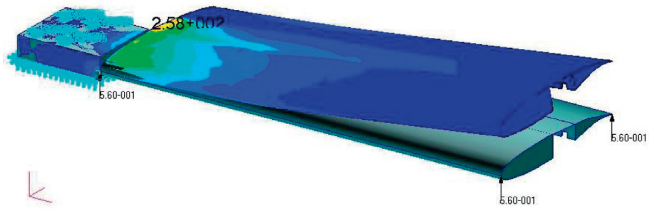

(a)

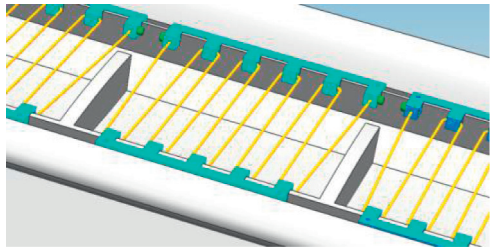

(b)

Figure 7: SMA actuator structure.

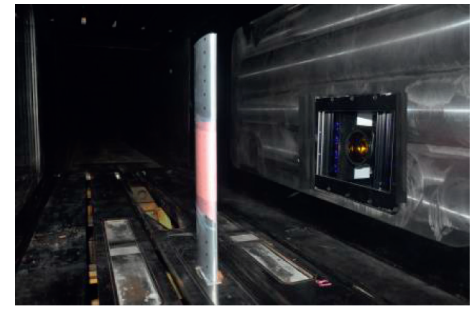

Figure 8: Model position in the test section.

3.2. Influence of Camber Deformation on Aerodynamic Characteristics. Figure 12 shows the influence of the extent of camber deformation on aerodynamics. It indicates that the larger the deformation, the stronger the unsteady-state effect and the larger the area of the hysteresis loop.

Figure 13 indicates that the higher the deformation frequency, the larger the area of the hysteresis loop, and the additional unsteady lift caused by the ratio of the velocity potential over time will also be greater.

When the angle of attack was increased to 6°, the same effect would be found as $\alpha = 2^{\circ}$. But, as can be seen in Figure 14, camber deformation would have less effect on aerodynamic characteristics at $\alpha = 6^{\circ}$ than at $\alpha = 2^{\circ}$; and the hysteresis characteristics of lift/drag force curves were not as regular at $\alpha = 6^{\circ}$ as at $\alpha = 2^{\circ}$. This resulted from the obvious shock wave and its induced boundary layer separation. As can be seen in Figure 15, strong separation happened, and position of flow separation moved forward when camber changing magnification angle θ was -3° again. We could obtain that flow structures were very different at the same position but different time. That was the unsteady flow that led to the hysteresis characteristics of lift/drag forces during morphing.

The above results show that the airfoil thickness and camber deformation will cause obvious instability, and the aerodynamic coefficient has obvious hysteresis characteristics. Moreover, the greater the amplitude of the airfoil parameter deformation and the higher the frequency, the stronger the flow instability. By comparing it with thickness deformation, the change of the camber angle will cause more severe instability, which will lead to greater additional instability. For example, the difference between lift and drag is close to 0.117 and 0.0034, respectively, which indicates that the instability of vehicle deformation should not be ignored.

3.3. Mechanism of Unsteady Flow during Airfoil Deformation. The effect of deformation on the surface pressure distribution is shown in Figure 12, which indicates that when the trailing edge returns to pass through the same position, the shock wave moves to the airfoil nose and its strength is weakened. This is caused by the hysteresis and strength of the shock wave position relative to geometric deformation. This phenomenon can also be observed in the PSP wind tunnel test results (Figure 16). It can be seen that, with the deflection of the trailing edge, the shock wave has been strengthened and pushed back. The flow near the center of

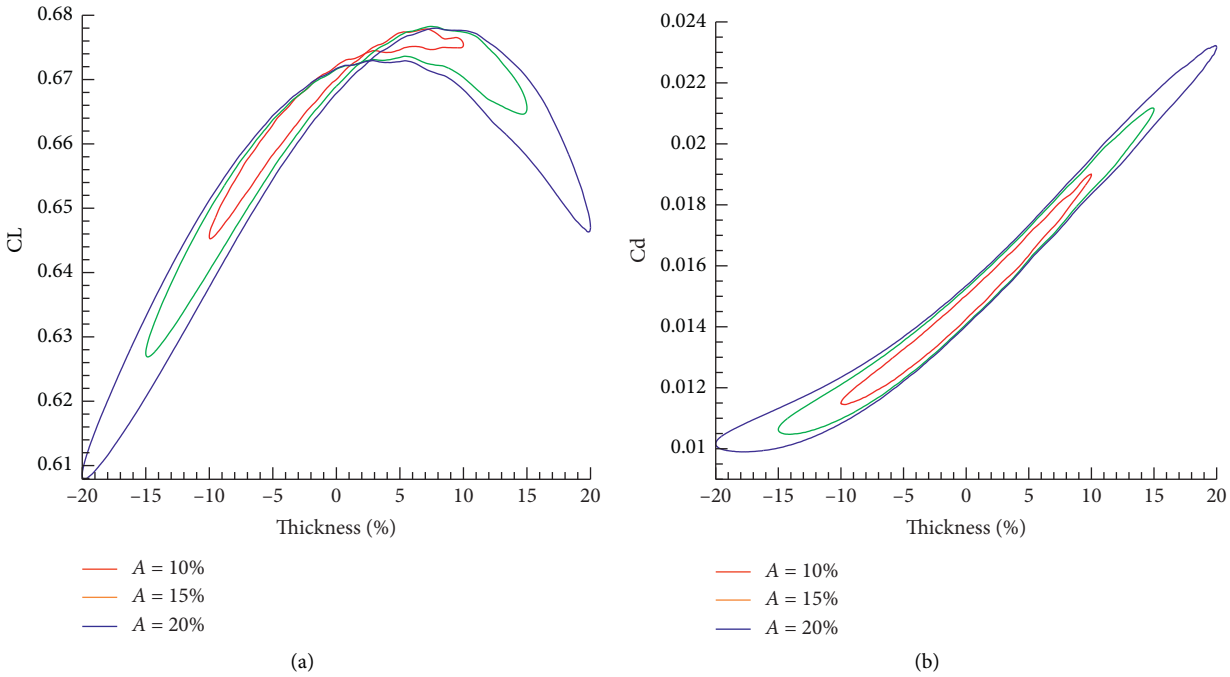

Figure 9: Influence of thickness deformation amplitude on aerodynamics ($M = 0.74$, $\alpha = 2^{\circ}$, and $f = 1$ HZ, CFD).

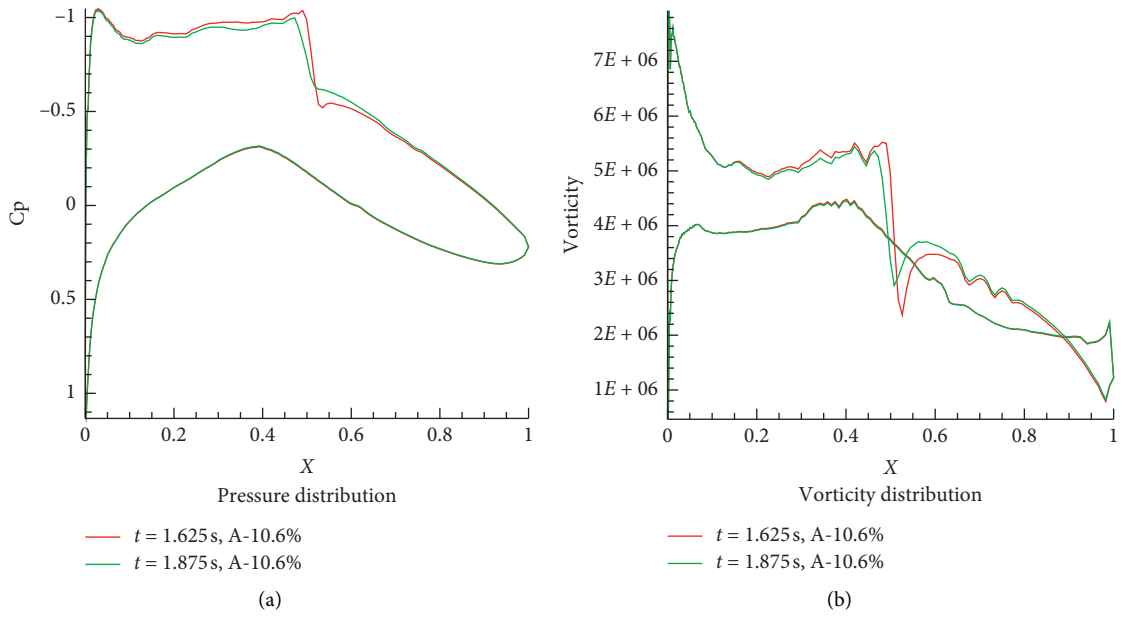

Figure 10: Pressure and vortex distribution at the same thickness (−10.6%) in one cycle ($M = 0.74$ and $\alpha = 2^{\circ}$, CFD). (a) Pressure distribution. (b) Vorticity distribution.

rotation accelerates again and shows a tendency to form a second shock wave.

The influence of deformation on the surface pressure distribution is shown in Figure 12, which indicates that when the trailing edge returns to pass through the same position, the shock wave moves to the airfoil nose and its strength is weakened. This is caused by the hysteresis and strength of the shock wave position relative to geometry deformation. This phenomenon can also be observed from PSP wind tunnel test results (Figure 17). It can be seen that, with the deflection of the trailing edge, the shock wave has been strengthened and pushed back. The flow near the center of rotation center accelerates again and shows a tendency to form the second shock wave.

Figure 18 shows how the amplitude and frequency of airfoil camber deformation affect the surface pressure distribution. The graph shows that larger amplitude and higher frequency will cause larger changes in pressure distribution.

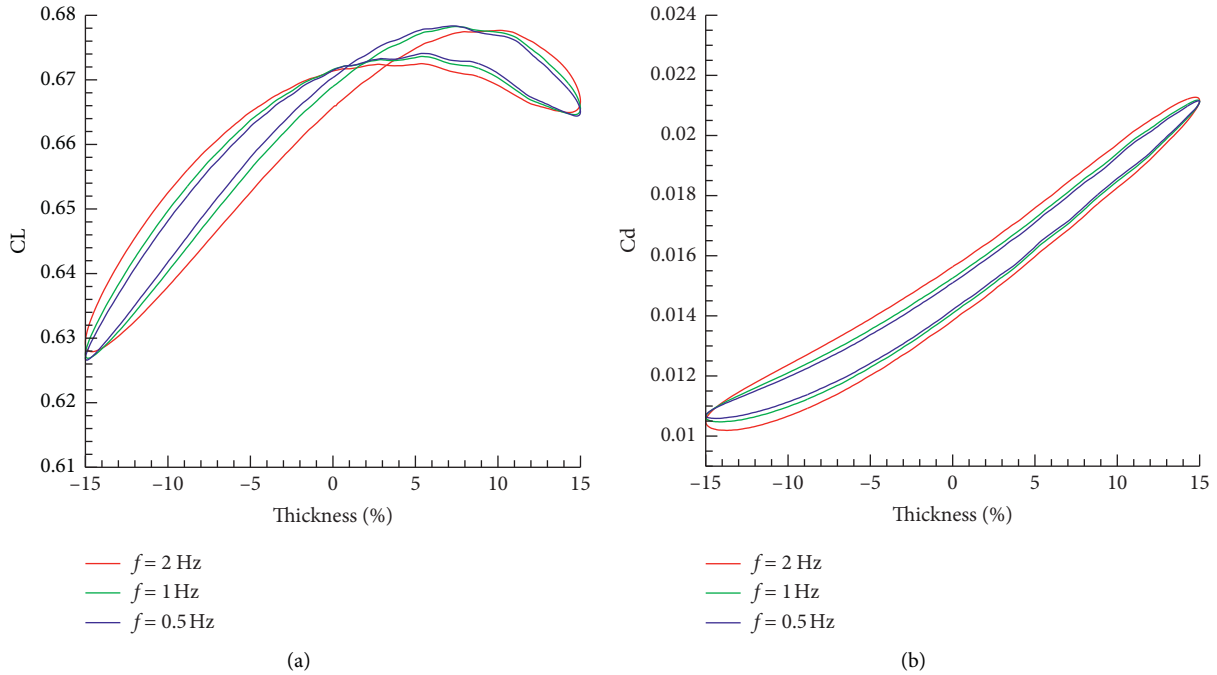

Figure 11: Influence of thickness deformation frequency on aerodynamics ($M = 0.74$ and $\alpha = 2^{\circ}$, CFD).

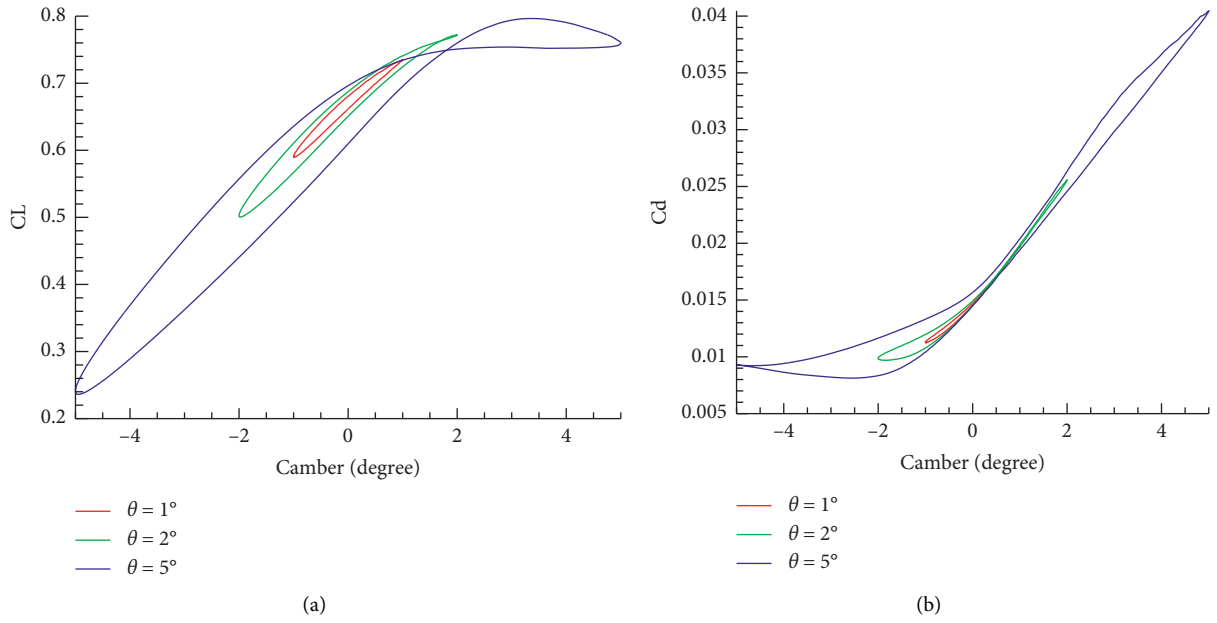

Figure 12: Influence of the extent of camber deformation on aerodynamics ($M = 0.74$, $\alpha = 2^{\circ}$, and $f = 1$ HZ, CFD).

For instance, such change can significantly enhance the shock wave and move the shock wave to the end of the airfoil, resulting in the increased unstable additional lift.

The results show that the unsteady flow effect in the wing morphing process is caused by flow separation, boundary layer transition, shock wave oscillation, and so forth. In the research of Yang [23], the author believes that the aerodynamics of an unsteady morphing airfoil can be represented by a constant item and a stable item. The additional unstable item is shown as

$$F_x - iF_y = -i\oint_{l_b} \rho\left[c\mathrm{d}\overline{z} - \frac{\partial \overline{x}}{\partial t}\mathrm{d}\overline{z} - \frac{1}{2}\cdot\left(\frac{\partial x}{\partial z}\right)^2 \mathrm{d}z\right]. \quad (4)$$

In the process of airfoil deformation, the rate of velocity potential change will cause virtual mass force, which may lead to unstable additional force. Because the velocity change rate of the airfoil parameters is different, the unstable additional force/moment is also different, thus forming a hysteresis loop.

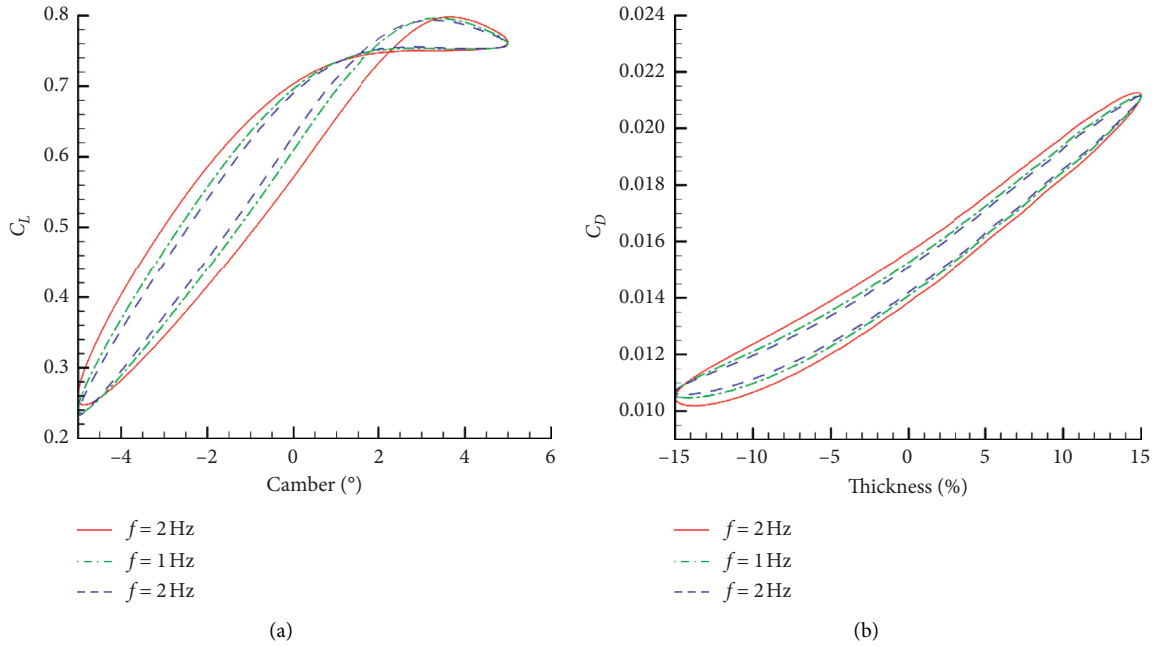

FIGURE 13: Influence of camber deformation frequency on aerodynamics ($M = 0.74$ and $\alpha = 2^{\circ}$, CFD).

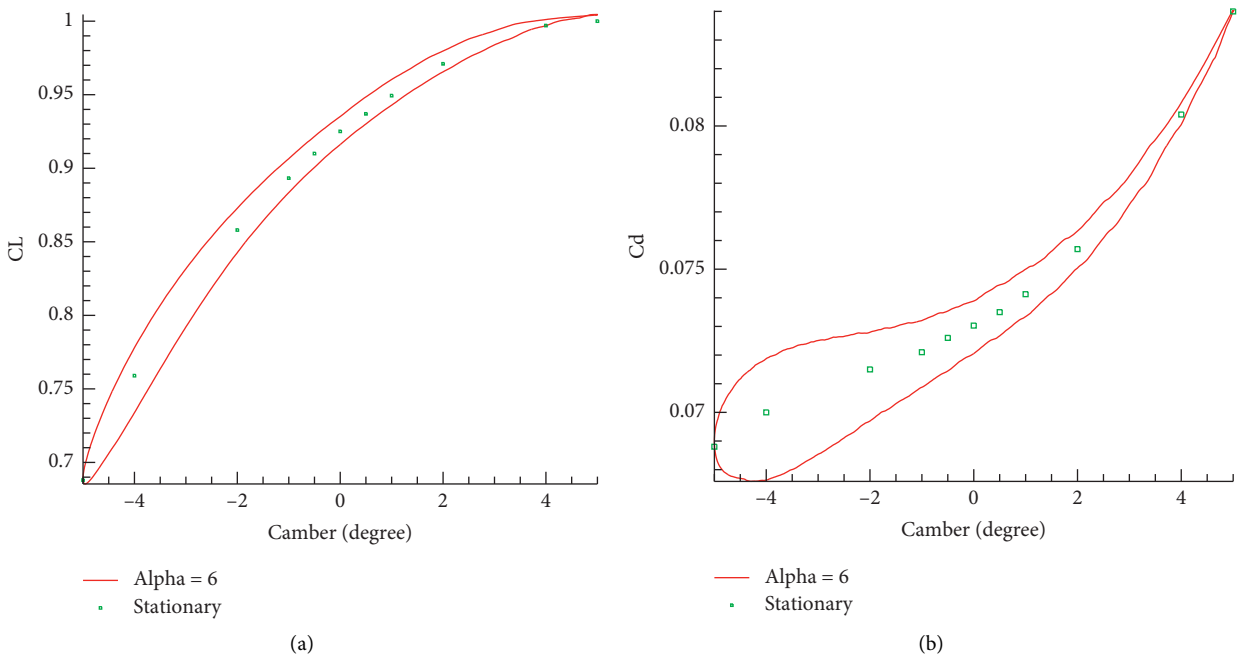

FIGURE 14: Influence of camber changing on aerodynamics ($M = 0.74$, $\alpha = 6^{\circ}$, and $f = 1$ Hz, CFD).

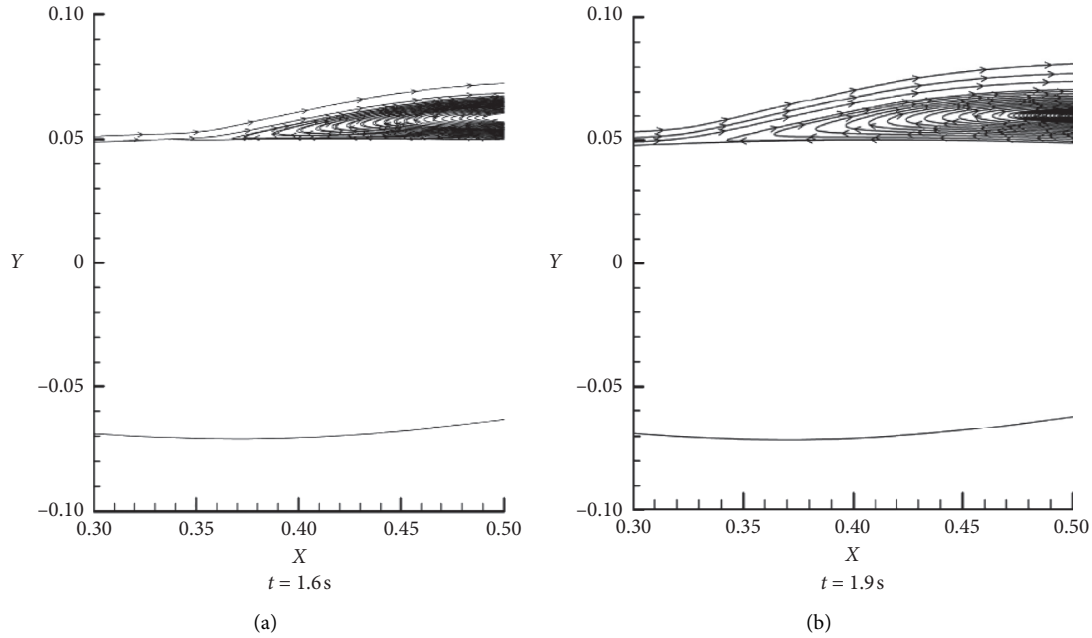

Figure 15: Streamline over leeward flow field of the airfoil at the same camber (−3°) in one cycle ($M = 0.74$, $\alpha = 6°$, and $f = 1$ Hz, CFD).

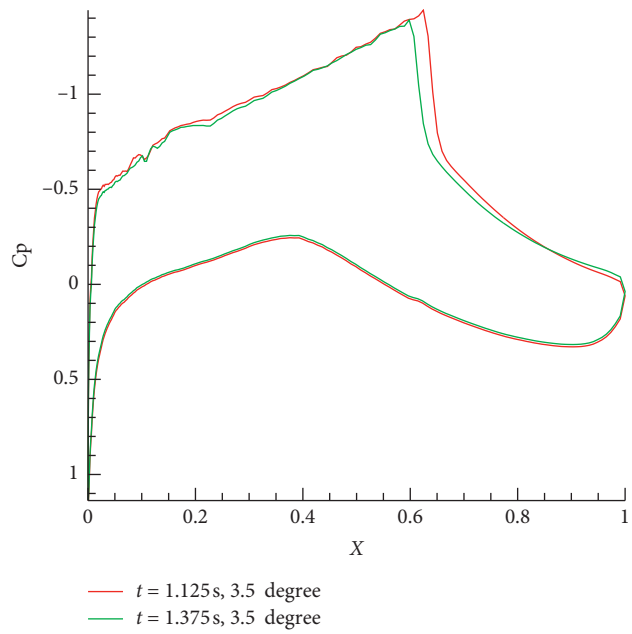

Figure 16: Pressure distribution passing through the same camber position in one cycle ($M = 0.74$, $\alpha = 2°$, and $\theta = 3.5°$, CFD).

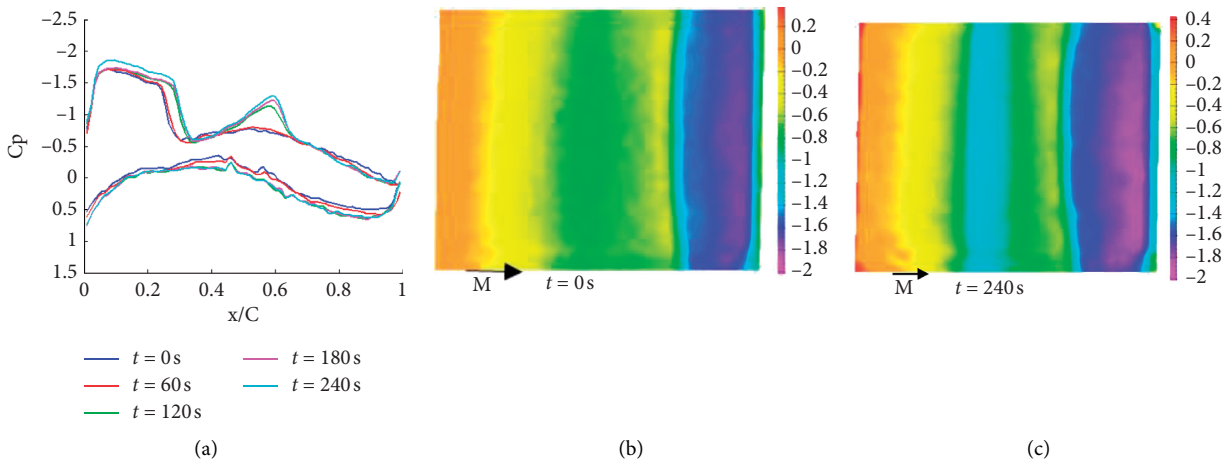

Figure 17: Wind tunnel test results (PSP, $M = 0.7$ and $\alpha = 6^{\circ}$, test).

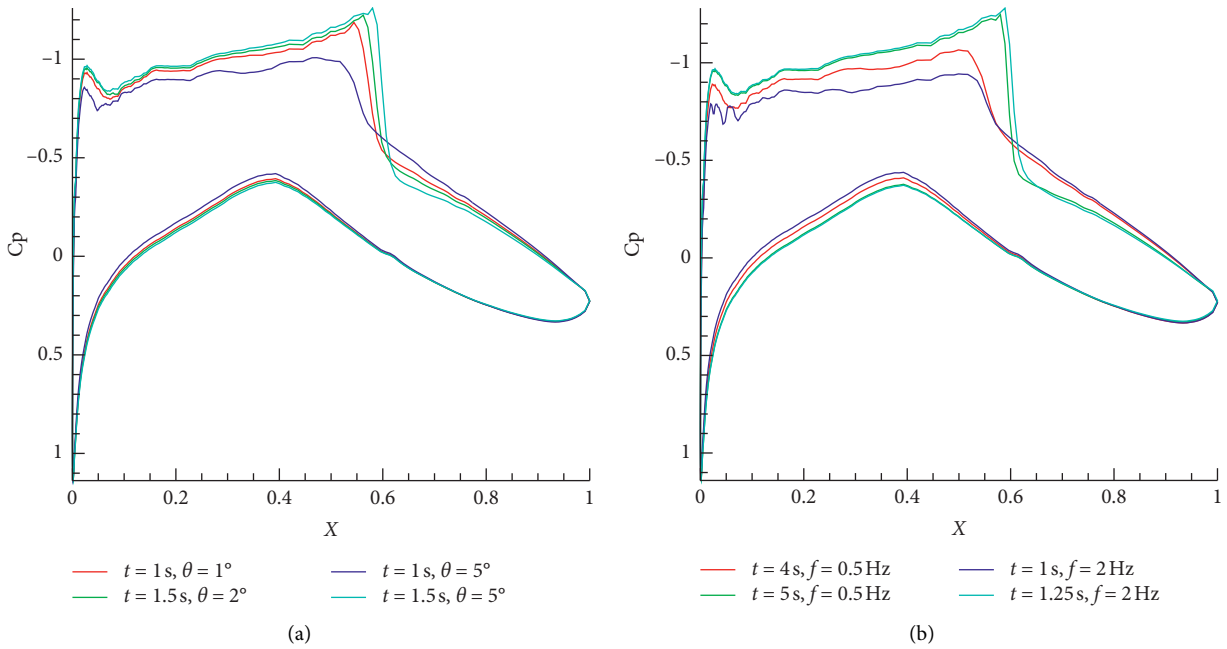

Figure 18: Influence of camber deformation on pressure distribution (CFD).

4. Conclusions

In this study, the influence of the thickness and camber deformation of the supercritical airfoil on flow instability and its mechanism was studied. The conclusions can be drawn as follows:

(1) Flow instability will occur with the change of airfoil thickness and camber angle, and it exhibits obvious hysteresis on the aerodynamics forces of the hysteresis loop. Therefore, in the design of morphing aircrafts, full attention must be paid to the unsteady aerodynamic characteristics of deformation.

(2) Larger morphing amplitude and higher morphing frequency will lead to stronger flow hysteresis and unstable effects. Compared with the influence of airfoil thickness deformation, the instability caused by airfoil camber deformation is more significant, which cannot be ignored.

(3) The flow instability originates from the response of the position and intensity of shock wave and the boundary separation characteristics to geometric deformation. It may result in obvious additional aerodynamic forces.

Data Availability

The data were measured in the wind tunnels at High Speed Aerodynamics Institute, China Aerodynamics Research and Development Center.

Conflicts of Interest

The authors declare that they have no conflicts of interest.

References

[1] M. Secanell, A. Suleman, and P. Gamboa, "Design of a morphing airfoil for a light unmanned aerial vehicle using high-fidelity aerodynamics shape optimization," in *Proceedings of the 46th AIAA/ASME/ASCE/AHS/ASC Structures, Structural Dynamics and Materials Conference*, Austin, TX, USA, April 2005.

[2] E. J. Cui, B. Peng, and J. M. Yang, "Development road of smart morphing aircraft," *Aeronautical Manufacturing Technology*, vol. 8, pp. 38–41, 2007.

[3] Z.-Q. Lu, K.-K. Zhang, H. Ding, and L.-Q. Chen, "Internal resonance and stress distribution of pipes conveying fluid in supercritical regime," *International Journal of Mechanical Sciences*, vol. 186, Article ID 105900, 2020.

[4] J. Florance, G. Fleming, A. Burner et al., "Contributions of the NASA langley research center to the DARPA/AFRL/NASA/ northrop grumman smart wing program," in *Proceedings of the 44th AIAA/ASME/ASCE/AHS/ASC Structures, Structural Dynamics, and Materials Conference*, Norfolk, VA, USA, April 2003.

[5] Z.-Q. Lu, D.-H. Gu, H. Ding, W. Lacarbonara, and L.-Q. Chen, "Nonlinear vibration isolation via a circular ring," *Mechanical Systems and Signal Processing*, vol. 136, Article ID 106490, 2020.

[6] J. N. Kudva, "Overview of the DARPA smart wing project," *Journal of Intelligent Material Systems and Structures*, vol. 15, no. 4, pp. 261–267, 2004.

[7] R. M. Ajaj, C. S. Beaverstock, and M. I. Friswell, "Morphing aircraft: the need for a new design philosophy," *Aerospace Science and Technology*, vol. 49, pp. 154–166, 2016.

[8] N. Nekoubin and M. R. H. Nobari, "Numerical investigation of transonic flow over deformable airfoil with plunging motion," *Applied Mathematics and Mechanics*, vol. 37, no. 1, pp. 75–96, 2016.

[9] W. P. Walker and M. J. Patil, "Unsteady aerodynamics of deformable thin airfoils," *Journal of Aircraft*, vol. 51, no. 6, pp. 1673–1680, 2014.

[10] F. Gandhi and P. Anusonti-Inthra, "Skin design studies for variable camber morphing airfoils," *Smart Materials and Structures*, vol. 17, no. 1, Article ID 015025, 2008.

[11] P. B. Andersen, M. Gaunaa, C. Bak et al., "A dynamic stall model for airfoils with deformable trailing edges," *Journal of Physics: Conference Series*, vol. 75, no. 1, Article ID 012028, 2007.

[12] G. W. Xu, B. Peng, and S. Wen, "Primary research of morphing scheme over 2D airfoil," *Chinese Quarterly of Mechanics*, vol. 4, pp. 570–576, 2011.

[13] B. B. Lv, P. X. Lei, Y. J. Wang et al., "Research on the aerodynamic characteristics of morphing super-critical airfoil airfoil," *Asia-Pacific International Symposium on Aerospace Technology*, pp. 828–835, Springer, Singapore, 2018.

[14] W. K. Shi, Y. J. Wang, and Z. Zhang, "Unsteady aerodynamic characteristics of deformable supercritical airfoil," *Acta Aerodynamic Sinica*, vol. 35, no. 2, pp. 192–197, 2017.

[15] N. S. Hao and W. C. Yang, "Experimental study of unsteady aerodynamic characteristics of variable camber wing at low reynolds number," *Journal of Experimental Mechanics*, vol. 3, pp. 294–301, 2014.

[16] Q. Chen, B. Peng, and L. Feng, "Morphing aircraft wing variable sweep: two practical methods and their aerodynamic characteristics," *Acta Aero-Dynamical Sinia*, vol. 30, no. 5, pp. 658–663, 2012.

[17] Y. F. Gao, Z. Liu, and X. Wang, "Study on the supersonic unsteady aerodynamic force for the morphing airfoil," *Acta Aero-Dynamical Sinia*, vol. 685, pp. 69–76, 2014.

[18] Y. F. Gao, X. Wang, and Z. Liu, "Study on the subsonic unsteady aerodynamic force for the morphing Joukowski airfoil," *Chinese Quarterly of Mechanics*, vol. 11, pp. 1–9, 2012.

[19] Z.-Q. Lu, D. Wu, H. Ding, and L.-Q. Chen, "Vibration isolation and energy harvesting integrated in a Stewart platform with high static and low dynamic stiffness," *Applied Mathematical Modelling*, vol. 89, pp. 249–267, 2021.

[20] Z.-Q. Lu, K.-K. Zhang, H. Ding, and L.-Q. Chen, "Nonlinear vibration effects on the fatigue life of fluid-conveying pipes composed of axially functionally graded materials," *Nonlinear Dynamics*, vol. 100, no. 2, pp. 1091–1104, 2020.

[21] Y. F. Zhang and X. L. Zhang, "Credibility analysis of RAE 2822 airfoil transonic flow computation," *Aeronautical Computing Technique*, vol. 39, no. 4, pp. 68–70, 2009.

[22] Y. F. Gao, *Study on the Unsteady Aerodynamics Characteristics for the Morphing Airfoil*, University of Science and Technology of China, Hefei, China, 2012.

[23] W. C. Yang, *Experimental Investigation on the Flow Separation Behaviours of a Variable Camber Wing*, University of Science and Technology of China, Hefei, China, 2012.

Hindawi
Shock and Vibration
Volume 2021, Article ID 6690192, 11 pages
https://doi.org/10.1155/2021/6690192

Research Article

Benefit of Relaxation-Type Damping on the Performance of a Six-Degree-of-Freedom Microvibration Isolation Device for Control Moment Gyroscope

Xingtian Liu, Changbao Shao, Liping Zhou, and Xiangsen Kong

Laboratory of Space Mechanical and Thermal Integrative Technology, Shanghai Institute of Satellite Engineering, Shanghai 201109, China

Correspondence should be addressed to Xingtian Liu; xtliu509@126.com

Received 8 October 2020; Revised 14 February 2021; Accepted 11 March 2021; Published 8 April 2021

Academic Editor: Zeqi Lu

In order to provide an ultraquiet environment for spacecraft payload, a six-degree-of-freedom microvibration isolation device for satellite control moment gyro (CMG) is proposed in this paper. The dynamic characteristics of the microvibration isolation device are analyzed theoretically and experimentally. The dynamic equations of the microvibration suppression device are established by using the Newton–Euler method. The dynamic responses are numerically solved and the frequency-domain characteristics of the microvibration isolation device under base excitation are analyzed. The analytical results are first verified numerically, and the two results are in good accordance. The experimental apparatus is built, and the vibration isolation performance is investigated. The acceleration transfer function is measured and the influence of the excitation amplitude on the vibration isolation performance is performed. It is shown that the amplification factor at the vicinity of the resonance frequency is within 10 dB, and the vibration isolation performance is significant at higher frequencies. The vibration attenuation performance at the main frequency of the CMG (100 Hz) is more than 30 dB. The microvibration suppression device can effectively suppress the microvibration generated by CMG during orbital operation.

1. Introduction

Remote sensing or observation of the Earth is one of the most important tasks of satellite. In order to get an ultra-high-resolution image, many disturbances that affect the performance of the sensitive payload need to be controlled on board. The most annoying disturbance that degrades the performance of payload is thermal deflection [1, 2] of satellite structure and microvibration ejected by moving parts such as cryocooler [3–5], flywheel [6, 7], and control moment gyroscope (CMG) [8]. As a matter of fact, CMGs are widely used in fast maneuver satellites because of their significant angular momentum. Nevertheless, the high-speed rotors in CMGs also make them become one of the largest microvibration sources. In a recently published paper [9], the on-orbit microvibration measurement in a remote-sensing satellite shows that flywheel and CMG are the main vibration source.

Therefore, it is urgent to isolate the microvibration generated by flywheel and CMGs in order to provide quiet environment for sensitive payload. Not surprisingly, many microvibration suppression methods including vibration source control and payload isolation [10] are employed to achieve the purpose. For example, the famous Hubble Telescope used the viscous damper developed by Honeywell to isolate flywheel vibration [11]. In Chandra X-ray Observatory [12], the Stewart-type passive vibration isolation device for flywheel is also considered, and the vibration isolation performance of which at the launch phase is also designed and tested. Li et al. [13] conducted research on the microvibration induced by flywheel and the effect on space camera; the experimental results on ground show that the camera can work normally after a vibration isolator is applied to the flywheel. Cobb et al. [14] proposed a passive-active vibration isolation system to protect the optical

payload from the unwanted microvibration on board. Spanos et al. [15] at JPL invented a flexible active vibration isolation and pointing system which was successfully applied in James Webb Space Telescope. Zhang et al. [16, 17] proposed a new method to achieve better image quality of optical payload. In their research, both the control strategy and the passive vibration source isolation are implemented. Li et al. [18] also considered a similar system and the difference of which laying on the vibration isolation system is active. Zhang et al. [19] focuse on the design of internal vibration isolation structures for the CMG to reduce the vibration generated by the imbalance of the rotor. A fully passive two-stage isolation system based on viscoelastic materials has been developed in order to minimize the CMG microvibrations by Kawak [20]. This paper proposed a new type of vibration isolation device to isolate the CMG vibration transmitted to satellite. The device not only can attenuate vibrations at the main frequency of the CMG but also can suppress resonance amplification factor to a considerable low level. Some useful design guidelines and concrete engineering based experimental results can enrich the vibration isolation field for CMGs.

This paper is organized as follows. Firstly, the dynamic model of the proposed vibration isolation device based on a relaxation-type damper is deduced using Euler–Newton method. The dynamic equation is then solved numerically. Secondly, the vibration isolation performances for all six degrees of freedom are analyzed and the coupling features in different directions are discussed. Thirdly, the experimental setup is built, and the vibration isolation performance is evaluated in three translational directions. Some valuable conclusions are drawn in the last section.

2. Dynamic Modeling

2.1. The Microvibration Isolation Device. The Stewart-type structure is used very popularly to get vibration isolation performance in six degrees of freedom [21]. The schematic of the proposed microvibration isolation device for single CMG in this paper is shown in Figure 1, which is also based on a Stewart-type structure. The platform includes upper platform to connect with the CMG and the lower platform to be installed on the satellite. In between, six relaxation-type isolators are configured in a cubic pattern, which provides proper stiffness and damping to isolate the vibration generated by the CMG transmitting to the satellite. Figure 2 shows a simplified representation of the vibration isolation device in which some useful coordinates are defined. The local coordinates on the upper and lower platforms are $Px_py_pz_p$ and $Bx_by_bz_b$, respectively. The global inertial coordinate system is $Gxyz$. The hinges of the upper and lower platforms with the isolator are defined as $P_ix_{pi}y_{pi}z_{pi}$ and $B_ix_{bi}y_{bi}z_{bi}$. $Oxyz$ is the inertial principal axis coordinate system of the CMG.

The following symbols are used to build the dynamic equation of the system. $\mathbf{t}_p$ is the position vector in coordinate $Gxyz$, $\mathbf{p}_i$ is the position vector of the hinge where the upper platform and the isolator connected in coordinate $Px_py_pz_p$, $\mathbf{b}_i$ is the position vector of the hinge where the lower platform and the isolator connected in coordinate $Bx_by_bz_b$, $\mathbf{t}_i$ is the length vector of each isolator between the upper and lower platforms in coordinate $Gxyz$, $\mathbf{R}_0$ is the position vector of the mass center of the CMG with the upper platform in coordinate $Px_py_pz_p$, ω_p and α_p are the angular velocity and angular acceleration of the upper platform, ω_b and α_b are the angular velocity and angular acceleration of the lower platform, $\mathbf{I}_p$ is the inertial matrix of the CMG with upper platform in coordinate $Gxyz$, and $\mathbf{I}_{u0i}$ and $\mathbf{I}_{d0i}$ are the inertial matrix of the upper and lower legs in coordinates $Px_py_pz_p$ and $Bx_by_bz_b$. $\mathbf{r}_{u0i}$ and $\mathbf{r}_{d0i}$ are the position vectors of the upper and lower legs in coordinates $Px_py_pz_p$ and $Bx_by_bz_b$.

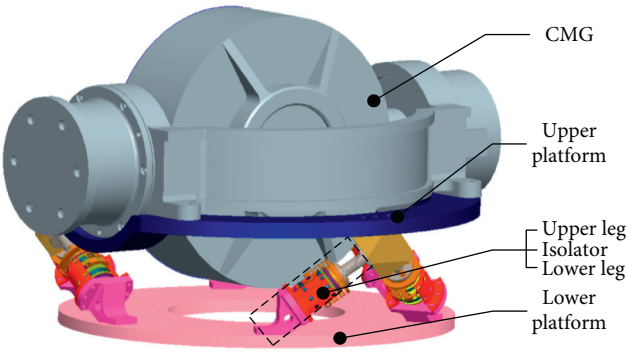

Figure 1: The 3D model of microvibration suppression device.

2.2. Modeling of the Strut and Upper Platform. Different from many researchers who consider the single strut as a Kevin model or an active actuator, the strut used in this paper is a relaxation-type damper. The strut model and the load applied to the strut are shown in Figure 3.

As this vibration isolation device is a Stewart-type platform, the strut is symmetric along the center axis of the upper and lower platforms. The position vector $\mathbf{l}_i$ of the i^{th} strut in coordinate $\{G\}$ can be expressed as

$$\mathbf{l}_i = \mathbf{P}_i - \mathbf{B}_i = \mathbf{t}_{pi} + \mathbf{t}_p - \mathbf{t}_{bi} - \mathbf{t}_b, \tag{1}$$

where $\mathbf{t}_{pi} = \mathbf{R}_p^g \mathbf{p}_i$, $\mathbf{t}_{bi} = \mathbf{R}_b^g \mathbf{b}_i$, $\mathbf{t}_p = [0 \;\; 0 \;\; h]^T$, and $\mathbf{t}_b = [0 \;\; 0 \;\; 0]^T$.

The unit vector for the i^{th} strut is given as

$$\boldsymbol{\tau}_i = \frac{\mathbf{l}_i}{|\mathbf{l}_i|}. \tag{2}$$

The translational velocity and acceleration along the strut for the i^{th} strut are

$$\begin{aligned} \mathbf{l}_i' &= \mathbf{t}_p' + \boldsymbol{\omega}_p \times \mathbf{t}_{pi} = \mathbf{v}_{pi}, \\ \mathbf{l}_i'' &= \mathbf{t}_p'' + \boldsymbol{\alpha}_p \times \mathbf{t}_{pi} + \boldsymbol{\omega}_p \times \left(\boldsymbol{\omega}_p \times \mathbf{t}_{pi}\right) = \mathbf{a}_{p_i} = \mathbf{a}_{p_i} + \mathbf{u}_{1i}, \end{aligned} \tag{3}$$

where $\mathbf{u}_{1i} = \omega_p \times (\omega_p \times \mathbf{t}_{pi})$.

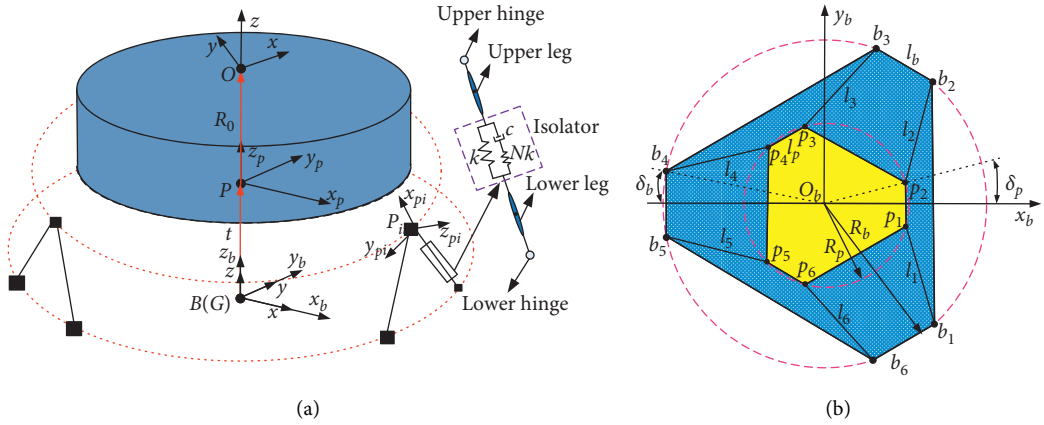

Figure 2: Schematic of the microvibration suppression device. (a) Simplified model. (b) Top view of the model.

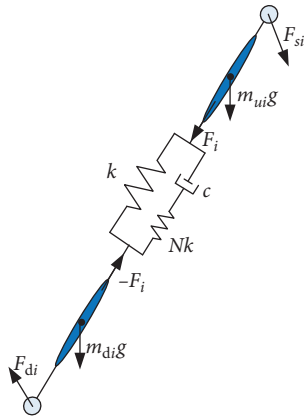

Figure 3: Force analysis diagram of the i^{th} leg.

The acceleration of the mass center of the upper and lower legs can be expressed as

$$\begin{aligned}\mathbf{a}_{ui} &= \left(\mathrm{E}_3 + \frac{1}{l_i}\left(\boldsymbol{\tau}_i^T \mathbf{r}_{ui} - \boldsymbol{\tau}_i \mathbf{r}_{ui}^T\right)\right)\mathbf{a}_{pi} + \mathbf{u}_{4i},\\ \mathbf{a}_{di} &= \frac{1}{l_i}\left(\boldsymbol{\tau}_i^T \mathbf{r}_{di} - \boldsymbol{\tau}_i \mathbf{r}_{di}^T\right)\mathbf{a}_{pi} + \mathbf{u}_{5i},\end{aligned} \tag{4}$$

where $\mathbf{u}_{4i} = \omega_p \times (\omega_p \times \mathbf{t}_{pi}) + \omega_i \times (\omega_i \times \mathbf{r}_{ui}) + \mathbf{u}_{3i} \times \mathbf{r}_{ui}$ and $\mathbf{u}_{5i} = \omega_i \times (\omega_i \times \mathbf{r}_{di}) + \mathbf{u}_{3i} \times \mathbf{r}_{di}$.

Equations of moment of momentum for the upper and lower legs are given as

$$\begin{cases} m_{ui}\mathbf{g} + \mathbf{F}_{si} + \mathbf{F}_i = m_{ui}\mathbf{a}_{ui}, \\ m_{di}\mathbf{g} + \mathbf{F}_{di} - \mathbf{F}_i = m_{di}\mathbf{a}_{di}, \end{cases} \tag{5}$$

$$\begin{cases} -\mathbf{r}_{ui} \times \mathbf{F}_{si} = I_{ui}\boldsymbol{\alpha}_i + \boldsymbol{\omega}_i \times I_{ui}\boldsymbol{\omega}_i, \\ -\mathbf{r}_{di} \times \mathbf{F}_{di} = I_{di}\boldsymbol{\alpha}_i + \boldsymbol{\omega}_i \times I_{di}\boldsymbol{\omega}_i. \end{cases} \tag{6}$$

Equation (6) can be simplified to express the force applied to the upper platform from one single strut, which is

$$\mathbf{F}_{si} = \mathbf{Q}_{pi}\left(\mathbf{t}_p'' - \tilde{t}_{pi}\boldsymbol{\alpha}_p\right) + \mathbf{Q}_{bi}\left(\mathbf{t}_b'' - \tilde{t}_{bi}\boldsymbol{\alpha}_b\right) + \mathbf{V}_i - f_i\boldsymbol{\tau}_i. \tag{7}$$

As shown in Figure 4, the force applied to the upper platform from one single strut is $-\mathbf{F}_{si}$. The gravity of the upper platform and the CMG is $m_0\mathbf{g}$, and the force and moment disturbance generated by the CMG are assumed as $\mathbf{F}_{\text{mac}}$ and $\mathbf{M}_{\text{mac}}$.

By using Newton–Euler method, the dynamic equation for the upper platform is given as

$$\begin{cases} -m_0\mathbf{q}_c'' + m_0\mathbf{g} + \mathbf{R}_p^g\mathbf{R}_o^p\mathbf{F}_{\text{mac}} - \sum_{i=1}^{N}\mathbf{F}_{si} = 0, \\ m_0\mathbf{R} \times \mathbf{g} - m_0\mathbf{R} \times \mathbf{q}_c'' + \mathbf{R}_p^g\mathbf{R}_o^p\mathbf{M}_{\text{mac}} + \mathbf{R}_p^g\mathbf{R}_o^p\mathbf{R} \times \mathbf{F}_{\text{mac}} - \mathbf{I}_p\boldsymbol{\alpha}_p - \boldsymbol{\omega}_p \times \mathbf{I}_p\boldsymbol{\omega}_p - \sum_{i=1}^{N}\mathbf{t}_{pi} \times \mathbf{F}_{si} = 0, \end{cases} \tag{8}$$

where $\mathbf{q}_c''$ is the absolute acceleration of the upper platform in coordinate $\{\mathbf{G}\}$, $\mathbf{R}$ is the position vector of the mass center of the upper platform in coordinate $\{\mathbf{P}\}$, and $\mathbf{I}_p$ is the inertia matrix of the upper platform in coordinate $\{\mathbf{G}\}$.

2.3. Response Solution. The force $\mathbf{F}_i$ applied to the upper platform from each strut can be expressed as

$$\mathbf{F}_i = -k_i(l_i - l_{i0})\boldsymbol{\tau}_i - c_i x_{di}'\boldsymbol{\tau}_i c_i x_d' + N_i k_i x_{di} = N_i k_i (l_i - l_{i0}), \tag{9}$$

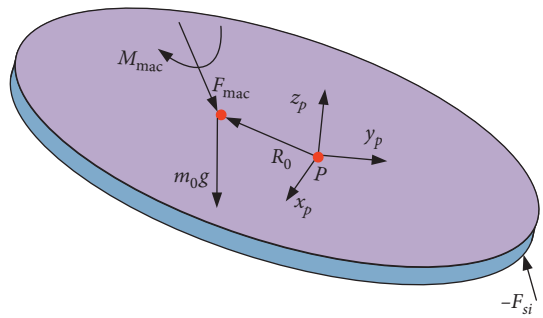

Figure 4: Force analysis diagram for the upper platform.

where x_{di} is the deflection of the joint of the damping and the parallel connected spring in the i^{th} strut.

Applying Laplace transform to equation (9), one can get the simplified equation

$$\mathbf{F}_i = -\frac{\left(N_i k_i^2 + c_i k_i (N_i + 1)s\right)}{\left(N_i k_i + c_i s\right)}\left(\mathbf{J}_{pi}\mathbf{x}_p - \mathbf{J}_{bi}\mathbf{x}_b\right), \tag{10}$$

where $\mathbf{J}_{pi} = \begin{bmatrix} \tau_i \tau_i^T & -\tau_i \tau_i^T \tilde{p}_i \end{bmatrix}$, $\mathbf{J}_{bi} = \begin{bmatrix} \tau_i \tau_i^T & -\tau_i \tau_i^T \tilde{b}_i \end{bmatrix}$, $\mathbf{x}_p = \begin{bmatrix} \mathbf{t}_p^T & \theta_p^T \end{bmatrix}^T$, and $\mathbf{x}_b = \begin{bmatrix} \mathbf{t}_b^T & \theta_b^T \end{bmatrix}^T$.

Combining equations (7)–(9), the dynamic equation of the vibration isolation device subjected to base excitation can be derived asw

$$\left(N_i k_i + c_i s\right)\mathbf{M}_p \mathbf{x}_p'' + \mathbf{C}_p \mathbf{x}_p' + \mathbf{K}_p \mathbf{x}_p = \left(N_i k_i + c_i s\right)\mathbf{M}_b \mathbf{x}_b'' + \mathbf{C}_b \mathbf{x}_b' + \mathbf{K}_b \mathbf{x}_b + \left(N_i k_i + c_i s\right)\mathbf{U}, \tag{11}$$

where

$$\mathbf{M}_p = \begin{bmatrix} m_0 \mathbf{E}_3 & -m_0 \tilde{R} \\ m_0 \tilde{R} & \mathbf{I}_p - m_0 \tilde{R}\tilde{R} \end{bmatrix} + \sum_{i=1}^{N} \begin{bmatrix} \mathbf{Q}_{pi} & -\mathbf{Q}_{pi}\tilde{t}_{pi} \\ \tilde{t}_{pi}\mathbf{Q}_{pi} & -\tilde{t}_{pi}\mathbf{Q}_{pi}\tilde{t}_{pi} \end{bmatrix},$$

$$\mathbf{C}_p = \sum_{i=1}^{N} c_i k_i (N_i + 1) \begin{bmatrix} \mathbf{J}_{pi} \\ \tilde{t}_{pi}\mathbf{J}_{pi} \end{bmatrix}, \qquad \mathbf{K}_p = N_i k_i^2 \begin{bmatrix} \mathbf{J}_{pi} \\ \tilde{t}_{pi}\mathbf{J}_{pi} \end{bmatrix},$$

$$\mathbf{M}_b = \sum_{i=1}^{N} \begin{bmatrix} \mathbf{Q}_{bi} & -\mathbf{Q}_{bi}\tilde{t}_{bi} \\ \tilde{t}_{pi}\mathbf{Q}_{bi} & -\tilde{t}_{pi}\mathbf{Q}_{bi}\tilde{t}_{bi} \end{bmatrix}, \qquad \mathbf{K}_b = \sum_{i=1}^{N} N_i k_i^2 \begin{bmatrix} \mathbf{J}_{bi} \\ \tilde{t}_{bi}\mathbf{J}_{bi} \end{bmatrix},$$

$$\mathbf{C}_b = \sum_{i=1}^{N} c_i k_i (N_i + 1) \begin{bmatrix} \mathbf{J}_{bi} \\ \tilde{t}_{bi}\mathbf{J}_{bi} \end{bmatrix}, \quad \text{and}$$

$$\mathbf{U} = \begin{bmatrix} \mathbf{R}_p \mathbf{F}_{\text{mac}} \\ \mathbf{R}_p \mathbf{M}_{\text{mac}} + \mathbf{R}_p \mathbf{R} \times \mathbf{F}_{\text{mac}} \end{bmatrix} - \eta.$$

Equation (11) gives the dynamic responses of the upper platform when the base is excited with harmonic vibration.

3. Performance of the Microvibration Isolation Device

The microvibration isolation device is designed to isolate vibration ejected by CMG and the parameters of which are given in Table 1. The relaxation-type damper has been manufactured beforehand and the parameters of which are tested and recorded in Table 2. Meanwhile, the structure parameters of the microvibration isolation device are summarized in Table 3.

3.1. Natural Frequency Analysis. First, the natural frequencies of the microvibration isolation in six directions are analyzed. By simplifying equation (11) and neglecting damping, one can get the free vibration equation of the isolation device without damping as

$$N_i k_i \mathbf{M}_p \mathbf{x}_p'' + \mathbf{K}_p \mathbf{x}_p = 0. \tag{12}$$

In equation (12), $\mathbf{K}_p x$ is the equivalent stiffness matrix and $N_i k_i \mathbf{M}_p$ is the equivalent mass matrix. The first six-order natural frequencies of the vibration isolation system can be obtained by solving equation (12). The modal analysis is also conducted by using finite element software and the model of which is shown in Figure 5. The results of the natural frequency obtained from the finite element software are compared with the theoretical results solved from equation (12). The comparison results are given in Table 4 and the two results are in good accordance. Moreover, in order to understand the natural characteristics of this system thoroughly, the corresponding mode shapes are also summarized in Figure 6.

From the results of natural frequency and the mode shape, one can conclude that the third-order mode and the fifth-order mode are the Z-direction translational and Z-axis twist pure mode, respectively. The other four modes are coupled mode in X-direction and Y-direction.

3.2. Relaxation-Type Damper Performance. As mentioned above, the flexible strut used here is a relaxation-type damper. The advantage of this kind of damper over a Kevin model damper is that it can control the resonance amplification without losing capacity of attenuating higher-frequency vibration if the parameters of the damper are chosen carefully. To clarify this point more clearly, the transmissibility of the relaxation-type damper used in this paper is plotted in Figure 7. For the sake of comparison convenience, the transmissibility curve of a system with a Kevin model is also plotted in the same figure. One can see that although the two dampers exhibit the

Table 1: Parameters of the CMG.

Parameters	Data
m	25.22 Kg
I_x	0.4469 Kg · m^2
I_y	0.1956 Kg · m^2
I_z	0.6074 Kg · m^2

Table 2: Parameters of the relaxation-type damper.

Parameters	Data
k	19.2 N/mm
c	1300 N · s/m
N	4

Table 3: Parameters of the vibration suppression device.

Parameters names	Data/ mm
Circumcircle of hinges on upper platform radius R_p	187
Circumcircle of hinges on the lower platform radius R_b	172
Shorter distance of hinges on upper platform l_p (see Figure 2(b))	28
Shorter distance of hinges on upper platform l_b (see Figure 2(b))	149
Height of the device h	76
Mass center of the CMG to the upper platform H	40

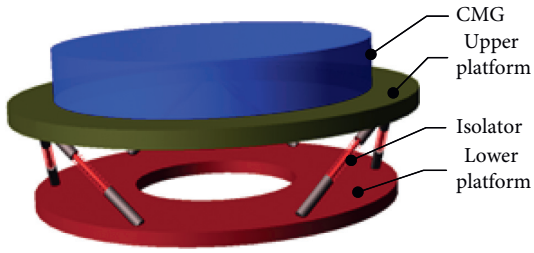

Figure 5: Finite element model of the microvibration suppression device.

Table 4: Comparison of nature frequencies solved by analytical and numerical methods.

Modal	Theoretical result	Numerical result	Relative error
1	8.1550	7.7400	5.08
2	8.8524	8.5763	3.11
3	13.3529	12.0770	9.55
4	16.6622	17.0831	−2.52
5	18.2286	18.6618	−2.37
6	22.0580	21.8344	−1.01

same resonance amplification factor, the vibration attenuation rate at the main frequency of CMG (100 Hz) has more than10 dB differences, which is the advantage of the relaxation-type damping.

3.3. Coupling Analysis. The main reason that induced the coupling in different directions for the vibration isolation device considered here is that the mass center is out of the plane of the upper platform. Without loss of generality, the parameters $h = 0$ mm and $h = 40$ mm are chosen to illustrate the coupling characteristic of the device. The transmissibility of the two cases is plotted in Figures 8 and 9 for base excitation.

By observing the two figures, one can conclude that if the mass center of the CMG is in the plane of upper platform, there is no coupling for the device. When the mass center of the CMG is higher than the plane of upper platform, the X-direction translation, Y-direction rotation, Y-direction translation, and X-direction rotation are coupled. Two peaks in the transmissibility are observed. However, the movements in Z-direction translation and rotation are independent of the other direction in spite of the changing of the mass center of the CMG. This conclusion is very important when designing such kind of device to acquire better vibration isolation performance in certain direction.

3.4. Vibration Isolation Performance in Translational and Rotational Direction. To evaluate the vibration isolation performance of the device, equation (13) is numerically solved by the Runge-Kutta method in MATLAB software. The base is applied with an excitation amplitude of 30 mg according to satellite experiment and the frequency range is from 2 to 40 Hz. The absolute transmissibility is used to represent the vibration performance, which is defined as the ratio of acceleration of upper and lower platforms. The translational transmissibility and rotational transmissibility are plotted in Figures 10(a) and 10(b). Meanwhile, the resonance amplification factor and the vibration attenuation rate at the main frequency of the CMG are summarized in Table 5.

The transmissibilities in X-direction and Y-direction translation are basically the same because of the symmetrical feature of the device. In all six directions, the minimum natural frequency is 6.84 Hz (X-direction translational) and the maximum natural frequency is 28.65 Hz (Y-direction rotational). The vibration attenuation rate at 100 Hz is beyond 30 dB, which means that the vibration isolation efficiency is more than 94%. Moreover, the resonant amplification factor is below 3 times.

4. The Experiment

4.1. The Scheme. The experimental scheme is shown in Figure 11. It includes a microvibration excitation table, the vibration isolation device, accelerometers, LMS data acquisition system, and suspension system.

To cancel the gravity, a soft suspension system is built in Figure 12. The vibration table which simulates the excitation of sweep sine frequency applies the excitation to lower platform; both the accelerations on the vibration table and on the CMG are measured in order to calculate the absolute transmissibility. The translational transmissibilities in X-direction, Y-direction, and Z-direction are tested.

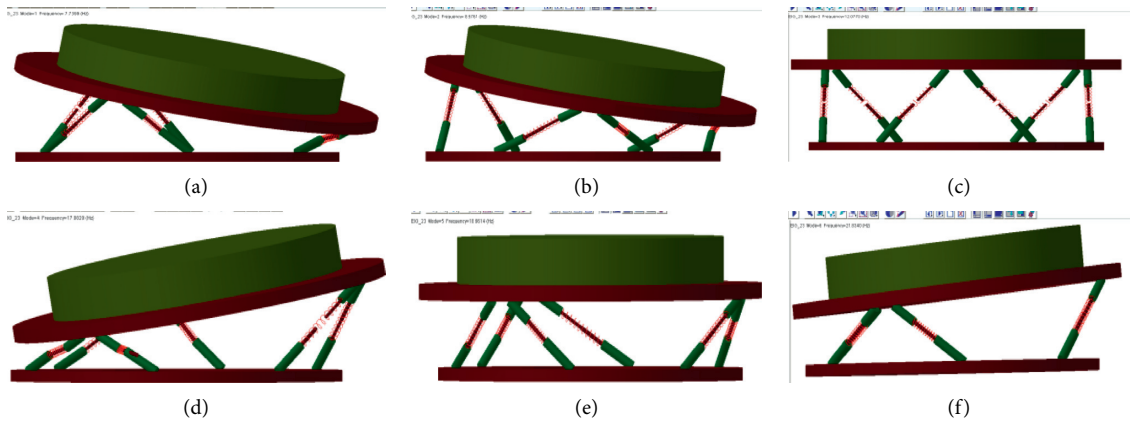

Figure 6: The first six modes of the microvibration suppression device. (a) First-order mode. (b) Second-order mode. (c) Third-order mode. (d) Fourth-order mode. (e) Fifth-order mode. (f) Sixth-order mode.

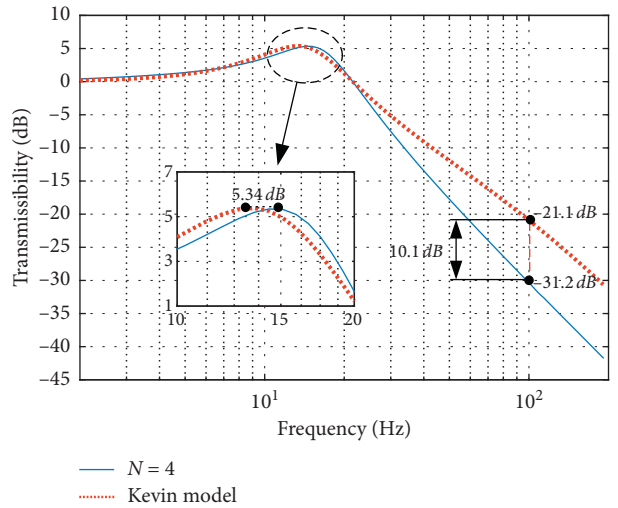

Figure 7: Comparison of the acceleration transmissibility of the relaxation-type damper for $N = 4$ and a Kevin model.

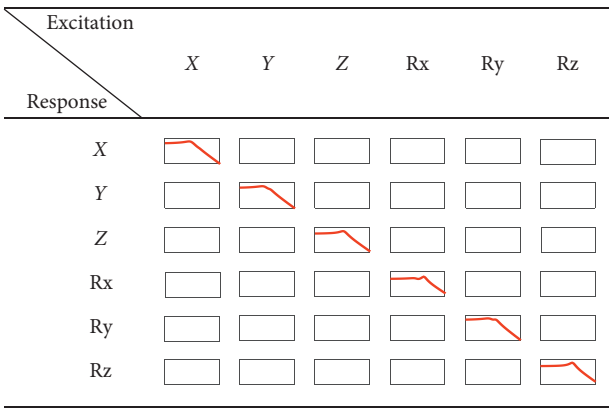

Figure 8: Response of the CMG when $h = 0$ mm.

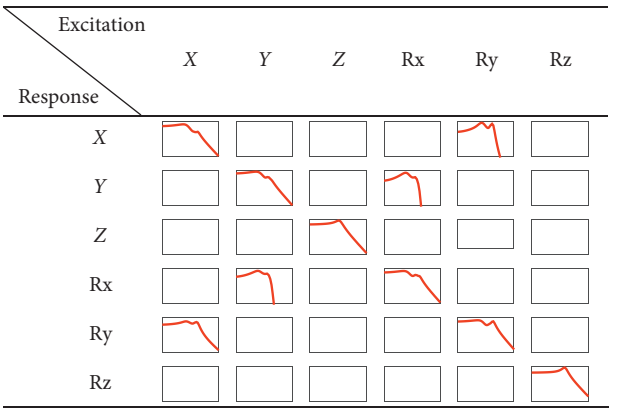

Figure 9: Response of the CMG when $h = 40$ mm.

4.2. The Soft Suspension System. Four elastic strips are used to suspend the CMG. First, the deflection length and the stiffness of the strip are tested. The force-deflection test apparatus is shown in Figure 13, and the force-deflection curve is fitted by the LMS method, which is given in Figure 14. In the figure, one can calculate that the stiffness of the

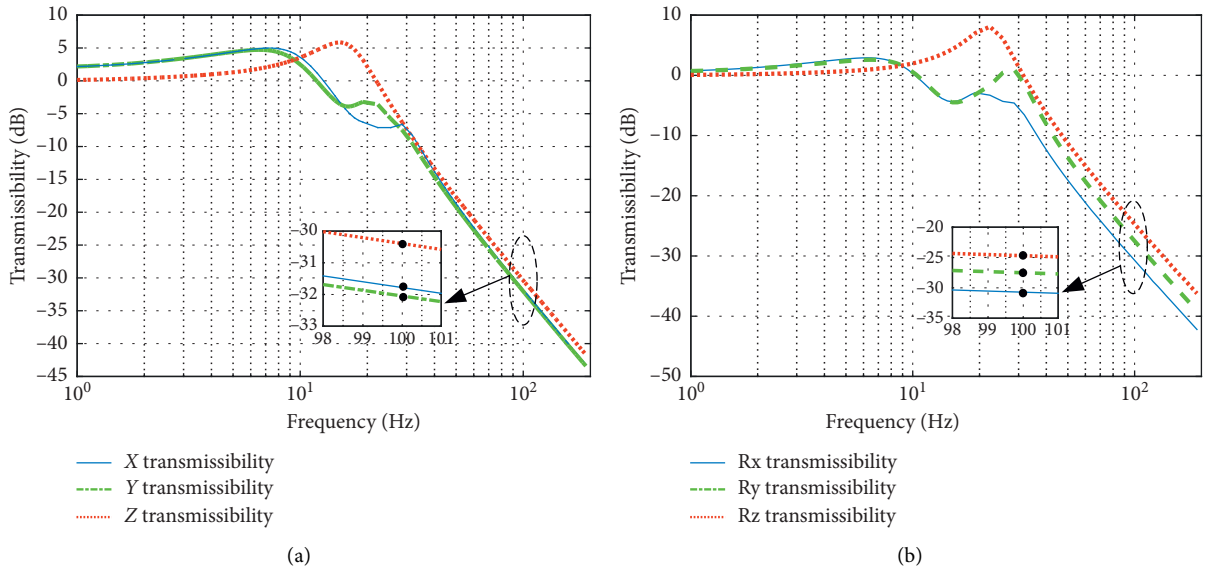

Figure 10: Transmittance curve of Stewart vibration isolation system in six directions. (a) Transmissibility in the translational direction. (b) Transmissibility in the rotational direction.

Table 5: Vibration isolation performance of microvibration suppression device in six directions.

Direction	X	Y	Z	Rx	Ry	Rz
100 Hz attenuation rate (%)	97	98%	96%	97%	96%	94%
Resonance amplification factor	1.75	1.72	1.95	1.39	1.34	2.53

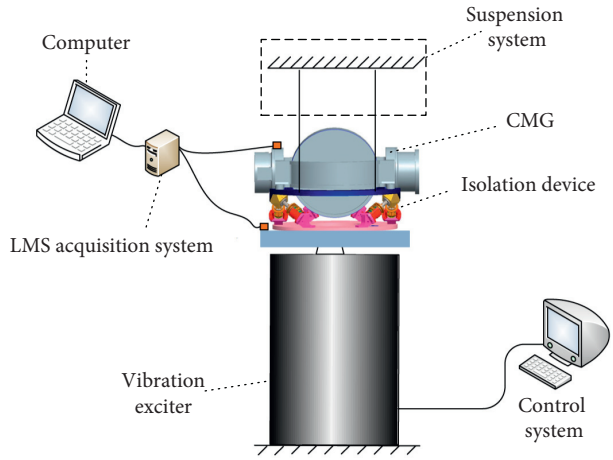

Figure 11: Experimental test system.

strip is about 0.245 N/mm, which yields a suspension frequency of about 0.3 Hz. The natural frequency of the suspension system is far lower than the first natural frequency of the vibration isolation system, which means that the suspension system can affect the experimental result a little. Moreover, in the vertical direction, the suspension length is more than 3 meters; therefore, the horizontal suspension frequency is also low enough.

4.3. Time-Domain Results. The input and output accelerations measured in the three directions are shown in Figures 15 to 17. The input signal of the vibration table is a 30 mg amplitude and 2–200 Hz sine sweep vibration. In the time domain in Figures 15 to 17, one can see clearly the amplification and attenuation of the vibration isolation device. In the Z-direction translational excitation, only one peak is observed, which means

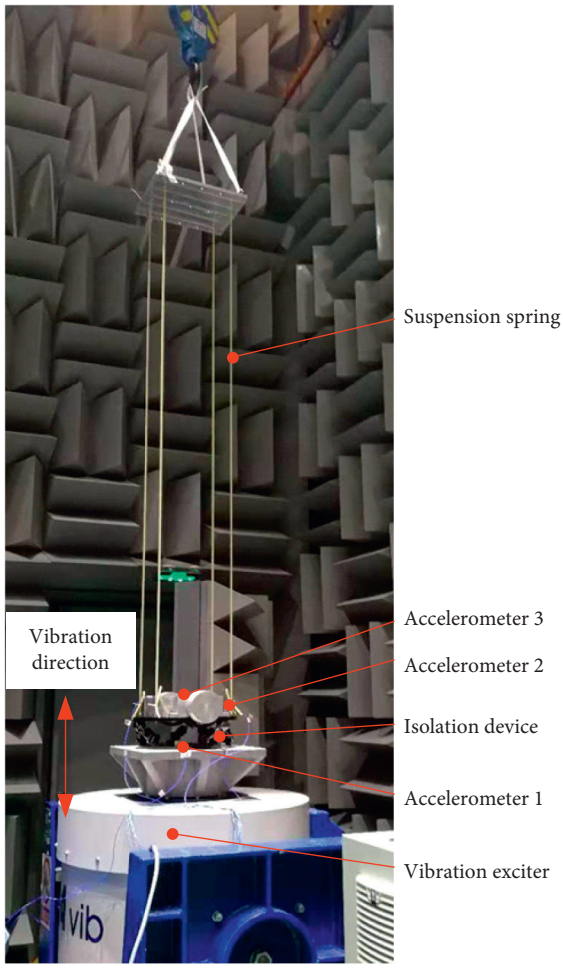

Figure 12: The picture of the experimental apparatus.

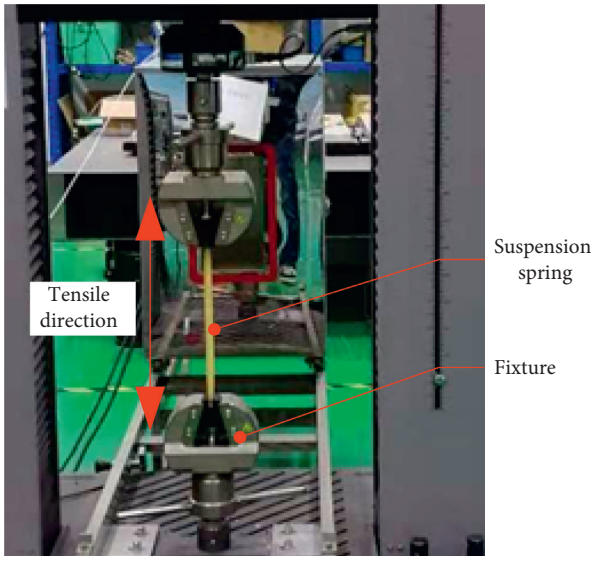

Figure 13: Picture of strip stiffness test experiment.

that there is no coupling in this direction. The amplification factor at the resonance frequency is less than 2 times.

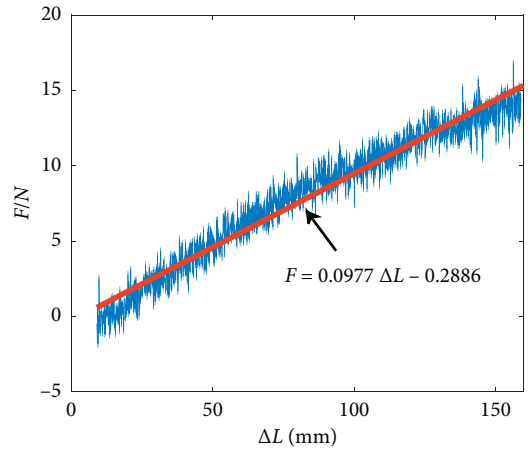

Figure 14: The force-deflection curve for a strip of the initial length of 410 mm.

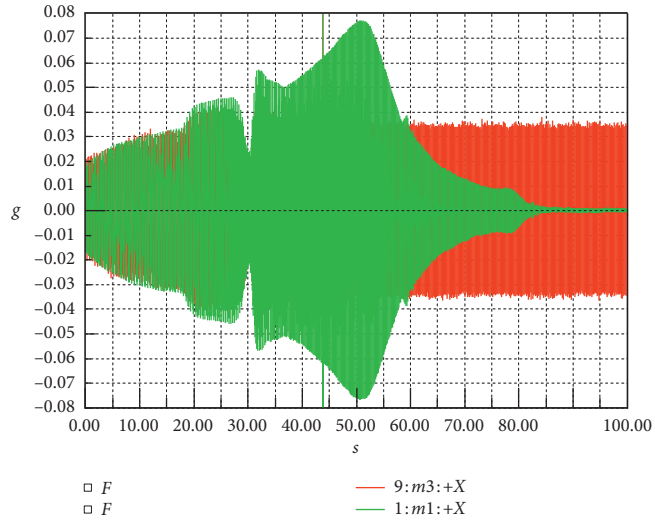

Figure 15: X-direction acceleration curve.

4.4. Frequency-Domain Results. The transmissibilities in the three directions are shown in Figures 18 to 20. Both the experimental and theoretical results are plotted. Overall, the proposed vibration isolation device has excellent vibration attenuation performance. More than 20 dB attenuation is obtained at the main frequency of CMG, which is 100 Hz. There are slight deviations of the theoretical and experimental results in X-direction and Y-direction, though the resonance frequency is basically accurate. The reason for the deviation is possibly the coupling and the joint friction or assembly error. Nevertheless, the theoretical results can be used to predict such kind of vibration isolation device in engineering, since the trends are in good consistency and the deviations only occur at frequencies of small range.

In the Z-direction transmissibility, the theoretical and experimental results are in superb accordance. This is mainly because, as mentioned above, there is no coupling in this direction. In Figure 20, a transmissibility of a vibration isolation system with Kevin model is also plotted for comparison convenience. The curve is plotted by assuming a

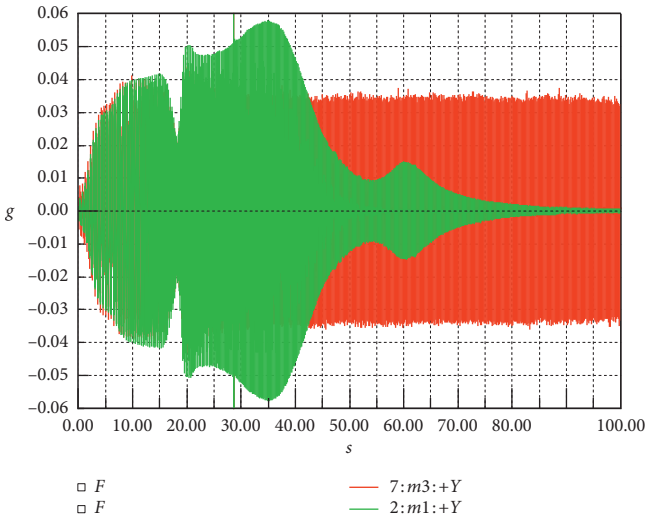

Figure 16: *Y*-direction acceleration curve.

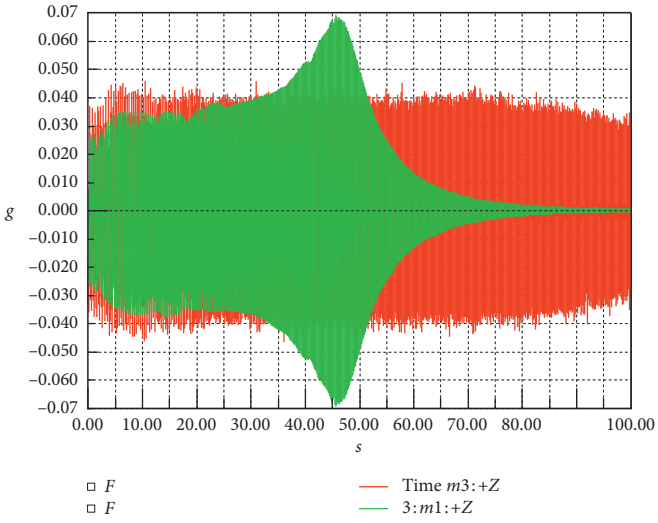

Figure 17: *Z*-direction acceleration curve.

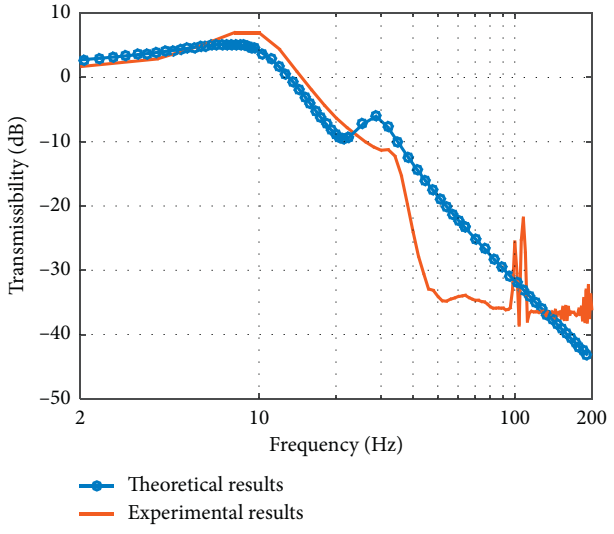

Figure 18: *X*-direction vibration isolation system transmission rate.

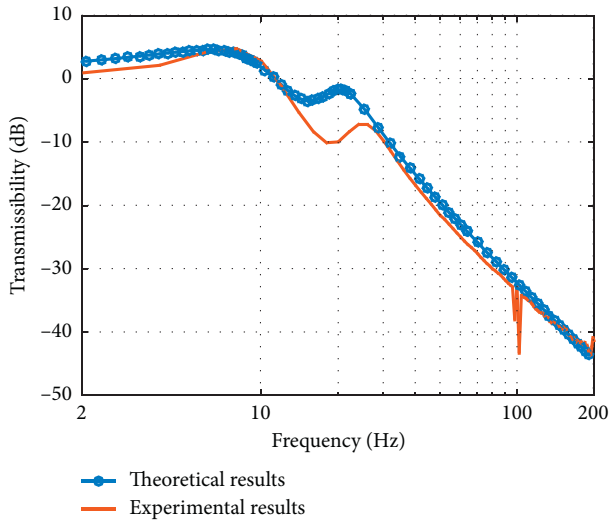

Figure 19: *Y*-direction vibration isolation system transmission rate.

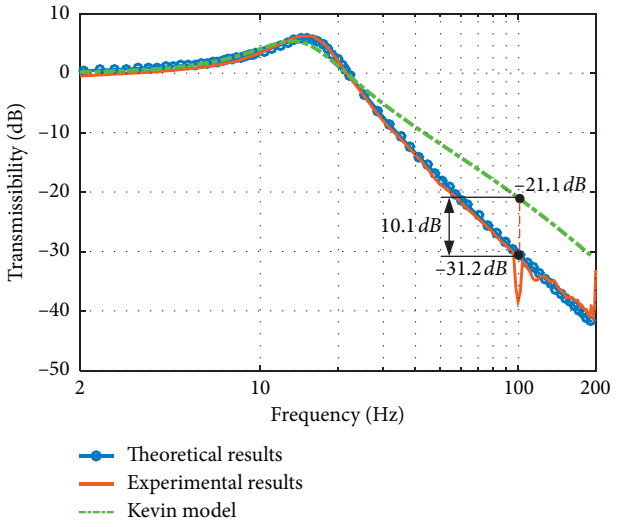

Figure 20: Comparison of the transmissibility of the proposed vibration isolation device with that of a Kevin model in *Z*-direction.

same resonance amplification factor for both systems. It can be seen from the figure that the device proposed in this paper can provide better vibration isolation performance at the main frequency of the CMG. The device with relaxation-type dampers may isolate 10 dB more vibration than that with a Kevin model according to the experimental results. Moreover, the amplification factor at resonance frequency of this device is below 10 dB, which is an excellent index compared with traditional vibration isolation systems on market.

4.5. Effect of the Excitation Amplitude. In fact, the model studied in this paper is a linear system. In other words, the amplitude of excitation is irrelevant to the vibration isolation performance. However, this feature is verified experimentally for the sake of completeness. The excitation amplitude

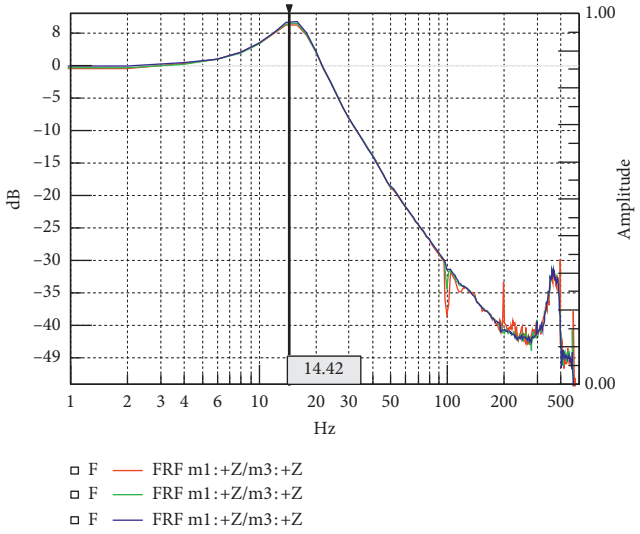

Figure 21: Acceleration transfer rate along Z-direction in different excitation amplitudes.

is varied as 10 mg, 20 mg, and 30 mg in Z-direction and the transmissibilities are plotted in Figure 21 for different excitation amplitudes. From the figure, one can easily distinguish that the amplitude of the excitation has rare effect on the vibration isolation performance.

5. Conclusions

A microvibration suppression device is proposed based on a relaxation-type damper and cubic configured Stewart platform in this paper. Both theoretical and experimental investigations are carried out. Some conclusions can be drawn as follows:

(1) The height between the mass center of the CMG and the upper platform of the device is the main factor that induces coupling effect; this parameter should be chosen carefully when designing this kind of device.

(2) The proposed device can provide more than 30 dB vibration attenuation at the main frequency of the CMG and less than 10 dB amplification at resonance, which is better than that of a traditional linear one.

(3) The excitation amplitude has rare effect on the vibration isolation performance and the device can function in a wide amplitude range.

Data Availability

The data are available upon request to the corresponding author.

Conflicts of Interest

The authors declare that they have no conflicts of interest.

Acknowledgments

The authors acknowledge the financial support from the National Natural Science Foundation of China under Grant no. 51875363.

References

[1] H. P. Frisch, "Thermally induced vibrations of long thin-walled cylinders of open section," *Journal of Spacecraft and Rockets*, vol. 7, no. 8, p. 897, 1970.

[2] Z. Shen, Q. Tian, X. Liu, and G. Hu, "Thermally induced vibrations of flexible beams using Absolute Nodal Coordinate Formulation," *Aerospace Science and Technology*, vol. 29, no. 1, pp. 386–393, 2013.

[3] B. Clapp, J. Sills, and C. Voorhees, "Hubble space telescope pointing performance due to micro-dynamic disturbances from the NICMOS cryogenic cooler," *AIAA J*, 2002.

[4] N. Jedrich, D. Zimbelman, M. Turczyn, et al., "Cryo cooler induced micro-vibration disturbances to the hubble space telescope," 2002.

[5] H.-U. Oh, K.-J. Lee, and M.-S. Jo, "A passive launch and on-orbit vibration isolation system for the spaceborne cryocooler," *Aerospace Science and Technology*, vol. 28, no. 1, pp. 324–331, 2013.

[6] J. Firth and J. Black, "Vibration interaction in a multiple flywheel system," *Journal of Sound and Vibration*, vol. 331, no. 7, pp. 1701–1714, 2012.

[7] H.-U. Oh, S. Taniwaki, N. Kinjyo, and K. Izawa, "Flywheel vibration isolation test using a variable-damping isolator," *Smart Materials and Structures*, vol. 15, no. 2, p. 365, 2006.

[8] C. Gurrisi, R. Seidel, S. Dickerson, S. Didziulis, P. Frantz, and K. Ferguson, "Space Station Control Moment Gyroscope Lessons Learned," in *Proceedings of the 40th Aerospace Mechanisms Symposium*, NASA Kennedy Space Center, Cocoa Beach, FL, USA, May 2010.

[9] D. Yu, G. Wang, and Y. Zhao, "On-orbit measurement and analysis of the micro-vibration in a remote-sensing satellite," *Advances in Astronautics Science and Technology*, vol. 1, no. 2, pp. 191–195, 2018.

[10] A. J. Bronowicki, "Vibration isolator for large space telescopes," *Journal of Spacecraft and Rockets*, vol. 43, no. 1, pp. 45–53, 2006.

[11] L. P. Davis, J. F. Wilson, R. E. Jewell, J. J. Roden, "Hubble space telescope reaction wheel assembly vibration isolation system," NASA report, 1986.

[12] K. J. Pendergast and C. J. Schauwecker, "Use of a passive reaction wheel jitter isolation system to meet the advanced X-ray astrophysics facility imaging performance requirements," *Proceedings of SPIE - The International Society for Optical Engineering*, vol. 3356, 1998.

[13] L. Li, L. Tan, L. Kong, D. Wang, and H. Yang, "The influence of flywheel micro vibration on space camera and vibration suppression," *Mechanical Systems and Signal Processing*, vol. 100, pp. 360–370, 2018.

[14] R. G. Cobb, J. M. Sullivan, A. Das et al., "Vibration isolation and suppression system for precision payloads in space," *Smart Materials and Structures*, vol. 8, no. 6, p. 798, 1999.

[15] J. Spanos, Z. Rahman, and G. Blackwood, "A Soft 6-axis active vibration isolator," in *Proceedings of the 1995 American Control Conference - ACC'95*, Seattle, WA, USA, June 1995.

[16] Y. Zhang, M. Li, and J. Zhang, "Vibration control for rapid attitude stabilization of spacecraft," *IEEE Transactions on Aerospace and Electronic Systems*, vol. 53, no. 3, p. 1308, 2017.

[17] Y. Zhang, Y. Zang, M. Li, Y. Wang, and W. Li, "Active-passive integrated vibration control for control moment gyros and its application to satellites," *Journal of Sound and Vibration*, vol. 394, p. 1, 2017.

[18] M. Li, Y. Zhang, Y. Wang, Q. Hu, and R. Qi, "The pointing and vibration isolation integrated control method for optical

payload," *Journal of Sound and Vibration*, vol. 438, p. 441, 2019.

[19] J. Zhang, Z. Guo, Y. Zhang, L. Tang, and X. Guan, "Inner structural vibration isolation method for a single control moment gyroscope," *Journal of Sound and Vibration*, vol. 361, pp. 78–98, 2016.

[20] B. J. Kawak, "Development of a low-cost, low micro-vibration CMG for small agile satellite applications," *Acta Astronautica*, vol. 131, p. 113, 2017.

[21] Z.-Q. Lu, D. Wu, H. Ding, and L.-Q. Chen, "Vibration isolation and energy harvesting integrated in a Stewart platform with high static and low dynamic stiffness," *Applied Mathematical Modelling*, vol. 89, pp. 249–267, 2021.

Hindawi
Shock and Vibration
Volume 2021, Article ID 5549045, 14 pages
https://doi.org/10.1155/2021/5549045

Research Article

Multibody Modeling Method for UHV Porcelain Arresters Equipped with Lead Alloy Isolation Device

Xiaochao Su,[1] Lei Hou ,[1] Zhubing Zhu,[2] and Yushu Chen[1]

[1]*School of Astronautics, Harbin Institute of Technology, Harbin 150001, China*
[2]*China Electric Power Research Institute, Beijing 102401, China*

Correspondence should be addressed to Lei Hou; houlei@hit.edu.cn

Received 19 January 2021; Revised 16 March 2021; Accepted 25 March 2021; Published 7 April 2021

Academic Editor: Gianluca Gatti

This paper presents a multibody modeling method for seismic analysis of UHV porcelain surge arresters equipped with a kind of seismic isolation device. An UHV arrester is modeled as a planar multibody system whose number of DOF is equal to the number of the arrester units. Joint coordinate method is adopted to construct the governing equations of motion. The seismic isolation device utilizing a number of lead alloy dampers as its core energy dissipation components is also investigated. An analytical model of this device is given by modeling each lead alloy damper as a hysteretic spring and reducing the entire device to a planar system consisting of a range of hysteretic springs. Its mechanical characteristic is derived theoretically, and the obtained moment-angle relationship is expressed as a system of differential algebraic equations. The initial rotational stiffness of the device is formulated in terms of the structural and mechanical parameters of the device. This analytic expression is used in estimating the fundamental frequency of the isolated equipment. By this modeling method, it is easy to construct the governing equations of motion for the isolated system. An UHV arrester specimen is analyzed by this proposed method. The effectiveness of the isolation device in terms of reducing the internal base moment is significant and the influence of system parameters on the effectiveness is also discussed. The proposed method shows its potential usefulness in optimal design of the isolation device.

1. Introduction

Surge arrester is one of the core components of an electrical substation. Nowadays, porcelain-housed metal oxide varistor (MOV) surge arresters are commonly equipped in substations. A typical ultra-high voltage (UHV) porcelain-housed MOV surge arrester is usually composed of several units and one grading ring, which are connected to each other in series with flanges. The structural schematic diagram of an UHV porcelain-housed surge arrester consisting of four units is depicted in Figure 1. Due to their structural characteristics and material property, porcelain surge arresters are easy to be damaged during earthquakes. Thus, improving the seismic performance of the surge arresters is one of the keys to increase the seismic resistance of the entire substation. This issue is faced especially by those UHV substations, because UHV porcelain arresters are almost 12 meters in height and 10 tons in weight and usually have fundamental frequencies ranging from 1 to 10 Hz that match the predominant frequencies of the most of earthquake ground motion [1].

In addition to porcelain surge arresters, many other porcelain post electrical equipment, such as post insulators and disconnect switches, also have high seismic vulnerability. Adopting seismic protective devices is one of the ways to improve their seismic performance. In recent research studies, the use of wire rope in base isolation for circuit breakers has been investigated in [2, 3]. The wire rope isolator was modeled by a modified Bouc–Wen model, and the isolated equipment was analyzed by finite element (FE) method. An innovative multiple tuned mass damper (MTMD) seismic mitigation strategy for porcelain post electrical equipment was investigated in [4, 5]. In [6] Xie et al. studied a new kind of assembled isolation device combining wire rope isolators and linear viscous dampers for bypass switch. The isolation device was modeled by a simplified system of 2-DOF, and its effectiveness was

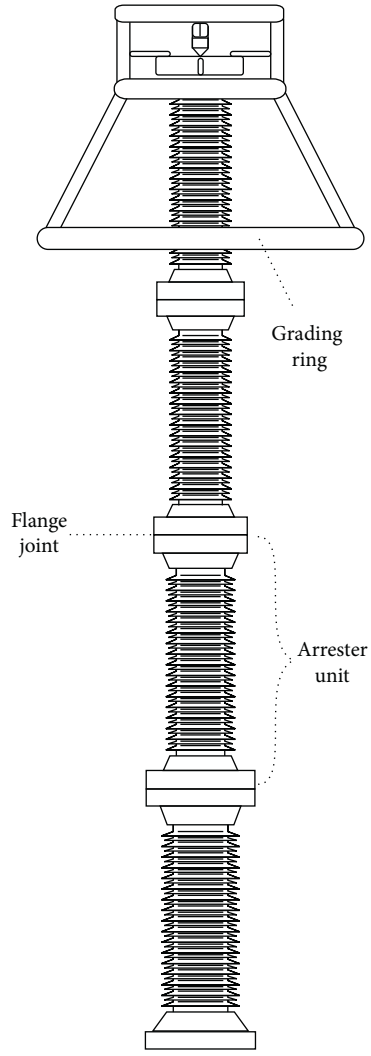

Figure 1: Structural schematic of an UHV porcelain arrester.

validated numerically by using FE analysis and experimentally through shaking table test. This kind of isolation device is also studied by Puff et al. in [7] for circuit breaker. A restraint system consisting of rods, springs, and viscous dampers was investigated in [8] for seismic protection of an 800 kV thyristor valve. A 4-DOF simplified model was developed to investigate the optimal parameters for the restraint system. In [9], friction springs damper used to retrofit tall high voltage equipment for seismic performance improving was discussed. The use of this kind of damping device on seismic protection for electrical equipment can also be found in [10, 11]. A novel seismic isolation device utilizing lead alloy dampers (LADs) as its core energy dissipation components has been studied by Cheng et al. in [12]. The isolation device is equipped between the base unit and the support structure. It is composed primarily of two steel connection plates, a cushion block (CB), and a circle of uniformly distributed LADs. The upside steel plate (USP) is connected to the base unit, and the downside steel plate (DSP) is mounted to the support. The schematic diagram of the assembly is depicted in Figure 2. When an isolated arrester undergoes rocking motion during seismic events, parts of the LADs are subjected to tension, and the others are subjected to compression. Seismic energy is dissipated through the LADs undergoing cyclic yielding deformation, so that the energy transmitted to the above structure is reduced. In [12], the LAD was modeled by the classical Bouc–Wen model, and the isolated electrical equipment was analyzed by using FE method.

It is common to adopt FE modeling method in seismic analysis for porcelain post electrical equipment, such as in [13–15], while simplified modeling methods are also adopted in research on electrical equipment in substations. In [16, 17], generalized single degree of freedom system was used to model a post type of electrical equipment. A 4-DOF system was introduced in [18] to model support-equipment structures in substations and the influence of structure parameters on the dynamic properties of the system was analyzed by using the proposed simplified model. In optimal design of an isolation device, an equivalent model having small number of DOF was proposed in [19] for isolated UHV bypass switches, because FE method is computational time consuming.

For porcelain postelectrical equipment, the current Chinese Code [20] in China recommends a simplified mass-spring modeling method with special care on the stiffness property of the flange joint. An arrester unit in Figure 1 mainly consists of one porcelain housing and core MOV, and each end of the porcelain housing is cemented to joint with metal flange, which is schematically shown in Figure 3. Due to the fact that the cement is generally mechanically weaker than the porcelain housing, an arrester has unevenly distributed stiffness in the axial direction. The third of the authors Zhu has verified in [21] that the simple cantilever beam model is unsuitable in modeling UHV porcelain arresters. Thus, more attention should be paid to the cement joints. An empirical formula to calculate the rotational stiffness at the cement joint was introduced in the Japanese Standard [22] and also the Chinese Code [20], which is expressed as follows:

$$K_c = \xi \frac{d_c h_c^2}{t_e}, \tag{1}$$

where K_c is the rotational stiffness of the porcelain arrester unit at the cement joint, d_c represents the outer diameter of the porcelain housing at the cement joint, h_c and t_e denote the height and the thickness of cement, respectively, and ξ is considered as the coefficient to compute the rotational stiffness. The value of ξ is given by the Chinese Code [20] as 6.54×10^7 with d_c, h_c, and t_e having the unit of meter (m) and K_c having the unit of $\mathrm{N \cdot m \cdot rad^{-1}}$. In recent researches [23, 24] on the coefficient ξ for UHV porcelain electrical equipment, a new formulation is given as follows:

$$\xi = 10^7 \times \begin{cases} 6.54, & d_c \le 0.275, \\ -15.4 d_c + 10.775, & 0.275 < d_c < 0.375, \\ 5.00, & d_c \ge 0.375. \end{cases} \tag{2}$$

Taking account of the rotation stiffness at cement joint, the Chinese Code [20] recommends one can model the flange joint as an equivalent beam element in FE analysis or as a rotational spring in mass-spring modeling. When

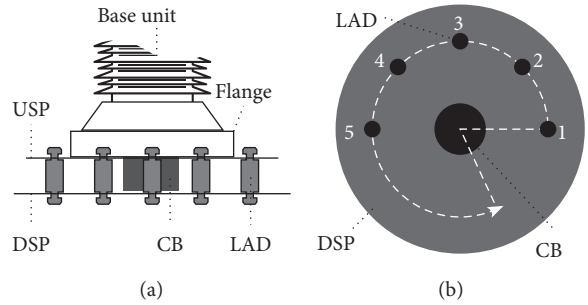

Figure 2: Schematic diagram of the seismic isolation device: (a) lateral view, (b) plan view.

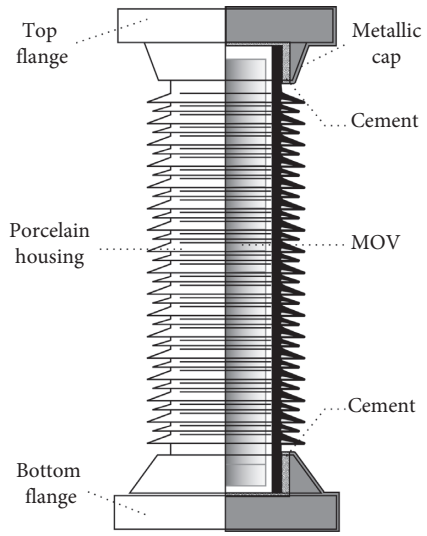

Figure 3: Structural schematic of one porcelain arrester unit.

following the recommendations, the UHV porcelain arrester shown in Figure 1 would be modeled as a nonuniform beam or a mass-spring system as depicted in Figures 4(a) and 4(b), respectively. An analytical model given in [25] modeling each unit as one beam element connected to each other by two rotational springs is shown in Figure 4(c).

The aim of this paper is to present a new modeling method for UHV porcelain surge arresters equipped with the novel seismic isolation device investigated in [12]. The contributions of this study are summarized as follows. Firstly, an UHV porcelain arrester is modeled as a planar multibody system, whose number of DOF is equal to the number of the porcelain units which is usually less than 6. The governing equations of motion are constructed through joint coordinate method. Secondly, an analytical model of the seismic isolation device is given and its mechanical characteristics are derived theoretically. On characterizing the moment-angle relationship of the device, the work in this paper goes a little further than that in [12]. A new parameter indicating the relation between ground motion and LADs distribution is introduced, which was not considered in the previous research work. An analytic expression for the initial rotational stiffness of the isolation device is obtained, which is formulated in terms of the structural and mechanical parameters of the device. Finally, a numerical analysis on a specimen of arrester shows the application of the proposed method in analyzing the effectiveness of the isolation device and the influence of the system parameters on it.

2. Multibody Model of an UHV Porcelain Arrester

Because the distributed stiffness decreases at cement joints and the structure of an arrester is planar symmetric, we model each arrester unit as a planar rigid rod and characterize its resistance to the deflection by two torsional springs separately attached to the ends of the rod. Practically, it is logical to assume uniform mass distribution for the rod, so that the rod's mass center is located at its geometric center. Figure 5(a) shows the rigid body model of an individual arrester unit. The flange joint between arrester units is modeled as a pin joint. The torsional springs at the linked ends are considered to be connected in series and can be represented by a single equivalent torsional spring located at the pin joint. The grading ring is modeled as a lumped mass fixed to the top flange of the uppermost unit. Figure 5(b) shows the multibody model of the UHV porcelain arrester depicted in Figure 1. Damping elements can be added to the pin joints when damping effect is considered. So in this paper, an UHV porcelain arrester is modeled as a planar multibody system, more specifically, a planar open-chain system containing only a single one-branch tree.

2.1. Constructing the Governing Equations of Motion. With regard to an UHV porcelain arrester consisting of n units and one grading ring, a $(n+1)$-body system can be constructed by using the above modeling method. For purpose of simplifying analysis, assumptions that linear torsional springs and linear viscous dampers are used at the pin joints are adopted in the following sections. The input ground motion is also reduced to a horizontal ground motion in the following analysis, but it is easy to extend to include vertical ground motion.

To construct the equations of motion for the $(n+1)$-body system, the joint coordinate method in [26] is mainly used. The main processes are summarized as follows:

(1) Index the bodies of the system

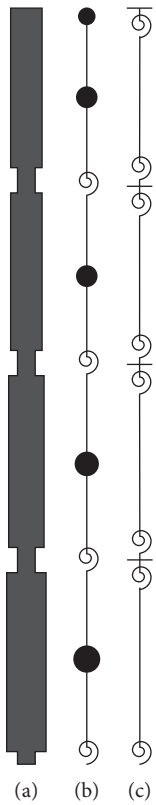

Figure 4: Three kinds of models of an UHV arrester: (a) non-uniform beam model, (b) mass-spring model, (c) analytical model in [25].

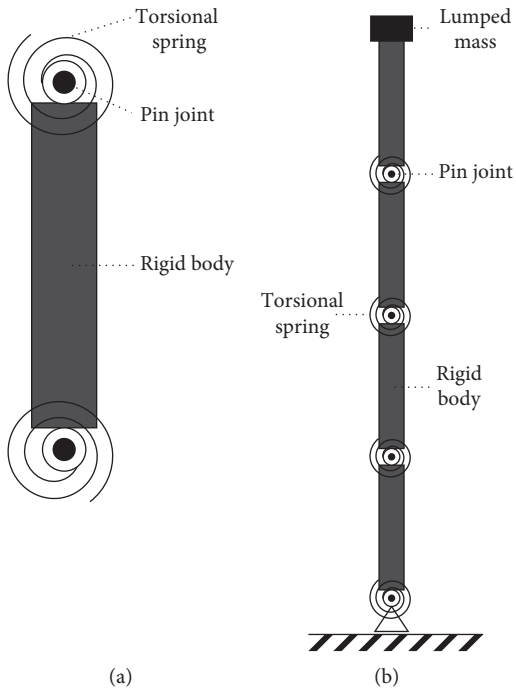

Figure 5: Diagram of the multibody model of an UHV porcelain arrester: (a) rigid body model of one unit; (b) multibody model of the entire arrester.

(2) Construct a global nonmoving Cartesian frame of reference

(3) Define a set of joint coordinates θ equaling in number to the number of system's DOF

(4) Express the absolute body coordinates $\mathbf{c}$ in terms of the joint coordinates θ

(5) Derive the velocity transformation matrix $\mathbf{B}$, i.e., the Jacobian of $\mathbf{c}$ with respect to θ

(6) Construct the mass matrix $\widetilde{M}$ and applied force array $\mathbf{h}$ of the multibody system

Once the matrices $\widetilde{M}$ and $\mathbf{B}$ and vectors $\mathbf{h}$ and $\mathbf{c}$ have been constructed, the equations of motion for the system can be derived by substituting them into the following equation:

$$\mathbf{B}^T(\widetilde{M}\ddot{c} - \mathbf{h}) = \mathbf{0}. \tag{3}$$

Detailed processes for constructing the equations are presented as follows. Assign numbers from 1 to n to the rods from the base to the top one, and assign index "top" to the lumped mass. Denote by joint (i) the one linking body $(i-1)$ and body (i). Choose a global nonmoving Cartesian frame of reference at initial rest state, whose origin O is located at the root joint, x-axis is along the direction of horizontal ground motion, and y-axis is along the axial direction of the arrester. Denote by $u_G(t)$ the horizontal ground displacement history. Denote by θ_i the absolute rotation angle of body (i). At some instant of time, the configuration of the multibody system and the reference frame is depicted in Figure 6.

Obviously, the system has n-DOF. Denote by $\theta = (\theta_1, \ldots, \theta_n)^T$ the joint coordinate of the system. The global coordinate of body (i), denoted by $\mathbf{c}_i = (x_i, y_i, \phi_i)^T$, can be easily expressed in terms of θ as follows:

$$\begin{cases} x_i = u_G(t) - l_1 \sin\theta_1 - \cdots - l_{i-1}\sin\theta_{i-1} - \dfrac{l_i}{2}\sin\theta_i, \\ y_i = l_1\cos\theta_1 + \cdots + l_{i-1}\cos\theta_{i-1} + \dfrac{l_i}{2}\cos\theta_i, \\ \phi_i = \theta_i. \end{cases} \tag{4}$$

where $i = 1, \ldots, n$ and l_i is the length of the rod (i), while for the top body

$$\begin{cases} x_{\text{top}} = u_G(t) - l_1\sin\theta_1 - \cdots - l_n\sin\theta_n, \\ y_{\text{top}} = l_1\cos\theta_1 + \cdots + l_n\cos\theta_n, \\ \phi_{\text{top}} = \theta_n. \end{cases} \tag{5}$$

Then, the configuration $\mathbf{c} = (\mathbf{c}_1^T, \ldots, \mathbf{c}_n^T, \mathbf{c}_{\text{top}}^T)^T$ of the system can be expressed in terms of the joint coordinate θ, and the velocity transform matrix $\mathbf{B}$ and acceleration vector $\ddot{c}$ can be derived accordingly.

To construct the mass matrix $\widetilde{M}$ of the system, denote by m_i the mass of rod (i) and m_{top} the mass of the top lumped mass. Then the moment of inertia for rod (i) about the mass center in the plane can be represented as $J_i = (m_i l_i^2/12)$. For the lumped mass, moment of inertia is ignored, represented by $J_{\text{top}} = 0$. Then, the mass matrix $\widetilde{M}$ is given as a block

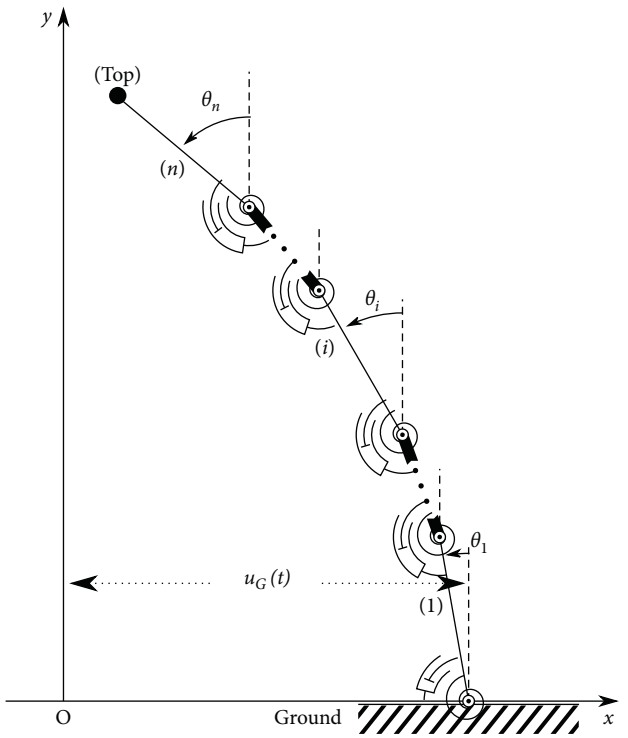

Figure 6: Reference frame and configuration of the multibody system at some instant of time.

diagonal matrix of the matrices $\widetilde{M}_1, \ldots, \widetilde{M}_n$ and $\widetilde{M}_{\text{top}}$ in which $\widetilde{M}_i = \begin{bmatrix} m_i & 0 & 0 \\ 0 & m_i & 0 \\ 0 & 0 & J_i \end{bmatrix}$ is a 3×3 diagonal matrix for $i = 1, \ldots, n$, top.

To construct the array of applied forces for the system, denote by $\mathbf{h}_i = (f_i^{(x)}, f_i^{(y)}, \eta_i)^T$ the applied force array on body (i), in which $f_i^{(x)}$ and $f_i^{(y)}$ represent, respectively, the horizontal and vertical resultant force and η_i represents the resultant moment. Benefitting from adopting joint coordinate, there is no need to consider the reaction forces between linked bodies in this dynamic equations construction. The forces and moments applied on body (i) resulting from gravity and springs are depicted in Figure 7. In horizontal direction, there is no applied force acting on mass center so that $f_i^{(x)} = 0$. In vertical direction, only gravitational force oriented in negative y-axis is applied through mass center, which can be expressed as $f_i^{(y)} = -m_i g$. Both springs located at joint (i) and $(i+1)$ contribute moments to body (i). Define $\Delta\theta_i = \theta_i - \theta_{i-1}$ as the relative rotational angle of body (i) to body $(i-1)$, and denote by s_i the stiffness of the linear torsional spring located at joint (i). Define $M_i^{(s)} = s_i \Delta\theta_i$, and then the moment associated with springs acting on the body (i) as shown in Figure 7 can be expressed as $\Delta M_i^{(s)} = M_{i+1}^{(s)} - M_i^{(s)}$. In a similar way, when considering the moments due to the linear dampers, denote by d_i the damping coefficient of the damper located at joint (i), and define $\Delta\dot{\theta}_i = \dot{\theta}_i - \dot{\theta}_{i-1}$ as the relative rotational velocity of body (i) to body $(i-1)$, and $M_i^{(d)} = d_i \Delta\dot{\theta}_i$. Then, the moment associated with rotational dampers acting on body (i) can be represented by $\Delta M_i^{(d)} = M_{i+1}^{(d)} - M_i^{(d)}$.

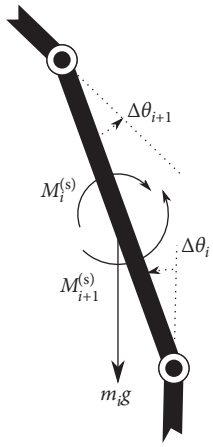

Figure 7: Forces applied on body (i).

To sum up, for body (i) the force array is $\mathbf{h}_i = (0, -m_i g, \Delta M_i^{(s)} + \Delta M_i^{(d)})^T$, and for the top lumped mass the force array is $\mathbf{h}_{\text{top}} = (0, -m_{\text{top}} g, 0)^T$. Then, the applied force array for the system is derived as $\mathbf{h} = (\mathbf{h}_1^T, \ldots, \mathbf{h}_n^T, \mathbf{h}_{\text{top}}^T)^T$.

The equations of motion for the system are derived by substituting the obtained $\mathbf{c}$, $\mathbf{B}$, $\widetilde{M}$, and $\mathbf{h}$ into equation (3). The result can be written in a compact form by using matrix and vector notation as follows:

$$\mathbf{M}(\boldsymbol{\theta})\ddot{\theta} + \mathbf{D}\dot{\theta} + \mathbf{S}\boldsymbol{\theta} + \mathbf{F}(\boldsymbol{\theta}, \dot{\theta}) = \ddot{u}_G(t)\mathbf{m}_t(\boldsymbol{\theta}). \tag{6}$$

It is worth noting that the above ordinary differential equations are nonlinear. The matrix $\mathbf{M}(\theta)$ is not constant. It includes terms in form of $\cos(\theta_i - \theta_j)$ that are nonlinear functions of the time dependent variable θ_i. The vector $\mathbf{F}(\theta, \dot{\theta})$ represents an array of nonlinear forces, and it contains terms in form of $\dot{\theta}_i^2$ and $\cos(\theta_i - \theta_j)$. It also contains nonlinear terms of form $\sin\theta_i$ because the effect of gravity has been considered in the construction of the equations of motion. On the right-hand side, the vector $\mathbf{m}_t(\theta)$ includes $\cos(\theta_i - \theta_j)$ form of terms.

From a practical point of view, the angle of rotation θ_i is so small that small angle approximation can be used to linearize equation (6). The linearized equations can be expressed as follows by adopting the notation of $\widehat{m}_i = m_{i+1} + \cdots m_n + m_{\text{top}}$

$$\mathbf{M}\ddot{\theta} + \mathbf{D}\dot{\theta} + (\mathbf{S} - \mathbf{G})\boldsymbol{\theta} = \ddot{u}_G(t)\mathbf{m}_t, \tag{7}$$

where $\mathbf{M}$ is the general mass matrix having the following form:

$$\mathbf{M} = \begin{bmatrix} \left(\frac{m_1}{3} + \widehat{m}_1\right) l_1^2 & \left(\frac{m_2}{2} + \widehat{m}_2\right) l_1 l_2 & \cdots & \left(\frac{m_n}{2} + \widehat{m}_n\right) l_1 l_n \\ \left(\frac{m_2}{2} + \widehat{m}_2\right) l_2 l_1 & \left(\frac{m_2}{3} + \widehat{m}_2\right) l_2^2 & \cdots & \left(\frac{m_n}{2} + \widehat{m}_n\right) l_2 l_n \\ \vdots & \vdots & \ddots & \vdots \\ \left(\frac{m_n}{2} + \widehat{m}_n\right) l_n l_1 & \left(\frac{m_n}{2} + \widehat{m}_n\right) l_n l_2 & \cdots & \left(\frac{m_n}{3} + \widehat{m}_n\right) l_n^2 \end{bmatrix}, \tag{8}$$

representing the general damping matrix having form as follows:

$$\mathbf{D} = \begin{bmatrix} d_1 + d_2 & -d_2 & \dots & 0 & 0 \\ -d_2 & d_2 + d_3 & \dots & 0 & 0 \\ \vdots & \vdots & \ddots & \vdots & \vdots \\ 0 & 0 & \dots & d_{n-1} + d_n & -d_n \\ 0 & 0 & \dots & -d_n & d_n \end{bmatrix}, \quad (9)$$

and $(\mathbf{S} - \mathbf{G})$ can be considered as the general stiffness matrix with $\mathbf{S}$ and $\mathbf{G}$ having the following forms, respectively:

$$\mathbf{S} = \begin{bmatrix} s_1 + s_2 & -s_2 & \dots & 0 & 0 \\ -s_2 & s_2 + s_3 & \dots & 0 & 0 \\ \vdots & \vdots & \ddots & \vdots & \vdots \\ 0 & 0 & \dots & s_{n-1} + s_n & -s_n \\ 0 & 0 & \dots & -s_n & s_n \end{bmatrix},$$

$$\mathbf{G} = \begin{bmatrix} g\left(\frac{m_1}{2} + \hat{m}_1\right) l_1 & 0 & \dots & 0 \\ 0 & g\left(\frac{m_2}{2} + \hat{m}_2\right) l_2 & \dots & 0 \\ \vdots & \vdots & \ddots & \vdots \\ 0 & 0 & \dots & g\left(\frac{m_n}{2} + \hat{m}_n\right) l_n \end{bmatrix}. \quad (10)$$

The vector $\mathbf{m}_l$ on the right-hand side of equation (7) has form as follows:

$$\mathbf{m}_l = \begin{bmatrix} \left(\frac{m_1}{2} + \hat{m}_1\right) l_1 \\ \left(\frac{m_2}{2} + \hat{m}_2\right) l_2 \\ \vdots \\ \left(\frac{m_n}{2} + \hat{m}_n\right) l_n \end{bmatrix}. \quad (11)$$

From the perspective of vibration mechanics, equation (7) represents a linear vibrating system that has a fully coupling mass matrix and excitation force induced by ground acceleration. At the present stage, an UHV porcelain arrester subjected to earthquake induced ground motion is modeled as a multibody system, and its governing equations of motion have been derived through joint coordinate method.

2.2. Analysis with the Equations of Motion. After the linear equation (7) has been established, the natural frequencies of the system can be derived by solving the generalized eigenvalue problem of matrix $(\mathbf{S} - \mathbf{G})$ and $\mathbf{M}$.

Seismic response history analysis can be taken by numerically integrating equation (7) in time-stepping methods. The methods commonly used include central difference method and Newmark's method [27]. Of greatest interests in the investigation of arrester's seismic performance are the responses of the internal force and the relative displacement and absolute acceleration at the top end. As soon as the response history of θ, $\dot{\theta}$, and $\ddot{\theta}$ is evaluated, the top horizontal displacement relative to the base can be expressed by applying small angle approximation as

$$\widetilde{x}_{\text{top}} = -\sum_{i=1}^{n} l_i \theta_i. \quad (12)$$

Similarly, the total absolute acceleration response at the top end can be formulated as the following linear approximation:

$$\ddot{x}_{\text{top}} = \ddot{u}_{\text{G}} - \sum_{i=1}^{n} l_i \ddot{\theta}_i. \quad (13)$$

The response of the internal moment at joint (i) can be expressed as follows:

$$M_i = -M_i^{(s)} = -s_i (\theta_i - \theta_{i-1}). \quad (14)$$

Static analysis can also be carried out to the system. In order to construct the equilibrium equations for the system subjected to external static load, the applied forces array $\mathbf{h}$ should be modified by removing the damping terms and adding external forces at associated position. Then substitute it into equation (3) and drop the inertia and damping terms; the static equilibrium equations can be derived as the following expression:

$$\mathbf{B}^T \mathbf{h} = \mathbf{0}. \quad (15)$$

The above equation is a system of nonlinear algebraic equations with respect to the joint coordinate θ. Newton–Raphson method can be used to compute the value of θ. Then the other concerned response quantities can be evaluated. For example, the relationship between the lateral force and displacement at the top end can be investigated analytically.

2.3. Parameters Specification. In a practical analysis, specific values of the parameters in the system equation (7) should be given. The mass and length of the arrester units can be obtained from the manufacturer. However, the stiffness at cement joint is usually unknown. As described at the start of this section, the torsional spring located at pin joint is considered as two associated torsional springs connected in series. Denote the rotational stiffness of the spring at the bottom end of rod (i) as s_i^- and that at the top end of rod $(i-1)$ as s_{i-1}^+, and then the equivalent rotational stiffness s_i can be evaluated as follows:

$$s_i = \frac{s_i^- s_{i-1}^+}{s_i^- + s_{i-1}^+}. \quad (16)$$

The values of s_i^- and s_{i-1}^+ can be calculated through equations (1) and (2), in which the cementing parameters can be obtained from manufacturer. Thus, the necessary stiffness parameters of the model can be obtained through the structural parameters of the equipment.

When performing numerical calculation in response history analysis, the damping matrix $\mathbf{D}$ in the system equation (7) needs to be specified. For lightly damped system that has similar damping mechanisms distributed throughout the structure, it is appropriate to assume that the system has classical damping [27]. Rayleigh damping assumption is usually adopted to construct the proportional damping matrix. Accordingly, the damping matrix $\mathbf{D}$ can be constructed from the following free vibration system induced by equation (7) without gravity effect:

$$\mathbf{M}\ddot{\theta} + \mathbf{D}\dot{\theta} + \mathbf{S}\boldsymbol{\theta} = \mathbf{0}. \tag{17}$$

In this paper, stiffness proportional damping $\mathbf{D} = b\mathbf{S}$ is used to specify the damping matrix. The coefficient b is determined by the first natural circular frequency ω and the first-order modal damping ratio ζ of the system (equation (17)).

3. Model of an UHV Arrester Equipped with Seismic Isolation Device

3.1. Modeling the Isolation Device. In this section, a model of the seismic isolation device introduced in [12] which is depicted in Figure 2 is presented. Denote by n_{d} the number of the LADs and by r the radius of the LAD circle. Construct two axes as shown in Figure 8(a), such that the x-axis coincides with the direction of the horizontal ground motion. Starting from the positive x-axis, number the LADs successively in a counterclockwise direction. Define the initial angle α as the angle between x-axis and the first LAD. Then, the location of LAD_i can be determined by the following angular expression:

$$\alpha_i = \alpha + (i-1)\frac{2\pi}{n_d}. \tag{18}$$

Under the assumption of connection steel plates being rigid, the effective arm of force due to LAD_i about x'-axis can be expressed as $a_i = r\cos\alpha_i$. Reduce the whole isolation device to a planar system by means of regarding the connection plates as rigid beams, treating the cushion block as a hinged support fixed to the downside beam and pinned to the midpoint of the upside beam, and modeling each LAD as a hysteretic spring placed at its projection on x-axis that connects the two beams. The schematic diagram of the planar isolation system is depicted in Figure 8(b).

Denote by M_0 the external bending moment applied to the upside beam and θ_0 the associated rotational angle responding to the moment, which is shown in Figure 9. The moment-angle relationship of the planar isolation system is derived theoretically in the following.

Denote the deformation of LAD_i caused by upside beam rotation as x_i. Then it can be expressed as a multiplication of the rotational angle and the effective arm of force associated with LAD_i as follows:

$$x_i = \theta_0 r\cos\alpha_i. \tag{19}$$

The sign of x_i indicates the deformation state of LAD_i in a manner that positive means it is in tension, while negative means it is in compression. Denote by f_i the applied force that induces the deformation x_i of LAD_i. Then the moment distributed on LAD_i is $f_i r\cos\alpha_i$, and the external moment M_0 is the summation of those distributions as follows:

$$M_0 = \sum_{i=1}^{n_d} f_i r\cos\alpha_i. \tag{20}$$

Once the relationship between f_i and x_i for an individual LAD is given, the relationship between M_0 and θ_0 can be determined through equations (18)–(20).

For LAD_i assembled in the isolation device, the classical Bouc–Wen model from [28] is used to describe its hysteretic characteristic. The relationship between its hysteretic restoring force history $f_i(t)$ and deformation displacement history $x_i(t)$ can be described by an operator Φ_{BW}: $x_i(t) \longrightarrow f_i(t)$, which is governed by the following equations:

$$\begin{cases} f_i = \lambda\dfrac{F_y}{\delta}x_i + (1-\lambda)F_y z_i, \\ \dot{z}_i = \dfrac{\dot{x}_i}{\delta}\left(A - \left(\beta + \gamma\,\mathrm{sgn}\left(\dot{x}_i z_i\right)\right)|z|^p\right), \end{cases} \tag{21}$$

where F_y is denoted as yield force, δ represents yield displacement, λ is the parameter of postyielding stiffness ratio, z_i is a dimensionless quantity served as an auxiliary internal state variable that obeys a single nonlinear differential equation, the model parameters A, β, γ, and p are dimensionless quantities controlling the shape of the hysteresis loop, and sgn $(\cdot)$ is the signum function. For mathematical and physical consistency discussed in [29], two constraints, $A = 1$ and $\beta + \gamma = 1$, are imposed to reduce the Bouc–Wen model to a strain-softening formulation with well-defined mechanical properties.

Combining equations (19)–(21) and applying the following equality for positive integer n as $n > 2$

$$\sum_{i=1}^{n}\cos^2\left(\alpha + (i-1)\frac{2\pi}{n}\right) = \frac{n}{2}, \tag{22}$$

it can be derived that the relationship between M_0 and θ_0 of the isolation device with LADs in Bouc–Wen type is governed by the following equations:

$$\begin{cases} M_0 = \dfrac{n_d}{2}\lambda\dfrac{F_y}{\delta}r^2\theta_0 + (1-\lambda)F_y r\displaystyle\sum_{i=1}^{n_d} z_i\cos\alpha_i, \\ \dot{z}_1 = \dfrac{r}{\delta}\dot{\theta}_0\cos\alpha_1\left(1 - \left(\beta + \gamma\mathrm{sgn}\left(\dot{\theta}_0 z_1\cos\alpha_1\right)\right)\left|z_1\right|^p\right), \\ \vdots \\ \dot{z}_{n_d} = \dfrac{r}{\delta}\dot{\theta}_0\cos\alpha_{n_d}\left(1 - \left(\beta + \gamma\mathrm{sgn}\left(\dot{\theta}_0 z_{n_d}\cos\alpha_{n_d}\right)\right)\left|z_{n_d}\right|^p\right). \end{cases} \tag{23}$$

From a mechanical point of view, the above equations can be considered as the constitutive equations of a hysteretic torsional spring with a group of n_d internal state

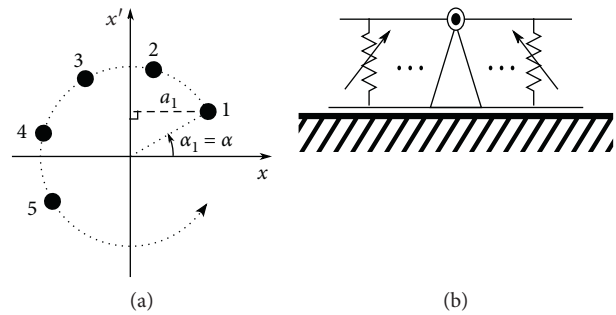

Figure 8: Model of the isolation device: (a) effective arm of force, (b) planar isolation system.

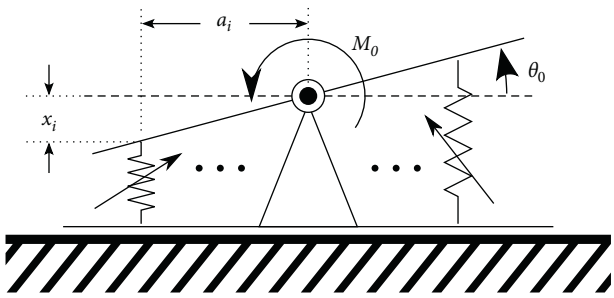

Figure 9: Moment and associated angle of the planar isolation system.

variables. The initial rotational stiffness of the isolation device, denoted by s_0, is defined as

$$s_0 = \frac{\mathrm{d}M_0}{\mathrm{d}\theta_0}\Big|_{t=0} = \frac{\dot{M}_0}{\dot{\theta}_0}\Big|_{t=0}. \tag{24}$$

Based on equations (22), (23) and the initial conditions $z_i(0) = 0$ for $i = 1, \ldots, n_d$, we can derive that

$$s_0 = \frac{n_d}{2}\frac{F_y}{\delta}r^2. \tag{25}$$

The above equation shows that the initial stiffness of the isolation device can be determined by the structural parameters of the device and the mechanical characteristics of the LAD. This analytic expression can be used in estimating the fundamental frequency of the isolated equipment. It is worth noting that the above derivation can be easily extended to the isolation device with LADs modeled by other types of, for example, bilinear or multilinear, hysteresis model.

3.2. Modeling the Isolated UHV Porcelain Arrester. The model of an UHV porcelain arrester equipped with the isolation device is depicted in Figure 10. The downside rigid beam of the isolation system is fixed to the ground. The upside rigid beam is indexed as body (0) and pinned to the body (1). The spring and damper attached to the bottom end of body (1) are connected to the body (0). So the isolated arrester consisting of n units and one grading ring is modeled as a $(n+2)$-body system.

Choose the absolute rotational angles $\theta_0, \theta_1, \ldots, \theta_n$ as the joint coordinates of the isolated system. Then the coordinate of body (0) can be formulated as $\mathbf{c}_0 = (u_G(t), 0, \theta_0)^T$. Compared with those arrester units, the mass of the upside plate in the isolation device is so small that it can be neglected. Accordingly, the mass matrix $\widetilde{M}_0$ is a 3×3 zero matrix, and the applied force array on body (0) can be expressed as $\mathbf{h}_0 = (0, 0, \dot{M}_1^{(s)} + M_1^{(d)} - M_0)^T$, where $M_1^{(s)} = s_1(\theta_1 - \theta_0)$, $M_1^{(d)} = d_1(\dot{\theta}_1 - \dot{\theta}_0)$ and M_0 is the moment due to the isolation system having expression of equation (23). Then, the body configuration, the mass matrix, the applied forces array, and the velocity transformation matrix of the isolated system can be constructed easily.

The governing equations of motion for the isolated system are derived, and by applying small angle approximation, they can be expressed in matrix and vector notation as follows:

$$\begin{bmatrix} 0 & \mathbf{0} \\ \mathbf{0} & \mathbf{M} \end{bmatrix}\begin{bmatrix} \ddot{\theta}_0 \\ \ddot{\theta} \end{bmatrix} + \begin{bmatrix} d_1 & -d_1\mathbf{e}_1^T \\ -d_1\mathbf{e}_1 & \mathbf{D} \end{bmatrix}\begin{bmatrix} \dot{\theta}_0 \\ \dot{\theta} \end{bmatrix} + \begin{bmatrix} s_1 & -s_1\mathbf{e}_1^T \\ -s_1\mathbf{e}_1 & \mathbf{S}-\mathbf{G} \end{bmatrix}, \begin{bmatrix} \theta_0 \\ \boldsymbol{\theta} \end{bmatrix} + \begin{bmatrix} M_0 \\ \mathbf{0} \end{bmatrix} = \ddot{u}_G(t)\begin{bmatrix} 0 \\ \mathbf{m}_l \end{bmatrix} \tag{26}$$

where $\mathbf{e}_1$ is a column vector of n elements with the first one being 1 and the others being 0. Equation (26) has a singular mass matrix. From a physical point of view, it represents that a hysteretic spring is directly connected in series to the base spring of the nonisolated system. Thus, the estimation of the fundamental frequency of the isolated system can be obtained through replacing s_1 in $\mathbf{S}$ by $(s_0 s_1^- / s_0 + s_1^-)$ and solving the generalized eigenvalue problems of $(\mathbf{S} - \mathbf{G})$ and $\mathbf{M}$. To solve equations (26), (23) has to be combined with; that results in a system of n second-order equations and $n_d + 1$ first-order equations. Convert the equations into first-order form and choose $\theta, \dot{\theta}, \theta_0, z_1, \ldots, z_{n_d}$ as the state variables. Because of equation (23), the first-order system can be solved by a solver for fully implicit ordinary differential equations.

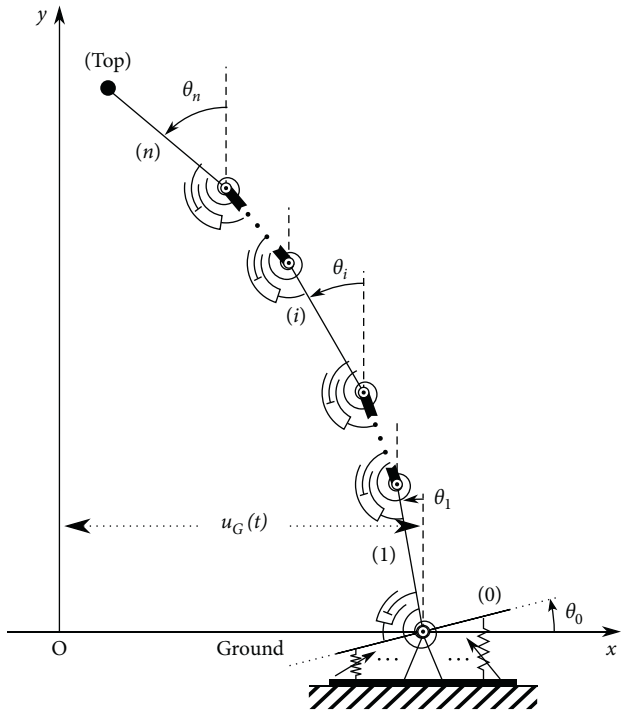

Figure 10: Reference frame and configuration of the isolated multibody system at some instant of time.

4. Analysis of an UHV Porcelain Arrester Specimen

In this section, a 1000 kV porcelain arrester specimen is analyzed by using the proposed method. The specimen is composed of five units of the same type and one different base unit. The cementing parameters of these units are listed in Table 1. The rotational stiffness parameters are calculated and listed in Table 2 together with the mass and length parameters.

The specimen of arrester was experimentally investigated in [21] for its flexural performance. Two levels of static testing were carried out to investigate the relationship between the force and horizontal displacement at the top free end. In the following computation, the gravitational acceleration is fixed to be $g = 9.8\,\mathrm{m}\cdot\mathrm{s}^{-2}$. The analytical results compared with the testing results are depicted in Figure 11. It shows very good agreement between them when loading does not exceed 35 kN. The analytical displacement to the first maximum 26.99 kN force is 167.33 mm, which has relative error 1% to the testing result of 169.02 mm, while under second maximum 43.10 kN lateral force, the analytical displacement is 267.15 mm, which has a relative error of 29.02% to the testing result of 376.39 mm. The reason why relative error increases can be summarized as the following statement. The force of 43.10 kN is nearly the lateral static load which could cause collapse of this specific arrester. The stiffness would decrease when cement joint experiences large deformations exceeding the range of linear stiffness. However, the computation has been performed without considering this nonlinear phenomenon of stiffness reduction.

The following presents a numerical analysis on the effectiveness of the seismic isolation device. The number of the LADs in the adopted device is $n_d = 8$ and the radius of the circle is $r = 0.305$ m. The LAD has the following parameters: $F_y = 22.0$ kN, $\delta = 0.2$ mm, $\lambda = 0.02$, $\beta = \gamma = 0.5$, and $p = 1$.

The fundamental frequency of the nonisolated arrester is calculated to be 1.57 Hz. After equipment with the isolation device, the fundamental frequency decreases to 1.24 Hz. For response history analysis, the input ground motion chosen here is an artificial acceleration history generated according to the required response spectrum (RRS) in the Chinese Code [20]. The artificial accelerogram is shown in Figure 12, and its response spectrum and the RRS are shown in Figure 13. It is normalized to have $1g$ peak ground acceleration (PGA). This motion is scaled with desired PGA to fit the required seismic qualification level and scaled up by a factor of 1.4 to represent the dynamic amplification of the supporting structure.

At seismic qualification level of 0.2 g, with assumed damping ratio $\zeta = 2\%$, under situation of $\alpha = 0$ (see Figure 8), numerical computations are carried out. The response histories of the internal moment at each joint are then calculated. Comparison of the internal base moment between nonisolated and isolated system is shown in Figure 14. It is evident that there is a noticeable decrease of the base moment over the whole duration of the ground motion. The peak value of the base moment shifted from $2.52 \times 10^5\,\mathrm{N}\cdot\mathrm{m}$ to $0.42 \times 10^5\,\mathrm{N}\cdot\mathrm{m}$ with a reduction of 83.2%. The response histories of the absolute acceleration at the top free end of the nonisolated and isolated system are shown in Figure 15. Similar to the base moment, the response of the top absolute acceleration has a noticeable reduction in the whole duration. The peak value changes from −1.26 g to −0.45 g with a 64.3% decrease in magnitude. In contrast to the base moment and the top absolute acceleration, the response of the relative displacement at the top free end increases in some duration of the motion, which is shown in Figure 16. The peak value changes from 126 mm to 166 mm with an increase of 31.4%. It is worth noting in Figure 16 that there is residual displacement at the end of motion, which is due to the hysteretic property of the isolation device.

In order to show the influence of the parameters of the device to the response, the maximum magnitudes of three selected quantities, the base moment (BM), top absolute acceleration (TAA), and top relative displacement (TRD), are calculated for the nonisolated and isolated system with damping of 1%, 2%, and 5% and at two seismic qualification levels of 0.2 g and 0.4 g. As the number of LADs in the isolation device is 8, these quantities are also calculated under $\alpha = 0$ and $\alpha = (\pi/8)$. The results and their changes due to the isolation device are illustrated in Figures 17–19. Firstly, these selected quantities of the nonisolated system are proportional to the seismic qualification level because of the linearity of the system. The isolated system does not have this property due to the nonlinearity introduced by the isolation device. It can be seen from Figure 17 that the effectiveness of the isolation system is significant in terms of reducing the maximum BM. The damping ratio has less influence on the maximum BM of the isolated system than

Table 1: Cementing parameters of the porcelain arrester specimen.

Unit	End	h_c (m)	t_e (m)	d_c (m)
Base unit	±	0.200	0.010	0.495
Units 1~5	±	0.200	0.010	0.510

Table 2: Multibody model parameters of the porcelain arrester specimen.

Body	Index	m_i (kg)	l_i (m)	s_i (N · m · rad^{-1})
Base unit	1	300	0.623	9.9×10^7
Unit 1	2	912	2.115	5.0×10^7
Units 2~5	3~6	912	2.115	5.1×10^7
Grading ring	Top	380	—	—

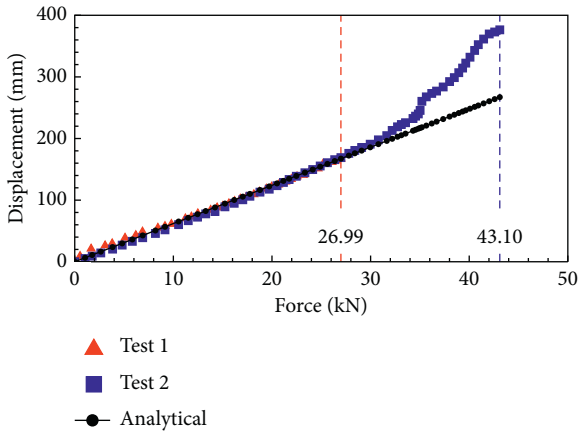

Figure 11: Force-displacement relationship at the top free end of the arrester specimen.

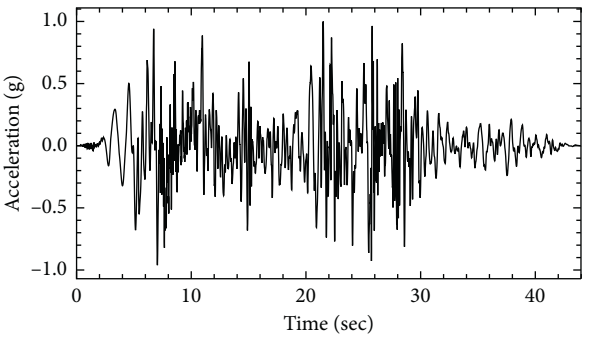

Figure 12: Artificial earthquake accelerogram.

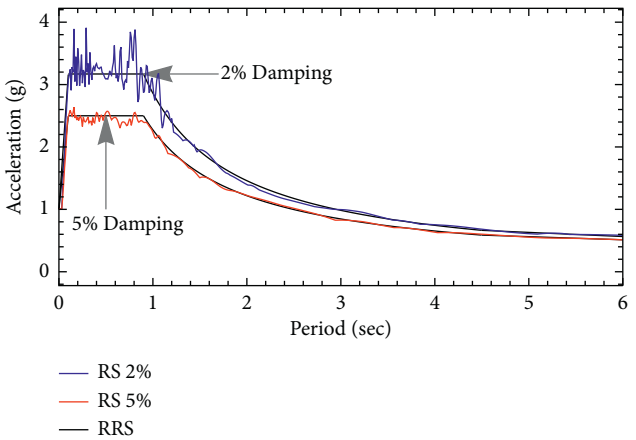

Figure 13: Response spectra of the artificial earthquake and the RRS.

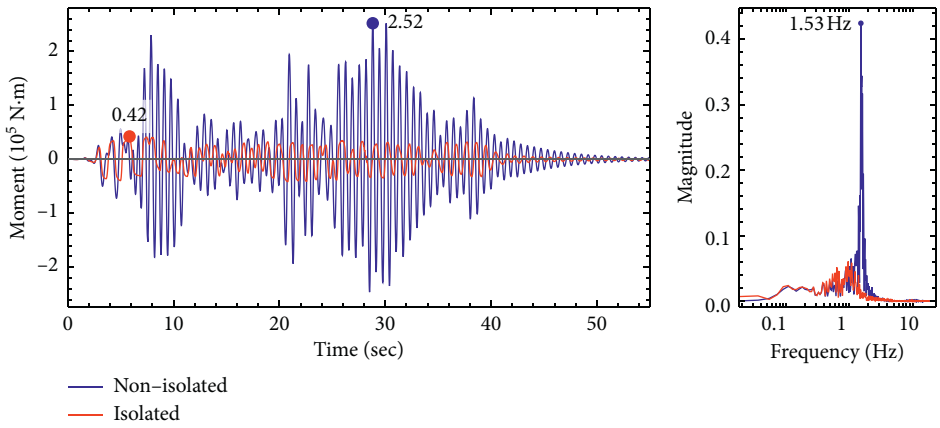

FIGURE 14: Response histories and corresponding Fourier spectra of the base moment of the nonisolated and isolated system with 2% damping at 0.2 (g) seismic qualification level under $\alpha = 0$.

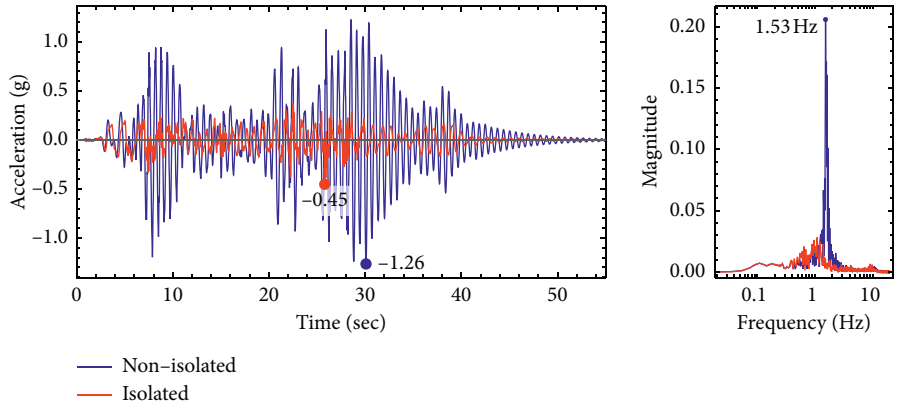

FIGURE 15: Response histories and corresponding Fourier spectra of the absolute top acceleration of the nonisolated and isolated system with 2% damping at 0.2 (g) seismic qualification level under $\alpha = 0$.

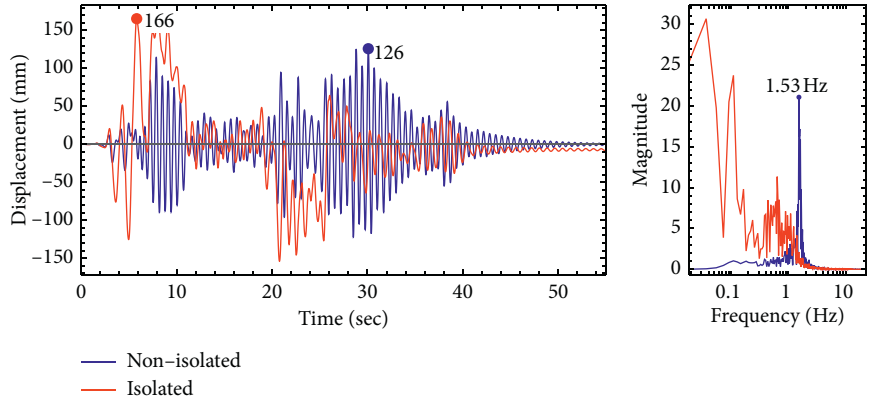

FIGURE 16: Response histories and corresponding Fourier spectra of the relative top displacement of the nonisolated and isolated system with 2% damping at 0.2 (g) seismic qualification level under $\alpha = 0$.

that of the nonisolated system. This is because the isolation device contributes the most damping effect in the isolated system. The parameter α has little influence on the maximum BM of the isolated system, which is expected. Figure 18 shows that the maximum TAA varies with the parameters of α, ζ and seismic level in a similar way to the maximum BM illustrated in Figure 17. The reduction of the TAA is also large but less than that of the BM. In contrast to the BM and TAA, Figure 19 shows that the maximum TRD is increased by the isolation system. The increase is notable especially at 0.4 g seismic qualification level. The maximum TRD is slightly influenced by ζ and relatively sensitive to α.

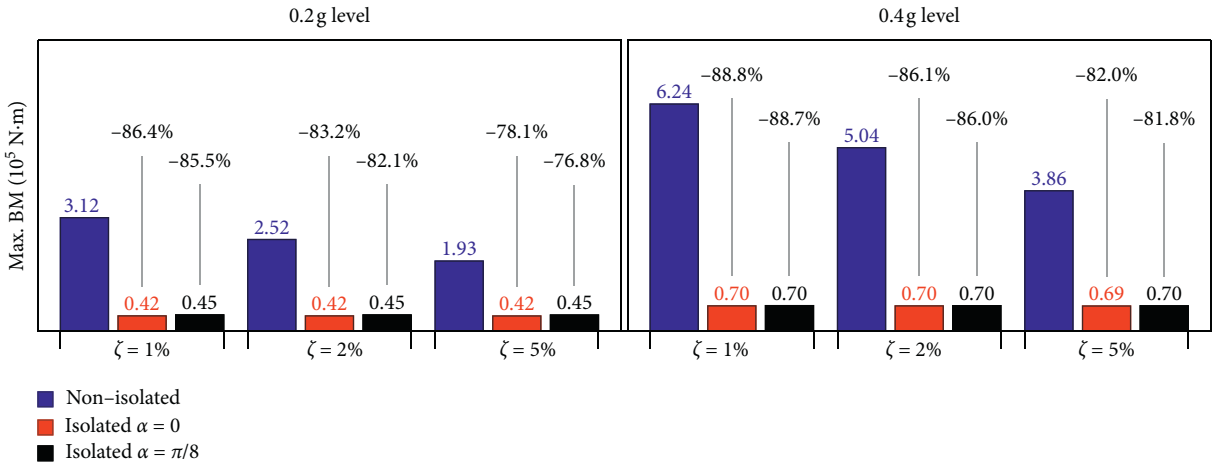

FIGURE 17: Maximum base moments (BM) of the nonisolated and isolated system and their change under different parameters of ζ and α at two seismic qualification levels.

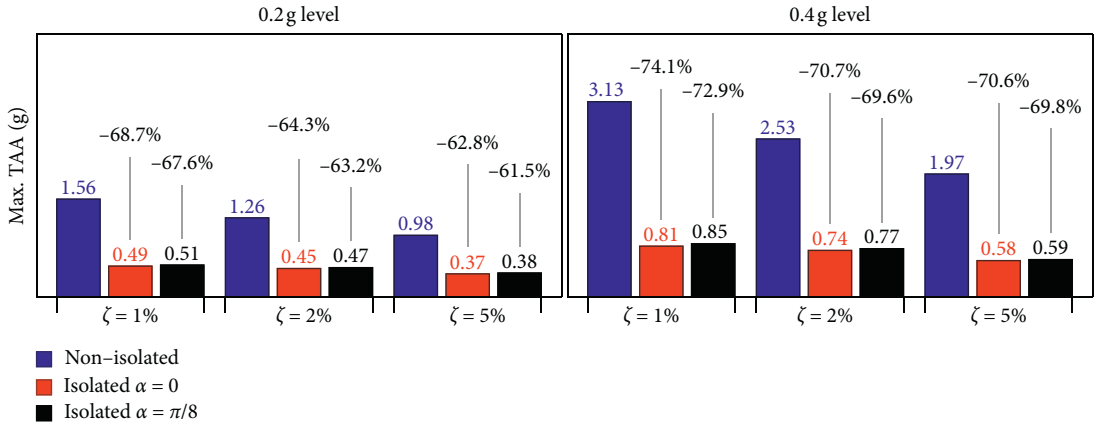

FIGURE 18: Maximum top absolute acceleration (TAA) of the nonisolated and isolated system and their change under different parameters of ζ and α at two seismic qualification levels.

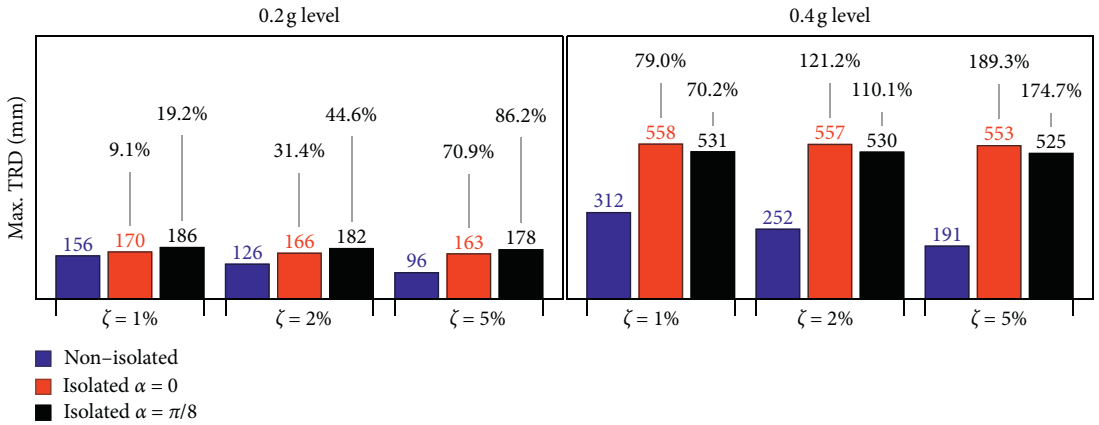

FIGURE 19: Maximum top relative displacement (TRD) of the nonisolated and isolated system and their change under different parameters of ζ and α at two seismic qualification levels.

5. Conclusions

In this paper, a novel modeling method has been proposed for the seismic analysis of UHV porcelain arresters equipped with an isolation device. An UHV porcelain arrester has been modeled as a planar multibody system based on the fact that the stiffness distribution is uneven along the axial direction of the arrester. A joint coordinate method has been chosen to

construct the governing equations of motion. The number of the DOF of the multibody system equals the number of the arrester units, which is usually less than 6. This is beneficial to analysis requiring less numerical computation for determining the optimal design of the isolation device.

With regard to the seismic isolation device, classical Bouc–Wen hysteretic model has been used in modeling its core energy dissipation components. The entire device has been reduced to a planar system, and its mechanical characteristic has been derived theoretically. The governing equations of motion for the isolated arrester have been constructed naturally by embedding the isolation system into the nonisolated multibody system. From a mechanical point of view, the isolation device is represented as a hysteretic rotational spring with a number of internal state variables. Its initial rotational stiffness is formulated in terms of the structural and mechanical parameters of the isolation device. This analytic expression can be used to estimate the fundamental frequency of the isolated equipment, which can guide the design of the isolation device.

An UHV porcelain arrester specimen has been analyzed by the proposed method. In the static analysis the relationship between lateral loading and displacement at the top free end shows good agreement with the test results before failure occurs. The relative error increases when loading force exceeds a limit which indicates that the nonlinearity of the stiffness at joints should be considered in the situation of near failure. This behavior could be studied in future research work. The presented numerical analysis shows that the effectiveness of the isolation device is significant in terms of reducing the maximum base moment. The reduction of the maximum top absolute acceleration is also noticeable. However, the enlargement of the top relative displacement at high seismic qualification level is a disadvantage of the isolation device.

The proposed method primarily focuses on modeling UHV porcelain arresters, while it can be extended to model other porcelain post electrical equipment, such as insulator and capacitor voltage transformer.

Data Availability

The data used to support the findings of this study are included within the article.

Conflicts of Interest

The authors declare that they have no conflicts of interest.

Acknowledgments

The authors are grateful for the financial supports from the National Natural Science Foundation of China (no. 11972129) and the National Major Science and Technology Projects of China (no. 2017-IV-0008-0045).

References

[1] Z. Liu, *Ultra-High Voltage AC/DC Grids*, Academic Press, Cambridge, MA, USA, 2014.

[2] S. Alessandri, R. Giannini, F. Paolacci, and M. Malena, "Seismic retrofitting of an HV circuit breaker using base isolation with wire ropes. Part 1: preliminary tests and analyses," *Engineering Structures*, vol. 98, pp. 251–262, 2015.

[3] S. Alessandri, R. Giannini, F. Paolacci, M. Amoretti, and A. Freddo, "Seismic retrofitting of an HV circuit breaker using base isolation with wire ropes. Part 2: shaking-table test validation," *Engineering Structures*, vol. 98, pp. 263–274, 2015.

[4] W. Bai, J. Dai, H. Zhou, Y. Yang, and X. Ning, "Experimental and analytical studies on multiple tuned mass dampers for seismic protection of porcelain electrical equipment," *Earthquake Engineering and Engineering Vibration*, vol. 16, no. 4, pp. 803–813, 2017.

[5] B. Wen, M. A. Moustafa, and D. Junwu, "Seismic response of potential transformers and mitigation using innovative multiple tuned mass dampers," *Engineering Structures*, vol. 174, pp. 67–80, 2018.

[6] Q. Xie, Z. Yang, C. He, and S. Xue, "Seismic performance improvement of a slender composite ultra-high voltage bypass switch using assembled base isolation," *Engineering Structures*, vol. 194, pp. 320–333, 2019.

[7] M. Puff, A. Kopanoudis, A. v. Seck, and S. Ruan, "Introduction of an innovative base isolation system for seismic protection of HV components based on a combination of wire ropes and viscous dampers," in *ERES 2015*, pp. 147–155, WIT press, Opatija, Croatia, 2015.

[8] Z. Yang, Q. Xie, Y. Zhou, and K. M. Mosalam, "Seismic performance and restraint system of suspended 800 kV thyristor valve," *Engineering Structures*, vol. 169, pp. 179–187, 2018.

[9] P. Dusicka, M. J. Riley, K. Kraxberger, and S. Knowles, "Shaking response of tall high-voltage equipment retrofitted with friction dampers," in *Structures Congress 2013: Bridging Your Passion with Your Profession*, pp. 1381–1390, American Society of Civil Engineers, Reston, VA, USA, 2013.

[10] M. Riley, C. Stark, L. Kempner, and W. Mueller, "Seismic retrofit using spring damper devices on high-voltage equipment stands," *Earthquake Spectra*, vol. 22, no. 3, pp. 733–753, 2006.

[11] R. Kar, J. H. Rainer, and A. C. Lefrançois, "Dynamic properties of a circuit breaker with friction-based seismic dampers," *Earthquake Spectra*, vol. 12, no. 2, pp. 297–314, 1996.

[12] Y. Cheng, S. Li, Z. Lu, Z. Liu, and Z. Zhu, "Seismic risk mitigation of cylindrical electrical equipment with a novel isolation device," *Soil Dynamics and Earthquake Engineering*, vol. 111, pp. 41–52, 2018.

[13] B. Wen, M. A. Moustafa, and D. Junwu, "Seismic fragilities of high-voltage substation disconnect switches," *Earthquake Spectra*, vol. 35, no. 4, pp. 1559–1582, 2019.

[14] F. Paolacci, R. Giannini, S. Alessandri, and G. De Felice, "Seismic vulnerability assessment of a high voltage disconnect switch," *Soil Dynamics and Earthquake Engineering*, vol. 67, pp. 198–207, 2014.

[15] F. Paolacci and R. Giannini, "Seismic reliability assessment of a high-voltage disconnect switch using an effective fragility analysis," *Journal of Earthquake Engineering*, vol. 13, no. 2, pp. 217–235, 2009.

[16] J. Song, A. D. Kiureghian, and J. L. Sackman, "Seismic interaction in electrical substation equipment connected by non-linear rigid bus conductors," *Earthquake Engineering & Structural Dynamics*, vol. 36, no. 2, pp. 167–190, 2007.

[17] J.-B. Dastous, A. Filiatrault, and J.-R. Pierre, "Estimation of displacement at interconnection points of substation

equipment subjected to earthquakes," *IEEE Transactions on Power Delivery*, vol. 19, no. 2, pp. 618–628, 2004.

[18] R. K. Mohammadi, V. Akrami, and F. Nikfar, "Dynamic properties of substation support structures," *Journal of Constructional Steel Research*, vol. 78, pp. 173–182, 2012.

[19] Z. Yang, Q. Xie, C. He, and L. Xie, "Isolation design for slender ultra-high–voltage composite equipment using modal parameters considering multiple responses," *Engineering Structures*, vol. 200, p. 109709, 2019.

[20] GB50260, *Code for Seismic Design of Electrical Installations*, China Planning Press, Beijing, China, 2013.

[21] Z. Zhu, Z. Dai, Z. Liu, and Z. Lu, "Experimental and simulation study on flexural performance of 1000 kV UHV arrester," *Insulators and Surge Arresters*, vol. 257, no. 1, pp. 32–38, 2014.

[22] JEAG 5003-2010, *Seismic Design Guideline for Electrical Equipment in Substations*, Japan Electric Association, Tokyo. Japan, 2010.

[23] X. Zhang, Z. Dai, Z. Lu, and M. Cao, *Coefficient of Bending Stiffness of Interconnected Parts between Ultra-high Voltage Porcelain Bushings and Flanges*, Engineering Journal of Wuhan University, 2014.

[24] Z. Zhu, "Experimental study of the bending rigidity at flange connection of UHV electrical equipment," *Electric Power*, vol. 47, no. 6, pp. 6–11, 2014.

[25] S. Li, H.-H. Tsang, Y. Cheng, and Z. Lu, "Considering seismic interaction effects in designing steel supporting structure for surge arrester," *Journal of Constructional Steel Research*, vol. 132, pp. 151–163, 2017.

[26] P. E. Nikravesh, *Planar Multibody Dynamics: Formulation, Programming and Applications*, CRC Press, Boca Raton, FL, USA, 2007.

[27] A. K. Chopra, *Dynamics of Structures*, Pearson Education, London, UK, 2012.

[28] Y.-K. Wen, "Method for random vibration of hysteretic systems," *Journal of the Engineering Mechanics Division*, vol. 102, no. 2, pp. 249–263, 1976.

[29] A. E. Charalampakis and V. K. Koumousis, "On the response and dissipated energy of Bouc-Wen hysteretic model," *Journal of Sound and Vibration*, vol. 309, no. 3-5, pp. 887–895, 2008.

Hindawi
Shock and Vibration
Volume 2021, Article ID 6690686, 14 pages
https://doi.org/10.1155/2021/6690686

Research Article

The Elliptic Harmonic Balance Method for the Performance Analysis of a Two-Stage Vibration Isolation System with Geometric Nonlinearity

Weilei Wu [1,2] **and Bin Tang** [1,2]

[1]*Key Laboratory of Ocean Energy Utilization and Energy Conservation of Ministry of Education, Dalian University of Technology, Dalian 116023, China*
[2]*Institute of Internal Combustion Engine, Dalian University of Technology, Dalian 116023, China*

Correspondence should be addressed to Bin Tang; btang@dlut.edu.cn

Received 16 November 2020; Revised 19 January 2021; Accepted 3 February 2021; Published 28 February 2021

Academic Editor: Jie Yang

This study develops a modified elliptic harmonic balance method (EHBM) and uses it to solve the force and displacement transmissibility of a two-stage geometrically nonlinear vibration isolation system. Geometric damping and stiffness nonlinearities are incorporated in both the upper and lower stages of the isolator. After using the relative displacement of the nonlinear isolator, we can numerically obtain the steady-state response using the first-order harmonic balance method (HBM1). The steady-state harmonic components of the stiffness and damping force are modified using the Jacobi elliptic functions. The developed EHBM can reduce the truncation error in the HBM1. Compared with the HBM1, the EHBM can improve the accuracy of the resonance regimes of the amplitude-frequency curve and transmissibility. The EHBM is simple and straightforward. It can maintain the same form as the balancing equations of the HBM1 but performs better than it.

1. Introduction

Nonlinearity has become the focus of recent research studies on improving vibration isolation performance [1, 2]. Many of them have the configuration of geometrically nonlinear springs [3–5] and dampers [6–8] whose arrangement can obtain low dynamic stiffness, thereby reducing the natural frequency without inducing large static deflection [9,10]. Furthermore, two-degree-of-freedom (2-DOF) vibration isolation systems with quasi-zero-stiffness (QZS) and geometrically nonlinear damping have been studied [11–14]. Lu et al. showed that both the force and displacement transmissibilities are mitigated in the isolation range as the horizontal stiffnesses in both stages are increased [11]. Comparing three kinds of nonlinear 2-DOF vibration isolation models, which are grounded-grounded, bottom-springs grounded, and top-springs grounded isolators, Wang et al. found that the bottom-springs grounded isolator has the best isolation performance when the excitation force amplitude is small [12]. The vibrational power flow method was applied to investigate the performance of a 2-DOF nonlinear isolation system [15]. Recently, Yang et al. illustrated that the addition of a nonlinear inertance mechanism to a QZS isolator could enhance vibration isolation performance [16]. Deng et al. illustrated that a multilayer QZS combined system might give distinguished isolation performance in low-frequency regime without losing supporting stability [17].

The harmonic balance method (HBM) is a technique for solving the equations of motion of strongly nonlinear oscillators in the papers mentioned above. However, when these nonlinear equations of motion are solved using the HBM, the truncation error is induced when the high-order harmonic components are neglected. To improve the results' accuracy, complex and numerous balance equations should be included [18–20]. Some modified methods, such as an incremental HBM [21], two-timescale HBM [22], and the

HBM with prior linearization [23], have been presented. In this respect, Zhou et al. illustrated that an accurate approximation solution for the resonance response of harmonically forced strongly nonlinear oscillator could be obtained by linearizing the governing equation before harmonic balancing [24].

Jacobi elliptic functions are widely used to solve the nonlinear dynamical systems [19, 25], especially for strongly nonlinear problems [26–28]. The exact solutions for certain conservative nonlinear solutions can be directly solved using the Jacobi elliptic functions, which can be equivalent to the Fourier series expansion with high orders [26]. A nonlinear vibration isolation system with a negative stiffness mechanism was investigated using the averaging method [29]. However, when the elliptic harmonic balance method is applied to solve two or multiple DOFs systems, the number of equations obtained by harmonic balancing is not equal to that of unknowns [30]. For this issue, Chen and Liu analysed a 2-DOF self-excited oscillator with strongly cubic nonlinearity by an additional equation prior to harmonic balancing using Jacobi elliptic functions [30]. Using an elliptic balance method, Elias-Zuniga and Beatty obtained the forced response of a 2-DOF undamped system with cubic nonlinearity [31]. Cveticanin proposed an approximate method for solving coupled strongly nonlinear differential equations with small nonlinearities based on the Krylov-Bogolyubov procedure with Jacobi elliptic functions [32]. Recently, Wu and Tang modified the harmonic components of the first-order terms of the damping and stiffness force of a single DOF nonlinear isolation system using Jacobi elliptic functions [33].

Herein, we developed an elliptic harmonic balance method (EHBM) and used it to obtain the transmissibility of a two-stage geometrically nonlinear vibration isolation system. The geometrically nonlinear damping and stiffness are included in both the upper and lower stages to improve the isolation characteristics. The steady-state response of the two-stage vibration isolator is derived using Jacobi elliptic functions and trigonometric functions. Using Jacobi elliptic functions, we modified the first-order harmonic balance method (HBM1) according to the orthogonal relationship between force components. After calculating the amplitude-frequency characteristics, we can obtain the force and displacement transmissibility. The accuracy of the results is analysed.

2. A Two-Stage Geometrically Nonlinear Vibration Isolator

A two-stage nonlinear vibration isolator is shown in Figure 1. In addition to the suspended mass and the vertical springs and dampers, horizontal springs and dampers are inserted in each stage to produce geometric nonlinearity [3–8]. The exciting force is applied in the vertical direction. The relative displacement between each adjacent stage are given by $x_r = x_1 - x_2$ and $x_m = x_2 - x_e$, respectively, where x_1 is the displacement of the mass of the upper stage m_{s1}, x_2 is the displacement of the mass of the lower stage m_{s2}, and x_e is the displacement of the base. The force transmitted from m_{s1} to m_{s2} and the force transmitted from m_{s2} to the basement are given by

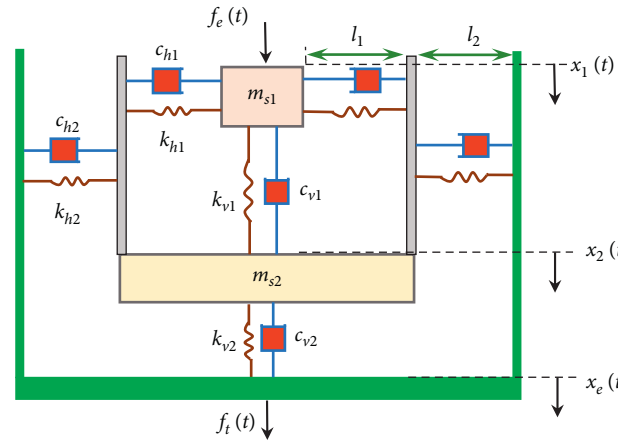

Figure 1: Model of a two-stage nonlinear vibration isolator.

$$f_r(x_r, \dot{x}_r) = c_{v1}\dot{x}_r + 2c_{h1}\frac{x_r^2}{x_r^2 + l_1^2}\dot{x}_r + k_{v1}x_r + 2k_{h1}\left(1 - \frac{l_{01}}{\sqrt{x_r^2 + l_1^2}}\right)x_r, \tag{1a}$$

$$f_m(x_m, \dot{x}_m) = c_{v2}\dot{x}_m + 2c_{h2}\frac{x_m^2}{x_m^2 + l_2^2}\dot{x}_m + k_{v2}x_m + 2k_{h2}\left(1 - \frac{l_{02}}{\sqrt{x_m^2 + l_2^2}}\right)x_m, \tag{1b}$$

where c_{v1} and c_{h1} are the damping coefficients of the vertical and horizontal dampers of the upper stage, c_{v2} and c_{h2} are the damping coefficients of the vertical and horizontal dampers of the lower stage, k_{v1} and k_{h1} are the stiffnesses of the vertical and horizontal springs of the upper stage, k_{v2} and k_{h2} are the stiffnesses of vertical and horizontal springs of the lower stages, l_1 and l_2 are the lengths of the upper and lower horizontal springs between the suspended mass and host structure in the state of rest, and l_{01} and l_{02} are the free lengths of the horizontal springs of the upper and lower stages, respectively.

If the relative displacement between each adjacent stage is less than 20 percent of the length of the horizontal spring, the series expansion of the forces f_r and f_m shown in equations (1a) and (1b) can be approximated as [8, 33]

$$f_r(x_r, \dot{x}_r) = f_{dr} + f_{sr} \approx c_{v1}\dot{x}_r + 2c_{h1}\left(\frac{x_r}{l_1}\right)^2\dot{x}_r + k_{r1}x_r + k_{r3}x_r^3, \tag{2a}$$

$$f_m(x_m, \dot{x}_m) = f_{dm} + f_{sm} \approx c_{v2}\dot{x}_m + 2c_{h2}\left(\frac{x_m}{l_2}\right)^2\dot{x}_m + k_{m1}x_m + k_{m3}x_m^3, \tag{2b}$$

where f_{dr} and f_{dm} are the approximated damping forces when $x_r^2/(x_r^2 + l_1^2) \approx (x_r/l_1)^2$ and $x_m^2/(x_m^2 + l_2^2) \approx (x_m/l_2)^2$, f_{sr} and f_{sm} are the approximated spring forces when

$k_{v1}x_r + 2k_{h1}(1 - l_{01}/\sqrt{x_r^2 + l_1^2})x_r \approx k_{r1}x_r + k_{r3}x_r^3$ and $k_{v2}x_m + 2k_{h2}(1 - l_{02}/\sqrt{x_m^2 + l_2^2})x_m \approx k_{m1}x_m + k_{m3}x_m^3$, where $k_{r1} = k_{v1} - 2k_{h1}(l_{01}/l_1 - t1)$, $k_{r3} = k_{h1}l_{01}/l_1^3$, $k_{m1} = k_{v2} - 2k_{h2}(l_{02}/l_2 - t1)$, and $k_{m3} = k_{h2}l_{02}/l_2^3$, and the percentage error is less than four percent [8,34]. It should also be noticed that if the amplitude of the excitation is large, so that the force-deflection characteristic of the two-stage system cannot be approximately described by a series expansion to the third order as in equations (2a) and (2b), the nonlinearity induces undesirable effects [35].

For the force excitation case, where the base displacement $x_e = 0$, $x_1 = x_r + x_m$, and $x_2 = x_m$, the equations of motion are written as

$$m_{s1}(\ddot{x}_r + \ddot{x}_m) + c_{v1}\dot{x}_r + 2c_{h1}\left(\frac{x_r}{l_1}\right)^2 \dot{x}_r + k_{r1}x_r + k_{r3}x_r^3 = F_e\cos(\omega_e t), \tag{3a}$$

$$m_{s2}\ddot{x}_m + c_{v2}\dot{x}_m + 2c_{h2}\left(\frac{x_m}{l_2}\right)^2 \dot{x}_m + k_{m1}x_m + k_{m3}x_m^3 - c_{v1}\dot{x}_r - 2c_{h1}\left(\frac{x_r}{l_1}\right)^2 \dot{x}_r - k_{r1}x_r - k_{r3}x_r^3 = 0, \tag{3b}$$

where F_e is the excitation force amplitude and ω_e is its frequency.

Setting $l_1 = l_2$, the nondimensional forms of equations (3a) and (3b) become

$$\hat{x}_r'' + \hat{x}_m'' + \hat{f}_{dr} + \hat{f}_{sr} = \hat{F}_e\cos(\Omega\tau), \tag{4a}$$

$$\mu\hat{x}_m'' + \hat{f}_{dm} + \hat{f}_{sm} - \hat{f}_{dr} - \hat{f}_{sr} = 0, \tag{4b}$$

where $x_s = \sqrt{l_{01}^2 - l_1^2} = \sqrt{l_{02}^2 - l_2^2}$, $\hat{x}_r = x_r/x_s$, $\hat{x}_m = x_m/x_s$, $\hat{l} = l_1/l_{01} = l_2/l_{02}$, $\tau = \omega_n t$, $\omega_n = \sqrt{k_{v1}/m_{s1}}$, $\Omega = \omega_e/\omega_n$, $\hat{F}_e = F_e/k_{v1}x_s$, $\mu = m_{s2}/m_{s1}$, $\zeta_{v1} = c_{v1}/2m_{s1}\omega_n$, $\zeta_{v2} = c_{v2}/2m_{s1}\omega_n$, $\zeta_{h1} = c_{h1}/2m_{s1}\omega_n$, $\zeta_{h2} = c_{h2}/2m_{s1}\omega_n$, $\zeta_{n1} = \zeta_{h1}(1 - \hat{l}^2)/\hat{l}^2$, $\zeta_{n2} = \zeta_{h2}(1 - \hat{l}^2)/\hat{l}^2$, $\Omega_1^2 = k_{r1}/k_{v1}$, $\Omega_2^2 = k_{m1}/k_{v1}$, $\gamma_1 = k_{r3}x_s^2/k_{v1}$, $\gamma_2 = k_{m3}x_s^2/k_{v1}$, $\hat{f}_{dr} = 2\zeta_{v1}\hat{x}_r' + 4\zeta_{n1}\hat{x}_r^2\hat{x}_r'$, $\hat{f}_{sr} = \Omega_1^2\hat{x}_r + \gamma_1\hat{x}_r^3$, $\hat{f}_{dm} = 2\zeta_{v2}\hat{x}_m' + 4\zeta_{n2}\hat{x}_m^2\hat{x}_m'$, and $\hat{f}_{sm} = \Omega_2^2\hat{x}_m + \gamma_2\hat{x}_m^3$.

When the excitation force $f_e = 0$ and the base displacement $x_e = X_e\cos(\omega_e t)$, where X_e and ω_e are the base excitation amplitude and frequency, the equations of motion of the base excited system are given by

$$\hat{x}_r'' + \hat{x}_m'' + \hat{f}_{dr} + \hat{f}_{sr} = \Omega^2\hat{X}_e\cos(\Omega\tau), \tag{5a}$$

$$\mu\hat{x}_m'' + \hat{f}_{dm} + \hat{f}_{sm} - \hat{f}_{dr} - \hat{f}_{sr} = \mu\Omega^2\hat{X}_e\cos(\Omega\tau), \tag{5b}$$

where $\hat{X}_e = X_e/x_s$.

3. Elliptic Harmonic Balance Method

3.1. HBM1. The solutions of equations (4a) and (4b) are assumed as

$$\hat{x}_r(\tau) = \hat{X}_r\cos(\Omega\tau + \phi_r), \tag{6a}$$

$$\hat{x}_m(\tau) = \hat{X}_m\cos(\Omega\tau + \phi_m), \tag{6b}$$

where $\hat{X}_r$ is the nondimensional amplitude of the relative displacement between m_{s1} and m_{s2}, $\hat{X}_m$ is the nondimensional amplitude of the relative displacement between m_{s2} and the base, ϕ_r is the phase difference between the relative displacement $\hat{x}_r$ and the excitation force, and ϕ_m is the phase difference between the relative displacement $\hat{x}_m$ and the excitation force.

The nondimensional damping and stiffness force can be approximately written as $\hat{f}_{dr} \approx \tilde{\alpha}_r(\hat{X}_r)\sin(\Omega\tau + \phi_r)$, $\hat{f}_{sr} \approx \tilde{\beta}_r(\hat{X}_r)\cos(\Omega\tau + \phi_r)$, $\hat{f}_{dm} \approx \tilde{\alpha}_m(\hat{X}_m)\sin(\Omega\tau + \phi_m)$, and $\hat{f}_{sm} \approx \tilde{\beta}_m(\hat{X}_m)\cos(\Omega\tau + \phi_m)$, where $\tilde{\alpha}_r$, $\tilde{\beta}_r$, $\tilde{\alpha}_m$, and $\tilde{\beta}_m$ are the amplitudes of the first order of series expansion of $\hat{f}_{dr}$, $\hat{f}_{sr}$, $\hat{f}_{dm}$, and $\hat{f}_{sm}$ at the steady-state response, respectively, which can be expressed as follows [18]:

$$\tilde{\alpha}_r(\hat{X}_r) \approx \frac{\Omega}{\pi}\int_0^{(2\pi/\Omega)} \hat{f}_{dr}\left(\hat{X}_r\cos(\Omega\tau + \phi_r), -\hat{X}_r\Omega\sin(\Omega\tau + \phi_r)\right)\sin(\Omega\tau + \phi_r)\mathrm{d}\tau, \tag{7a}$$

$$\tilde{\beta}_r(\hat{X}_r) \approx \frac{\Omega}{\pi}\int_0^{(2\pi/\Omega)} \hat{f}_{sr}\left(\hat{X}_r\cos(\Omega\tau + \phi_r), -\hat{X}_r\Omega\sin(\Omega\tau + \phi_r)\right)\cos(\Omega\tau + \phi_r)\mathrm{d}\tau, \tag{7b}$$

$$\tilde{\alpha}_m(\hat{X}_m) \approx \frac{\Omega}{\pi}\int_0^{(2\pi/\Omega)} \hat{f}_{dm}\left(\hat{X}_m\cos(\Omega\tau + \phi_m), -\hat{X}_m\Omega\sin(\Omega\tau + \phi_m)\right)\sin(\Omega\tau + \phi_m)\mathrm{d}\tau, \tag{7c}$$

$$\tilde{\beta}_m(\hat{X}_m) \approx \frac{\Omega}{\pi}\int_0^{(2\pi/\Omega)} \hat{f}_{sm}\left(\hat{X}_m\cos(\Omega\tau + \phi_m), -\hat{X}_m\Omega\sin(\Omega\tau + \phi_m)\right)\cos(\Omega\tau + \phi_m)\mathrm{d}\tau. \tag{7d}$$

Substituting equations (6a) and (6b) into equations (4a) and (4b) and equating coefficients of the harmonic components $\sin(\Omega\tau + \phi_r)$, $\cos(\Omega\tau + \phi_r)$, $\sin(\Omega\tau + \phi_m)$, and $\cos(\Omega\tau + \phi_m)$, we obtain

$$-\frac{\Omega^2\widehat{X}_m\sin(\theta)}{\Omega\widehat{X}_r}\widehat{x}_r'(\tau)+\widehat{f}_{dr}=-\frac{\widehat{F}_e\sin(\phi_r)}{\Omega\widehat{X}_r}\widehat{x}_r'(\tau), \tag{8a}$$

$$\frac{\widehat{X}_r+\widehat{X}_m\cos(\theta)}{\widehat{X}_r}\widehat{x}_r''(\tau)+\widehat{f}_{sr}=\frac{\widehat{F}_e\cos(\phi_r)}{\widehat{X}_r}\widehat{x}_r(\tau), \tag{8b}$$

$$\frac{\Omega^2\widehat{X}_r\sin(\theta)}{\Omega\widehat{X}_m}\widehat{x}_m'(\tau)+\widehat{f}_{dm}=-\frac{\widehat{F}_e\sin(\phi_m)}{\Omega\widehat{X}_m}\widehat{x}_m'(\tau), \tag{8c}$$

$$\frac{(1+\mu)\widehat{X}_m+\widehat{X}_r\cos(\theta)}{\widehat{X}_m}\widehat{x}_m''(\tau)+\widehat{f}_{sm}=\frac{\widehat{F}_e\cos(\phi_m)}{\widehat{X}_m}\widehat{x}_m(\tau), \tag{8d}$$

where $\widehat{x}_r'(\tau)=-\Omega\widehat{X}_r\sin(\Omega\tau+\phi_r)$, $\widehat{x}_r''(\tau)=-\Omega^2\widehat{X}_r\cos(\Omega\tau+\phi_r)$, $\widehat{x}_m'(\tau)=-\Omega\widehat{X}_m\sin(\Omega\tau+\phi_m)$, $\widehat{x}_m''(\tau)=-\Omega^2\widehat{X}_m\cos(\Omega\tau+\phi_m)$, and $\theta=\phi_m-\phi_r$.

Combining equations (7a)–(7d) and (8a)–(8d), the amplitude-frequency equations of equations (4a) and (4b) are given by

$$\widetilde{\alpha}_r\approx\widehat{F}_e\sin(\phi_r)+\Omega^2\widehat{X}_m\sin(\phi_r-\phi_m), \tag{9a}$$

$$\widetilde{\beta}_r-\Omega^2\widehat{X}_r\approx\widehat{F}_e\cos(\phi_r)+\Omega^2\widehat{X}_m\cos(\phi_r-\phi_m), \tag{9b}$$

$$\widetilde{\alpha}_m\approx\widehat{F}_e\sin(\phi_m)+\Omega^2\widehat{X}_r\sin(\phi_m-\phi_r), \tag{9c}$$

$$\widetilde{\beta}_m-(1+\mu)\Omega^2\widehat{X}_m\approx\widehat{F}_e\cos(\phi_m)+\Omega^2\widehat{X}_r\cos(\phi_m-\phi_r). \tag{9d}$$

3.2. Jacobi Elliptic Function Solutions. Using Jacobi elliptic functions, we assume that the steady-state solutions of equations (4a) and (4b) are in the following form:

$$\widehat{x}_r(\tau)=\widehat{X}_r\mathrm{cn}(\psi_r|m_r), \tag{10a}$$

$$\widehat{x}_r'(\tau)=-\widehat{X}_r\omega_r\mathrm{sn}(\psi_r|m_r)\mathrm{dn}(\psi_r|m_r), \tag{10b}$$

$$\widehat{x}_m(\tau)=\widehat{X}_m\mathrm{cn}(\psi_m|m_m), \tag{10c}$$

$$\widehat{x}_m'(\tau)=-\widehat{X}_m\omega_m\mathrm{sn}(\psi_m|m_m)\mathrm{dn}(\psi_m|m_m), \tag{10d}$$

where $\psi_r=\omega_r\tau+\varphi_r$ and $\psi_m=\omega_m\tau+\varphi_m$ are the complete phases, m_r and m_m are the squares of the elliptic modulus, ω_r and ω_m are the Jacobi elliptic frequencies, and φ_r and φ_m are the Jacobi phases of the corresponding displacement responses, respectively. It should also be noticed that $\partial\mathrm{cn}(\psi|m)/\partial\psi=-\mathrm{sn}(\psi|m)\mathrm{dn}(\psi|m)$. Following a similar procedure in [33], the relationship between the second derivative and the linear and cubic terms of equations (10a) and (10c) are given by

$$\widehat{x}_r''(\tau)=-\omega_r^2(1-2m_r)\widehat{x}_r(\tau)-\frac{2m_r\omega_r^2\widehat{x}_r(\tau)^3}{\widehat{X}_r^2}, \tag{11a}$$

$$\widehat{x}_m''(\tau)=-\omega_m^2(1-2m_m)\widehat{x}_m(\tau)\frac{2m_m\omega_m^2\widehat{x}_m(\tau)^3}{\widehat{X}_m^2}. \tag{11b}$$

Substituting equations (10a) and (10c) and equations (11a) and (11b) into equations (8b) and (8d), respectively, the equations of the cosine harmonic component become

$$\frac{\widehat{X}_r+\widehat{X}_m\cos(\theta)}{\widehat{X}_r}\left(\omega_r^2(1-2m_r)\widehat{x}_r(\tau)+\frac{2m_r\omega_r^2\widehat{x}_r(\tau)^3}{\widehat{X}_r^2}\right)=\left(\Omega_1^2-\frac{\widehat{F}_e\cos(\phi_r)}{\widehat{X}_r}\right)\widehat{x}_r(\tau)+\gamma_1\widehat{x}_r(\tau)^3, \tag{12a}$$

$$\frac{(1+\mu)\widehat{X}_m+\widehat{X}_r\cos(\theta)}{\widehat{X}_m}\left(\omega_m^2(1-2m_m)\widehat{x}_m(\tau)+\frac{2m_m\omega_m^2\widehat{x}_m(\tau)^3}{\widehat{X}_m^2}\right)=\left(\Omega_2^2-\frac{\widehat{F}_e\cos(\phi_m)}{\widehat{X}_m}\right)\widehat{x}_m(\tau)+\gamma_2\widehat{x}_m(\tau)^3. \tag{12b}$$

Equating the coefficients of $\widehat{x}_r(\tau)$ and $\widehat{x}_r(\tau)^3$ of equation (12a), the coefficients of $\widehat{x}_m(\tau)$ and $\widehat{x}_m(\tau)^3$ of equation (12b) give

$$\omega_r^2=\frac{\Omega_1^2\widehat{X}_r-\widehat{F}_e\cos(\phi_r)+\gamma_1\widehat{X}_r^3}{\left(\widehat{X}_r+\widehat{X}_m\cos(\theta)\right)}, \tag{13a}$$

$$m_r=\frac{\gamma_1\widehat{X}_r^3}{2\left(\Omega_1^2\widehat{X}_r-\widehat{F}_e\cos(\phi_r)+\gamma_1\widehat{X}_r^3\right)}, \tag{13b}$$

$$\omega_m^2=\frac{\Omega_2^2\widehat{X}_m-\widehat{F}_e\cos(\phi_m)+\gamma_2\widehat{X}_m^3}{(1+\mu)\widehat{X}_m+\widehat{X}_r\cos(\theta)}, \tag{13c}$$

$$m_m=\frac{\gamma_2\widehat{X}_m^3}{2\left(\Omega_2^2\widehat{X}_m-\widehat{F}_e\cos(\phi_m)+\gamma_2\widehat{X}_m^3\right)}. \tag{13d}$$

When $\Omega_1^2>0$, $\Omega_2^2>0$, $\gamma_1>0$, and $\gamma_2>0$, the relationship between the excited frequency Ω and the Jacobi elliptic frequencies ω_r and ω_m can be expressed as

$$\Omega=\frac{\pi\omega_r}{2K(m_r)}=\frac{\pi\omega_m}{2K(m_m)}, \tag{14}$$

where $K(m_r)$ and $K(m_m)$ are the complete elliptic integrals of the first kind when $0<m_r,m_m<1/2$.

3.3. Modifying the Stiffness Force Components. Because equations (7a) and (7d) are the first-order harmonic components, both the damping force components $\widetilde{\alpha}_r$ and $\widetilde{\alpha}_m$ and the stiffness force components $\widetilde{\beta}_r$ and $\widetilde{\beta}_m$ are approximate terms. The stiffness force components $\widetilde{\beta}_r$ and $\widetilde{\beta}_m$ are first modified using Jacobi elliptic functions.

Using equation (14), $\phi_r = \pi\varphi_r/2K(m_r)$, and $\phi_m = \pi\varphi_m/2K(m_m)$, equations (7b) and (7d) can be rewritten as

$$\widetilde{\beta}_r \approx \frac{\omega_r}{2K(m_r)} \int_0^{(4K(m_r)/\omega_r)} \widehat{f}_{sr}(\widehat{x}_r, \widehat{x}_r')\cos\left(\frac{\pi\psi_r}{2K(m_r)}\right)\mathrm{d}\tau, \tag{15a}$$

$$\widetilde{\beta}_m \approx \frac{\omega_m}{2K(m_m)} \int_0^{(4K(m_m)/\omega_m)} \widehat{f}_{sm}(\widehat{x}_m, \widehat{x}_m')\cos\left(\frac{\pi\psi_m}{2K(m_m)}\right)\mathrm{d}\tau. \tag{15b}$$

Substituting the first Fourier series expansion of $\mathrm{cn}(\psi_r|m_r) \approx c_r\cos(\pi\psi_r/2K(m_r))$ and $\mathrm{cn}(\psi_m|m_m) \approx c_m\cos(\pi\psi_m/2K(m_m))$, where $\pi\psi_r/2K(m_r)$ and $\pi\psi_m/2K(m_m)$ are the approximate phases of the displacement responses $\widehat{x}_r$ and $\widehat{x}_m$ respectively, into equations (15a) and (15b), the modified stiffness components become

$$\widetilde{\beta}_{re} \approx \frac{1}{2c_rK(m_r)} \int_0^{4K(m_r)} \widehat{f}_{sr}(\widehat{x}_r, \widehat{x}_r')\mathrm{cn}(\psi_r|m_r)\mathrm{d}\psi_r, \tag{16a}$$

$$\widetilde{\beta}_{me} \approx \frac{1}{2c_mK(m_m)} \int_0^{4K(m_m)} \widehat{f}_{sm}(\widehat{x}_m, \widehat{x}_m')\mathrm{cn}(\psi_m|m_m)\mathrm{d}\psi_m, \tag{16b}$$

where $c_r = 2\pi\sqrt{q_r}/\sqrt{m_r}K(m_r)(1+q_r)$, $c_m = 2\pi\sqrt{q_m}/\sqrt{m_m}K(m_m)(1+q_m)$, $q_r = \exp(-\pi K(1-m_r)/K(m_r))$, and $q_m = \exp(-\pi K(1-m_m)/K(m_r))$.

3.4. Modifying the Damping Force Components. Similar to the stiffness force components modification, equations (7a) and (7c) can be expressed as

$$\widetilde{\alpha}_r \approx \frac{\omega_r}{2K(m_r)} \int_0^{(4K(m_r)/\omega_r)} \widehat{f}_{dr}(\widehat{x}_r, \widehat{x}_r')\sin\left(\frac{\pi\psi_r}{2K(m_r)}\right)\mathrm{d}\tau, \tag{17a}$$

$$\widetilde{\alpha}_m \approx \frac{\omega_m}{2K(m_m)} \int_0^{(4K(m_m)/\omega_m)} \widehat{f}_{dm}(\widehat{x}_m, \widehat{x}_m')\sin\left(\frac{\pi\psi_m}{2K(m_m)}\right)\mathrm{d}\tau. \tag{17b}$$

Substituting the first Fourier series expansion of $\mathrm{sn}(\psi_r|m_r)\mathrm{dn}(\psi_r|m_r) \approx a_r\sin(\pi\psi_r/2K(m_r))$ and $sn(\psi_m|m_m)\mathrm{dn}(\psi_m|m_m) \approx a_m\sin(\pi\psi_m/2K(m_m))$ into equations (17a) and (17b), the modified damping components become

$$\widetilde{\alpha}_{re} \approx \frac{1}{2a_rK(m_r)} \int_0^{4K(m_r)} \widehat{f}_{dr}(\widehat{x}_r, \widehat{x}_r')\mathrm{sn}(\psi_r|m_r)\mathrm{dn}(\psi_r|m_r)\mathrm{d}\psi_r, \tag{18a}$$

$$\widetilde{\alpha}_{me} \approx \frac{1}{2a_mK(m_m)} \int_0^{4K(m_m)} \widehat{f}_{dm}(\widehat{x}_m, \widehat{x}_m')\mathrm{sn}(\psi_m|m_m)\mathrm{dn}(\psi_m|m_m)\mathrm{d}\psi_m, \tag{18b}$$

where $a_r = \pi^2\sqrt{q_r}/\sqrt{m_r}K^2(m_r)(1+q_r)$ and $a_m = \pi^2\sqrt{q_m}/\sqrt{m_m}K^2(m_m)(1+q_m)$.

3.5. EHBM. When the modified stiffness and damping force components shown in equations (16a), (16b), (18a), and (18b) are obtained, we rewrite equations (9a)–(9d) as

$$\widetilde{\alpha}_{re} \approx \widehat{F}_e\sin(\phi_r) + \Omega^2\widehat{X}_m\sin(\phi_r - \phi_m), \tag{19a}$$

$$\widetilde{\beta}_{re} - \Omega^2\widehat{X}_r \approx \widehat{F}_e\cos(\phi_r) + \Omega^2\widehat{X}_m\cos(\phi_r - \phi_m), \tag{19b}$$

$$\widetilde{\alpha}_{me} \approx \widehat{F}_e\sin(\phi_m) + \Omega^2\widehat{X}_r\sin(\phi_m - \phi_r), \tag{19c}$$

$$\widetilde{\beta}_{me} - (1+\mu)\Omega^2\widehat{X}_m \approx \widehat{F}_e\cos(\phi_m) + \Omega^2\widehat{X}_r\cos(\phi_m - \phi_r). \tag{19d}$$

Using equations (9a)–(9d) and (19a)–(19d), we plot the orthogonal relationship between force components on m_{s1} and m_{s2} in Figures 2(a) and 2(b), respectively. It shows how the EHBM improves the accuracy of the results.

4. Force and Displacement Transmissibility

This section solves the transmissibility of the two-stage nonlinear vibration isolator using the HBM1 and EHBM and discusses the results.

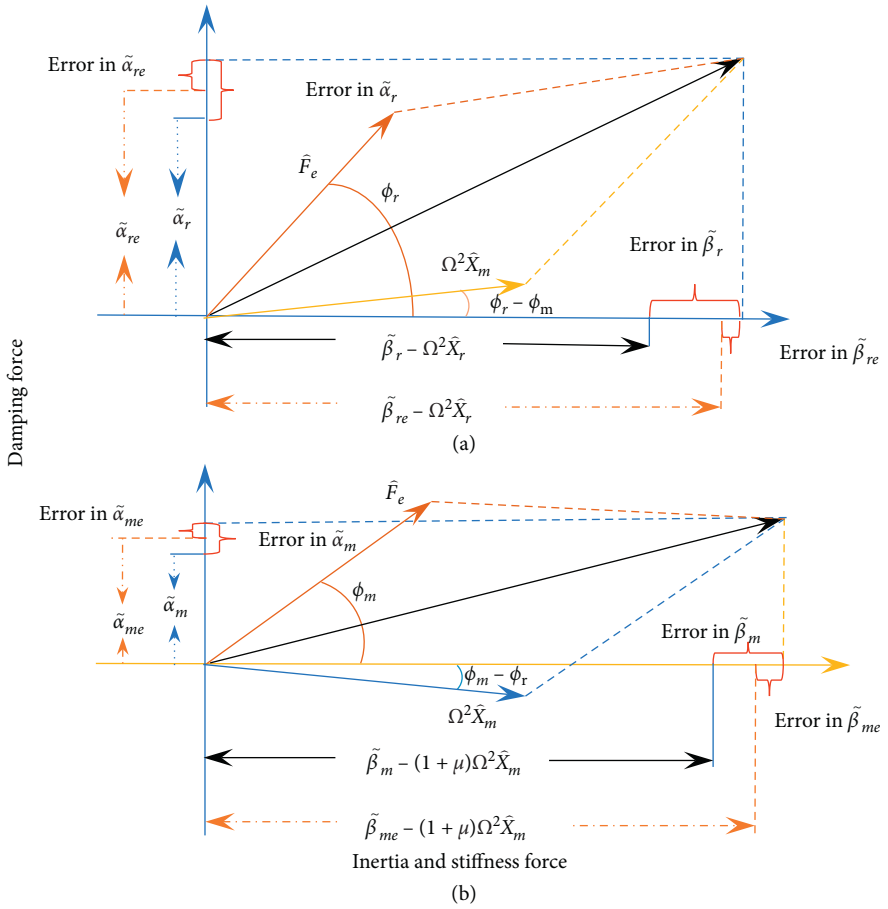

Figure 2: The orthogonal relationship between force components.

4.1. Amplitude-Frequency Characteristics. Integrating equations (7a)–(7d) and substituting the results into equations (9a)–(9d), we obtain

$$-\hat{X}_r\Omega\left(2\zeta_{v1} + \zeta_{n1}\hat{X}_r^2\right) \approx \hat{F}_e \sin(\phi_r) + \Omega^2\hat{X}_m \sin(\phi_r - \phi_m), \tag{20a}$$

$$\Omega_1^2\hat{X}_r + \frac{3\gamma_1\hat{X}_r^3}{4} - \Omega^2\hat{X}_r \approx \hat{F}_e \cos(\phi_r) + \Omega^2\hat{X}_m \cos(\phi_r - \phi_m), \tag{20b}$$

$$-\hat{X}_m\Omega\left(2\zeta_{v2} + \zeta_{n2}\hat{X}_m^2\right) \approx \hat{F}_e \sin(\phi_m) + \Omega^2\hat{X}_r \sin(\phi_m - \phi_r), \tag{20c}$$

$$\Omega_2^2\hat{X}_m + \frac{3\gamma_2\hat{X}_m^3}{4} - (1+\mu)\Omega^2\hat{X}_m \approx \hat{F}_e \cos(\phi_m) + \Omega^2\hat{X}_r \cos(\phi_m - \phi_r). \tag{20d}$$

Integrating equations (16a), (16b), (18a), and (18b), in which the nondimensional nonlinear stiffness forces $\hat{f}_{sr} = \Omega_1^2\hat{X}_r \mathrm{cn}(\psi_r|m_r) + \gamma_1(\hat{X}_r \mathrm{cn}(\psi_r|m_r))^3$ and $\hat{f}_{sm} = \Omega_2^2\hat{X}_m \mathrm{cn}(\psi_m|m_m) + \gamma_2(\hat{X}_m \mathrm{cn}(\psi_m|m_m))^3$ and the nondimensional nonlinear damping forces $\hat{f}_{dr} = (2\zeta_{v1} + 4\zeta_{n1}(\hat{X}_r \mathrm{cn}(\psi_r|m_r))^2)(-\hat{X}_r\omega_r \mathrm{sn}(\psi_r|m_r)\mathrm{dn}(\psi_r|m_r))$ and $\hat{f}_{dm} = (2\zeta_{v2} + 4\zeta_{n2}(\hat{X}_m \mathrm{cn}(\psi_m|m_m))^2)(-\hat{X}_m\omega_m \mathrm{sn}(\psi_m|m_m)\mathrm{dn}(\psi_m|m_m))$, yields

$$\widetilde{\alpha}_{re} \approx \frac{-4\widehat{X}_r\omega_r}{a_r}\left(\zeta_{v1}R_1 + 2\zeta_{n1}\widehat{X}_r^2R_2\right), \tag{21a}$$

$$\widetilde{\alpha}_{me} \approx \frac{-4\widehat{X}_m\omega_m}{a_m}\left(\zeta_{v2}R_3 + 2\zeta_{n2}\widehat{X}_m^2R_4\right), \tag{21b}$$

$$\widetilde{\beta}_{re} \approx \frac{2\widehat{X}_r}{c_r}\left(\Omega_1^2R_5 + \gamma_1\widehat{X}_r^2R_6\right), \tag{21c}$$

$$\widetilde{\beta}_{me} \approx \frac{2\widehat{X}_m}{c_m}\left(\Omega_2^2R_7 + \gamma_2\widehat{X}_m^2R_8\right), \tag{21d}$$

where R_1 to R_8 are given in Appendix A.

Substituting equations (21a) and (21b) into equations (19a) and (19c), respectively, and combining equation (14), we can numerically solve the amplitudes ($\widehat{X}_r$ and $\widehat{X}_m$) and phases (ϕ_r and ϕ_m) of the steady-state response of the two-stage nonlinear isolator.

The amplitude-frequency solutions obtained using the HBM1 and EHBM are plotted in Figure 3. The numerical solutions calculated using the fourth-order Runge-Kutta method with a step-size control algorithm are also plotted. The parameters are $\mu = 0.2$, $\zeta_{v1} = \zeta_{v2} = 0.01$, $\zeta_{h1} = \zeta_{h2} = 0.1$, $k_{v2}/k_{v1} = 1$, $k_{h1}/k_{v1} = k_{h2}/k_{v1} = 0.5$, $\widehat{l} = 0.7$, and $\widehat{F}_e = 1$. The EHBM improves the accuracy of the amplitude-frequency curve around the peak region. In the low-amplitude regime, the solutions of both the EHBM and HBM1 are compared well with the numerical results.

When $\widehat{l} = 0.7$ and the nondimensional linear stiffness terms $k_{v2}/k_{v1} = 1$ and $k_{h1}/k_{v1} = k_{h2}/k_{v1} = 7/6$, the system becomes a two-stage QZS system. The amplitude-frequency curves of the relative displacement between m_{s1} and m_{s2} of the two-stage geometrically nonlinear isolation system, when $\mu = 0.2$, $\zeta_{v1} = \zeta_{v2} = 0.01$, $\zeta_{h1} = \zeta_{h2} = 0.1$, $k_{v2}/k_{v1} = 1$, $k_{h1}/k_{v1} = k_{h2}/k_{v1} = 7/6$, $\widehat{l} = 0.7$, and $\widehat{F}_e = 0.01$, 0.1, 1, and 10, respectively, are plotted in Figure 4. When the system becomes a QZS system, the solutions of the EHBM can still be compared well with the numerical solutions. To improve the accuracy of the harmonic balance method, we should include enough terms and the calculation complexity is simultaneously increased [25]. Because the base displacement x_e is zero, the displacement of the upper mass m_{s2} $x_2 = x_m$. The amplitude-frequency curves of m_{s2} of the two-stage geometrically nonlinear isolation system are plotted in Figure 5, and the accuracy of the EHBM can be seen.

To investigate the accuracy of the EHBM at different damping cases, we choose $\zeta_{v1} = \zeta_{v2} = 0.02$ and $\zeta_{h1} = \zeta_{h2} = 0.2$ as Case 1 and $\zeta_{v1} = \zeta_{v2} = 0.03$ and $\zeta_{h1} = \zeta_{h2} = 0.3$ as Case 2. The system parameters are the same as those in Figure 5 and $\widehat{F}_e = 0.1$. The results are shown in Figure 6. The EHBM works well for these two cases.

This two-stage nonlinear isolation system extends the frequency range of isolation to low frequencies [13]. Furthermore, as shown in Figures 3–6, the values of the relative amplitude between upper and lower stages in the resonance region are at a similar level, but in the high frequency region, the isolation performance of the lower stage is better than that of the upper stage.

4.2. Force Transmissibility. The force transmissibility of the two-stage nonlinear isolator is expressed by [11]

$$\left|T_F\right| = \frac{\widehat{F}_m}{\widehat{F}_e}, \tag{22}$$

where the nondimensional force transmitted from m_{s2} to the ground can be written as

$$\widehat{f}_m\left(\widehat{x}_m, \widehat{x}_m'\right) = 2\zeta_{v2}\widehat{x}_m'(\tau) + 4\zeta_{n2}\widehat{x}_m(\tau)^2\widehat{x}_m'(\tau) + \Omega_2^2\widehat{x}_m(\tau) + \gamma_2\widehat{x}_m(\tau)^3. \tag{23}$$

Substituting the amplitude of the first-order component of $\widehat{F}_m$ obtained from equation (23) into equation (22) yields

$$\left|T_F\right| = \frac{1}{\widehat{F}_e}\sqrt{\left(-\frac{4\omega_m\widehat{X}_m}{a_m}\left(\zeta_{v2}R_3 + 2\zeta_{n2}\widehat{X}_m^2R_4\right)\right)^2 + \left(\frac{2\widehat{X}_m}{c_m}\left(\Omega_2^2R_7 + \gamma_2\widehat{X}_m^2R_8\right)\right)^2}. \tag{24}$$

When the numerical solution of equations (4a) and (4b) is obtained, the force transmissibility can be solved using equation (24) and is shown in Figure 7. It can be seen that the solution of the EHBM can be compared well with the numerical results. More detailed analyses of the force transmissibility are given in [11–15].

4.3. Displacement Transmissibility. The solutions of equations (5a) and (5b) can be assumed as equations (6a) and (6b) or equations (10a)–(10d). The amplitude-frequency equations of the two-stage geometrically nonlinear isolation system with base excitation obtained by using the HBM1 are given by

$$\widetilde{\alpha}_r \approx \Omega^2\left(\widehat{X}_e\sin\left(\phi_r\right) - \widehat{X}_m\sin\left(\theta\right)\right), \tag{25a}$$

$$\widetilde{\beta}_r - \Omega^2\widehat{X}_r \approx \Omega^2\left(\widehat{X}_m\cos\left(\theta\right) + \widehat{X}_e\cos\left(\phi_r\right)\right), \tag{25b}$$

$$\widetilde{\alpha}_m \approx \Omega^2\left((1+\mu)\widehat{X}_e\sin\left(\phi_m\right) + \widehat{X}_r\sin\left(\theta\right)\right), \tag{25c}$$

$$\widetilde{\beta}_m - (1+\mu)\Omega^2\widehat{X}_m \approx \Omega^2\left((1+\mu)\widehat{X}_e\cos\left(\phi_m\right) + \widehat{X}_r\cos\left(\theta\right)\right), \tag{25d}$$

where the expressions of $\widetilde{\alpha}_r$, $\widetilde{\beta}_r$, $\widetilde{\alpha}_m$, and $\widetilde{\beta}_m$ are the same as in equations (20a)–(20d).

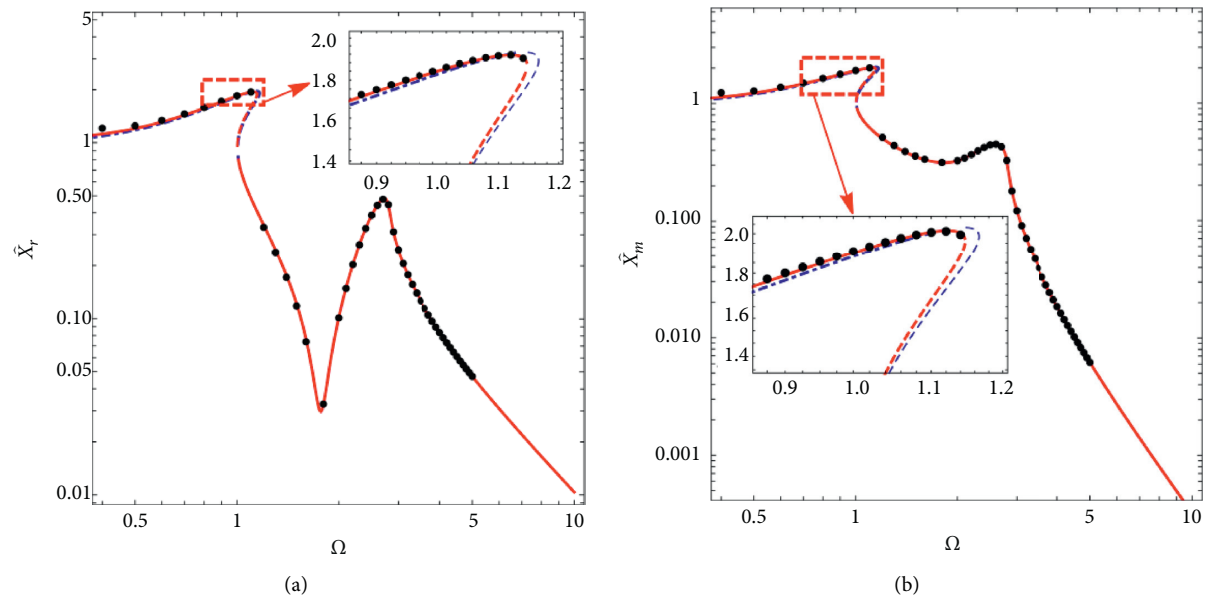

FIGURE 3: (a) Amplitude-frequency curves of the relative displacement between m_{s1} and m_{s2}. (b) Amplitude-frequency curves of m_{s2}, when $\mu = 0.2$, $\zeta_{v1} = \zeta_{v2} = 0.01$, $\zeta_{h1} = \zeta_{h2} = 0.1$, $k_{v2}/k_{v1} = 1$, $k_{h1}/k_{v1} = k_{h2}/k_{v1} = 0.5$, $\tilde{l} = 0.7$, and $\tilde{F}_e = 1$. Dashed-dotted line —·—, stable solution by the HBM1; thin-dashed line — —, unstable solution by the HBM1; solid line ——, stable solution by the EHBM; thick-dashed line — —, unstable solution by the EHBM; dot •, numerical results.

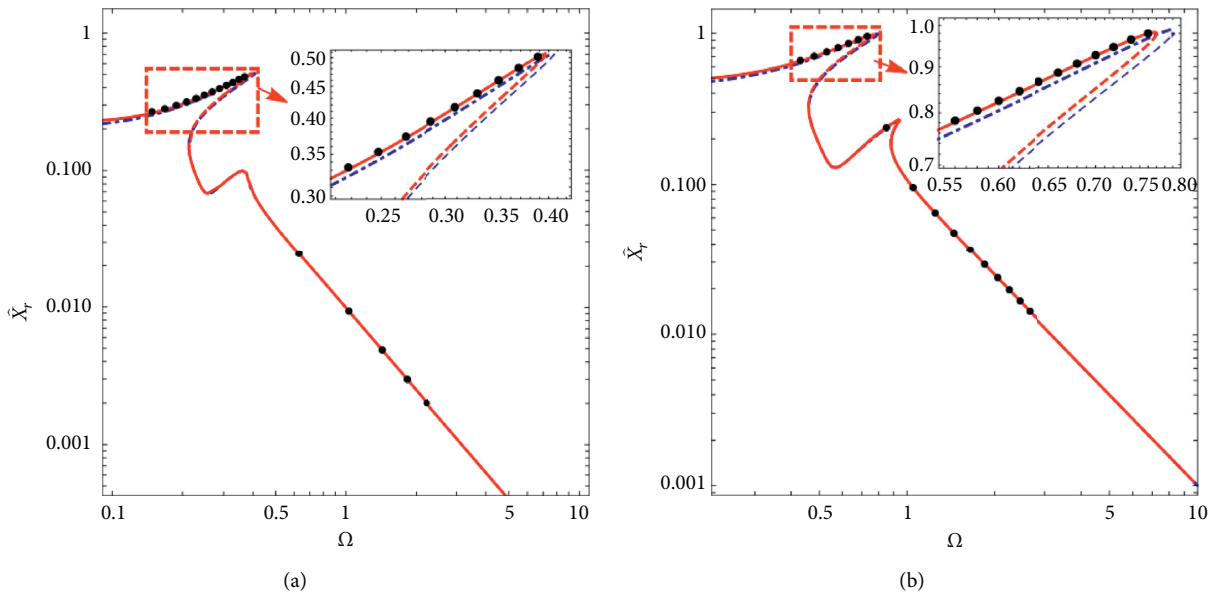

FIGURE 4: Continued.

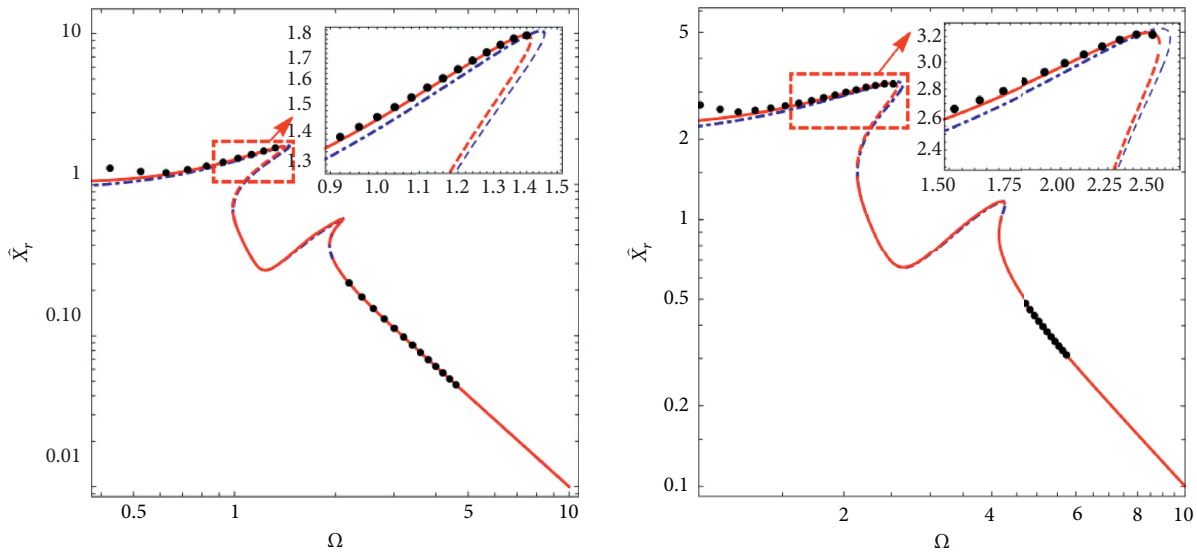

(c) (d)

Figure 4: Amplitude-frequency curves of the relative displacement between m_{s1} and m_{s2} when $\mu = 0.2$, $\zeta_{v1} = \zeta_{v2} = 0.01$, $\zeta_{h1} = \zeta_{h2} = 0.1$, $k_{v2}/k_{v1} = 1$, $k_{h1}/k_{v1} = k_{h2}/k_{v1} = 7/6$, $\hat{l} = 0.7$, and (a) $\hat{F}_e = 0.01$, (b) $\hat{F}_e = 0.1$, (c) $\hat{F}_e = 1$, and (d) $\hat{F}_e = 10$, respectively. Dashed-dotted line —·—, stable solution by the HBM1; thin-dashed line — —, unstable solution by the HBM1; solid line ——, stable solution by the EHBM; thick-dashed line — —, unstable solution by the EHBM; dot •, numerical results.

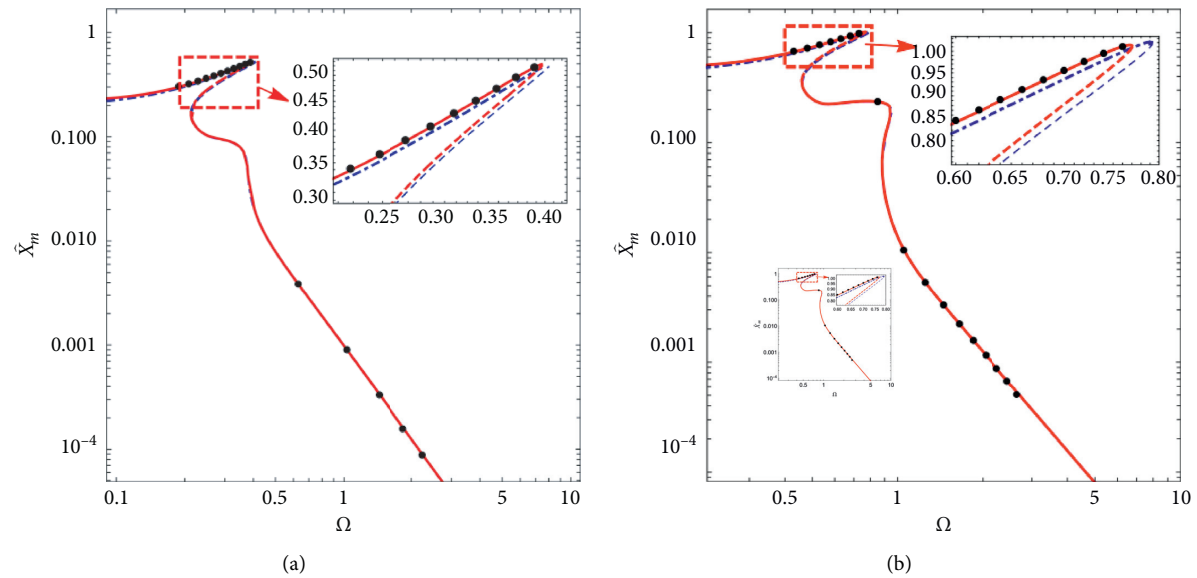

(a) (b)

Figure 5: Continued.

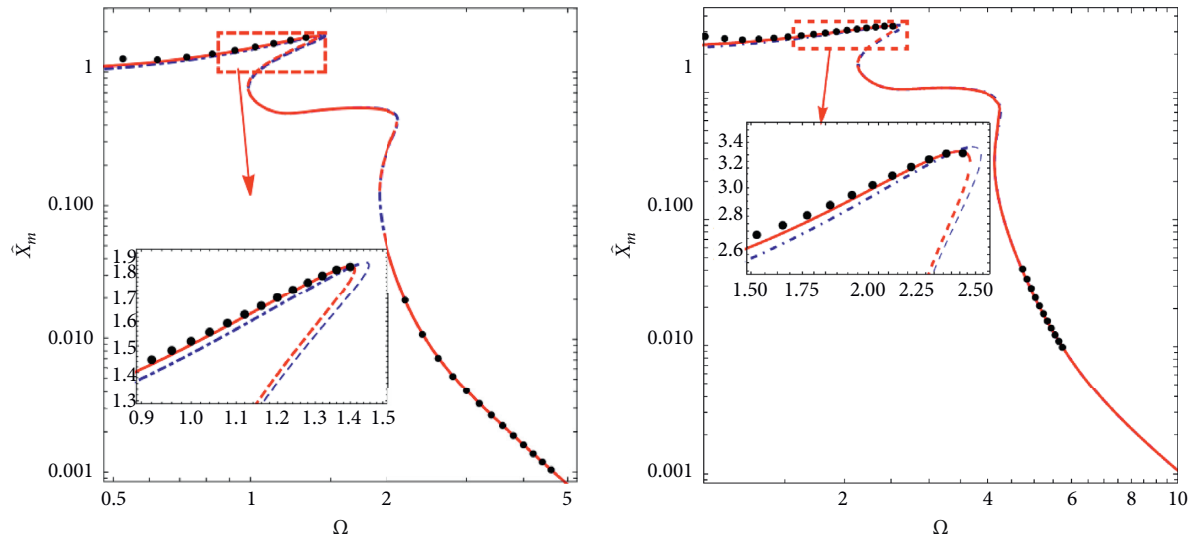

FIGURE 5: Amplitude-frequency curves of m_{s2} when $\mu = 0.2$, $\zeta_{v1} = \zeta_{v2} = 0.01$, $\zeta_{h1} = \zeta_{h2} = 0.1$, $k_{v2}/k_{v1} = 1$, $k_{h1}/k_{v1} = k_{h2}/k_{v1} = 7/6$, $\hat{l} = 0.7$, and (a) $\hat{F}_e = 0.01$, (b) $\hat{F}_e = 0.1$, (c) $\hat{F}_e = 1$, and (d) $\hat{F}_e = 10$, respectively. Dashed-dotted line —·—, stable solution by the HBM1; thin-dashed line — —, unstable solution by the HBM1; solid line ——, stable solution by the EHBM; thick-dashed line — —, unstable solution by the EHBM; dot •, numerical results.

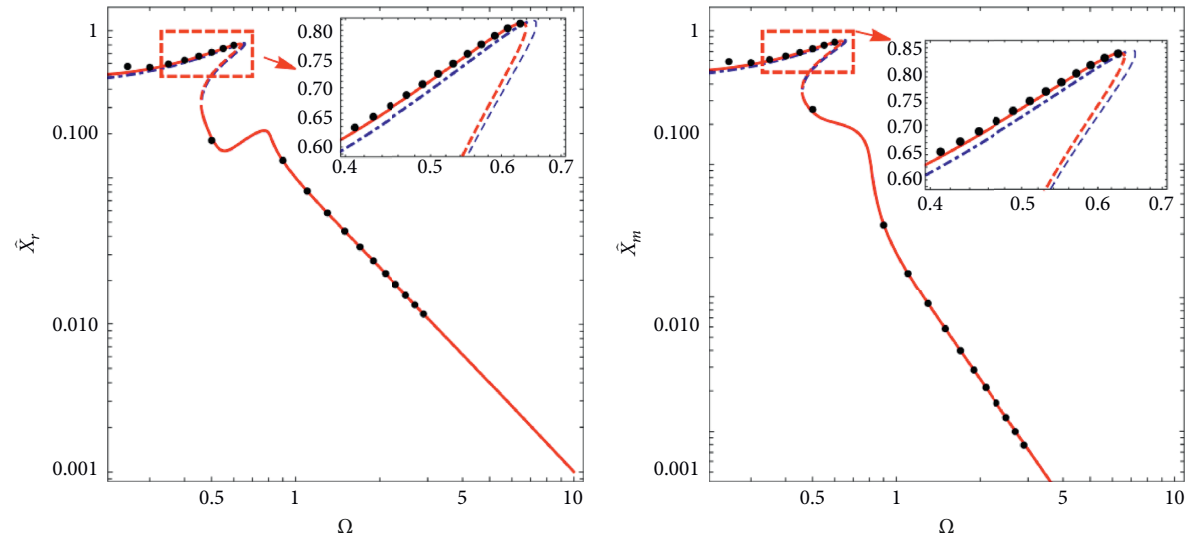

FIGURE 6: Continued.

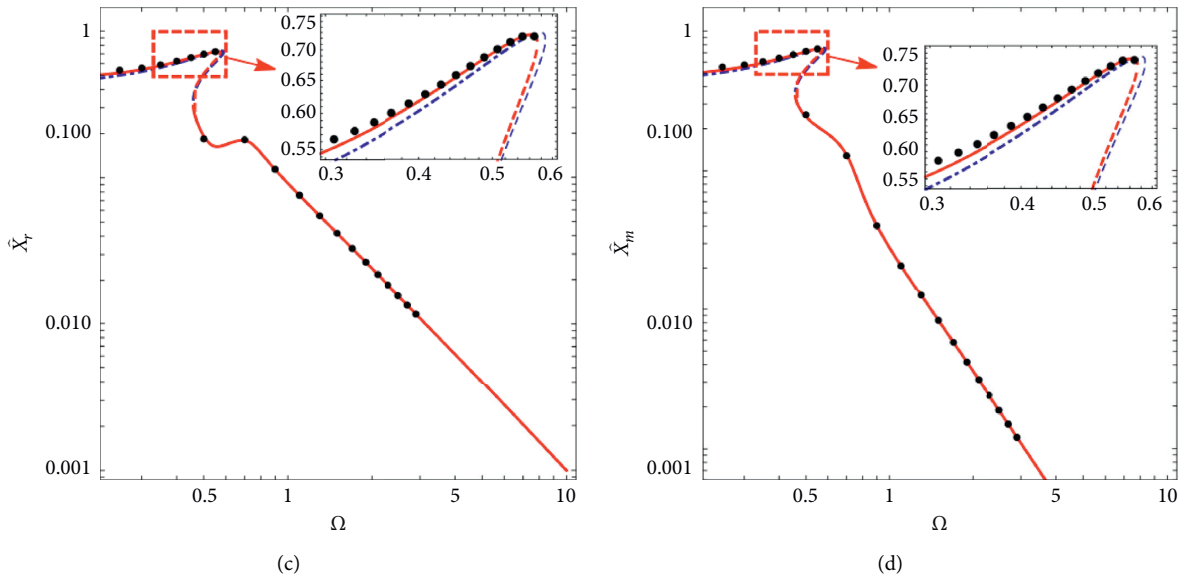

FIGURE 6: (a) and (c) are amplitude-frequency curves of the relative displacement between m_{s1} and m_{s2}, and (b) and (d) are amplitude-frequency curves of m_{s2}, when $\mu = 0.2$, (a-b) $\zeta_{v1} = \zeta_{v2} = 0.02$, and $\zeta_{h1} = \zeta_{h2} = 0.2$, (c-d) $\zeta_{v1} = \zeta_{v2} = 0.03$ and $\zeta_{h1} = \zeta_{h2} = 0.3$, and $k_{v2}/k_{v1} = 1$, $k_{h1}/k_{v1} = k_{h2}/k_{v1} = 7/6$, $\hat{l} = 0.7$, and $\hat{F}_e = 0.1$. Dashed-dotted line —·—, stable solution by the HBM1; thin-dashed line — —, unstable solution by the HBM1; solid line ——, stable solution by the EHBM; thick-dashed line — —, unstable solution by the EHBM; dot •, numerical results.

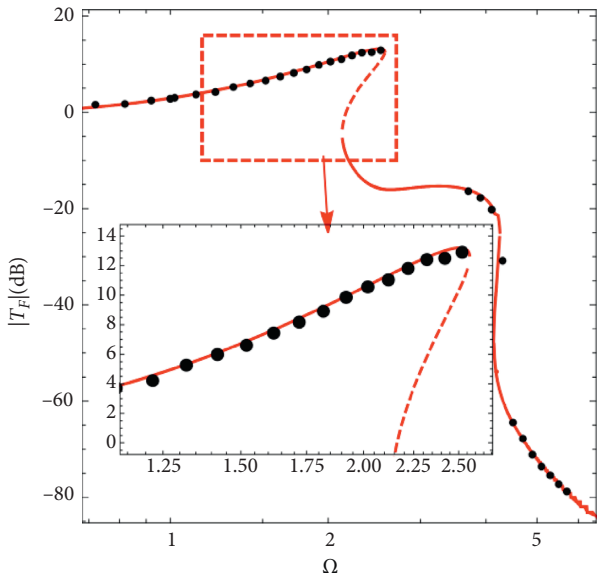

FIGURE 7: Force transmissibility when $\mu = 0.2$, $\zeta_{v1} = \zeta_{v2} = 0.01$, $\zeta_{h1} = \zeta_{h2} = 0.1$, $k_{v2}/k_{v1} = 1$, $k_{h1}/k_{v1} = k_{h2}/k_{v1} = 7/6$, $\hat{l} = 0.7$, and $\hat{F}_e = 10$. Solid line ——, stable solution by the EHBM; dashed line — —, unstable solution by the EHBM; dot •, numerical results.

Substituting $\tilde{\alpha}_{re}$, $\tilde{\beta}_{re}$, $\tilde{\alpha}_{me}$, and $\tilde{\beta}_{me}$, which are given in equations (21a)–(21d), into equations (25a)–(25d), respectively, we can obtain the results of the EHBM. The square of the elliptic modulus and the Jacobi frequency functions are given by $m_r = \gamma_1 \hat{X}_r^2/2(\Omega_1^2 + \gamma_1 \hat{X}_r^2)$, $m_m = \gamma_2 \hat{X}_m^2/2$ $(\Omega_2^2 + \gamma_2 \hat{X}_m^2)$, $\omega_r^2 = (\Omega_1^2 + \gamma_1 \hat{X}_r^2)\hat{X}_r/(\hat{X}_r + \hat{X}_m \cos(\theta) + \hat{X}_e \cos(\phi_r))$, and $\omega_m^2 = (\Omega_2^2 + \gamma_2 \hat{X}_m^2)/((1+\mu) + ((1+\mu)\hat{X}_e \cos(\phi_m) + \hat{X}_r \cos(\theta))/\hat{X}_m)$. Using $\Omega = \pi\omega_r/2K(m_r) = \pi\omega_m/2K(m_m)$ and equations (25a) and (25c), the amplitudes ($\hat{X}_r$ and $\hat{X}_m$) and phases (ϕ_r and ϕ_m) of the steady-state response can be solved using the EHBM. The relative and absolute displacement transmissibilities can be determined by $|T_r| = |\hat{x}_1 - \hat{x}_e|/\hat{X}_e = \sqrt{(\hat{X}_r \sin(\phi_r) + \hat{X}_m \sin(\phi_m))^2 + (\hat{X}_r \cos(\phi_r) + \hat{X}_m \cos(\phi_m))^2}/\hat{X}_e$ and $|T_d| = |\hat{x}_1|/\hat{X}_e = \sqrt{(\hat{X}_r \cos(\phi_r) + \hat{X}_m \cos(\phi_m) + \hat{X}_e)^2 + (\hat{X}_r \sin(\phi_r) + \hat{X}_m \sin(\phi_m))^2}/$

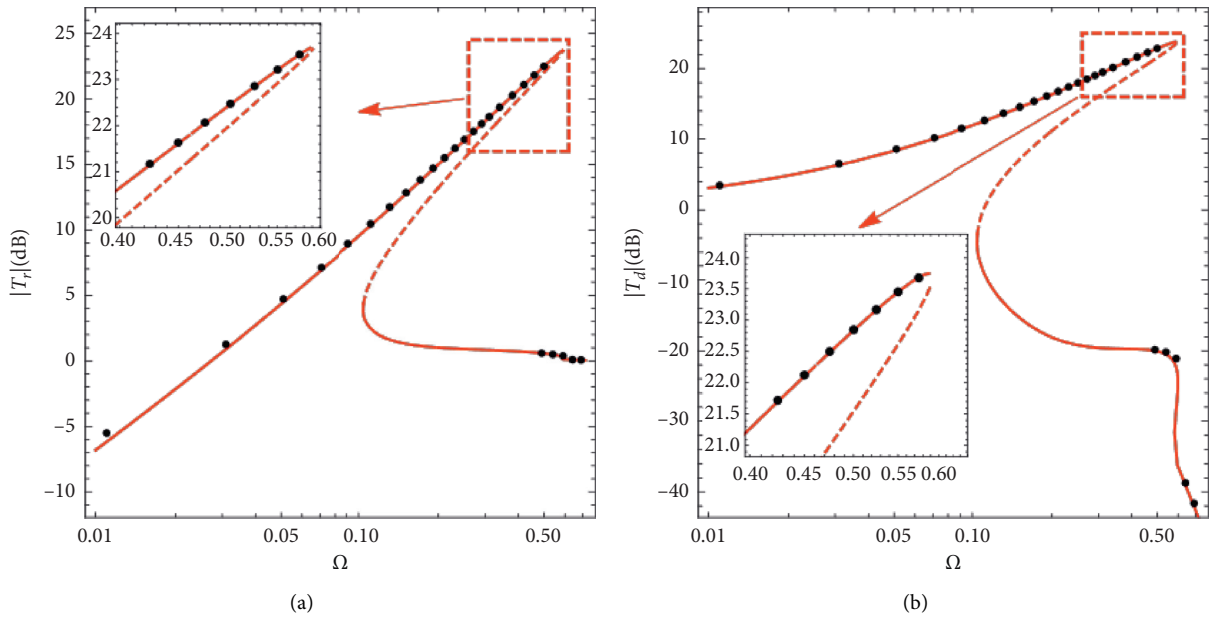

FIGURE 8: (a) Relative displacement transmissibility and (b) absolute displacement transmissibility when $\mu = 0.2$, $\zeta_{v1} = \zeta_{v2} = 0.01$, $\zeta_{h1} = \zeta_{h2} = 0.1$, $k_{v2}/k_{v1} = 1$, $k_{h1}/k_{v1} = k_{h2}/k_{v1} = 7/6$, $\widehat{l} = 0.7$, and $\widehat{X}_e = 0.1$. Solid line ——, stable solution by the EHBM; dashed line — —, unstable solution by the EHBM; dot •, numerical results.

$\widehat{X}_e$ and are shown in Figure 8. The solutions of the EHBM are compared well with the numerical results. More detailed analyses of the isolation characteristics are given in [11–15].

5. Conclusions

This study concerns an elliptic harmonic balance method (EHBM) used to calculate the force and displacement transmissibility of a two-stage nonlinear vibration isolator with geometric stiffness and damping. Through the first-order harmonic balance method (HBM1), we can obtain the amplitude-frequency equations of the two-stage nonlinear isolator. The orthogonal relationships between the nondimensional stiffness, damping, inertia, and excitation force components in the two-stage nonlinear isolator have been presented. The relationship between the Jacobi elliptic frequency and modulus and the excitation frequency is obtained during the steady-state response of the system. With the same number of balancing equations as HBM1, the EHBM can improve the accuracy of the harmonic components and perform better than the HBM1 for the solutions of amplitude-frequency response and transmissibility. Furthermore, multistage nonlinear vibration isolation systems can be analysed using the proposed procedure.

Appendix

A. R_1–R_8

$$R_1 = \int_0^{4K(m_r)} \frac{\mathrm{sn}(\psi_r|m_r)^2 \mathrm{dn}\ (\psi_r|m_r)^2 \mathrm{d}\psi_r}{4K(m_r)} = \frac{[(1-m_r)K(m_r) + (2m_r-1)E(m_r)]}{3m_r K(m_r)},$$

$$R_2 = \int_0^{4K(m_r)} \frac{\mathrm{cn}(\psi_r|m_r)^2 \mathrm{dn}\ (\psi_r|m_r)^2 \mathrm{sn}(\psi_r|m_r)^2 \mathrm{d}\psi_r}{4K(m_r)} = \frac{\left[2\left(m_r^2 - m_r + 1\right)E(m_r) - \left(m_r^2 - 3m_r + 2\right)K(m_r)\right]}{15m_r^2 K(m_r)},$$

$$R_3 = \int_0^{4K(m_m)} \frac{\mathrm{sn}(\psi_m|m_m)^2 \mathrm{dn}\ (\psi_m|m_m)^2 \mathrm{d}\psi_m}{4K(m_m)}$$

$$= \frac{\left[(1-m_m)K(m_m) + (2m_m-1)E(m_m)\right]}{3m_m K(m_m)},$$

$$R_4 = \int_0^{4K(m_m)} \frac{\mathrm{cn}(\psi_m|m_m)^2 \mathrm{dn}(\psi_m|m_m)^2 \mathrm{sn}(\psi_m|m_m)^2 \mathrm{d}\psi_m}{4K(m_m)}$$

$$= \frac{\left[2\left(m_m^2 - m_m + 1\right)E(m_m) - \left(m_m^2 - 3m_m + 2\right)K(m_m)\right]}{15m_m^2 K(m_m)},$$

$$R_5 = \int_0^{4K(m_r)} \frac{\mathrm{cn}(\psi_r|m_r)^2 \mathrm{d}\psi_r}{4K(m_r)} = \frac{\left((m_r-1)K(m_r) + E(m_r)\right)}{m_r K(m_r)}, \tag{A.1}$$

$$R_6 = \int_0^{4K(m_r)} \frac{\mathrm{cn}(\psi_r|m_r)^4 \mathrm{d}\psi_r}{4K(m_r)} = \frac{\left(2(2m_r-1)E(m_r) + (m_r-1)(3m_r-2)K(m_r)\right)}{3m_r^2 K(m_r)},$$

$$R_7 = \int_0^{4K(m_m)} \frac{\mathrm{cn}(\psi_m|m_m)^2 \mathrm{d}\psi_m}{4K(m_m)} = \frac{\left((m_m-1)K(m_m) + E(m_m)\right)}{m_m K(m_m)},$$

$$R_8 = \int_0^{4K(m_m)} \frac{\mathrm{cn}(\psi_m|m_m)^4 \mathrm{d}\psi_m}{4K(m_m)} = \frac{\left(2(2m_m-1)E(m_m) + (m_m-1)(3m_m-2)K(m_m)\right)}{3m_m^2 K(m_m)}.$$

where $E(m_m)$ and $E(m_r)$ are the complete elliptic integrals of the second kind of $\hat{x}_m$ and $\hat{x}_r$, respectively.

Data Availability

The research data used to support the findings of this study are included within the article.

Conflicts of Interest

The authors declare that there are no conflicts of interest regarding the publication of this article.

Acknowledgments

The authors acknowledge the support of the National Natural Science Foundation of China (Grant no. 11672058).

References

[1] C. C. Liu, X. J. Jing, S. Daley, and F. M. Li, "Recent advances in micro-vibration isolation," *Mechanical Systems and Signal Processing*, vol. 56-57, pp. 55–80, 2015.

[2] R. A. Ibrahim, "Recent advances in nonlinear passive vibration isolators," *Journal of Sound and Vibration*, vol. 314, no. 3–5, pp. 371–452, 2008.

[3] A. Carrella, M. J. Brennan, and T. P. Waters, "Static analysis of a passive vibration isolator with quasi-zero-stiffness characteristic," *Journal of Sound and Vibration*, vol. 301, no. 3–5, pp. 678–689, 2007.

[4] I. Kovacic, M. J. Brennan, and T. P. Waters, "A study of a nonlinear vibration isolator with a quasi-zero stiffness characteristic," *Journal of Sound and Vibration*, vol. 315, no. 3, pp. 700–711, 2008.

[5] G. N. Jazar, R. Houim, A. Narimani, and M. F. Golnaraghi, "Frequency response and jump avoidance in a nonlinear passive engine mount," *Journal of Vibration and Control*, vol. 12, no. 11, pp. 1205–1237, 2006.

[6] D. Andersen, Y. Starosvetsky, A. Vakakis, and L. Bergman, "Dynamic instabilities in coupled oscillators induced by geometrically nonlinear damping," *Nonlinear Dynamics*, vol. 67, no. 1, pp. 807–827, 2012.

[7] B. Tang and M. J. Brennan, "A comparison of the effects of nonlinear damping on the free vibration of a single-degree-of-freedom system," *Journal of Vibration and Acoustics-Transactions of the ASME*, vol. 134, no. 2, Article ID 024501, 2012.

[8] B. Tang and M. J. Brennan, "A comparison of two nonlinear damping mechanisms in a vibration isolator," *Journal of Sound and Vibration*, vol. 332, no. 3, pp. 510–520, 2013.

[9] B. Balachandran and E. B. Magrab, *Vibrations*, Cambridge University Press, Cambridge, MA, USA, Third edition, 2019.

[10] W. Zou, C. Cheng, R. Ma, Y. Hu, and W. P. Wang, "Performance analysis of a quasi-zero stiffness vibration isolation system with scissor-like structures," *Archive of Applied Mechanics*, vol. 91, pp. 117–133, 2021.

[11] Z. Q. Lu, T. J. Yang, M. J. Brennan, X. H. Li, and Z. G. Liu, "On the performance of a two-stage vibration isolation system which has geometrically nonlinear stiffness," *Journal of Vibration and Acoustics-Transactions of the ASME*, vol. 136, no. 6, Article ID 06501, 2014.

[12] Y. Wang, S. Li, S. A. Neild, and J. Z. Jiang, "Comparison of the dynamic performance of nonlinear one and two degree-of-freedom vibration isolators with quasi-zero stiffness," *Nonlinear Dynamics*, vol. 88, no. 1, pp. 635–654, 2017.

[13] Z. Q. Lu, M. J. Brennan, H. Ding, and L. Q. Chen, "High-static-low-dynamic-stiffness vibration isolation enhanced by damping nonlinearity," *Science China Technological Sciences*, vol. 62, no. 7, pp. 1103–1110, 2019.

[14] Z. Q. Lu, D. Shao, H. Ding, and L. Q. Chen, "Power flow in a two-stage nonlinear vibration isolation system with high-static-low-dynamic stiffness," *Shock and Vibration*, vol. 2018, Article ID 1697639, 13 pages, 2018.

[15] J. Yang, Y. P. Xiong, and J. T. Xing, "Vibration power flow and force transmission behaviour of a nonlinear isolator mounted

on a nonlinear base," *International Journal of Mechanical Sciences*, vol. 115-116, pp. 238–252, 2016.

[16] J. Yang, J. Z. Jiang, and S. A. Neild, "Dynamic analysis and performance evaluation of nonlinear inerter-based vibration isolators," *Nonlinear Dynamics*, vol. 99, no. 3, pp. 1823–1839, 2020.

[17] T. C. Deng, G. L. Wen, H. Ding, Z. Q. Lu, and L. Q. Chen, "A bio-inspired isolator based on characteristics of quasi-zero stiffness and bird multi-layer neck," *Mechanical Systems and Signal Processing*, vol. 145, Article ID 106967, 2020.

[18] R. E. Mickens, *Truly Nonlinear Oscillations: Harmonic Balance, Parameter Expansions, Iteration, and Averaging Methods*, World Scientific, Hackensack, NJ, USA, 2010.

[19] A. H. Nayfeh and D. T. Mook, *Nonlinear Oscillations*, John Wiley and Sons, New York, NY, USA, 1995.

[20] Z. Q. Lu, D. H. Gu, H. Ding, W. Lacarbonara, and L. Q. Chen, "Nonlinear vibration isolation via a circular ring," *Mechanical Systems and Signal Processing*, vol. 136, Article ID 106490, 2020.

[21] S. L. Lau and Y. K. Cheung, "Amplitude incremental variational principle for nonlinear vibration of elastic systems," *Journal of Applied Mechanics*, vol. 48, no. 4, pp. 959–964, 1981.

[22] J. L. Summers and M. D. Savage, "Two timescale harmonic balance. I. Application to autonomous one-dimensional nonlinear oscillators," *Philosophical Transactions of the Royal Society of London Series A-Mathematical Physical and Engineering Sciences*, vol. 340, no. 1659, pp. 473–501, 1992.

[23] B. S. Wu and P. S. Li, "A method for obtaining approximate analytic periods for a class of nonlinear oscillators," *Meccanica*, vol. 36, no. 2, pp. 167–176, 2001.

[24] Y. Zhou, B. S. Wu, C. W. Lim, and W. P. Sun, "Analytical approximations to primary resonance response of harmonically forced oscillators with strongly general nonlinearity," *Applied Mathematical Modelling*, vol. 87, pp. 534–545, 2020.

[25] R. H. Rand, *Lecture Notes on Nonlinear Vibrations*, http://audiophile.tam.cornell.edu/randdocs/nlvibe52.pdf, 2019.

[26] I. Kovacic, L. Cveticanin, M. Zukovic, and Z. Rakaric, "Jacobi elliptic functions: a review of nonlinear oscillatory application problems," *Journal of Sound and Vibration*, vol. 380, pp. 1–36, 2016.

[27] S. B. Yuste and J. D. Bejarano, "Improvement of a Krylov-Bogoliubov method that uses Jacobi elliptic functions," *Journal of Sound and Vibration*, vol. 139, no. 1, pp. 151–163, 1990.

[28] R. V. Roy, "Averaging method for strongly non-linear oscillators with periodic excitations," *International Journal of Non-Linear Mechanics*, vol. 29, no. 5, pp. 737–753, 1994.

[29] J. Yang, Y. P. Xiong, and J. T. Xing, "Dynamics and power flow behaviour of a nonlinear vibration isolation system with a negative stiffness mechanism," *Journal of Sound and Vibration*, vol. 332, no. 1, pp. 167–183, 2013.

[30] Y. M. Chen and J. K. Liu, "Elliptic harmonic balance method for two degree-of-freedom self-excited oscillators," *Communications in Nonlinear Science and Numerical Simulation*, vol. 14, no. 3, pp. 916–922, 2009.

[31] A. Elías-zúñiga and M. F. Beatty, "Elliptic balance solution of two-degree-of-freedom, undamped, forced systems with cubic nonlinearity," *Nonlinear Dynamics*, vol. 49, no. 1-2, pp. 151–161, 2007.

[32] L. Cveticanin, "Vibrations of a coupled two-degree-of-freedom system," *Journal of Sound and Vibration*, vol. 247, no. 2, pp. 279–292, 2001.

[33] W. L. Wu and B. Tang, "An approximate method for solving force and displacement transmissibility of a geometrically nonlinear isolation system," *International Journal of Non-Linear Mechanics*, vol. 125, Article ID 103512, 2020.

[34] A. Carrella, M. J. Brennan, I. Kovacic, and T. P. Waters, "On the force transmissibility of a vibration isolator with quasi-zero-stiffness," *Journal of Sound and Vibration*, vol. 322, no. 4-5, pp. 707–717, 2009.

[35] M. Bikdash, B. Balachandran, and A. Nayfeh, "Melnikov analysis for a ship with a general roll-damping model," *Nonlinear Dynamics*, vol. 6, no. 1, pp. 101–124, 1994.